OXIDATIONAL AND TRIBOLOGICAL STUDIES OF AUSTENITIC STAINLESS STEELS UNDER CO_2 - BASED ENVIRONMENTS.

by

L.R. WALLACE, BSc, MSc.

A Thesis submitted to the
University of Aston in Birmingham
for the degree of

Doctor of Philosophy.

November 1980.

A B S T R A C T

The oxidational and tribological behaviour of austenitic stainless steels under CO_2-based environments is investigated. An oxidising facility capable of simulating AGR-type environment is developed. It is shown that the oxidational behaviour of the AISI 316 and 310 stainless steels follow Wagnerian parabolic kinetics. The behaviour of the AISI 321 stainless steels is shown to be non-parabolic and logarithmic in nature. Such behaviour is shown to be due to the replacement of the Cr_2O_3 oxide by an iron-rich nodular oxide. The nodular oxide is shown to be double layered in structure and consisting of Fe_2O_3 and complex spinel oxides. Reaction-rate constants and Activation energies are determined for parabolic oxidation. Two models based upon electronic transport and elemental diffusion are proposed. It is shown by the electronic model that a three staged oxidation process leads to the anomalous nodular oxidation. The diffusion model predicts alloy-oxide and alloy sub-surface elemental concentrations during oxidation.

Tribological behaviour of the AISI 316 and 310 steels is studied under conditions of room and high temperatures and environments of air and CO_2. The wear of the AISI 316 steels is shown to be transitional, changing from mild to severe wear about a transition load. For the AISI 310 steels no such transitional behaviour is observed; a severe mode of wear is encountered for all conditions. High friction coefficients are observed within a load dependent friction region and low friction coefficient within a load independent friction region. The dominant mild wear mechanisms are shown to be shearing, delamination, ploughing and oxidation. Rhombohedral, Cubic, Spinel and Wustite are shown to be the major constituents of the mild wear debris. Severe adhesive wear is shown to be the dominant mechanism producing severe wear. A contact mechanical model is proposed to understand the mechanisms of shearing and delamination and the major stress components σ_z, σ_r, σ_θ and τ max are determined. Heat flow analysis predict relatively low numbers of contacting asperities and low contact temperatures of $\sim$100°C. Reaction-rate activation energies are predicted to be lower than obtained by static oxidation experiments.

L. R. Wallace. BSc., MSc.
Doctor of Philosophy
1980

Stainless-steel/Oxidation/Friction/Wear/Carbon-dioxide

ACKNOWLEDGMENTS

I wish to thank Professor S.E.Hunt for providing the laboratory facilities. I am greatly indebted to my Supervisor, Dr.T.F.J. Quinn, for his continued advice and encouragement and the benefit of many useful discussions throughout the work.

I also wish to thank Mr.J.Sullivan, Dr.D.M.Rowson and Mr. C.J.Chapman for their comments and suggestions. Thanks are also due to Mr.F.Lane and other members of the Physics technical staff for their helpful assistance. I am grateful to Mr.T.Kennedy, the laboratory superintendent, and his staff for their continued support. My special thanks to Mssrs., R.Howell and S.Fogden for their instructions in the use of the Scanning Electron Microscope and the Electron Probe Micro-Analyser, their assistance and for the use of their laboratory facilities.

Finally, I wish to thank the Central Electricity Generating Board, Berkeley Nuclear Laboratories and in particular Dr.L.A. Mitchell and Mr.S.C.Gordelier for their collaborative support and provision of experimental facilities.

L.R.Wallace,

CONTENTS PAGE

CONTENTS (cont.)

CONTENTS (cont.)

CONTENTS (cont.)

CONTENTS (cont.) PAGE

List of Illustrations.

List of Illustrations (cont.)

List of Illustrations.(cont.)

List of Illustrations (cont.)

List of Illustrations (cont.)

List of Tables.

CHAPTER ONE

INTRODUCTION

1. INTRODUCTION

1.1 Unlubricated Wear

There are many areas of Industry where liquid lubrication is either not practical or extremely undesirable as for example in the Nuclear Power and Aerospace Industries. In such areas where mechanisms commonly have to operate under high temperature, hostile environments and without liquid lubrication, the understanding of the unlubricated condition is of fundamental importance. It is one such area, namely, the Nuclear Power Generation Industry upon which the present work is based.

Wear, in general, whether under lubricated, un-lubricated, hostile or temparate conditions is commonly defined as the gradual removal of discrete particles from the operating surface of a body as a result of relative motion or mechanical action at that surface. Unfortunately however, wear is not such a clear-cut phenomena but as is recognised by many Tribologists is a complex situation consisting of many diverse mechanisms. Many of these mechanisms at any particular instance during wear, as is pointed out by Burwell (1), can operate either singly or in combination. Further complexities are introduced by the recognition of Wrights (2) view that the overall concept of wear cannot merely consist of two solid bodies in sliding contact but must also include wear at a solid surface by its gaseous or liquid environment, and as such include many forms of boundary interaction.

It has been found by workers such as Archard (3) that the wear rates of common engineering materials under unlubricated conditions cover a vast range of approximately five orders

of magnitude whereas the corresponding coefficient of friction fall well within a factor of 10. (4)

In spite of all the published technical data on the wear of engineering materials, a universal law of wear, such as for example Ohm's law in electricity or Newton's laws of motion in mechanics, to embrace the many complex combinations of different wear mechanisms and the wide range of possible wear rates has yet to be proposed.

1.1.1 Classifications of Wear

The various analytical theories of wear, all of which endeavour to quantify observations of wear to the conditions of wear, can be better studied by firstly considering the various classes of wear.

Two groups of workers in the early 1950's, namely, Burwell and Strang (5) and Archard and Hirst (6) originally proposed the major classifications of wear. In general, it was the Burwell and Strang classifications which gained the most support with little support for the Archard and Hirst classifications. However, it is maintained by some, e.g., Quinn (7), that most of the Burwell and Strang classifications are special cases of the simpler classifications proposed by Archard and Hirst, namely, those of Mild and Severe wear.

Mild wear is proposed to be characterised by high contact resistances, small debris particle size and extremely smooth wear surfaces. Severe wear is characterised by low interface contact resistances, large metallic debris particles and gross plastic deformation of the wear surface. However, whilst the classifications define separate modes of wear they do not define specific ranges

of wear rates for each class of wear.

The Burwell and Strang classifications of wear categorise wear into seven major classes: (1) Adhesive wear, (2) Corrosive wear, (3) Surface Fatigue wear, (4) Fretting corrosion, (5) Abrasive wear, (6) Erosional wear and (7) Cavitational wear.

(i) Adhesive Wear

Adhesive wear is proposed to occur under wear circumstances where adhesion, at submicron levels, between the sliding members occurs. In general, it is firstly the adhesive contacts by asperity-asperity interactions, by means of cold welding mechanism, and the subsequent shear and fracturing of the microscopic adhered junctinns which result in adhesive wear. The fracturing of the junctions can lead either to the formation of a wear particle or to the transfer of material to one of the slidng members. It is maintained by Quinn (7) that the severe wear classifications of Archard and Hirst is synonymous to the present adhesive wear classification of Burwell and Strang.

(ii) Corrosive Wear.

In a corrosive environment the products of corrosion may form a thin film on the interacting surfaces of the sliding members, which as a result inhibit further corrosion. However, under the action of sliding, the protective film is removed, either in part or wholly, hence allowing corrosive attack to continue. It is the removal of the corrosion film in this way during sliding which constitutes the wear. If the corrosion product results in the development of a protective film, i.e. in a manner similar to the protective oxide films, then corrosive wear may be classified as a special case of Archard and Hirst's "mild wear" condition. However,

if severe corrosion is obtained where the corrosion product offers little protection to the sliding surfaces then the wear condition may be classified under Archard and Hirst's "severe wear".

(iii) Surface Fatigue Wear

Wear by means of surface fatigue is defined to occur through the application of a high frequency of cyclic loading and unloading contacts at a surface asperity. The contact stresses induced into the substrate as a result of the cyclic loading lead to the nucleation of sub-surface cracks which eventually propogate to the surface to form large scale surface damage and pitting. The pitting phenomenon commonly found at the sliding surfaces of journal roller bearings cams, tappets and gear teeth, for example, are generally considered to be the direct result of surface fatigue wear. Under conditions of severe surface fatigue, wear of the kind characteristic of Archard and Hirst's severe wear can be obtained. However, in general, surface fatigue wear is considered to be representative of mild wear.

(iv) Fretting Wear

The relative tangential displacement between two tightly fitting surfaces in the form of very low-slip amplitude oscillations is considered to lead to fretting wear. The wear debris collected (or trapped) between the sliding surfaces, unable to escape, is considered to induce considerable stresses within the constraining geometries of the components and in addition to behave as a third-body cutting agent. In this way, the initation of fretting wear is thought to occur. It is considered by numerous workers, primarily Quinn, Sullivan and Rowson (8), that fretting wear is also a form of oxidational wear. Since oxidational wear is representative of mild wear it follows therefore, that fretting wear

may also be considered as mild wear.

(v) Abrasive Wear

The sliding action of a rough hard surface, under load, upon a softer smoother substrate is considered to give rise to abrasive wear. The ploughing affect of the hard surface upon the softer substrate, producing well delineated wear grooves, is the primary mechanism initiating abrasive wear. This type of wear is observed to occur in varying degrees of extent at different stages of both mild or severe wear.

1.1.2 Concepts, Theories and Laws of Friction and Wear. Real Area of Contact

An important concept in the study of friction and wear is that of the true or real area of contact between two nominally flat and smooth surfaces. On a microscopic scale, two flat surfaces are seen to be in contact at only a fraction of the apparent area of contact. The determination of this area quantitatively by experiment is difficult to achieve exactly and cannot be deduced by examination of the wear topography. However precisely or approximately the quantity is deduced, this can only be an approximate figure, however, since the magnitude of the contact area continually varies with time of sliding. (9)(10)

Analytically, the true or real area of contact, Ar, is given by the ratio of the applied load, L, to the flow pressure of the softer material. That is,

$$Ar = \frac{L}{pm} \qquad [1.1]$$

Under circumstances where purely elastic contact is made, in which plastic deformation is absent, a much greater area of contact will

be achieved, where the magnitude of the area is given by Hertz's equation for elastic deformation,[11] namely,

$$Ar = 2.9[Lr(\frac{1}{E_1} + \frac{1}{E_2})]^{\frac{2}{3}} \qquad [1.2]$$

assuming that Poisson's ratio for both surfaces is 0.3. In equation [1.2] E_1 and E_2 are the respective Young's Moduli for the sliding members and r is the radius of apparent contact.

(i) Friction

Friction is commonly defined as resistance to motion which exists when a solid object is moved tangentially with respect to the surface of another which it contacts. Quantitatively, friction is expressed in terms of a force, being the force exerted by either of two contacting bodies tending to oppose relative tangential displacement of the other.[12]

Three quantitative relations are required to express the magnitude of the friction force as a function of the principal operating variables, namely, the applied load, the magnitude of the region of contact and the sliding velocity. The quantitative relations are: (1) The friction force, F, is proportional to the normal force, L, that is,

$$F = \mu L$$

where μ is the constant of proportionality and known as the static coefficient of friction. (2) The friction force is independent of the apparent area of contact and (3) the friction force is independent of the sliding velocity v.[13]

It is well known that the friction force required to start sliding is usually greater than the force required to maintain

sliding. This suggests that there are two coefficients of friction, namely, static (for surfaces at rest) and kinetic (for surfaces in motion). Work by Dokes (14), however, has shown that this is a gross over simplification and that the static friction coefficient is a function of the time of contact whereas the kinetic coefficient of friction is a function of velocity.

(ii) Archard's Wear Law

Work carried out by Bowden and Tabor and Archard has shown that it is the areas where real contact is made that are the true load bearing areas and that it is at these regions where the plastic deformation of asperities occur. It is therefore the damage to these load-bearing asperities upon interaction with asperities on the opposite surface, during sliding, that produce wear particles. It is further proposed by Archard (15) that not all load bearing asperity-asperity encounters result in the formation of a wear particle although all such encounters necessarily contribute to the friction.

On the basis of such a simple model, Archard and also Burwell and Strang produced a quantitative relation expressing the total worn volume in terms of Ar, the real area of contact and S, the distance of sliding, in the form:

$$V = KA_rS \qquad [1.3]$$

V in the relation is the sum of all worn particles of volume δV as produced from individual asperity-asperity interactions. K in the relation, known as the wear coefficient defines that not all asperity interactions produce a wear fragment but that only a proportion K do so. From the work done by Archard on a wide range of engineering

materials it is seen that K is very small and less than 1, thus suggesting that an asperity encounter producing a wear fragment is a relatively rare event.

On rewriting Ar of equation [1.3] in the form Ar = L/Pm, where Pm is the flow pressure, we arrive at a wear rate equation which is related directly to the operating conditions, namely the applied load, sliding distance and sliding speed, as given by:

$$w = \frac{V}{S} = \frac{KL}{3Pm} \qquad [1.4]$$

This relation which forms the fundamental law of adhesive wear is based on the principle that each wear fragment is a hemisphere of diameter, d, and that the volume of wear per centimetre of sliding producing the fragment is,

$$\frac{\delta V}{\delta x} = \frac{K \cdot N \cdot \pi d^3}{12} = \frac{kL}{3Pm}$$

where N, the total number of junctions produced per centimetre of sliding = n/d and n, the total number of junctions present at any instant is

$$n = \frac{4Ar}{\pi d^2} = \frac{4L}{\pi Pm d^2}$$

w of equation [1.4] is known as the wear rate, an expression widely used in describing the tribological properties of engineering materials, and is the total volume of material worn per unit sldiing distance.

(iii) Wear Theories

The recent theories of wear which have become increasingly more substantiative are those of (1) the Oxidational

theory of mild wear, originally proposed by Quinn (16) in 1971 and (2) the Delamination wear Theory, proposed by Suh (17) in 1973.

For mild wear, the Oxidational wear theory leads to the following expression for the wear rate (w):-

$$w = \frac{d\ Ap\ .\ \exp(-Qp/RT)L}{\varepsilon_c^2 \cdot \rho_o^2 \cdot f^2 \cdot UPm} \qquad [1.5]$$

where ρ_o is the density of the oxide, f is the fraction of the oxide which is oxygen, U is the linear sliding velocity, d is the distance of sliding contact during which oxidation occurs at a temperature To, Ap is the Arrhenius constant for parabolic oxidation and R is the gas constant.

By rearranging equation [1.5] it is observed that the oxidation theory of mild wear is in accordance with Archard's wear law. That is,

$$w = \left[\frac{d\ Ap\ \exp(-Qp/RT)}{\varepsilon_c^2 \cdot \rho_o^2 \cdot f^2\ U}\right] \frac{L}{Pm} \qquad [1.6]$$

where the portion inside the brackets is the expression for the k-factor of equation [1.3].

The delamination theory of wear, as proposed by Suh in 1973, advances the idea of subsurface crack propagation leading eventually to the delamination of the wear surface into thin wear sheets parallel to the surface. The derivation of the wear equation is based on the removal of a number of layers of surface material of thickness, h, from the wear track. The theory predicts the total wear, w, from both material partners occuring during wear by the relation:

$$w = N_1 h_1 AT_1 + N_2 h_2 AT_2 = \frac{x}{x_{c1}} h_1 AT_1 + \frac{x}{x_{c2}} h_2 AT_2 \qquad [1.7]$$

where h_1, AT_1 and h_2, AT_2 are the removed layer thickness and the

annular wear track areas of the sliding component and the stationary counter component respectively; N, and N_2 are the respective number of layers removed and x is the sliding distance.

Using equation [1.7], Engel (18) shows how Suh's mechanism leads to an expression which is in accordance with Archard's wear law. That is,

$$w = \left[\frac{B_1^1 h_1}{d_{c1}} + \frac{B_2^1 h_2}{d_{c2}}\right] \frac{L}{Pm} \qquad [1.8]$$

where the portion inside the brackets is the expression for the k-factor of equation [1.3].

1.2 Technological Background

The first generation of Britain's Nuclear Power Reactors, namely, the Magnox reactors, have in recent years been in the process of becoming gradually superceded by a second generation of nuclear reactors, namely, the Civil Advanced Gas Cooled Reactors or AGR's.

Their principle mode of operation has been that of using a greatly pressurised continually circulating gas to convey the heat generated at the reactor core to boilers, in which the water is as a result converted to steam. The usage of a pressurised high-speed fluid in this way combined with the associated high temperature environment has led to numerous unforseen engineering and design problems within the AGR's.Essentially, these problems have been those of premature component failure, component deterioration and component malfunction due to excessive wear and corrosion. In many cases the basis of the problems have been identified to be due either directly or indirectly to vibration mechanisms produced by the fluid-flow.

In order that the smooth operation of the reactor is not impaired by component failure, the immediate removal and subsequent replacement of the relevant components must be of vital necessity. However, the mere replacement of failed components is clearly not a sensible solution since synonymous failure would inevitably reoccur. Thus, it is important that the cause and extent of the failure be analysed and diagnosed and that such diagnosis be subsequently used in the modification of the original design to ensure the non-occurence or minimisation of component failure. In the diagnosing and analysing of component failure the principles of Engineering Tribology and associated tribological techniques are found to be most useful.

Component failures and component malfunctions that develop in the AGR's as a result of the fluid flow arise within many areas where close association with the coolant has occurred. Chivers, Gordelier et al (19) report of an example of component damage to the gas-coolant circulators of the AGR's as a result of excessive low amplitude mechanical vibration. They show by tribological examination of the damaged surfaces that wear damage to the isolating dome flange and the scaling ring flange components of the circulators was caused as a result of fretting wear. Since fretting is commonly the result of vibration of very low slip amplitudes it is concluded that the components have experienced vibratory wear failure and must have been subjected to significant gas coolant induced vibration. As a second example, the work by Levy (20) shows that even under well damped conditions vibration can still occur and as a result cause excessive metal-loss. The conditions for effecient heat transfer require turbulent gas coolant

flow. This can cause substantial mechanical vibration of the boiler tubes suspended into the coolant. Normally, the tubes are supported via welds and clamps to minimise the vibration by virtue of coulomb frictional damping. If sufficient damping is not provided ultimate failure of the tube can arise by means of fatigue and impact wear. Assuming sufficient damping, Levy shows that damage still occurs, resulting in excessive metal-loss through wear at the sliding joints.

In addition to the mechanical damage sustained by AGR components, evidence of corrosion damage due to the coolant gas is also widely observed. The codant gas generally used in the AGR's is an accurate and carefully controlled mixture of several gases. The precise composition of the coclant is frequently varied to suit operating conditions but in general the mixture is composed of Co_2 - 1 vol % Co - 300 to 700 VPPmCH_4 - 100 to 200 VPPmH_2 - 250 WPPmH_2O. To all intents and purposes the coolant is predominantly carbon dioxide but the doping of the coolant by small concentrations of carbon monoxide (Co), methane (CH_4) and water, however, serve an important purpose, as described in the following.(21)

In the Advanced gas cooled reactors, a carbon moderator positioned directly in the path of the coolant gas circuit and composed of keyed graphite bricks provides structural support for the fuel elements. Due to the ionisation of the coolant gas and to subsequent radiolytic processes, as shown by Wood (22), oxidation of the moderator-graphite occurs. Such oxidation leads ultimately if not inhibited to a general reduction in density and mechanical strength. Essentially, the oxidation of the moderator

is thought to be caused by the complex positive ion, $(Co_2.Co_2)^+$, which arises as a result of the coolant-gas ionisation. The oxidation can be broadly represented as:

$$(Co_2.Co_2)^+ + C \xrightarrow{e'} 2CO + CO_2$$

To inhibit the moderator corrosion and to protect the structural integrity of the graphite the coolant is doped with small concentrations of carbon monoxide, methane and water vapour. The addition of such gases, in particular carbon monoxide, inhibit graphite corrosion by reacting with the oxidising ions to give other ions which do not attack the graphite. Additionally, the methane and water vapour constituents offer protection by the formation of carbonaceous deposits on the pore surfaces of the moderator, which protect by reacting with the oxidising ions instead of the underlying graphite. (23)

While the doped coolant gas is effecient in the inhibition of the moderator corrosion, the presence of the minority gases affect other plant components in an adverse manner. For example, deposited carbon on the surface of the stainless steel fuel-elements results in distinctly non-beneficial effects since a layer as thin as 50 μm can significantly restrict heat transfer to the gas-coolant and in consequence lead to an increase in the temperature of the fuel. Non-beneficial effects in terms of plant corrosion are also found on other plant components such as boiler tubes, where a corrosion process known as 'breakaway oxidation' affects the strength of the tubes.

Breakaway Oxidation

At the normal operating temperature in high pressure water, steam or carbon dioxide environments, 9%-Cr steel, the material commonly used for boiler tubes, reacts to form a two-layer

spinel-oxide.[24]

$$3M + 4H_2O \longrightarrow M_3O_4 + 4H_2; \quad 3M + 4Co_2 \longrightarrow M_3O_4 + 4CO$$

Here, M represents the metal atoms and M_3O_4 is a protective oxide, which is thought to arise by the diffusion of iron atoms through the growing oxide film to the oxide/oxidant interface where they react to form essentially pure magnetite (Fe_3O_4). Breakaway oxidation arises subsequently, as a result of the reactive carbon monoxide in the coolant diffusing through the magnetite to the metal-oxide interface where reaction with the metal forms a range of chromium and iron carbides. When the metal surface becomes saturated with carbon, the rate of growth of the protective magnetite decreases and the rate of formation of the iron/chromium spinel increases and a more porous structure with a high carbon content develops. The stresses built up are sufficient to push aside the outer magnetite layer. This behaviour is termed 'breakaway oxidation'.

PRESENT WORK

Until recently, oxidation tests showed the austenitic stainless steels to be suitable for use under AGR environments. On the basis of this, high temperature AGR components were fabricated from austenitic steels and subsequently commissioned for reactor operation. Recently, however, initial long-term oxidation tests carried out on actual inoperation stainless steel components have showed evidence of a tendency towards adverse oxidational behaviour.

The specimens investigated for such adverse oxidational behaviour were supplied from the Dungeness and Hinckley AGR power plants and were of the AISI 316 and AISI 321 varieties of

austenitic stainless steels.

These were tested under simulated AGR environments at temperatures of 650°C, coolant-gas pressures of 490-52.5 x 10^2 KN/m^2 and an oxidising coolant-gas mixture of composition Co_2-1 vol% CO-250 wppm H_2O-300 to 700 Vppm CH_4 and 100 to 200 Vppm H_2 for long periods of several thousands of hours. The examination of representative specimens (25) showed that the tested steels were, in general, behaving significantly differently from the vast majority of stainless steel specimens previously tested, under short-term conditions. In general, they were found to show comparatively high weight gains combined with excessive amounts of oxidation. Large localised areas of thick grey oxide in addition to the normal protective oxide were observed to account for the increased oxidation. In the areas where the grey oxide had nucleated much of the normal protective oxide had been removed and partially replaced by the new oxide. (26)

Identification investigations showed that the additional oxidation was not due to the familiar breakaway oxidation but that a significantly different oxidation process had occured. Metallographic examination of the grey oxide found this to be double layered in cross-section, essentially iron enriched, distinctly coarse in character and very different in structure compared to the protective oxides. Due to the double layered nature of the oxide the oxidation process giving rise to the oxide has been collectively referred to as duplex oxidation and the oxides produced by the process termed duplex oxides. In summation, the results of the oxidation tests showed that the oxidational behaviour demonstrated by the Dungeness and Hinckley stainless steels were inconsistent with the normally expected protective oxidation behaviour of austenitic steels.

The morphology of duplex oxides has been reported by several workers (27) to be of uniform or nodular character. Both forms of the oxide have been found to occur in combination. The uniform variety of the oxide is found to nucleate in colonies with eventual coalescence to produce a blanketing surface coverage effect (28). The nodular variety of the oxide however, are found to nucleate singularly and in isolation so as to produce partial surface coverage by isolated mounds of duplex oxide. The nodules of this form of oxide have been shown (29) to be, in general, hemispherical in shape and typically of 10-40 μm in size.

In general, the properties of anomalous oxidational behaviour are such that both forms of duplex oxides are found to occur in combination in which the uniform variey nucleate in well delineated directions whereas the nodular variety nucleate randomly and are normally distributed. Under circumstances, however, where only the nodular oxides nucleate, in the absence of the uniform variety, the original polished stainless steel surface upon which they nucleate can undergo severe metrological consequences. Depending upon the density of nucleation of the nodular oxide, the original smooth and polished surface can be transformed into a greatly coarse and undulating surface. Where, however, uniform oxide is nucleated in combination, the roughening effect of the nodular oxide is diminished since to some extent the hemispherical nodules are buried wuthin the uniform duplex oxide, and the exposed hinterland areas between the oxide nodules are in-filled.

Considering a situation where an austenitic stainless steel component is employed for long term operation within an

Advanced gas cooled reactor, the occurence of duplex oxidation upon its surface can lead, ultimately, to excessive metal loss by oxide formation and to excessive surface roughening by nodular oxide. Under circumstances where excessive metal loss is obtained a general structural weakening of the component may result. Where, however, gross surface roughening is obtained excessive abrasive wear of bearing counter-surfaces can result. Overall, therefore, the effects of duplex oxidation can lead to extensive component damage and to eventual component failure.

The damaging effect of duplex oxidation upon reactor components was originally experienced during component leakage tests on AGR re-entrant seals (i.e. seals associated within the fuelling channelsof the reactor core), Stevens (30). Seals tested on an AGR test-rig for leakage rates and mechanical break-down mechanisms were found to show excessive wear. This represented 7% of the total sliding movement experiencable by the seal in reactor service. Visual inspection of the seals and the seal bore showed discoloration and distinctive roughening of the seal bore. This was diagnosed to be the obvious cause of the rapid attrition of the graphite seals. Subsequent detailed examination of the austenitic stainless steel seal-bore revealed evidence to indicate that, under the conditions obtained in the test rig, considerable degeneration and oxide roughening of the metal surface had taken place (31)(32)(33).

The operating conditions under which excessive wear was experienced were those of high temperature, namely 530°C at the seal bore face, and continuously circulating hot pressurised CO_2

gas at 570°C and 49.0 x 10^2 KN/m^2. The re-entrant seals commonly used in the AGR's are graphite seal mechanisms operating within the fuel channels of the reactor core. Such seals, used to prevent the deviation of the coolant gas from the gas circuit, within the fuel channels, are essential for the efficient operation of the coolant gas circuit and therefore in an indirect manner for the optimum conveyance of heat to the steam generating boilers. The failure of the seals, consequently, due to reasons of excessive wear, for example, would be far-reaching and would ultimately lead to in-efficiencies in performance.

Since, as described above, the surface degradation effects of stainless steels by duplex oxidation can lead ultimately to component failure, by means of excessive wear and/or excessive metal loss, it is evident that the phenomena of duplex oxidation must be fully understood since it is with its understanding that a cure can be effected and component failure minimised. In addition, since the extent to which stainless steel components are damaged, by the roughened duplex-oxidised counterpart surfaces, depend to a large extent upon their intrinsic tribological properties, the fundamental tribological behaviour of austenitic stainless steels must therefore also be well understood, under conditions where their oxidation may occur. The present work, therefore, is in general concerned with the oxidational and tribological behaviour of austenitic stainless steels under conditions of AGR-type environments. In the present work, research has been carried out to investigate (1) the normal and abnormal oxidational characteristics of austenitic stainless steels when subjected to long term

conditions of high temperatures and AGR-type coolant gas environments and (2) the friction and wear behaviour of austenitic stainless steels under conditions of continuous sliding, room and high ambient temperatures and a predominantly carbon dioxide based gas environment.

In relation to the main sections of the work indicated above, an additional third area of interest has involved a study of the wear of graphite by rough counterface surfaces. Since many components in the AGR's utilise the good lubrication and heat resisting properties of graphite in their construction, namely, in particular seals and bearing materials, the potential wear of such elements by oxidation-roughened stainless steel components e.g., the wear of graphite re-entrant seals by oxidised seal bores, must require to be determined and the fundamental mechanisms giving rise to the wear investigated. The third category of the present work has therefore been concerned with the investigation of the wear of graphite, by rough surfaces, under conditions of gas flow between the sliding interfaces and low amplitude reciprocated sliding. An emphasis on the wear of graphite material under gas flow situations is made since it is the components operating under such conditions that have been found to be the most adversley affected by the oxide roughening phenomena.

CHAPTER 2

OXIDATION STUDIES OF AUSTENITIC STAINLESS STEELS.

2.1 OXIDATION EXPERIMENTS

2.1.1 Introduction

The oxidation studies carried out in the present research can be broadly divided into two major areas:

1) Investigations into the affect of simulated Advanced Gas-cooled Reactor (AGR) environments upon the oxidational behaviour of Austenitic stainless steels, and

2) Investigations into the nature and morphology of the resultant oxidation.

By exposing specimens of austenitic stainless steels to conditions of simulated AGR environments and studying the resultant general oxidation and the oxide forms, important information about the corrosion resistance of austenitic stainless steels operating under hostile reactor environments can be gained. Additionally, information can also be acquired on aspects of oxidation kinetics, sub-surface compositional change and surface degradation of the steels as a result of oxidation.

In order to study the oxidational behaviour of the steels when subjected to AGR environments, it was required firstly to develop an oxidation apparatus which could simulate the correct conditions.

2.1.2 Design of the Oxidation Apparatus

The conditions that were required in the simulation of the AGR environments were principally those of high ambient temperatures at 650°C, a continually circulating AGR-type coolant gas and the long-term stability and duration of these conditions.

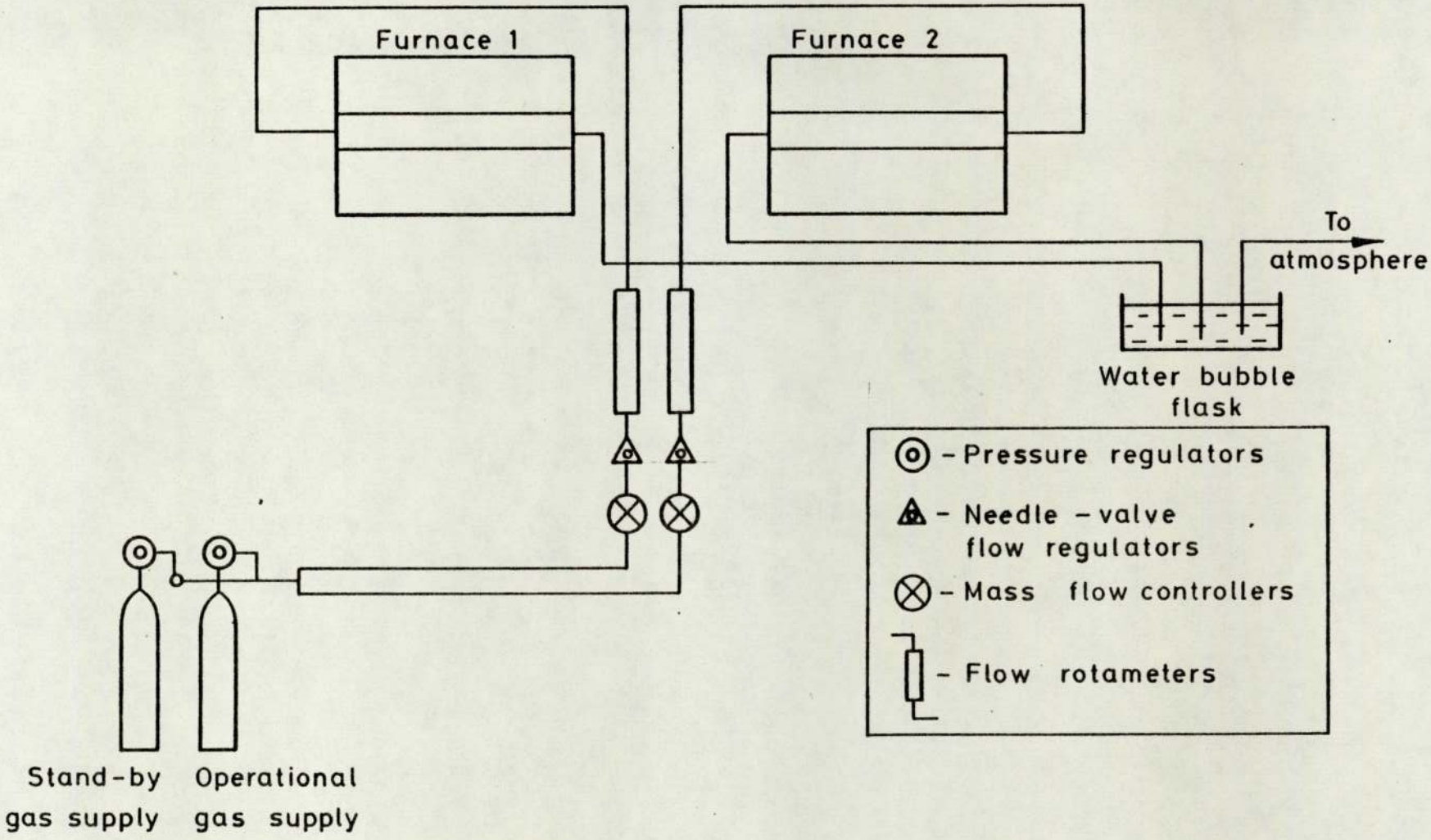

FIG. 2.1 Schematic Circuit Diagram of the Oxidation Apparatus

Other conditions inherent in the Advanced Gas-cooled Reactors, such as the high coolant-gas pressures, nominally set at 4137 KN/m^2 and essential for good heat transfer and thermodynamic qualities, and the high energy radiation, necessary for true simulation, were considered non-contributory factors towards the oxidational behaviour and therefore not simulated.

Additional facilities necessary in an oxidation apparatus capable of simulating AGR environments needed to be the accurate monitoring and control of the gas flow, accurate control of the temerature, continuous long-term operation, a facility allowing specimen removal (without the interruption of gas flow conditions) and finally a leak-proof gas-flow circuit allowing little possibility of gas contamination.

A schematic diagram of the complete oxidation system is illustrated in figure (2.1) and a plate photograph of the assembled system is shown in figure (2.2).

(i) Temperature Monitoring and Control

To provide the continuous high temperatures necessary Wild-Barfield tubular baffle furnaces were employed. Prior to use, the temperature variations, due to radiation losses, along the length of the furnaces were determined and on this basis a central zone where variations were less than 5% used for test purposes.

Ungrounded Thermocouples. To monitor the temperatures Nickel/Chromium versus Nickel/aluminium mineral insulated thermocouples were used. In order to achieve fast measurement response times and to avoid excessive e.m.f. errors due to the switching arrangements of the thermo-

Figure 2.2

General view of the fully assembled Oxidation Apparatus.

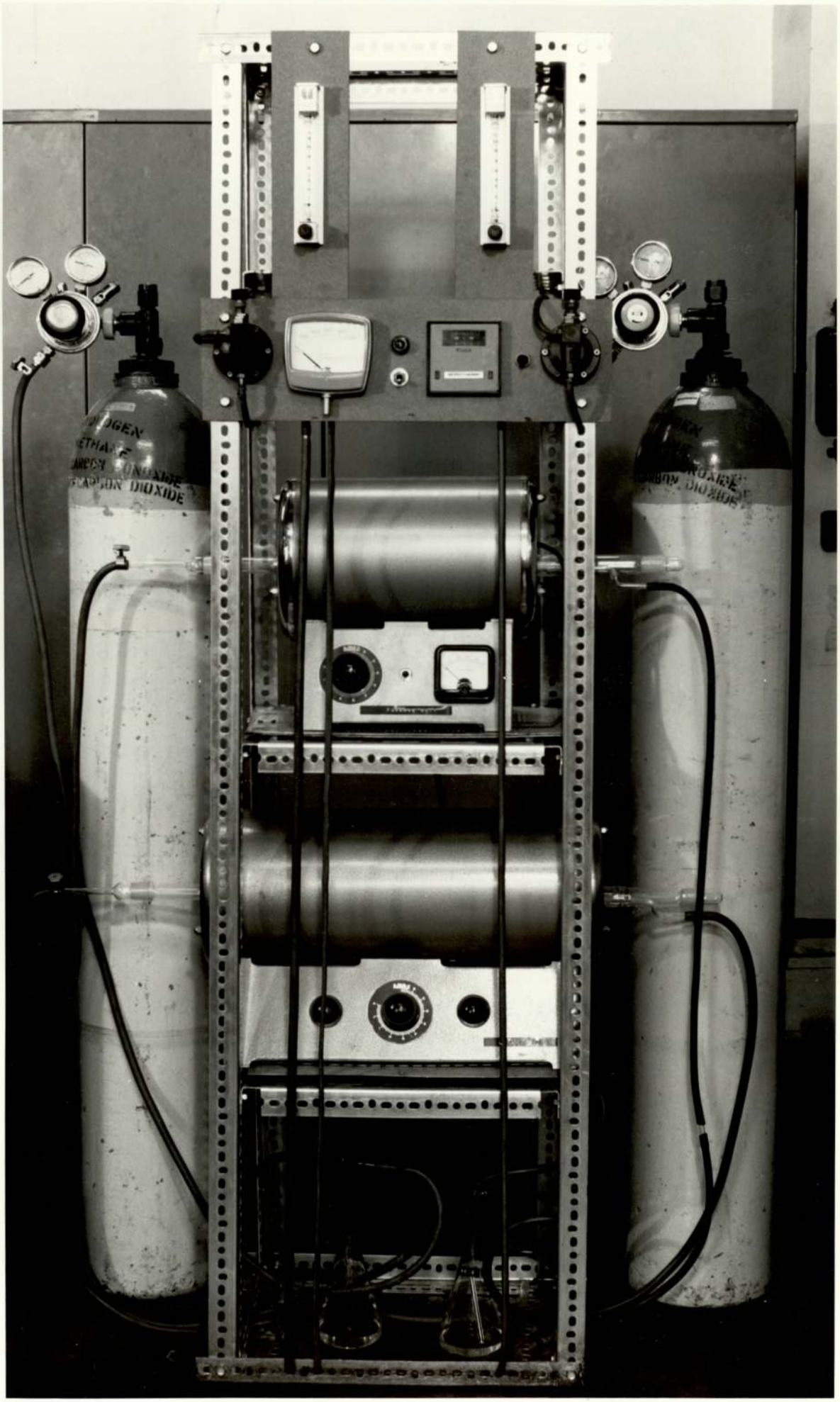
CARBON DIOXIDE

couples, Ungrounded rather than Grounded thermocouples were considered a good choice, in which the hot junctions were totally insulated from the sheath. Since the long-term operation of the thermocouples at high temperatures was essential it was necessary to utilise thermocouples which could be periodically checked for correct operation and insulation breakdown. Such reliability checks could be readily carried out with the ungrounded thermocouples due to their ease of installation and the possibility of measuring their insulation resistance.(34)

Temperature Controllers. To avoid large variations in the heating temperature due to fluctuations in the ambient temperature, as a result of large temperature transitions at night, accurate temperature controlling was considered to be essential. This was achieved by the use of Eurotherm relay-output temperature controllers capable of operation within the temperature range -100°C to +1600°C and suitable for use with Iron/Constantan, Nickel Chrome/Nickel Aluminium and Platinum v Platinium/Rhodium thermocouples. By feeding the thermocouple output voltages into the controller and comparing with a set reference voltage (corresponding to the required operating temperature) and amplifying the resultant error signal and subsequently using this signal to operate a triggered relay, accurate controlling could be obtained. The controllers that were used employed sensitive output relays which could operate with a differential input signal of less than 50mV, equivalent to approximately 1°C change in temperature on base metal thermocouples, hence providing sensitive temperature controlling.

Initially, temperature controlling by means of inexpensive power regulators was attempted. The regulators that were used, which essentially functioned by means of a bimetal pressing, carrying a

heater winding, deflecting to operate a switch when energised, supplied the power, to the heating load, and also provided control by periodically switching the power on and off. The ratio of the on time to the total operational time determined the average power input. However, in view of the large temperature transients at night power regulators were subsequently found to be ineffectual.

(ii) Coolant-gas Simulation

To provide the oxidising environment and the correct oxidising conditions, AGR coolant-gas of composition 1% Carbon monoxide, 0.02% Hydrogen, 0.03% Methane and balance Carbon dioxide, needed to be used. A continuous circulation of the gas at atmospheric pressure was necessary. In view of the latter and of the cost of the gas, a very low flow rate of 15×10^{-6} m^3/min was selected. Such a flow rate would economise on gas consumption and also be sufficiently rapid to prevent a stagnant oxidising environment.

The flowmeters used in the oxidation apparatus were standard 100mm scale meters with angled (as opposed to on-line) Kematal connections in corporating a stainless-steel needle-valve for flow control. Since the flow of a predominantly Co_2 gas was being metered, a flow scale calibrated specifically for Co_2 at N.T.P. was considered necessary instead of an air calibrated scale.

Due to the very low flow rates required, for reasons of economy, an essential feature of the oxidation apparatus needed to be the accurate control of small mass-flows. In addition, the selected flow rates also needed to be accurately maintained for long durations regardless of pressure changes. For these purposes mass-flow control

Figure 2.3 Mass Flow control valve.

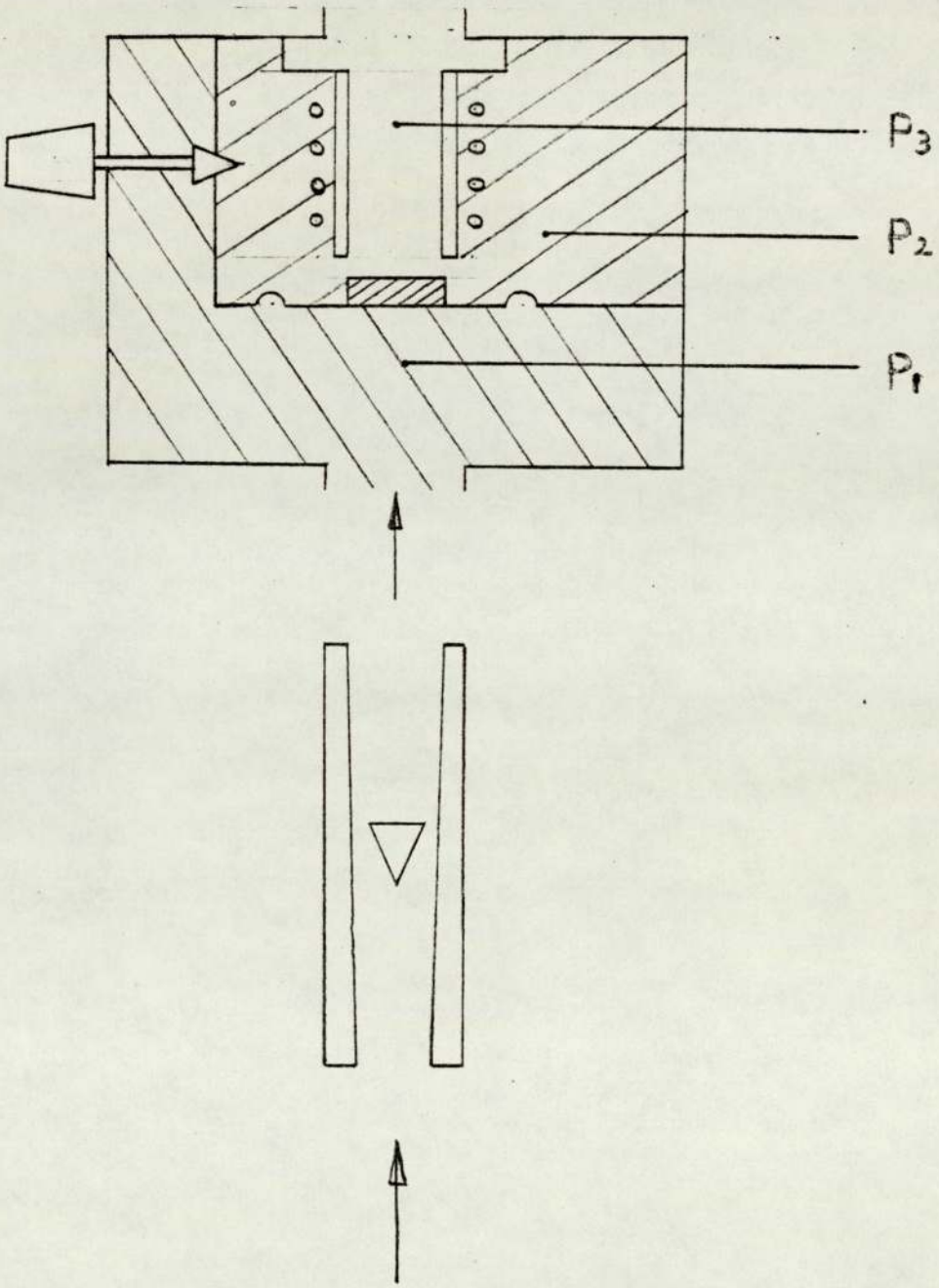

valves were employed. In these, a pressure-responsive diaghragm is used to position the control valve and thereby effect control. A pressure P_1-P_2 (figure 2.3) produced at the flow selector operates the pressure-responsive diaghragm.

Any fluctuation in pressure acting to increase the pressure difference P_1-P_3 moves the valve towards the closed position and restores the flow-rate to the selected value.

(iii) Flow Rate Correction

Density Changes. For realistic flow control, consideration to correction factors for the rate of flow must be given. In general, standard flow-meter scales are calibrated in gas volumes at N.T.P. (20°C, 760torr). Hence the readings of the flow rates are affected if the gas flow conditions are not at N.T.P. It is the changes in the density of the gas, due to variation in temperature and pressure, that give rise to the discrepancies. However, since the oxidation apparatus is designed to operate at atmospheric pressure, over all parts of the gas-flow circuit, the affect of pressure on gas density is considered not significant.

Considering the worst possible case and assuming that the gas flowing through the flow meters is at 100°C, one sixth of the temperature of the oxidising environment, the new density ρ_2 of the gas is then determined by:

$$\rho_2 = \rho_1 \left(\frac{1.013 + PE}{1.013}\right)\left(\frac{293}{273 + TE}\right)$$

where ρ_1 = gas density at N.T.P., PE = effective pressure in bars and TE = effective temperature in °C.

Hence for PE = 1 bar and TE = 100°C and assuming 100% Co_2 gas of ρ_1 = 1.98 $kg.m^{-3}$

$$\rho_2 = 3.09$$

Correction to Volumetric Flow. Using ρ_2, the correction factor f(v) for the volumetric flow scale is therefore:

$$f(v) = \left(\rho_1/\rho_2\right)^{1/2} = 0.64$$

The actual flow rate QF_2 is therefore smaller than the observed flow rate QF_1 by a factor of 0.64 as given by

$$QF_2 = QF_1 \times f(v) = QF_1 \times 0.64$$

In controlling the flow rates it was thus required to adjust observed flow rates to values equal to QF_2, in order to compensate for the high operating temperatures.

To contain the test specimens and the oxidising environment, tubular silica glass specimen chambers of dimensions 2.7 cms I.D. were used. Gas inlet was achieved by means of an inlet injection device; this allowed the removal of specimens without the interruption of the gas flow. Ground glass quick-fit end connections were used and found to be adequately gas-tight at the operating pressures.

Since continuous operation of the oxidation apparatus was required for prolonged periods a stand-by gas supply line was incorporated into the system. This ensured uninterrupted gas supply in the event of gas exhaustion.

2.1.3 Specimen Preparation and Specimen History

(i) Specimen Preparation

The test specimens were initially guillotined from the as-received stainless steel plates and subsequently correctly dimensioned by machining. Due to the structural deformations and stresses introduced into the steels by guillotining it was important to entirely remove the guillotined edge. In this way, the constricted

grain boundaries and the disarranged grain structure, caused by the structural damage, could be eliminated.

Subsequently, the specimens were polished to achieve the necessary surface finish. Commencing with a 100 grit grade of Silicon carbide (SiC) paper, polishing was carried out with increasingly finer grades of SiC paper using a polishing wheel. By this method, a 1-5μm surface finish was given to all test specimens. The effect of surface polishing by SiC paper is to abrade a thin film of base metal from the specimen surface and thereby expose a clean and unoxidised substrate.

Finally, prior to testing, the specimens were marked, for identification purposes, cleaned and degreased with Inhibisol and petroleum vapour and subsequently weighed.

(ii) Specimen History

The austenitic stainless steel materials used as specimens in the investigation were of types AISI 316, AISI 310 and AISI 321. These were supplied in strip form and in the annealed and descaled states. The compositional and mechanical properties of the steels are shown in tables 2.1 and 2.2.

For purposes of the present investigation the specimens were divided into two groups A and B. These were tested separately in separate furnaces of the same oxidation apparatus. Essentially, the group A set of specimens received continuous exposure to AGR conditions for 3500 hours without thermal cycling, whereas group B specimens were regularly cycled at 1000 hour intervals, for a total of 3000 hours. The procedure of periodic shut-down of the oxidation apparatus, allowing specimens to gradually cool to room temperature under the oxidising gas, and the subsequent gradual reheating is

Stainless Steel	Elemental Composition (%)										
	C	Si	Mn	S	P	Ni	Cr	Ti	Mo	Co	Fe
AISI 316	0.05	0.35	1.74	0.021	0.030	11.40	17.2	-	2.55	-	Bar
AISI 310	0.062	0.51	1.45	0.013	0.016	19.09	24.30	-	-	-	Bar
AISI 321	0.05	0.85	1.89	0.019	0.023	10.5	17.1	0.34	-	-	Bar

Table 2.1 Elemental Composition of Austenitic Stainless Steels.

Stainless Steel	Max.Strength $N.mm^{-2}$ Yeild	ULT.	Max.Stress $N.mm^{-2}$ Yeild	ULT.	Elongation %	Izod.Impact $N.mm^{-2}$	Brinell Hardness
AISI 316	244	-	-	562	61.0	265	154
AISI 310	308	-	-	574	56.0	-	167
AISI 321	251	-	-	571	66.0	-	157

TABLE 2.2 Mechanical Properties of Austenitic Stainless Steels.

known as thermal cycling. This treatment is used to induce breakdown of the initial protective oxides.

With the group A set of specimens, the monitoring of oxidational developments was carried out by the examination of discreetly removed representative specimens. Specimens thus removed were not replaced for further oxidising since it was considered that such removal and cooling would simulate thermal cycling. With the group B specimens, the procedure of thermal cycling allowed direct access to all specimens for the purposes of analysis.

2.2 OXIDATION RESULTS

In the present section, the oxidational behaviour of the thermally-cycled stainless steels is discussed. This is described in terms of the surface character of the oxides nucleating on the surfaces of the steels. The oxidational behaviour of the non-cycled steels is described in Chapter 3.

Moreover, the oxidational behaviour as described here is correlated to the gravimetric data in terms of linear, parabolic and logarithmic oxidation kinetics.

2.2.1 The Oxidational Behaviour of the Thermally-Cycled Steels

By using low magnification microscopy, the three types of stainless steels investigated were found to show characteristically different oxidational behaviour.

At 1000 Hours

At the first stage of inspection following 1000 hours of oxidation, the AISI 310 and AISI 316 steels were found to be wholly covered by very thin light-green and light-brown protective

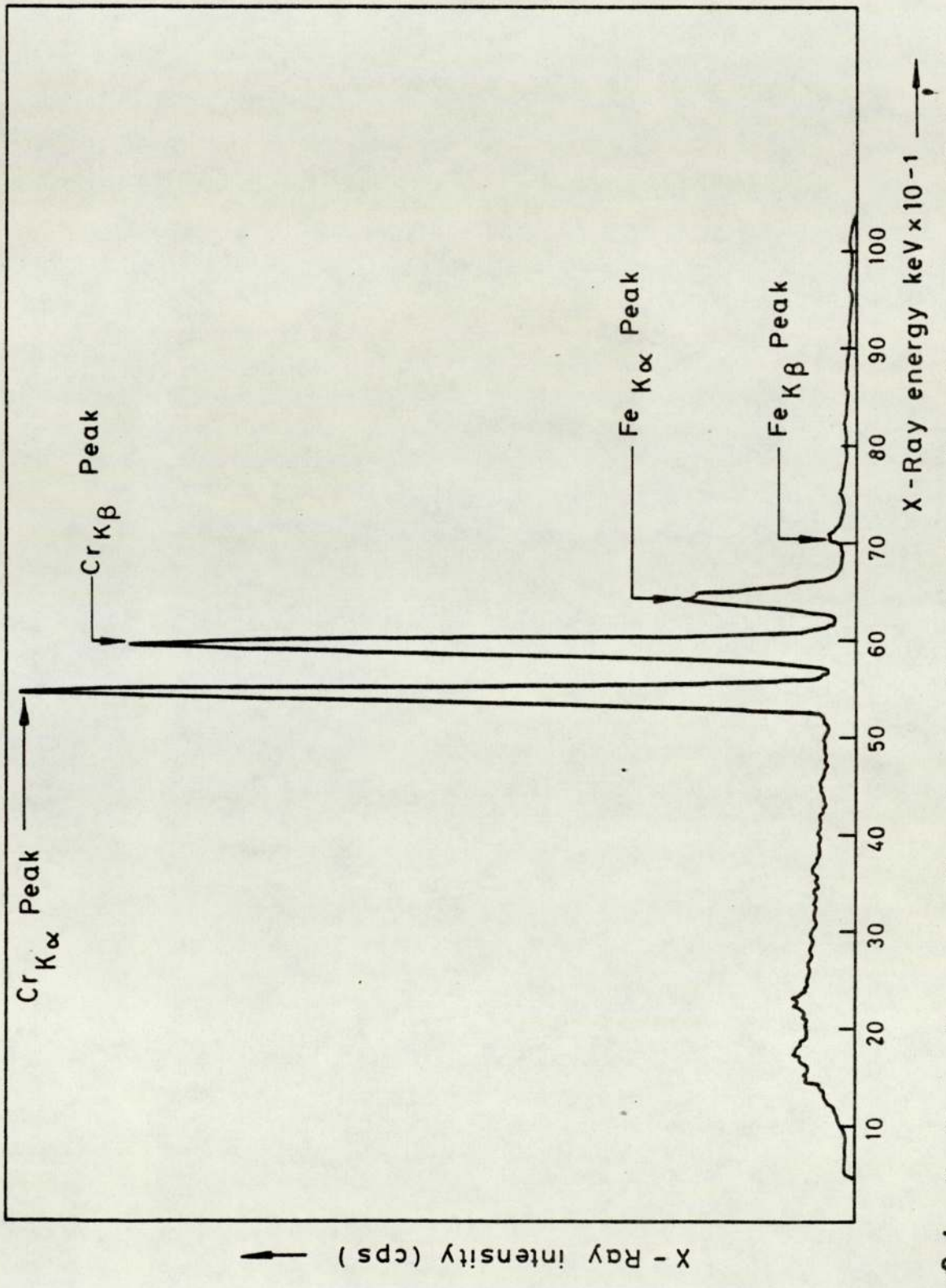

FIG. 2.4 X-Ray Energy Spectrum Illustrating the Chromium Rich Nature of the Protective Oxide.

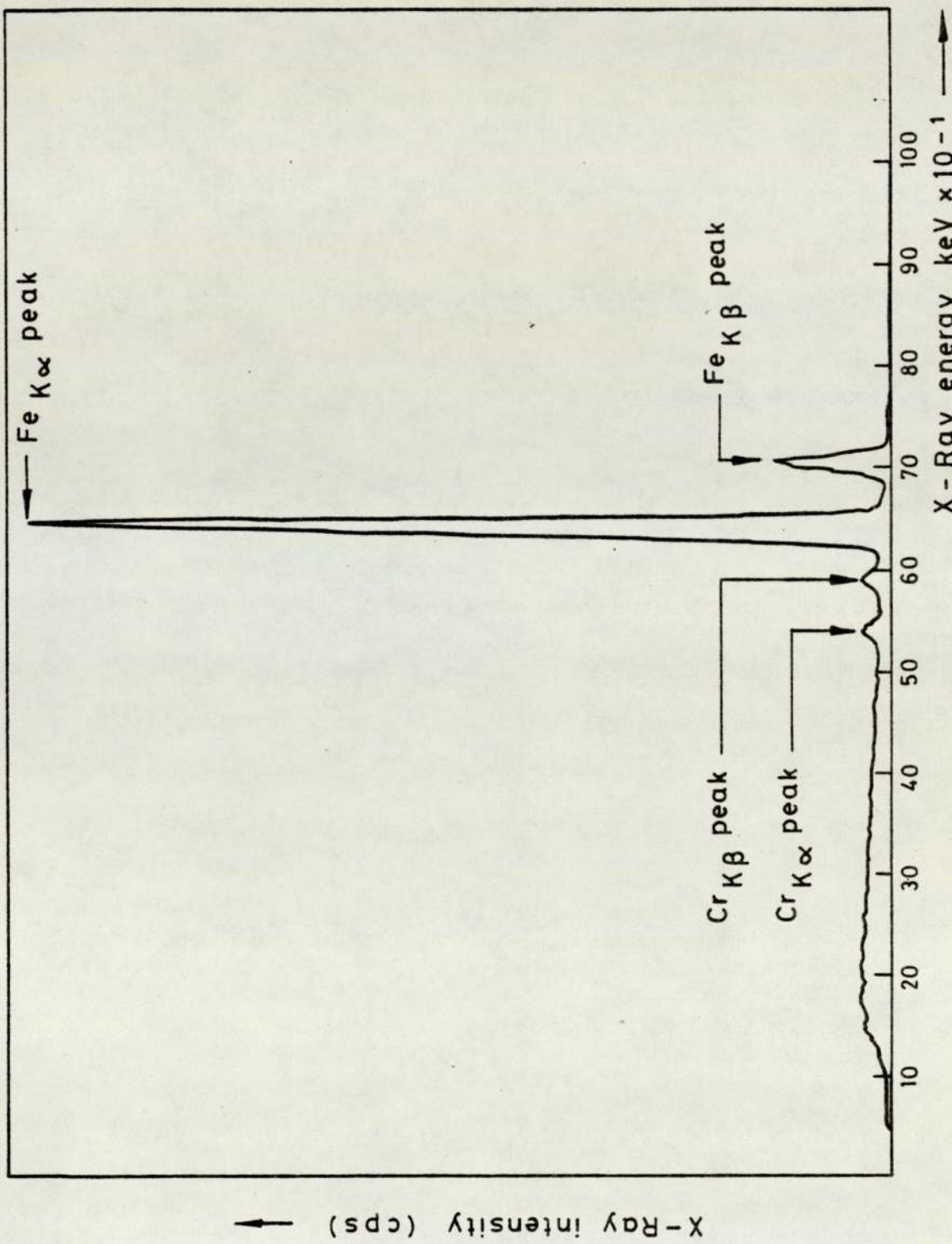

FIG. 2.5 X-Ray Energy Spectrum Illustrating the Iron-Rich Composition of the Non-Protective Dark Blue Oxide.

oxides. Although visually different in character the oxides of both steels were found to be Chromium rich, as illustrated by an X-ray energy spectrum of figure (2.4). Figures (2.5a) and (2.5b) illustrate the general character of the protective oxides.

With the AISI 321 steels, in addition to the chromium rich protective oxide there had also developed isolated islands of light-grey iron rich oxide of a distinctly nodular nature. Figure (2.6) indicates the iron rich character of the light-grey oxide. Figure (2.7a.b) shows the nucleation of this oxide within a matrix of protective oxide.

At 2000 Hours

An additional 1000 hours of exposure resulted in little change in the oxidation of the AISI 316 and 310 steels, although exfoliation (or spalling) was clearly in evidence on some specimens. Figures (2.8a) and (2.8b) indicate this oxide character.

With the AISI 321 steels, however, much of the protective oxide had been replaced by a uniform, dark-blue, crystalline oxide of a characteristically iron rich composition. Figure (2.8c) illustrates the nature of this oxide.

At 3000 Hours

At this stage the partial nucleation of the dark-blue oxide had now also occurred on the AISI 316 steels. This is illustrated in figure (2.9a). With the AISI 310 steels, however, no such behaviour had yet developed (figure (2.9b)). As illustrated by figure (2.9c) all of the protective oxide on the AISI 321 steels had by this stage been completely replaced by the iron-rich dark-blue oxide.

2.2.2 OXIDATION KINETICS

The determination of the oxide growth kinetics is an essential and an instructive part of the overall investigation into the oxidational behaviour of austenitic stainless steels, operating under AGR environments.

(i) Linear Oxidation Kinetics

The oxidational behaviour as described above can be very vividly illustrated in terms of a linear weight gain-time relationship. Such a relationship of specimen weight gain (mg/cm^2) versus time of exposure is represented in figure (2.10).

It can be seen that there are two major trends of oxide development. Trend [1] is characterised by an initially rapid and then an equilibrium oxide development pattern and trend [2] by a rapid and a subsequent hyper-rapid development pattern with a characteristic absence of an equilibrium stage. Trend [1] is found to be exhibited by the AISI 316 and AISI 310 steels and as a result relates to the development of protective oxidation whereas trend [2] is exhibited only by the AISI 321 steels and hence corresponds to the development of the iron-rich dark-blue (duplex) oxide.

Evidently, the onset of secondary iron enriched oxidation gives rise to much greater metal corrosion and therefore metal loss than is produced by protective oxidation. In calculating the metal losses due to such oxidation it was assumed that the iron rich oxide scale was essentially Fe_2O_3 of normal theoretical density and that the oxides fully covered the specimen surface area. In this way, a metal loss to weight gain factor of 2.54×10^{-3} cms $\equiv$ 7.5 mg/cm^2 was calculated.

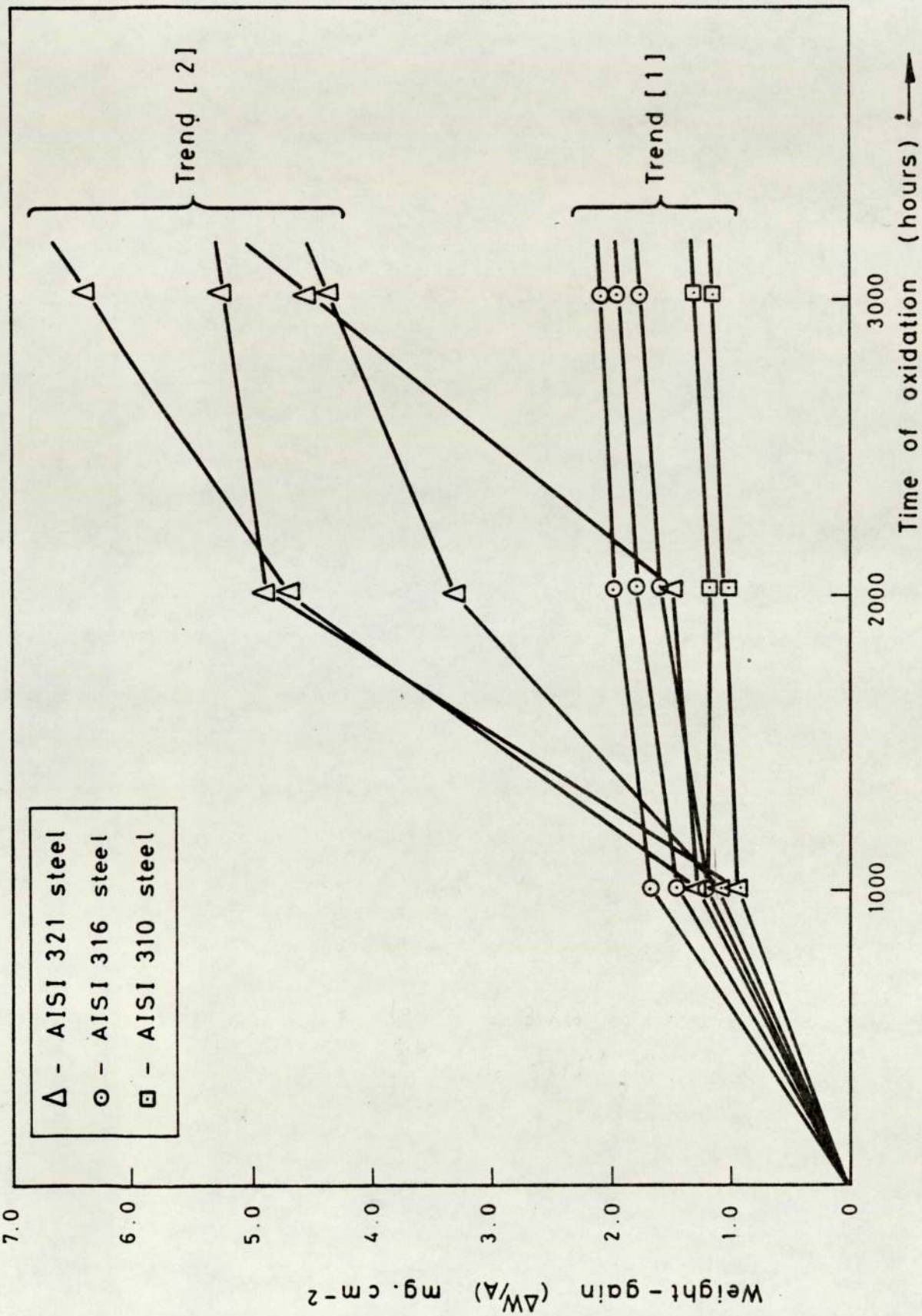

FIG. 2.10 Relationship Between Weight Gain and the Time of Oxidation for the Thermally Cycled Austenitic Stainless Steels.

Calibrating figure (2.10) by this factor, it is found that an average weight gain of 5mg/cm^2 gives rise to an overall metal loss of 15.24×10^{-4} cms in within a period of 3000 hours.

From this, extrapolations can be made to predict metal losses arising after 30 years of reactor life.

(ii) Parabolic Oxidation Kinetics

From first appearances trend [1] of figure (2.10) would seem to be following a typical Wagnerian parabolic rate law.[35][36] That is, the oxidation rate continuously decreases with increasing time. However, a plot of the square of the weight gain versus time of exposure shows that the oxidation under consideration does not perfectly obey this simple relationship. In fact, the reaction rate deviates from the parabolic law with increasing time. Such a plot is shown in figure (2.11).

Initially, as indicated by slopes, A, of the figure (2.11) the oxidation reaction is defined by a normal parabolic rate law of the form:

$$\left(\frac{\Delta W}{A}\right)^2 = K_{p1}.t$$

where W = the gain in weight, k_{p1} = the Arrhenius Reaction-rate constant, A = surface area and t = time of exposure.

In the longer term, however, for $t > 1000$ hours, the reaction as shown by slopes B deviates to a lesser oxidation reaction rate and is defined by the parabolic relationship of the form:

$$(W/A)^2 = k_{p2}.t + C$$

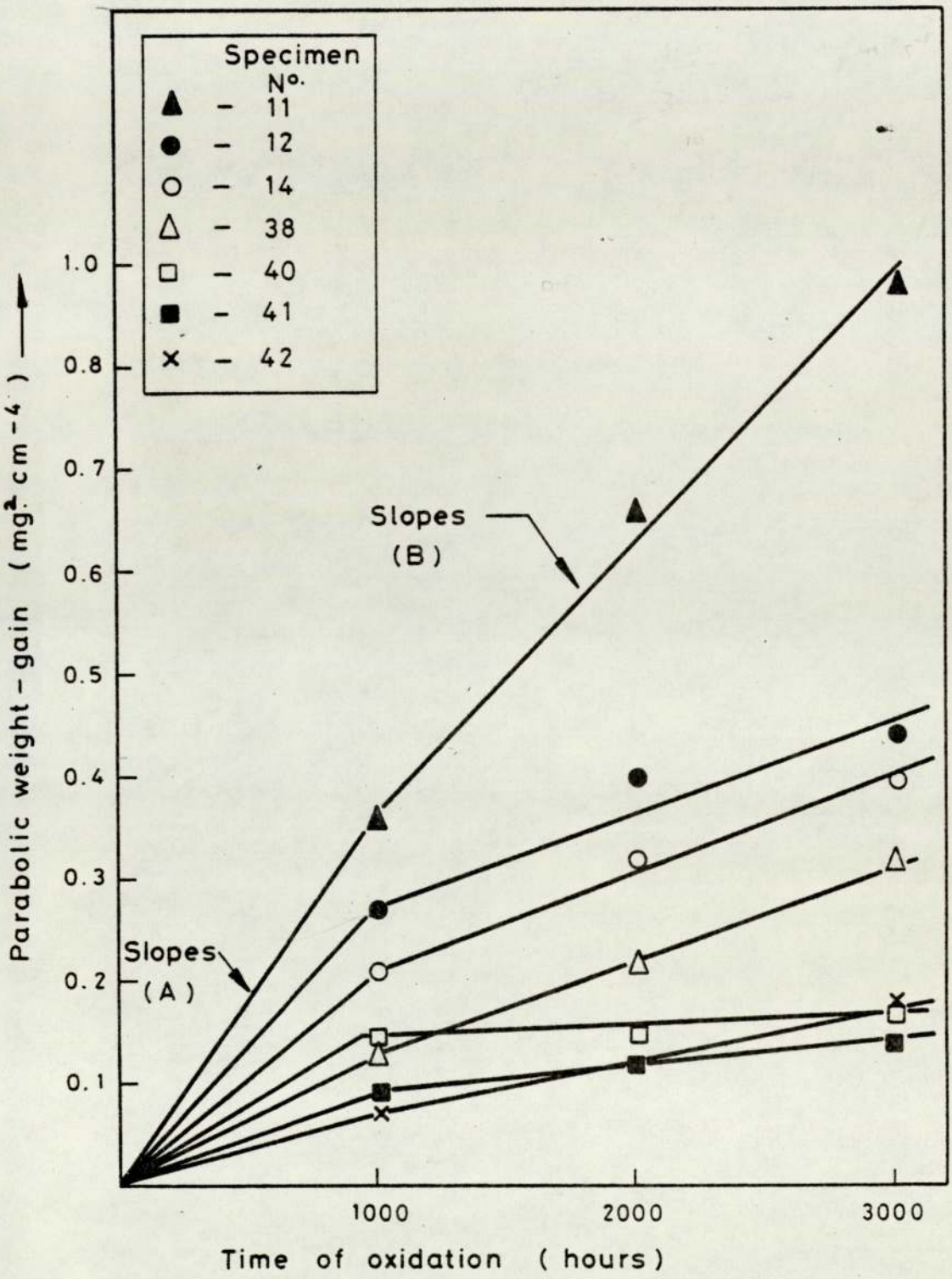

FIG.2.11 Parabolic Relation Between Corrected Weight-Gain and Time of Oxidation.

where k_{p2} is the new reaction rate and C an intercept parameter. The variations in k_{p1} and k_{p2} are shown in table 2.3.

(iii) Logarithmic Oxidation Kinetics

It is evident that the oxidational behaviour of the AISI 321 stainless steels cannot be defined by straight forward parabolic kinetics. Unlike oxidation following typical Wagnarian kinetics, the oxidation pattern for these steels continuously increases with increasing time.

In an attempt to fit the oxidation data to parabolic and cubic rate laws, severe deviations from such relationships were found. In all cases, such deviations were found to stem from the first stage of thermal cycling. Prior to this stage the oxidation conformed to normal parabolic kinetics.

Correlation of the data to logarithmic functions was found to be successful. The logarithmic oxidation-rate function that provided the best fit to the data, overall stages of oxidation, was found to be of the form:

$$\mathrm{Log}_{10}\left(\frac{\Delta W}{AC}\right) = a.t$$

where, a = logarithmic reaction-rate constant and c = the intercept. Figure (2.12) illustrates such a function graphically in the form of a plot of log ($\Delta W/A$) against t, the time of oxidation.

A table showing the variation in the logarithmic reaction-rate constant, a, for logarithmic oxidation, as exhibited by the AISI 321 steels, is given in table 2.4.It can be seen that, a, varies between the range 2.33×10^{-4} to 3.2×10^{-4}.

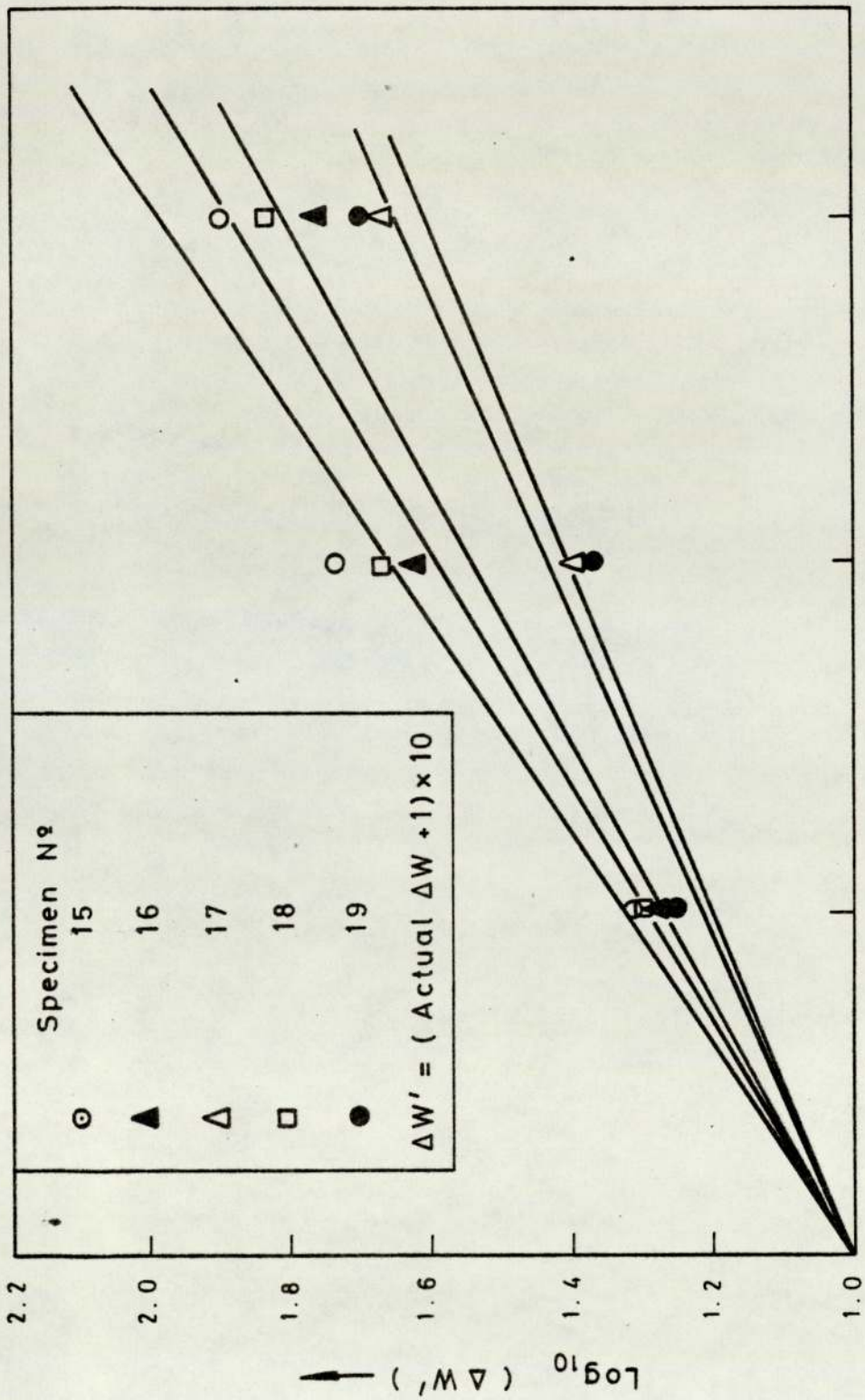

FIG.2.12 Logarithmic Relation Between Weight-Gain and Time of Oxidation.

Stainless Steel	Test No	Parabolic Reaction Rates	
		$k_{p1}(kg^2.m^{-4}.s^{-1})$	$k_{p2}(kg^2.m^{-4}.s^{-1})$
AISI 316	11	1.0×10^{-1}	7.5×10^{-12}
AISI 316	12	9.2×10^{-12}	2.42×10^{-12}
AISI 316	14	5.8×10^{-12}	5.5×10^{-12}
AISI 310	38	3.2×10^{-12}	2.6×10^{-12}
AISI 310	40	4.8×10^{-12}	3.8×10^{-13}
AISI 310	41	2.5×10^{-12}	6.9×10^{-13}
AISI 310	42	2.0×10^{-12}	1.3×10^{-12}

TABLE 2.3 Parabolic Reaction-Rate Constants, k_{p1} and k_{p2}.

Stainless Steel	Test No	Logarithmic Reaction Rate Coefficient, a.
AISI 321	15	3.2×10^{-4}
AISI 321	16	2.65×10^{-4}
AISI 321	17	2.33×10^{-4}
AISI 321	18	2.33×10^{-4}
AISI 321	19	2.92×10^{-4}

TABLE 2.4 Logarithmic Reaction-Rate Coefficient, a.

(iv) Reaction-Rate Activation Energy

The parabolic reaction-rate constant k_p and the corresponding reaction rate activation energy, Q_p, can be used to define the parabolic oxidation process by the expression:

$$K_p = A_p \exp(-Q_p/RT) \quad \ldots\ldots\ldots \quad (21)$$

where A_p = Arrhenius's constant, T = the temperature of oxidation and R = the Universal Gas constant. (36)(37)

This expression can be used to define the oxidational behaviour of the AISI 316 and 310 stainless steels. By using the generally accepted values of A_p (39) for the oxidation of austenitic stainless steels, under the temperatures and environments considered here, equation 2.1 can be solved for the reaction rate activation energy, Q_p. An A_p value of 1×10^{-7} $kg^2 . m^{-4} . s^{-1}$ as given by Gulbransen and Andrew and Goodison, Norton and Wall (38,39) was used in conjunction with the experimentally derived k_p values from the present work.

A table of results showing the calculated Q_p values for the oxidation of the AISI 316 and AISI 310 stainless steels is given in table 2.5 Q_{p1} corresponds to the activation energy associated with the initial rapid growth stage and Q_{p2} to the final equilibrium stage.

Stainless Steel	Test No	For kp_1	For kp_2
		Q_{p1} ($J.mole^{-1}$)	Q_{p2} ($J.mole^{-1}$)
AISI 316	11	-76.8×10^3	-74.5×10^3
AISI 316	12	-85.9×10^3	-75.2×10^3
AISI 316	14	-79.3×10^3	-79.0×10^3
AISI 310	38	-85.4×10^3	-83.7×10^3
AISI 310	40	-100.96×10^3	-80.4×10^3
AISI 310	41	-96.1×10^3	-85.7×10^3
AISI 310	42	-91.0×10^3	-87.5×10^3

TABLE 2.5 Parabolic Activation Energies Qp_1 and Qp_2.

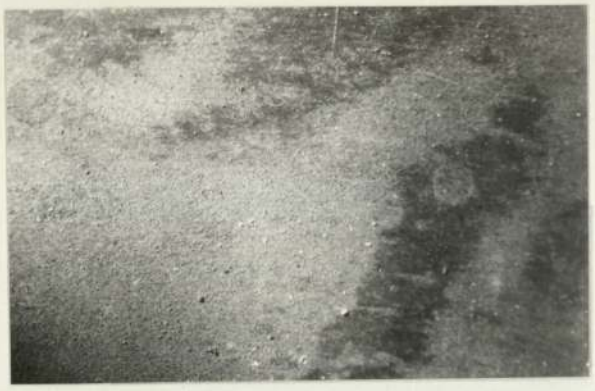

2.5 (a)
(Mag.x 20)

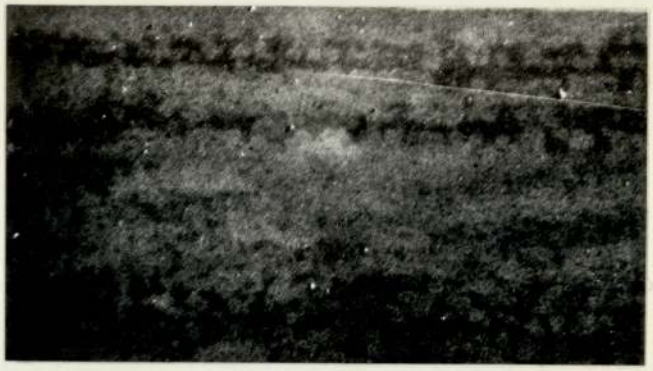

2.5 (b)
(Mag.x 10)

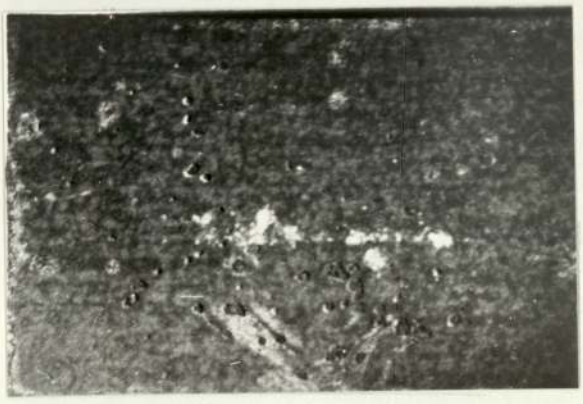

2.7 (a)
(Mag.x 20)

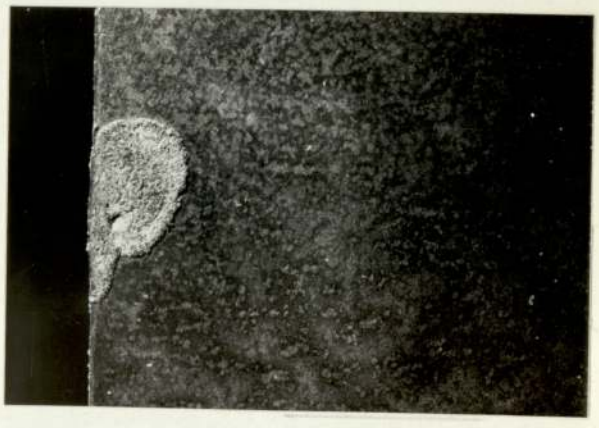

2.7 (b)
(Mag.x 10)

Figure 2.5 a) and b) Protective oxide nucleation after 1000 Hrs. of oxidation.

Figure 2.7 a) and b) Nodular oxide nucleation after 1000 Hrs. of oxidation.

Figure 2.8 a) Protective oxide on AISI 310 specimens following 2000Hrs. of oxidation. (Magnification x 2.)

Figure 2.8 b) Protective oxide on AISI 316 specimens following 2000 Hrs. of oxidation exhibiting spalling. (Magnification x 2.)

Figure 2.8 c) Uniform dark blue Fe-rich oxide on AISI 321 specimens following 2000 Hrs. of oxidation. (Magnification x 2.)

Figure 2.9 a) Partial coverage of AISI 316 specimens by Fe-rich oxide following 3000 Hrs. of oxidation. (Magnification x 2.)

Figure 2.9 b) Absence of Fe-rich oxide on AISI 310 steel specimens following 3000 Hrs. of oxidation. (Magnification x 2.)

Figure 2.9 c) Full coverage by the Fe-rich oxide on AISI 321 specimens following 3000 Hrs. of oxidation. (Magnification x 2.)

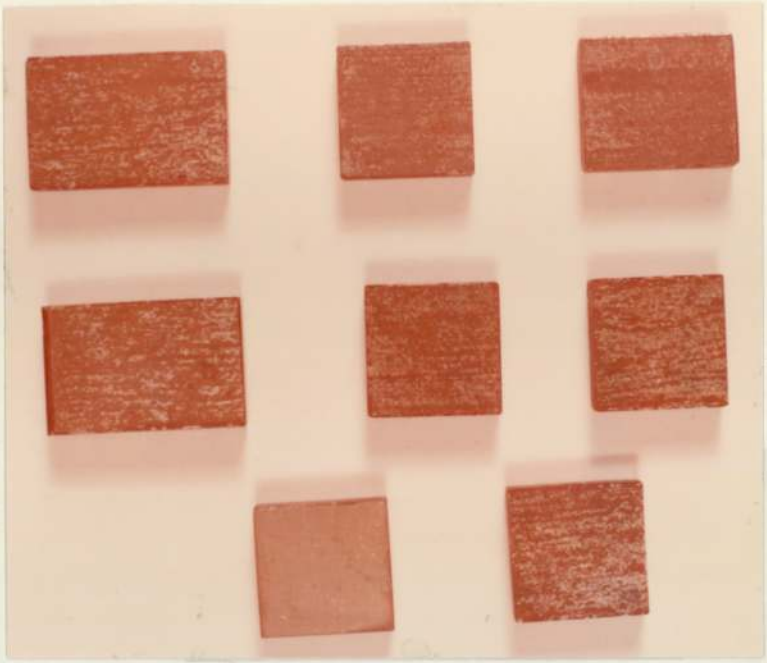

Figure
2.8 (a)

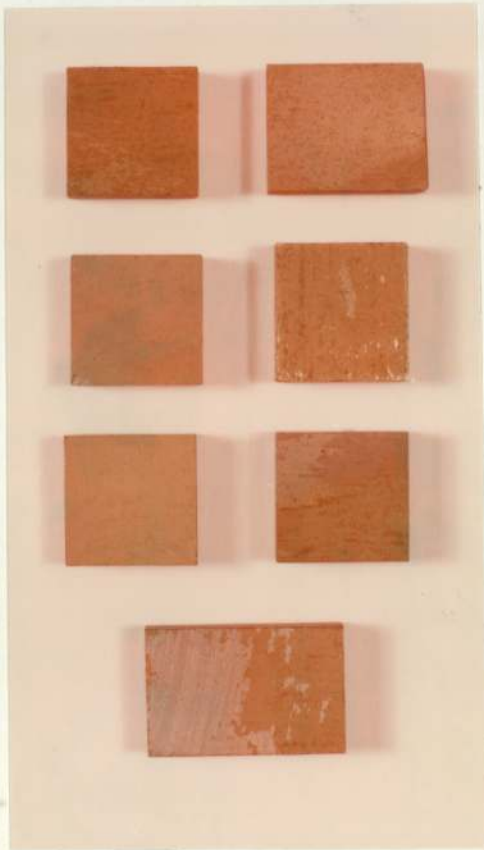

Figure
2.8 (b)

Figure
2.8 (c)

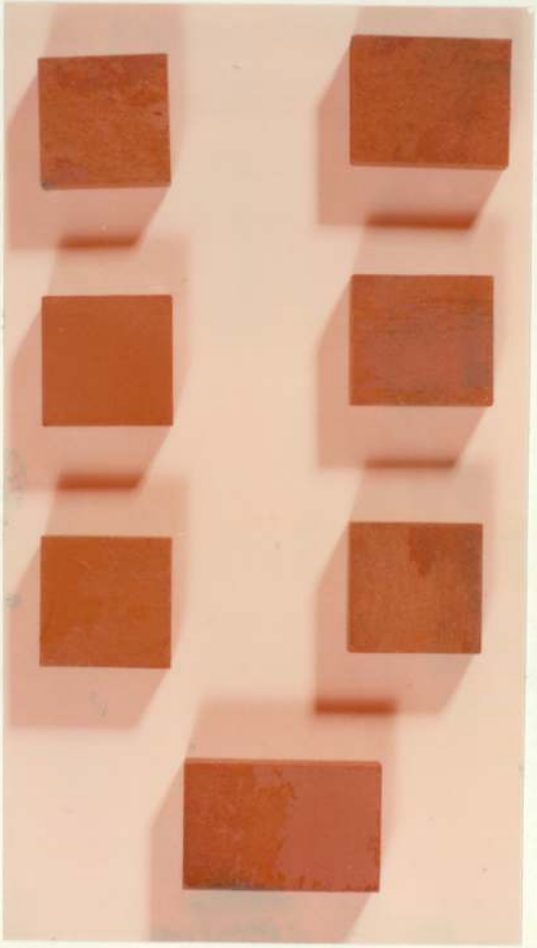

Figure
2.9 (a)

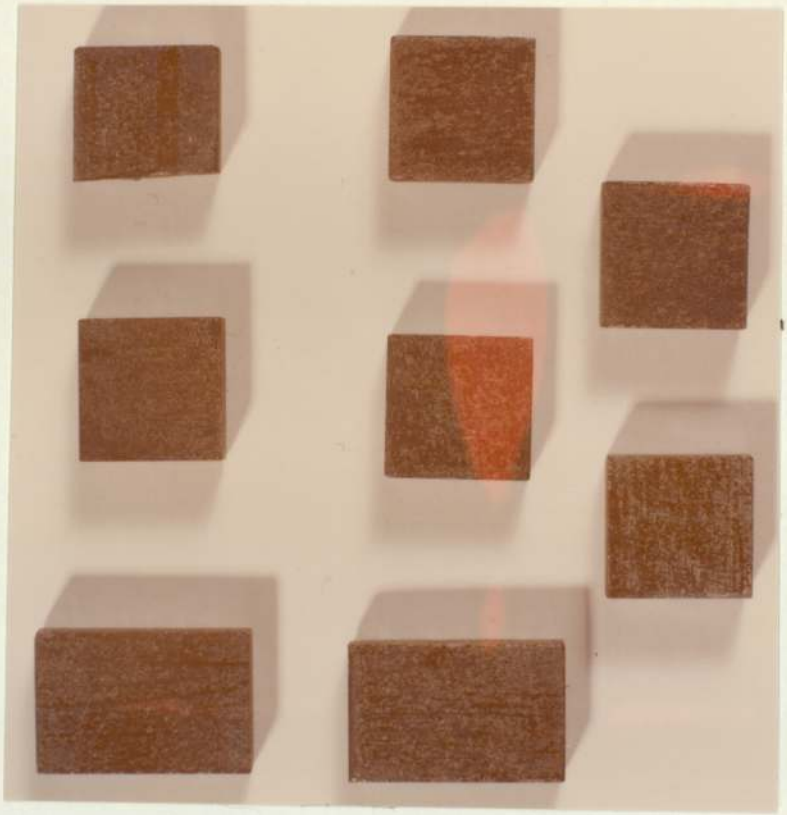

Figure
2.9 (b)

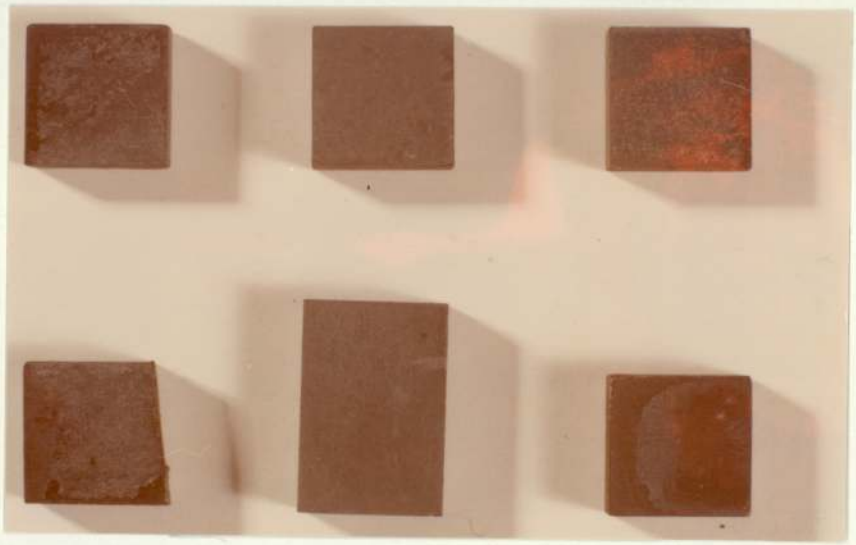

Figure
2.9 (c)

CHAPTER 3

ANALYSIS OF OXIDISED SPECIMENS

3.1 INTRODUCTION

The analyses described in the present section investigate the nature and properties of the surface oxides growing on oxidised austenitic stainless steels, and of their affect upon the alloy structure and alloy composition. Oxide characteristics such as surface character, surface and sub-surface morphology and elemental constitution are investigated. Additionally, oxide development characteristics such as surface coverage, oxide distribution and oxide abundance are also investigated.

The physical techniques of analyses that have been used in the examination of the specimens have been principally those of Scanning electron microscopy (SEM), Electron probe micro-analysis (EPMA), X-ray diffractometry, Optical micrography and Gravimetric analysis. Scanning electron microscopy was found most useful in the examination of oxide morphology and physical structure, whilst oxide composition and chemical structure could be conveniently investigated by means of the Electron probe microanalyser and X-ray diffractometry. In the examination of the oxide and alloy sub-surface structure, analysis by optical microscopy was found to be ideally suited. Gravimetric analysis was used chiefly in the determination of the oxide growth-rate characteristics and oxidation kinetics (as described in Chapter 2).

3.2 General Surface Character of the Non-Thermally Cycled Austenitic Steels

Examination of the non-thermally cycled stainless steels proved to show no substantial difference in oxidational behaviour when compared with the thermally cycled steels. Although the two sets

of specimens were very similar with respect to oxide character and oxide type, a much slower rate of oxide growth was however apparent in some specimens of the non-thermally cycled steels.

At 500 Hours

Inspection of representative AISI 310 and AISI 316 stainless steel specimens after an initial 500 hours showed that as with the thermally cycled steels a thin layer of protective oxide had formed. With the AISI 321 steels, however, in addition to a background of protective oxide there had also developed isolated islands of course light-grey crystalline oxide.

At 1000 Hours

Inspection after an additional 500 hours of exposure revealed a change in oxide character. Whilst the AISI 310 steels still exhibited only protective oxide,the AISI 316 steels had by this stage developed isolated mounds of nodular oxides. An optical micrograph of this is shown in figure (3.1). With the AISI 321 steels much of the protective oxide had been replaced by the light-grey (light-blue) crystalline oxide.

An illustration of the oxidational character described here is shown in figure (3.2), in chronologic order.

At 1500 Hours

By this stage, the protective nature of the oxide on the AISI 310 steels was clearly in evidence since the total surface coverage by this oxide precluded the nucleation of any other oxide. In contrast, spalling of protective oxide and coalescence of the nodular oxides was clearly apparent with the AISI 316 steels. Examination of the AISI 321 steels by X-ray energy dispersive

analysis showed the light-grey (blue) crystalline oxide to be markedly iron enriched in composition.

Figure (3.3) illustrates the oxidational developments at this stage.

At 3500 Hours

Following 3500 hours of oxidation, a total replacement of the protective oxide by the light-grey crystalline oxide (although of dark-blue colouration at this stage) on all steels had occured. An illustration of such substitutional behaviour is shown in figure (3.2).

3.3 Oxide Distribution and Abundance

By means of the Electron probe microanalyser, the semi-quantitative determination of elemental concentrations within the oxides were made. In this way, oxide growth developments, in terms of change in elemental concentrations could be monitored. Moreover, electron probe microanalysis was also used in acquiring X-ray distribution images of surface oxides. This allowed the distribution of elemental abundances within the oxide, with respect to surface coverage, to be determined and observed visually.(40)

In the AISI 310 Steels

The gradual transition in character of the oxide nucleating on the AISI 310 steels from an exclusively chromium enriched oxide to an oxide becoming increasingly richer in iron, by the gradual replacement of spalled oxide, with continued exposure, is clearly evident from the elemental concentration measurements. It is observed that following 2000 hours of exposure, the elemental composition of the surface oxides is found to consist of 45%Cr, 2.5%Fe, 2%Ni and negligible Mn, whereas however,

with an additional 1000 hours the composition is markedly changed in Fe and Cr content, resulting in a composition of 21% Fe, 34% Cr and <1% Mn and Ni.

Such characteristic oxide transitions are even more vividly illustrated by the X-ray distribution images of figures (3.4a)(3.4b) and (3.4c) which correspond to images of Ni, Cr and Fe after 2000, 2000 and 3000 hours respectively. It is clear that the surface oxide is chromium abundant following 2000 hours of oxidation (figure (3.4a)) and iron deficient, but that with continued oxidation the oxide changes character becoming increasingly iron enriched due to replacement by an iron rich and chromium deficient oxide (figure (3.4c)). Figure (3.4d) illustrates a corresponding secondary electron image of figure (3.4c) exhibiting such oxide behaviour by a conventional scanning-micrograph.

In the AISI 316 Steels

The nodular oxide character of the AISI 316 steels in combination with protective oxide is illustrated very clearly by figure (3.5a) which is an X-ray distribution image for iron. A corresponding secondary electron image is shown in figure (3.5b). This is in contrast to the AISI 310 steels where nodular oxide behaviour is not found.

In the AISI 321 Steels

The elemental composition of the light-blue crystalline oxide or duplex oxide of the AISI 321 steels is observed to be clearly chromium deficient as is seen from a typical oxide composition of 62.5% Fe, 1% Cr, 1% Ni and 1.5% Mn, taken after exposure for 2000 hours.

A characteristic property of the duplex oxides, it seems, is the relatively high abundance in manganese, in contrast to the manganese lacking Cr rich oxides of the AISI 310 and 316 steels. This property is further illustrated by the increase in Mn concentration found upon examination of a heavily duplex oxidised specimen at the 3000 hours stage. Figure (3.6) shows a Mn distribution image taken at a specimen edge where the oxidation is severest.

3.4 Oxide Morphology

By means of the Scanning electron microscope the above-surface morphology and habit of the oxides could be very readily investigated. The minimal effort required in specimen preparation combined with the large field of depth, high spatial resolution (typically 100-200 Å) and the high magnifications of the SEM made this an ideal analytical instrument, for the purposes of the analysis required in the present work.

3.4.1 Morphology of the Protective Oxides

Figures (3.7a) and (3.7b) illustrate scanning electron micrographs of stainless steels exhibiting protective oxide. From these the very flat and typically scale-like nature of the oxide is apparent. The characteristic whiskery appearance of the oxide is also evident.

Most importantly, however, is the illustration of the exfoliating habit of the oxide. Figure (3.7a) shows the oxide character after 2000 hours of exposure, and the large extent to which spalling and fracturing can take place to expose large areas

of unprotected base-alloy. Figure (3.7b) indicates the oxide-fracturing beginning to occur after 1000 hours of oxidation.

The highly vulnerable state of the base-alloy, following spalling, is clearly marked in figure (3.7a). It would seem that protective oxidation has the effect of enlarging and deepening the grain-pores of the base-alloy and thus creating a densley void-filled substrate. Voids as large as 3-4μm in diameter appear to be formed. Clearly, a porous substrate of this type would be very susceptible to further oxidational attack, offering little resistance to intergranular penetration by newly forming oxide species.

The blanketing effect of the surface oxide, giving total protection to the substrate where spalling has not occurred is plainly evident. In combination, further protection is provided by the very dense voidfree structure of the oxide allowing little access to penetrating oxidising gases.

3.4.2 Morphology of the Duplex Oxides

In comparison with the protective oxides the very different nature of the duplex oxides is evident. Figure (3.8) illustrates a scanning electron micrograph of typical duplex oxide on AISI 321 stainless steels after 3500 hours of oxidation. From this, the porous and more importantly the very rough and uneven character of the oxide is clearly apparent. Moreover, the dense and prolific growth of the oxide, resulting in the total coverage of the surface, is also clearly illustrated. The consequence of such total coverage is of course the complete degradation of the

original surface from the point of view of surface finishing. The resulting surface finish after such oxidation is clearly many times rougher.

The lack of the oxide at the specimen edge could be significant in that properties peculiar to such areas retard duplex oxidation. During specimen preparation it is the specimen edges that are subjected to the most cold working and grain-structure deformation by processes such as machining and polishing. The consequence of such effects could lead to improved oxidation resistance.

Crystalline Structure. Under very high magnifications, the crystalline structure of the oxide is clearly observed. A structure of this kind is illustrated in figures (3.9a) and (3.9b). The very angular and irregularly oriented character of the duplex oxide crystals is very distinctive and to a large degree must be responsible for the abrasive nature of the oxide. It can be seen from figure (3.9a) that, in general, the crystals are large and vary between 5 - 10μm in size.

3.5 Oxide Cross-Sectional Structure

By the metallographic examination of cross-sectioned oxidised specimens the internal physical structure of the surface oxides can be observed.

Standard metallographic techniques (41) were used in the preparation of the cross-sectioned specimens as described in section 3.6. Additionally, to reveal the sub-surface alloy structure etching was necessary. Initially etching by chemical means was attempted.

For this, recommended chemical reagents, namely, Marbles reagent and acid ferric chloride solution were used but with little success. It was found that the acid solutions tended to dissolve the iron rich oxides and that secondarily considerable brown staining was produced by the chloride cations in solutions. Consequently, as an alternative an electrochemical/electrolytic method was used where oxalic acid was employed as the electrolyte and etchant.

3.5.1 Protective Chromium III Oxide

Figure (3.10) shows an optical micrograph of a cross-sectioned layer of protective oxide.From this, the single layered and the un-intrusive character of the oxide is apparent. The very slight intrusion of the oxide into the bulk alloy, being in general an overlaying oxide, would tend to render it protective rather than corrosive.

Also evident from the illustration is the disrupted and fractured nature of the oxide which eventually leads to failure. Although appearing undulating (due to the disrupting nature of the metallographic preparation technique) the surface profile is comparatively uniform and non-nodular.

3.5.2 Duplex Oxide

In contrast, the surface structure of the duplex oxides is clearly rough, nodular and abrasive, as illustrated by figures (3.11a) and (3.11b). Such nodular character is demonstrated by both forms of the oxide, namely, the 'uniform' variety of figures (3.11a) and (3.11b) and also by the 'singular-nodules' variety of which examples are shown in figures (3.12a) and (3.12b).

The distinctive double layered character of this oxide is exemplified in figures (3.12b) and (3.11b) where the separation of the upper and lower layers of the oxide are distinctly marked. Moreover, the differences in structure between the two layers are also clearly evident; the lower layer is fractured and disjointed whereas the upper layer is uniform and crystalline. Unlike the protective oxides, the intrusion of the lower layer into the bulk alloy is extensive and in consequence must contribute to excessive metal-loss.

Intergranular Penetration

The influence of the grain structure and of the grain boundaries upon oxide development is illustrated by figures (3.12b), (3.13a) and (3.13b). The grain structure it appears has the effect of inhibiting oxide development by blocking inwardly growing oxide. This is well illustrated by figure (3.13b). The effect of the grain boundaries, however, is to allow access to the inwardly growing oxide, and as such act as skeletal nucleation sites for the further lateral expansion of the oxides. This effect is well illustrated by figures (3.12b) and (3.13a).

The intergranular penetration of the duplex oxides in this way, via the grain boundaries, is evidently greatly damaging and must add substantially to the corrosive power of the oxide. It is interesting to observe, as illustrated by figure (3.10), that in the case of protective oxidation such intergranular penetration via the grain boundaries is characteristically absent.

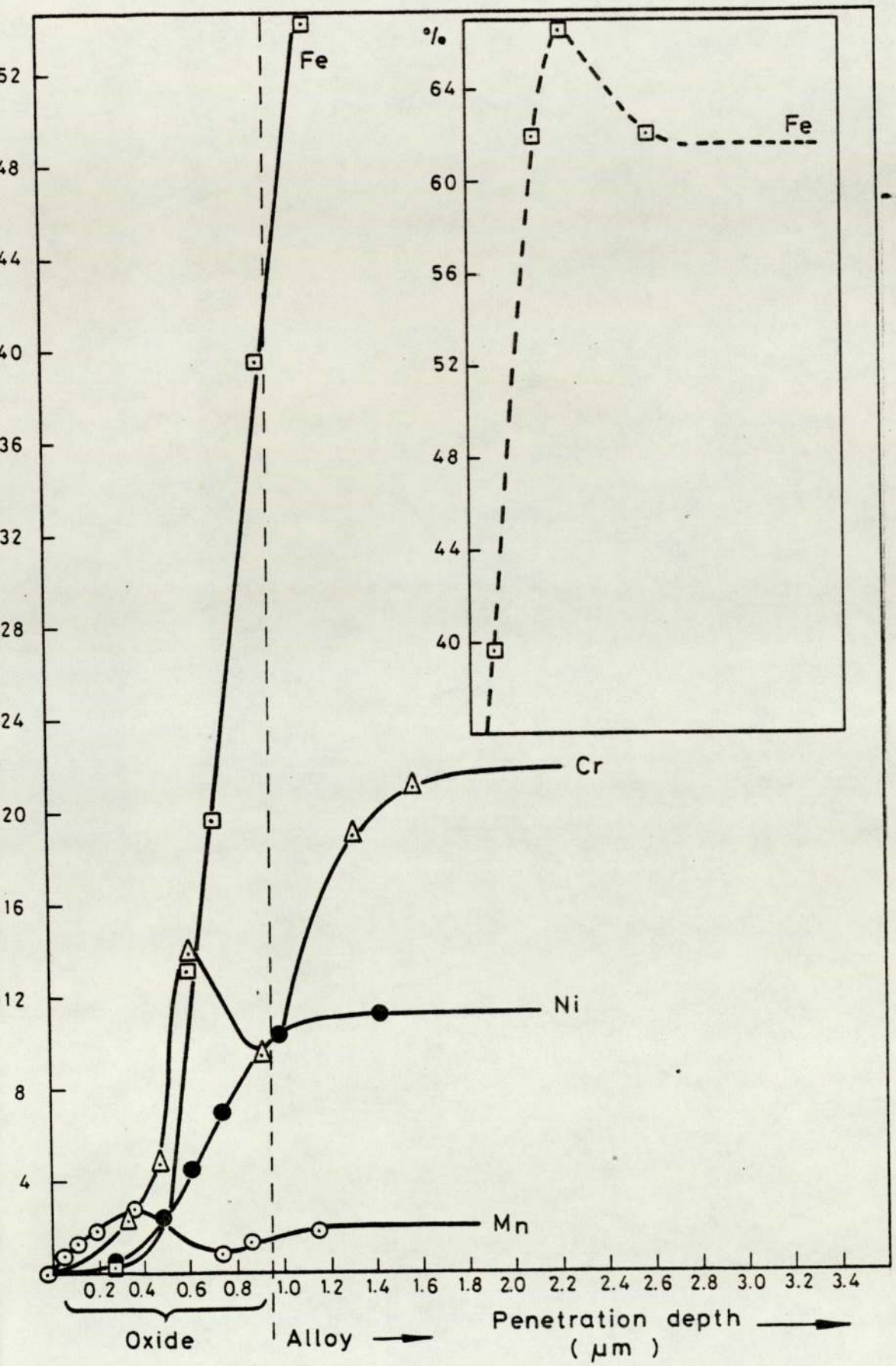

FIG. 3.14 AISI 321 Stainless Steel Subsurface Elemental Concentrations Following 500 Hrs. of Oxidation.

3.6 Subsurface Elemental Analysis

Using Electron probe micro-analysis, changes in subsurface elemental concentrations due to oxidation can be investigated. By monitoring such variations with depth, the concentration profiles of the major alloying elements within the alloy and over-lying oxide can be determined.

For analysis of this kind representative specimens were carefully prepared by standard metallographic techniques; that is, by mounting in bakelite to preserve the friable surface oxides, abrading to reveal a cross-sectioned structure and finally polishing on SiC paper (as described in Chapter 2) to a 1μm surface finish. To prevent contamination of the EPMA, subsequent degreasing and ultrasonic cleaning prior to analysis was essential.

Figures (3.14), (3.15) and (3.16) illustrate subsurface concentration profiles for AISI 321 stainless steel specimens oxidised for 500, 1500 and 3500 hours respectively. These represent electron probe scans taken perpendicularly through the oxide cross-sections.

Prominent features of the profiles are the peaks, indicating elemental abundance, and the complementary troughs indicating elemental depletion.

3.6.1 Oxide Structure

The double layered nature of the duplex oxides, as found by optical micrography (described in section 3.5), is very clearly demonstrated by figures (3.15) and (3.16). This is demonstrated by the variations in elemental concentrations which define the boundaries of the double layered oxide. It is evident that not

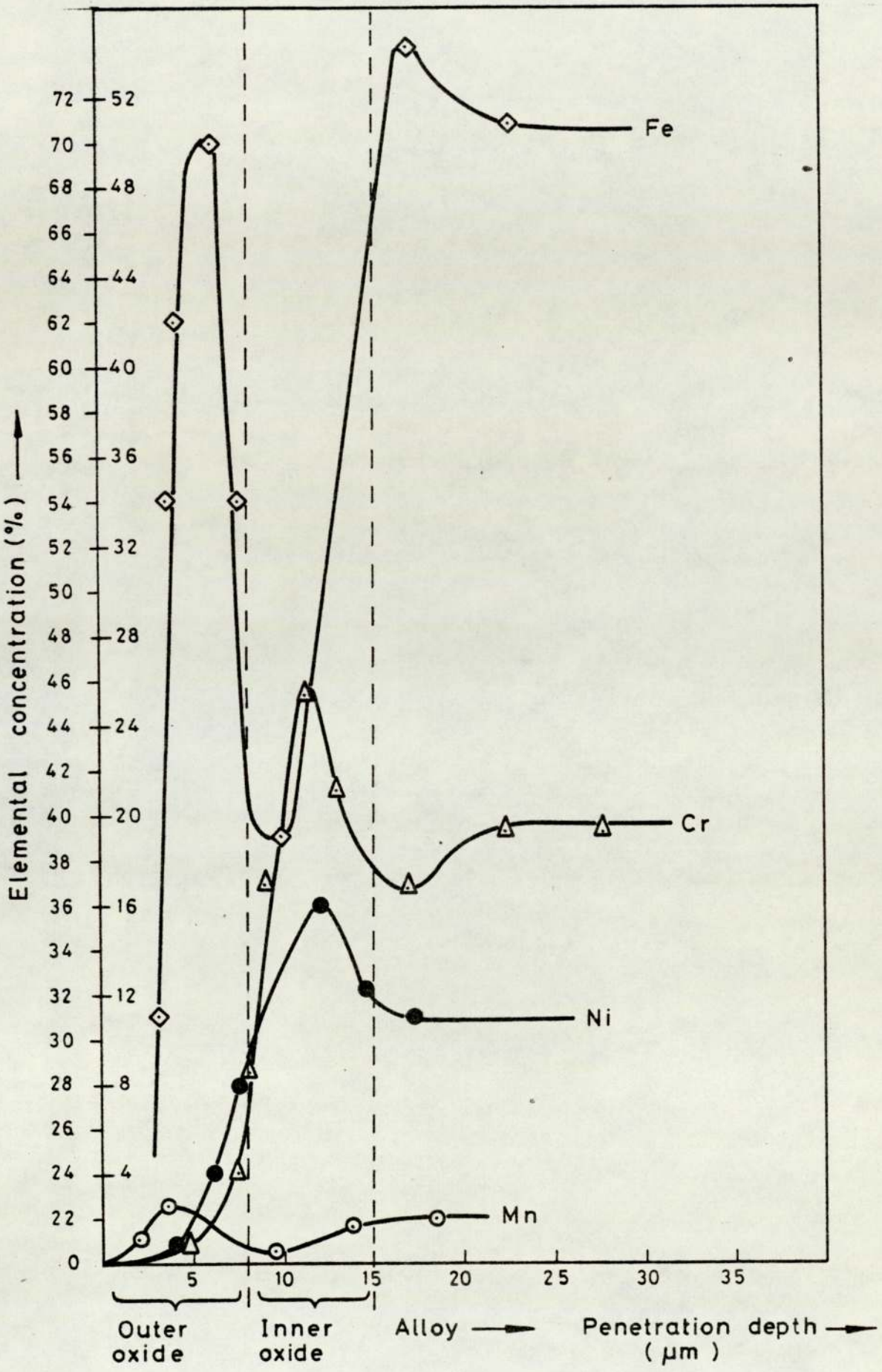

FIG.3.5 AISI 321 Stainless Steel Subsurface Elemental Concentrations Following 1500 Hrs. of Oxidation.

only is the oxide non-uniform in physical structure but also inhomogenous in elemental composition.

(i) Outer Oxide

The high abundance of Fe and Mn(>1.5%) and the characteristic deficiency of Ni (<1%) and Cr(~1%) in duplex oxides is illustrated very clearly as previously described (section 3.3) by electron probe analysis of the surface oxides. In accordance with such analysis, this character is also clearly exemplified by the concentration profiles of figures (3.15) and (3.16), where the outer oxide conforms exactly to such a composition.

The variations in the Fe and Mn content of the outer oxide with increasing time of oxidation are well illustrated by the concentration profiles. It is evident that with increasing time the Fe content falls and the Mn level rises within the ranges 71%-35.5% for Fe and 2%-8.8% for Mn, at oxidation times of 1500 and 3500 hours respectively.

(ii) Inner Oxide

The analysis detailed in section 3.3 can only be applied to the understanding of the properties of the outer layer of the duplex oxides. A fuller understanding can be gained by examining the concentration profiles of the whole oxide, which would in addition also illustrate the compositional properties of the inner oxide.

The characteristic feature of the inner oxide, as illustrated by figures (3.15) and (3.16), is the abundance in Cr and Ni and the deficiency in Fe and Mn, resulting in an oxide of completely opposite compostional properties to that of the outer oxide. With

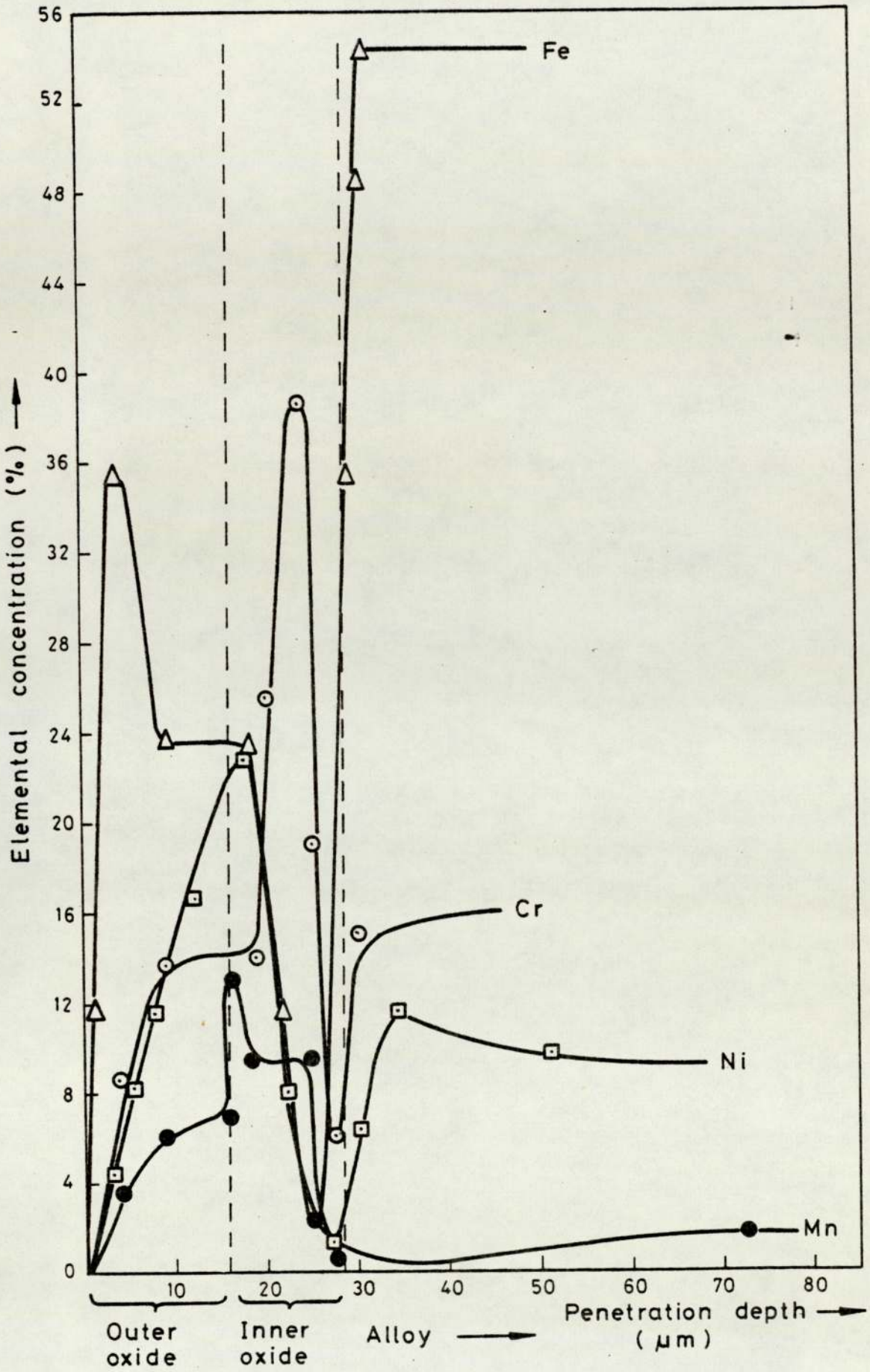

FIG.3.15 AISI 321 Stainless Steel Subsurface Elemental Concentrations Following 3500 Hrs of Oxidation

increasing time of oxidation, the oxide is found to become richer in Cr and greatly deficient in Fe, the latter reducing from 19% after 1500 hours to an insignificant 2% after 3500 hours of oxidation.

(iii) Single Layer Oxide

Figure (3.14) illustrates the oxidational behaviour of the AISI 321 steels following 500 hours. Represented here is the Chromium (III) protective oxide variety of the oxides. Consequently, the duplex structure is absent.

It is evident that element enrichment increases sharply at the lower surface of the oxide in the vicinity of the alloy-oxide interface, but is distinctly deficient at the upper regions. The oxide composition is Cr and Mn-abundant at its upper surface but becoming depleted in these elements at its lower regions (by 5% and 2% respectively) and greatly enriched in Fe and Ni.

In comparison with the protective oxide behaviour of the AISI 316 and AISI 310 steels (as described in Section 3.2 and 3.3) it is evident that the protective oxide of the AISI 321 steels is, in contrast, less chromium abundant and more Mn and Fe enriched.

3.6.2 Depletion Zones

Elemental depletion profiles of the sort described are also observed at the alloy-oxide interface. As illustrated by figure (3.15), the concentration profiles for chromium exhibit prominent depletion profiles in this region. It is apparent that within a narrow region immediately below the alloy-oxide interface a reduction in Cr content to a level below that of the bulk is found. Such reduction in chromium can lead to zones that are severely depleted in Cr.

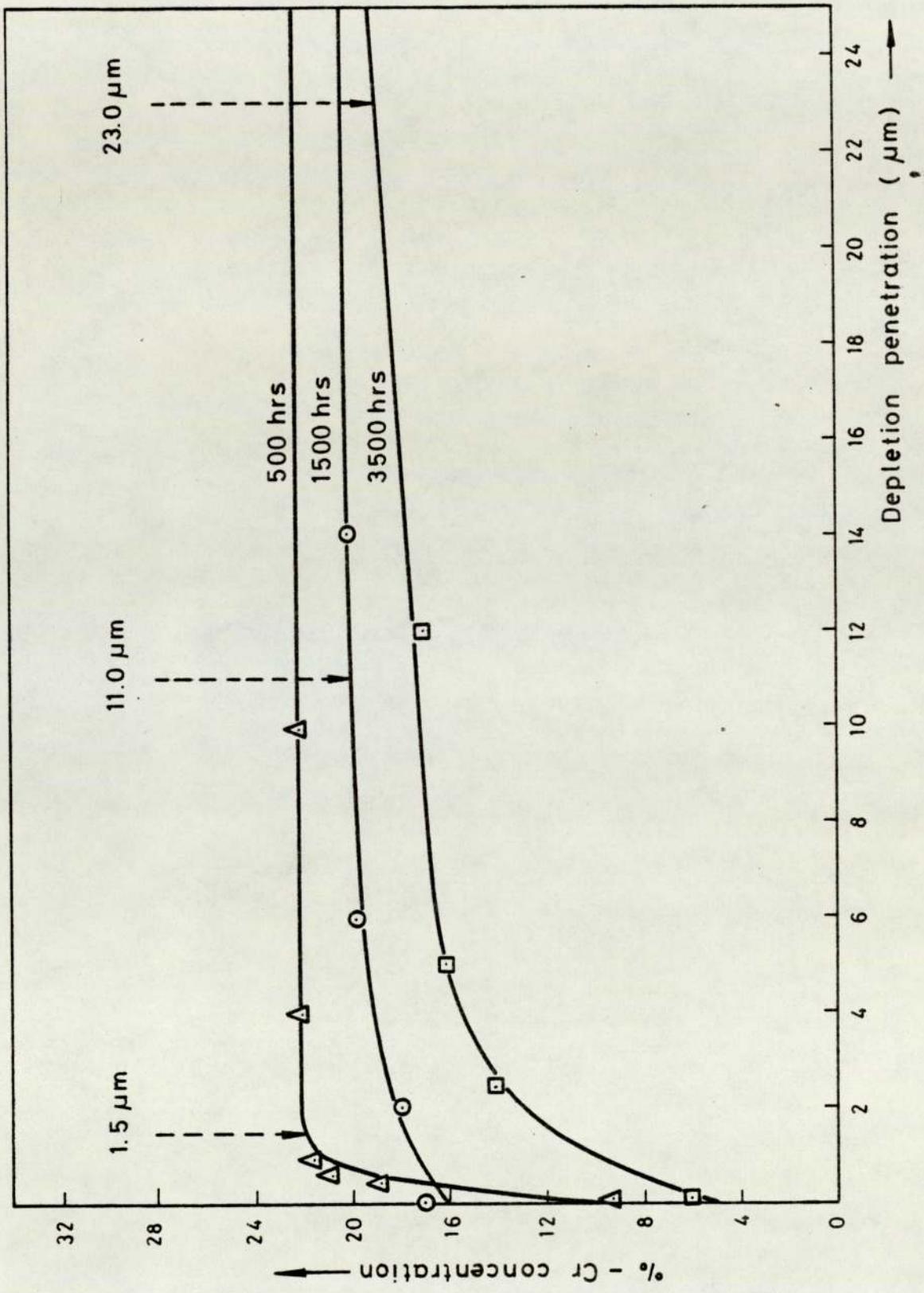

FIG. 3.17 Subsurface Depletion Zones.

It is found from the present results that the depths to which such depletions occur (from the interface into the alloy) increase with continued oxidation. This is demonstrated by figure (3.17) where the depletion widths rise from 1.5μm at the 500 hours stage to 11.0μm and 23.0μm at the 1500 hours and 3500 hours stages respectively.

3.6.3 In General

Figure (3.18) illustrates an Fe X-ray distribution image of an oxidised AISI 321 steel showing duplex oxidation. Corresponding sample concentration profiles of Fe, Cr, Ni and Mn, taken through a typical oxide nodule, in the position indicated by the vertical line, are represented by figures (3.19a), (3.19b), (3.19c) and (3.19d) respectively. Exemplified by the sample traces are the characteristic properties of duplex oxides, as described above. The duplex structure is displayed by figures (3.19a), (3.19b) and (3.19c). Additionally, the variations in the concentration profiles since they are at equal sensitivity and magnification, illustrate clearly the elemental enrichments and deficiencies of the oxide.

The nodular character of duplex oxides, which was illustrated in a previous section by optical micrography to be, in particular, characteristic of the 'singular-nodule' variety of the oxide, is also well demonstrated by the electron probe X-ray distribution images, as shown by figures (3.10a) and (3.20b). The latter correspond to Cr and Fe distribution images, respectively. Evident in the illustrations is the Cr rich nature of the lower oxide (figure 3.20a) and the Cr deficient Fe rich nature of the upper oxide (figure 3.20b).

Figure 3.1 Duplex oxide mounds on AISI 316 steel after 1000 Hrs. of oxidation. (Magnification x 50.)

Figure 3.3 Surface oxide character following 1500 Hrs. of oxidation. (Magnification x 3.)

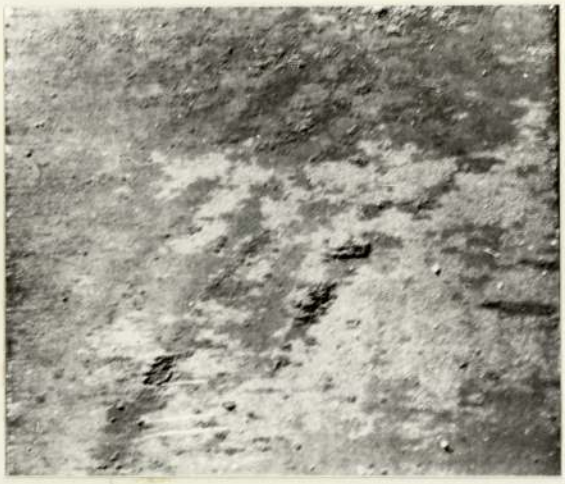

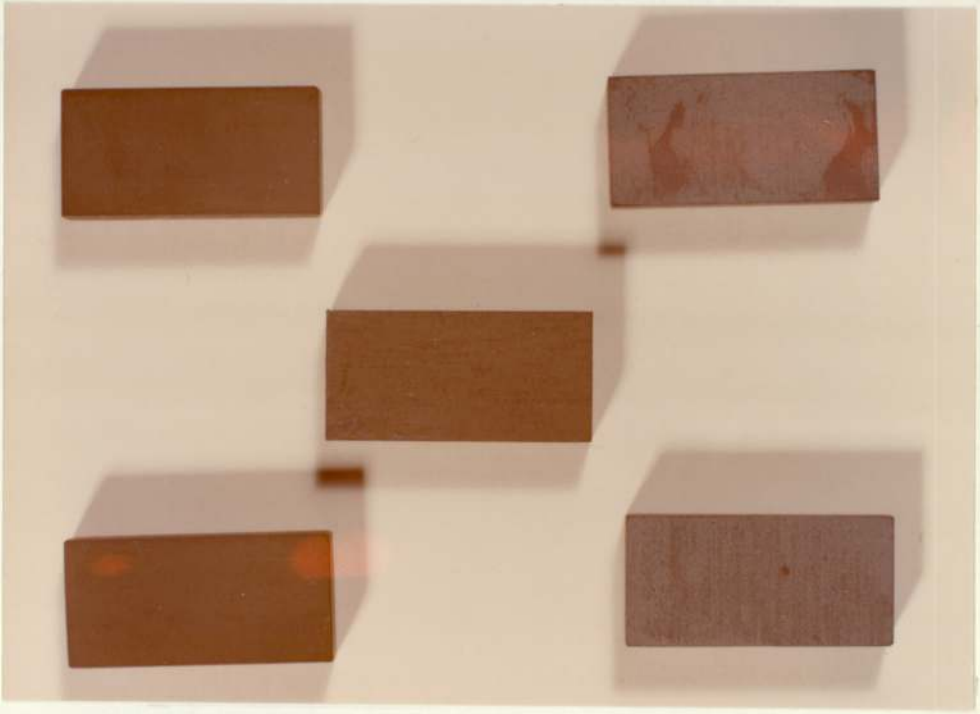

310

316

321

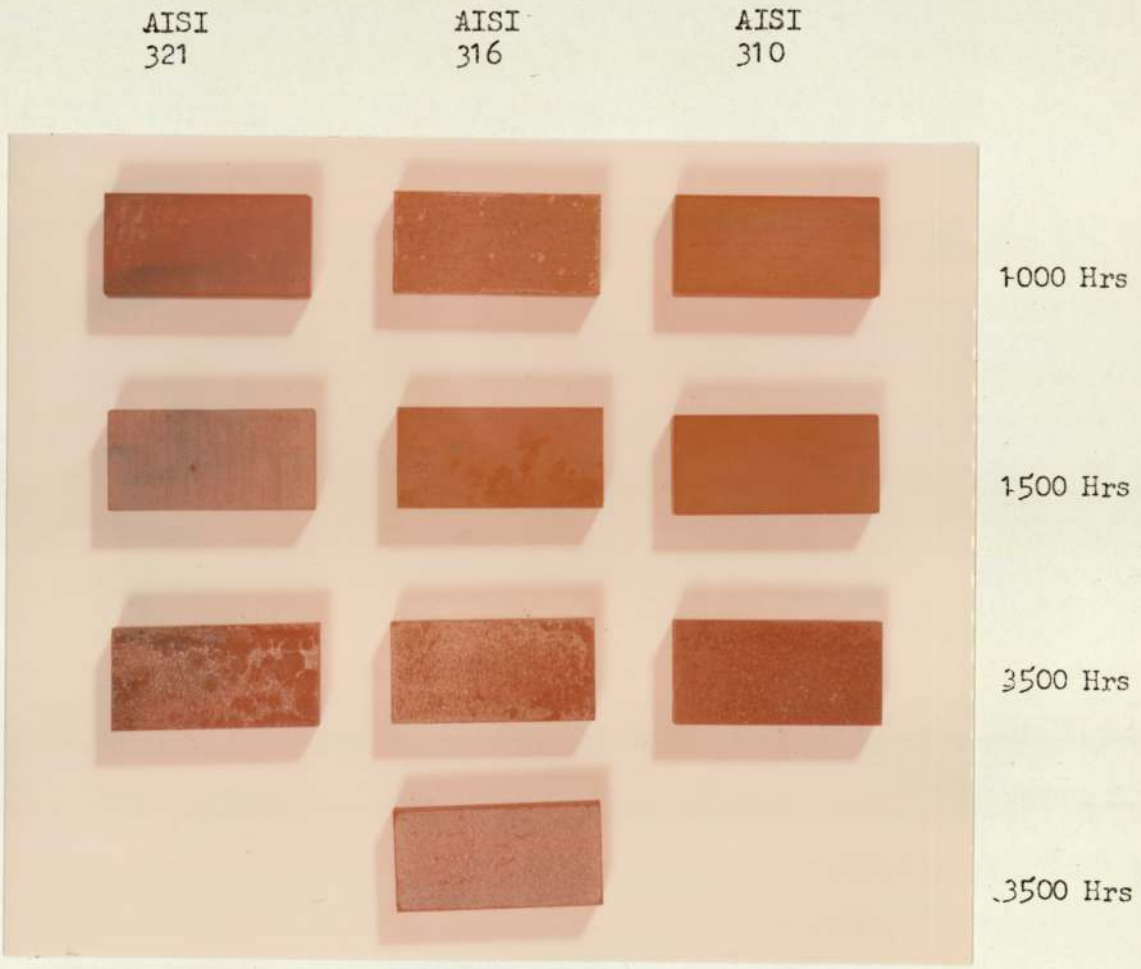

Figure 3.2 Surface oxide characteristics with respect to increasing time of oxidation. (Magnification x 1.)

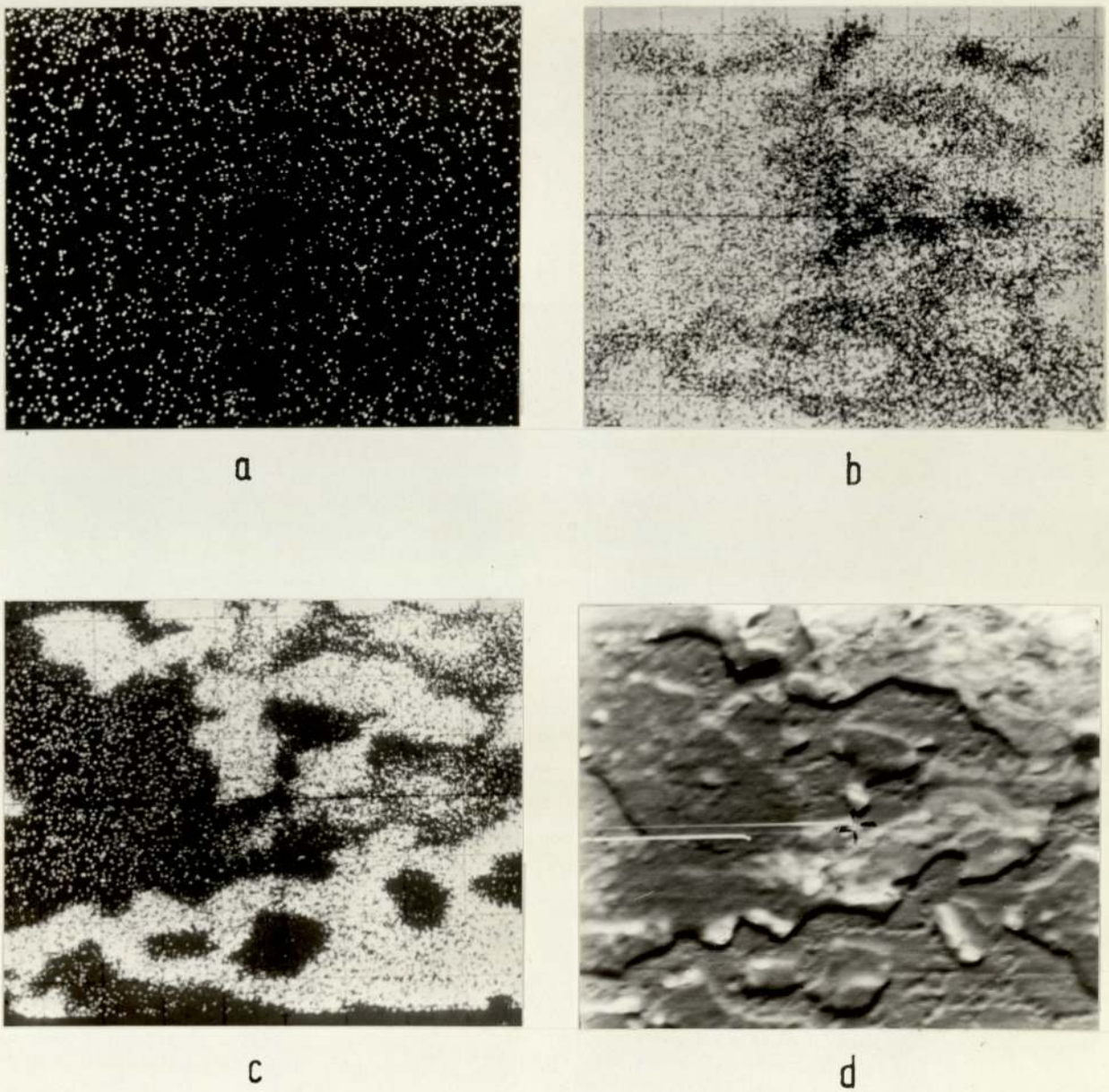

Figure 3.4 Electron-probe X-ray distribution images of a) Ni, b) Cr and c) Fe; d) secondary electron image of (c). (Magnification x 300.)

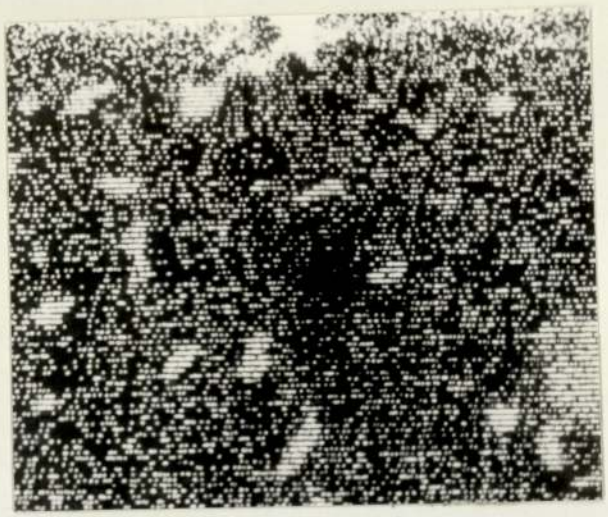

a

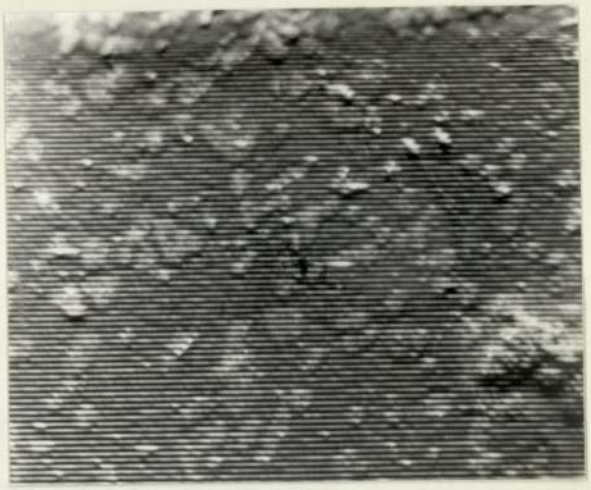

b

Figure 3.5 a) Electron-probe X-ray distribution image of Fe showing nodular character of oxide.
b) Secondary electron image of (a). (Magnification x 190.)

Figure 3.6 Electron-probe X-ray distribution image of Mn taken at specimen edge. (Magnification x 300.)

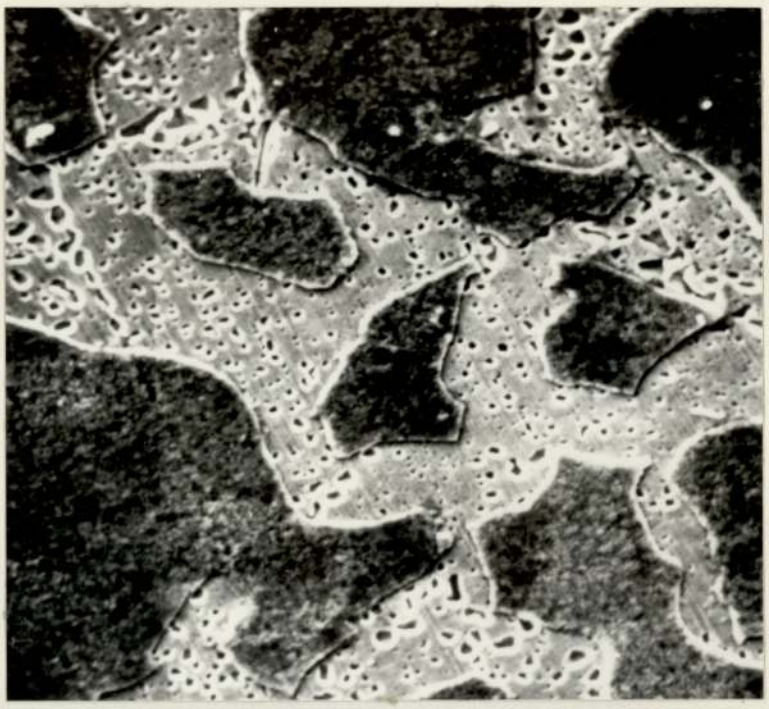

a.

b.

Figure 3.7 a) Chromium oxide exhibiting spalling. (Magnification x 500.)

b) Chromium oxide structure. (Magnification x 2k.)

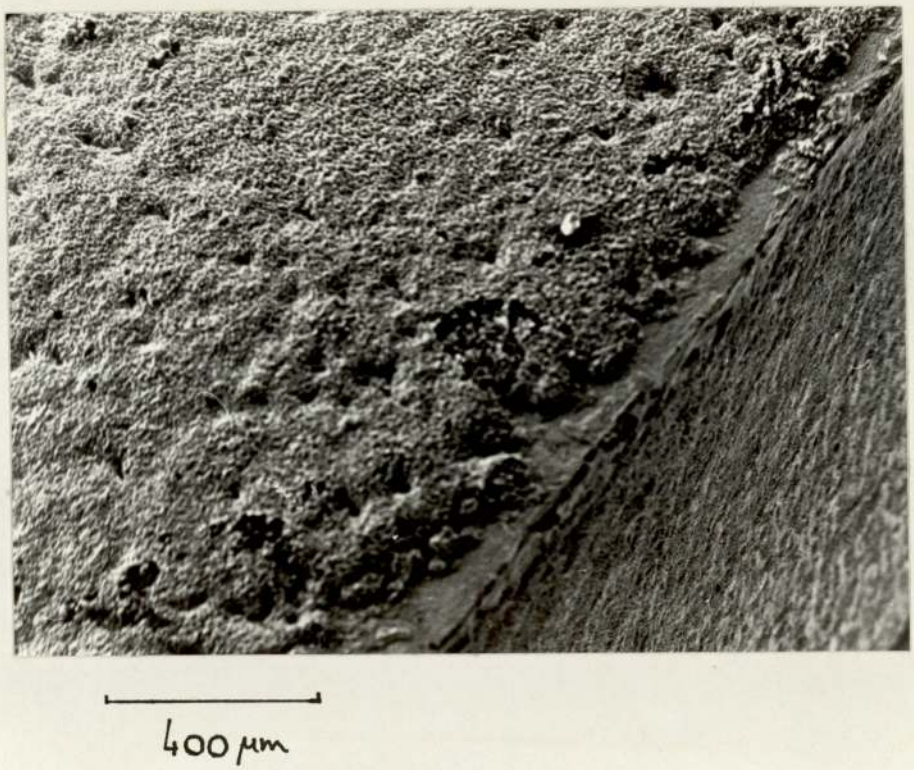

Figure 3.8 Duplex oxide growth.

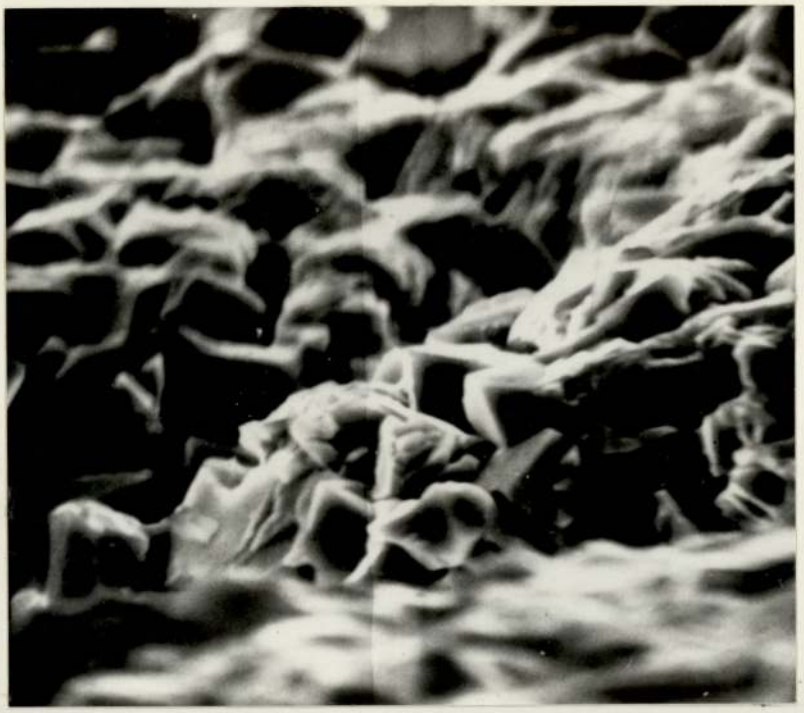

(a)

(b)

Figure 3.9 a) and b) Crystalline Duplex oxide.

Figure 3.10 Cross section morphology of protective Chromium (III) oxide. (Magnification x 300.)

Figure 3.11 (a) Cross section morphology of nodular, Fe-rich, duplex oxide. (Magnification x 600.)

Figure 3.11 (b) Cross section morphology of nodular, Fe-rich, duplex oxide. (Magnification x 300.)

Figure
3.10

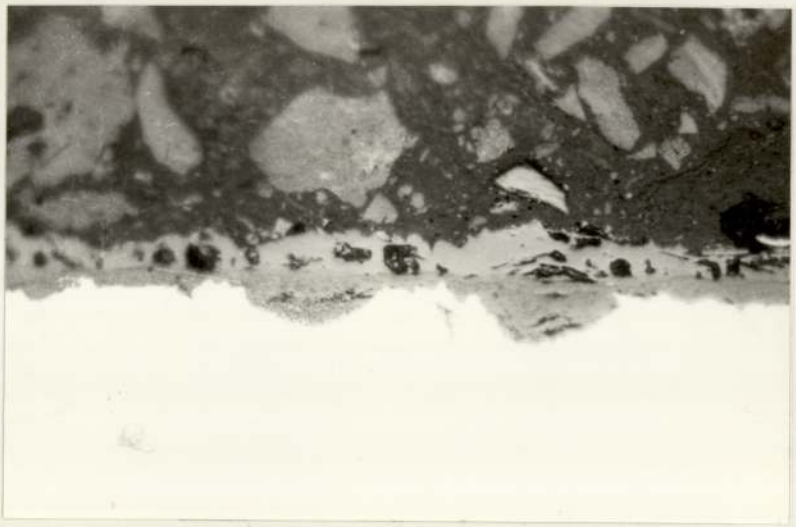

Figure
3.11 (a)

Figure
3.11 (b)

(a)

-(b)

Figure 3.12 a) and b) Etched Cross section morphology of single duplex oxide nodules showing hemispherical shape and duplex structure. (Magnification x 600.)

(a)

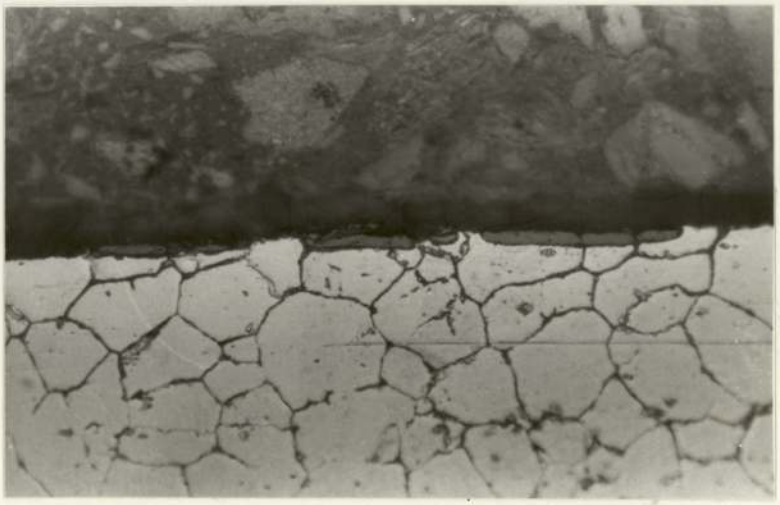

(b)

Figure 3.13 a) Etched cross section morphology of nodular duplex oxide. (Magnification x 150.)

Figure 3.13 b) Etched cross section morphology of uniform duplex oxide showing the affect of grain boundaries. (Magnification x 300.)

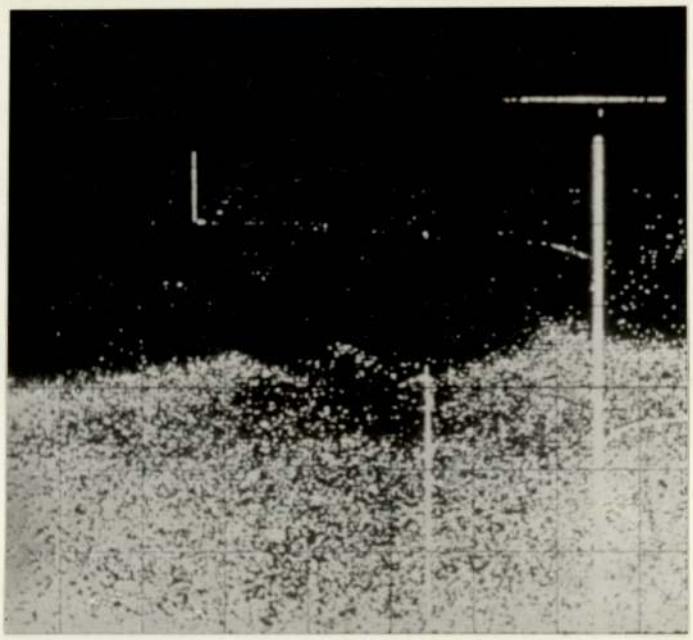

Figure 3.18 Electron-probe Fe X-ray distribution image of a duplex oxide nodule in cross section. (Magnification x 1k.)

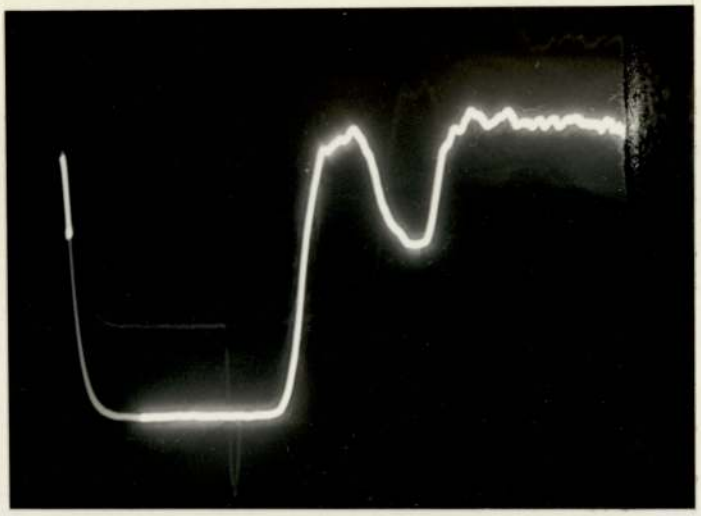

a)

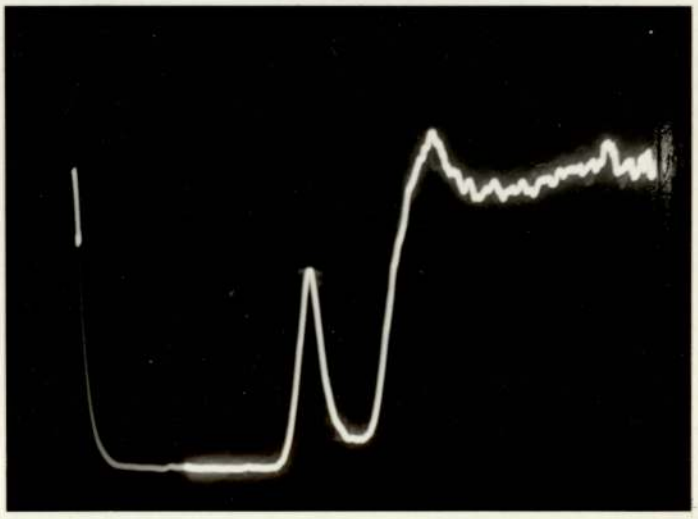

b)

Figure 3.19 a) and b) Electron Probe Subsurface concentration profiles of Fe and Cr respectively. (Magnification x 1k.)

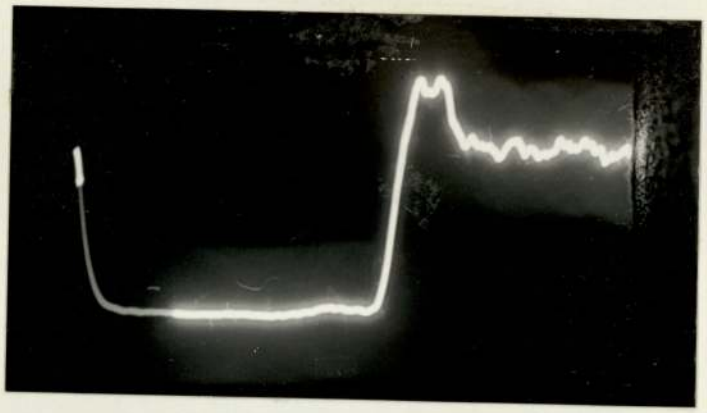

c)

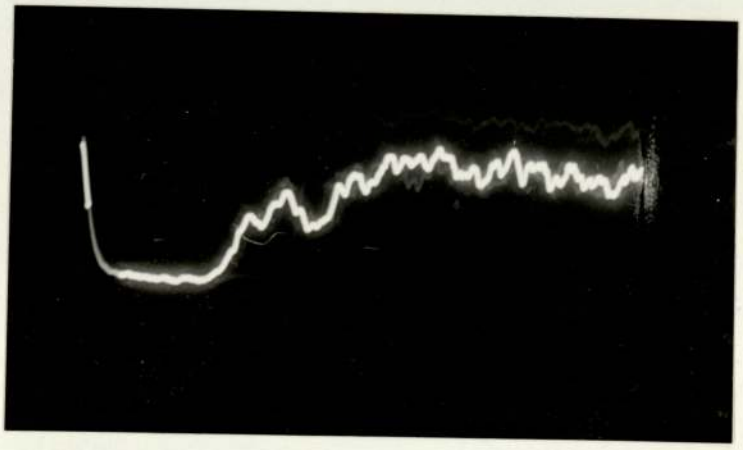

d)

Figure 3.19 c) and d) Electron probe subsurface concentration profiles of Ni and Mn respectively. (Magnification x 1k.)

Figure 3.20 a) and b) Electron probe Cr and Fe X-ray distribution images of nodular oxide in cross section, respectively. ((a) Magnification x 300; (b) Magnification x 300.)

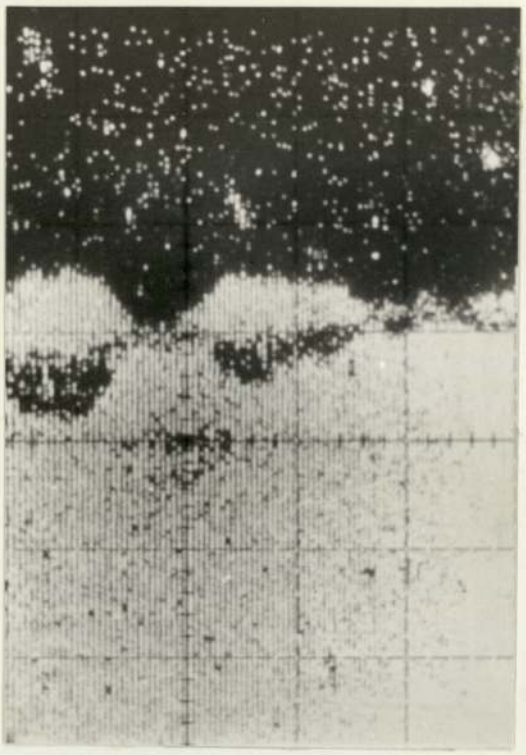

Figure
3.20 (a)

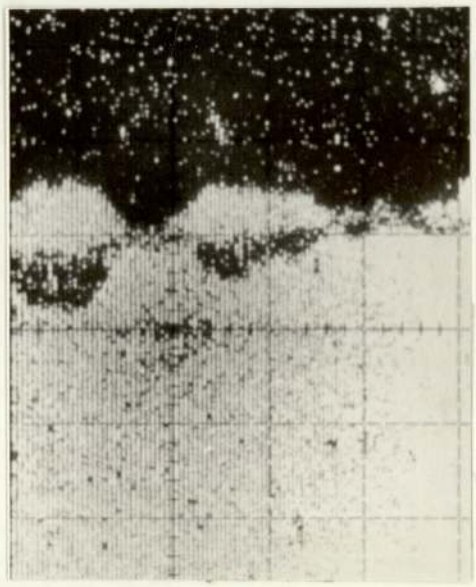

Figure
3.20 (b)

CHAPTER 4

TRIBOLOGICAL STUDIES OF AUSTENITIC STAINLESS STEELS

4.1 EXPERIMENTAL DETAILS

4.1.1 Introduction

The wear experiments carried out in the present work study the unlubricated friction and wear behaviour of the austenitic stainless steels under various operating conditions.

The operating conditions involved are those of artificial gaseous environments, externally induced high temperatures and various sliding velocities and loads. The influence of Chromium content upon the wear behaviour is also investigated. Consequently, it is the AISI 316 and AISI 310 stainless steel varieties, being of significantly different chromium compositions, that are tested.

In general, the work described in the present section can be divided into three main areas:-

(i) The friction and wear behaviour of austenitic stainless steels operating at room temperature and under a CO_2 environment.

(ii) The friction and wear behaviour of austenitic stainless steels operating at room temperature and under an air environment.

(iii) The friction and wear behaviour of austenictic stainless steels operating at elevated temperatures and under a CO_2 environment.

4.1.2 Wear Testing Machine

The wear experiments carried out in the present work were conducted on a continuous sliding pin on disc wear machine.[42] The pin on disc facility of the machine provided a flat on flat geometry test situation, as opposed, for example, to the very different geometries of a crossed-cylinders or disc on disc (Amsler-type) wear testing machines.

Figure 4.1

General view of the pin on disc continuous sliding Wear Test Rig.

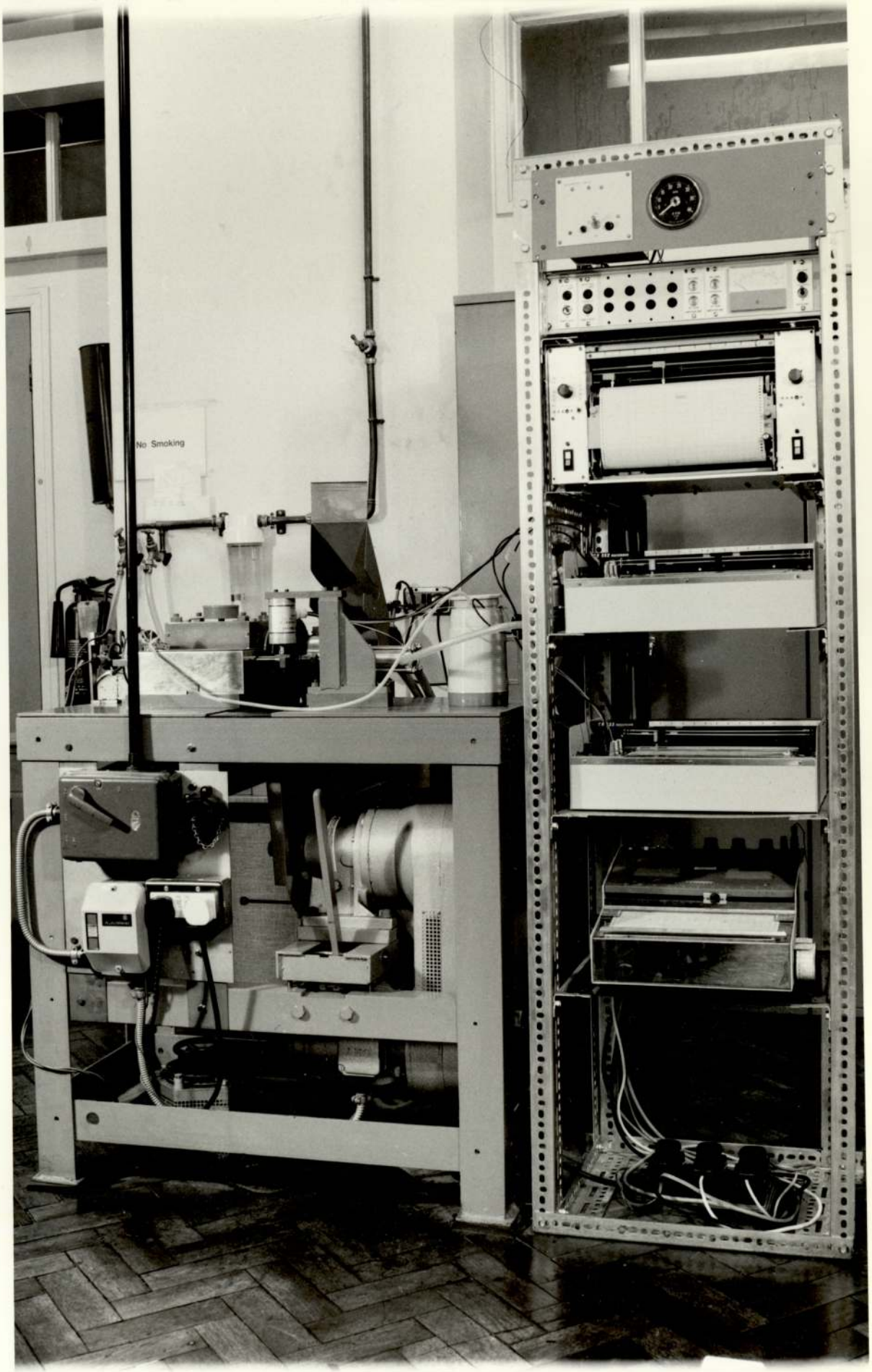
No Smoking

An illustration of the pin on disc wear testing machine is shown in figure (4.1). This apparatus was designed to fulfill a wide range of applications in wear testing. It was designed to operate over a wide range of loads and speeds. Incorporated in the apparatus is a heating facility capable of raising the bulk temperature of the disc up to 700°c. Facilities to continuously monitor wear rates, sliding friction, pin and disc temperatures and sliding speeds are also incorporated.

(i) General Features

Sliding Velocities and the Drive System. A 3-phase, 4H.P. electric driving motor, a variable speed pulley and a reduction gear-box provides the main driving mechanism for the machine. By this, rotational speeds in the range 60 to 1440R.P.M. corresponding to linear sliding velocities in the range 0.31 to 7.5 ms^{-1} could be achieved. To measure the speeds of rotation a magnetic impulse tachometer was used.

Loading. A loading shaft is used to convey the applied load to the pin. Linear and rotary bearings are used in housing the shaft to allow freedom of movement. The loading shaft assembly is shown in figure (4.2).

The necessary loads required could be applied in two ways: firstly, by means of a pneumatic system where compressed air could power a piston mounted along the axis of the loading shaft and secondly by direct dead weight loading. In this way, loads in the range 1.0N to 49.0N could be applied. Due to the friction and debris contamination of the loading-shaft bearings and seals very light loads could not be applied.

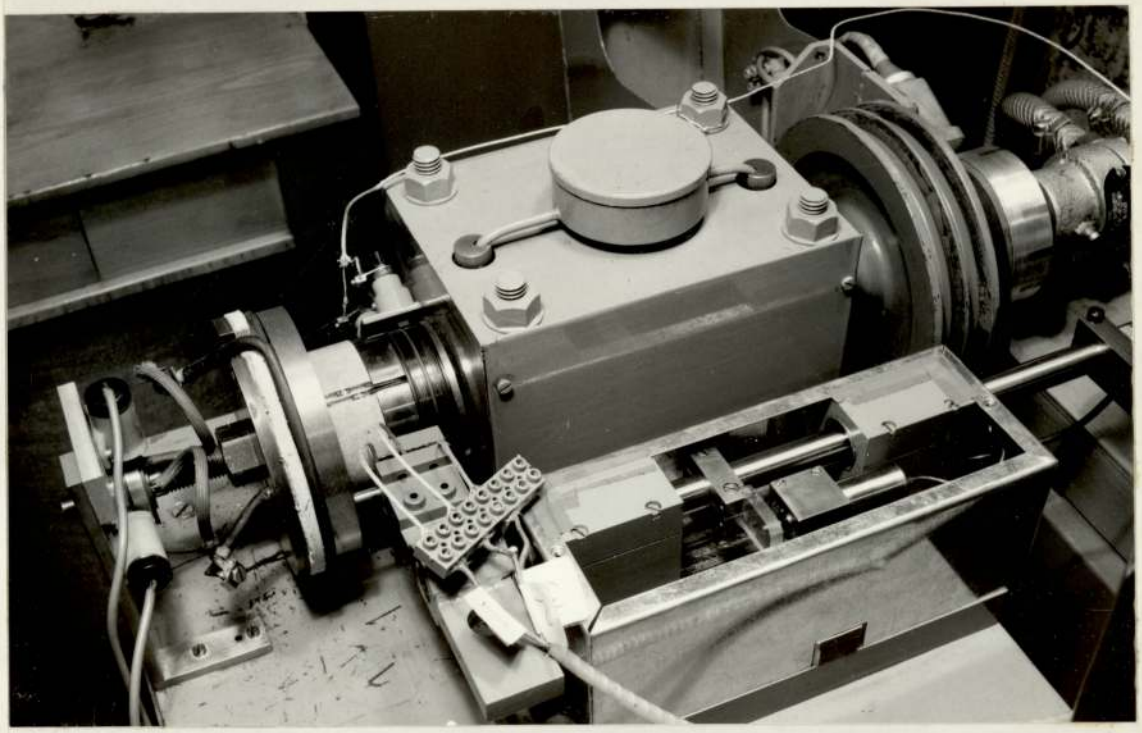

Figure 4.2

Pin loading assembly and the heating facility.

Electrical Assembly of the Wear Testing Rig

1. Power supply transformer.
2. Disc resistance heater.
3. Pin.
4. Pin thermocouples.
5. Cold junction - Ice bath.
6. Slip ring commutator.
7. Disc.
8. Slip ring shaft commutator.
9. Linear voltage differential transformer.
10. Friction strain guage.
11. Magnetic Pick-offs.
12. Impulse tachometer.
13. Strainstall transducer amplifiers.
14,15 & 16. X-t potentiometric recorders.

Figure 4.3

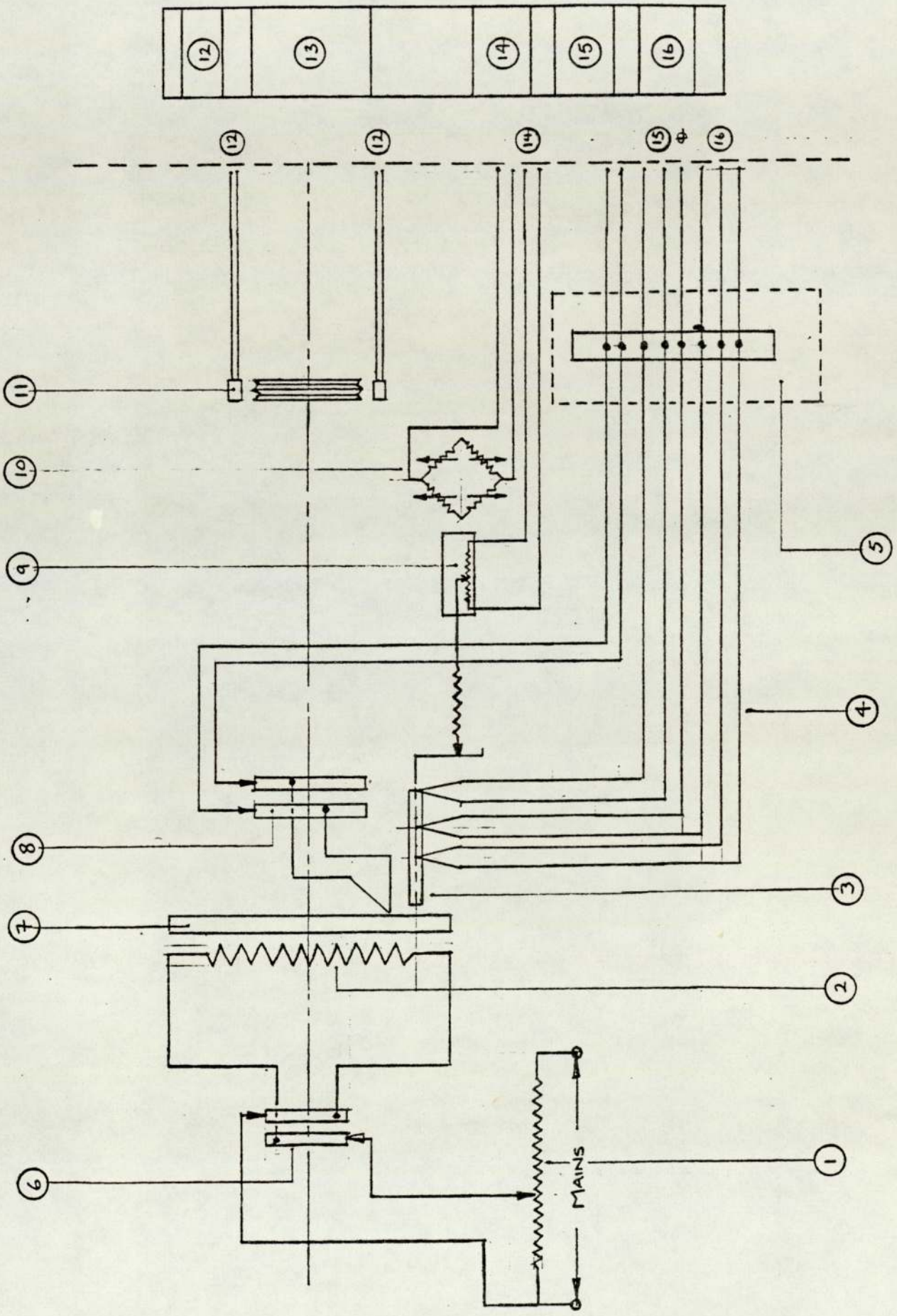

Disc Heating Assembly. By means of a 2KW electrical resistance heater, in the form of a ring attached to the non-wearing side of a specimen disc, disc temperatures upto 720°c could be obtained. The heating assembly was mounted on a secondary shaft screwed into the main shaft and consisted of an insulating annulus, a securing plate and a set of copper slip rings to provide electrical contact. A 270 volt auto-transformer connected to the heater via carbon brushes supplied the energy. The full heater assembly is illustrated in figure (4.2) and schematically in figure (4.3).

Calorimeter Pin-Holder. The pin-holding mechanism consisted of a split cylinder flow calorimeter arrangment where the pin, sandwiched between the two halves of a calorimeter, is tightly gripped when housed into the loading shaft. Such a calorimetric arrangement provided a convenient method of measuring the frictionally generated heat flow along the pin. A schematic diagram of the pin-holding mechanism is shown in figure (4.4)

Carbon Dioxide Gas Environment Assembly. A suitably sealed metal container, incasing the specimen area, was used in providing a gaseous carbon dioxide environment. By appropriate modification to the main shaft and loading-shaft housings, the container could be positioned to completely cover the disc, pin-holder-arm and the heater assembly, to create an isolated compartment within which to develop the gaseous environment. Figure (4.5) illustrates the assembly.

In sealing the container, initially silicone rubber cement and a sealing compound (used extensively in high temperature applications) were used. However, although being resistant to high

Calorimetric Pin-Holder Assembly

1. Pin.
2. Pin thermocouples; T_A, T_B and T_C.
3. Pin copper calorimeter.
4. Sindanyo insulation.
5. Calorimeter copper base.

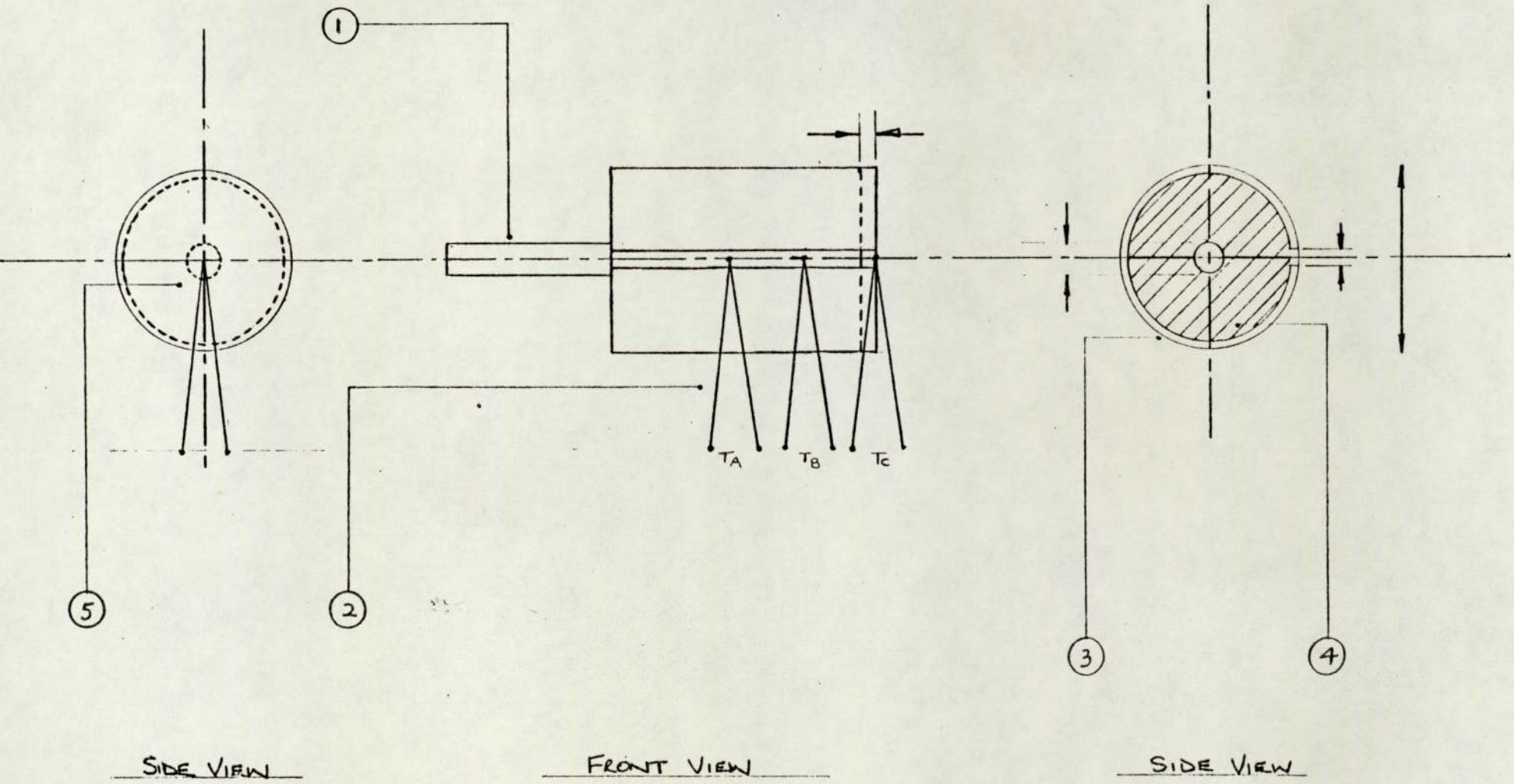

Figure 4.4 Calorimetric Pin-Holder

Components of the Wear Testing Rig

1. Environment container.
2. Central shaft.
3. Cooling assembly.
4. Drive pulley.
5. Disc.
6. Pin.
7. Loading shaft roller bearings.
8. Loading shaft.
9. L.V.D.T.
10. Friction strain guage.
11. Pneumatic thrust piston.
12. Drive motor.
13. Drive belt.

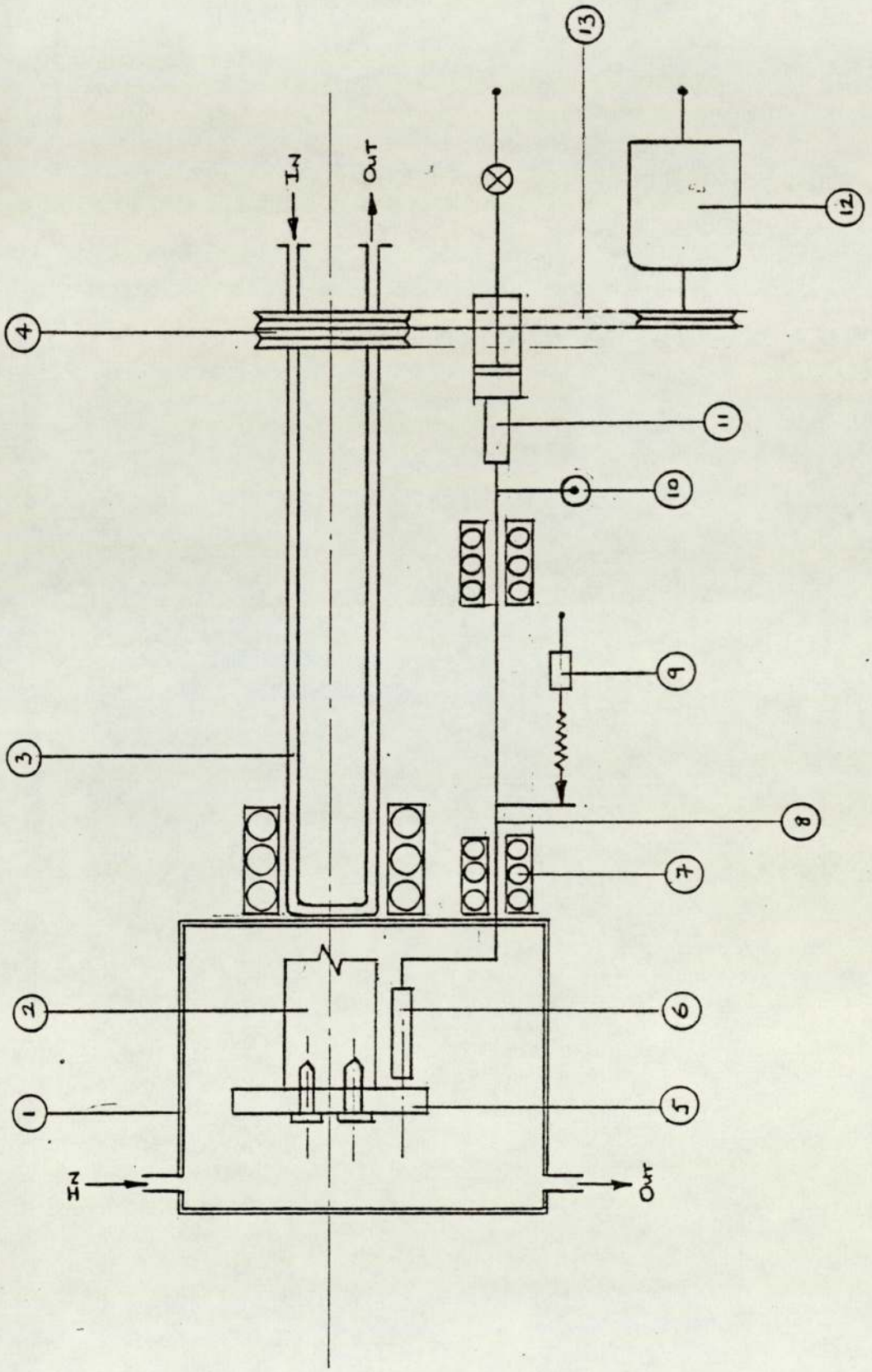

Figure 4.5 Schematic representation of the Wear Test Rig.

temperatures and achieving gas-tight seals they were found to be difficult to apply and remove. In consequence, a readily removable plasticine based sealing compound was finally used although this was found to be relatively unstable with long-term exposure to high temperatures.

Gas Supply. A schematic diagram of the gas supply circuit is shown in figure (4.6). Carefully regulated CO_2 gas was supplied on a continuous basis via a gas cylinder filled to $15 \times 10^3 kN/m^2$. Due to the eventual slow leakage of the gas through the main shaft clearance a continuous supply of gas was necessary to ensure a dominantly CO_2 and non-stagnant environment.

For the control and regulation of the gas flow, a flow restrictor, a needle valve flow-controller and a standard gas-cylinder pressure regulator were employed. A narrow-bore coiled tubing or flow restrictor, in combination with a needle valve flow controller, provided stable control and allowed and maintained flow into the specimen area at a low rate, Vi_3, 100-200cm^3/m. To monitor the rates of flow, an auxillary flow rotameter was occasionally employed and used also for the purposes of adjusting the flow controller.

To ensure that a predominantly Co_2 environment prevailed, within the specimen area, a positive gas pressure of the gas inside the container was necessary. With adequate sealing, as described above, a gas pressure of 0.2 bar could be achieved and maintained. A pressure gauge, situated at the end of the gas-line, could be used to monitor this pressure and to ensure against over pressurisation.

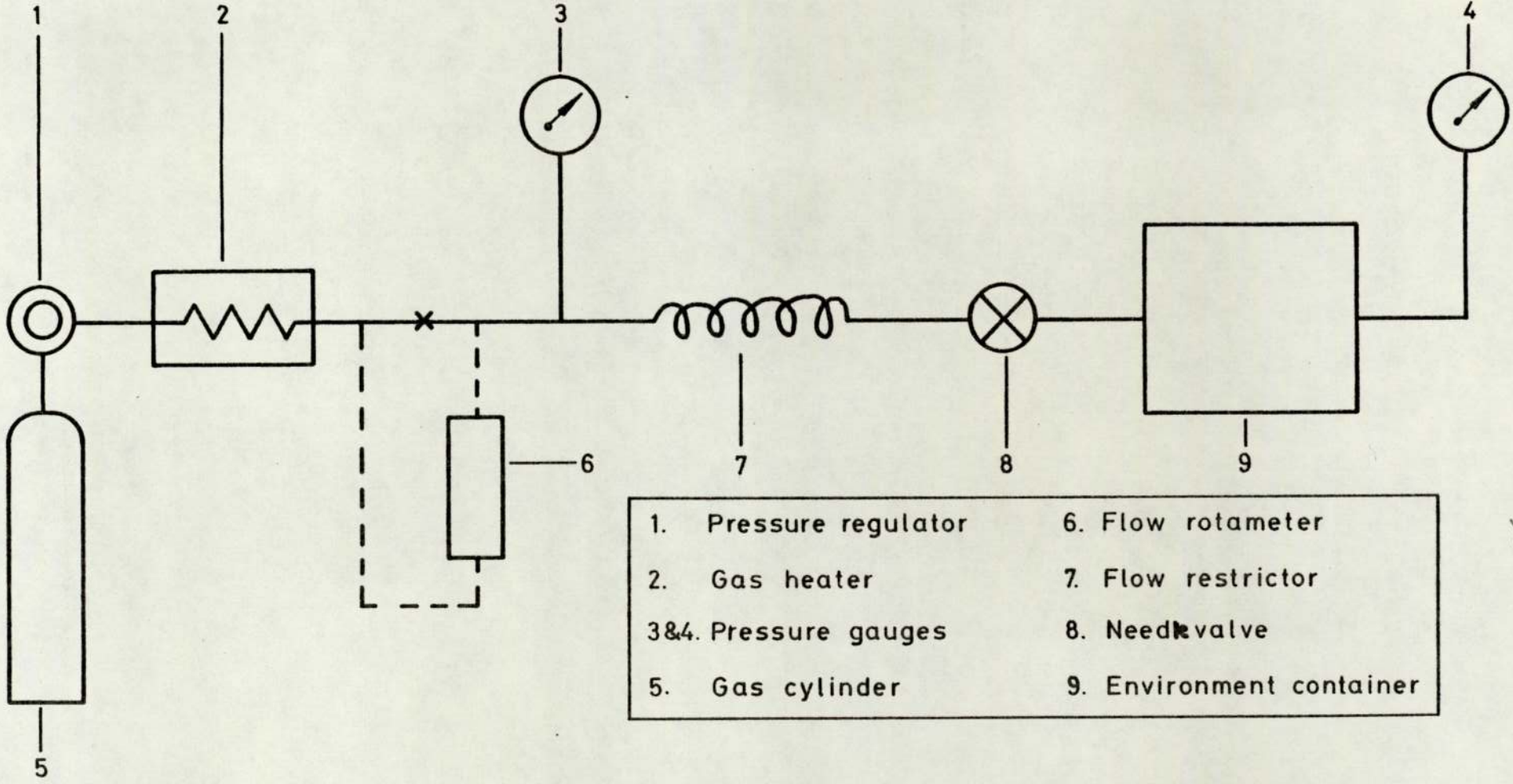

FIG. 4.6 Schematic Diagram of the CO_2 Gas - Environment Assembly.

In providing a continual supply of gas to the specimen area, a gradual cooling of the specimens, particularly at high temperatures, by the cold in-flowing gas was found to be significant. To minimise such an effect a gas pre-heater connected to the outlet of the gas pressure regulator was used. This maintained the ambient temperature of the gas flowing into the environment area at just above room temperature.

(ii) Temperature Measurement

Disc Temperature: To measure the bulk disc temperatures Chromel-Alumel thermocouples, spot-welded close to the disc wear-track, were used. The thermocouple leads were connected to carbon slip rings mounted on the main shaft and through these connected externally to a cold-junction and finally to a signal recording x-t recorder. In this way, the continuous recording of the disc temperature was possible. A circuit diagram illustrating the thermocouple connections is shown in figure (4.3).

Pin Temperature. To determine the heat flow through the pin, due to frictional heating, temperature measurements at set distances along the pin were monitored. For this, chromel-alumel thermocouples spot-welded at three positions along the pin were used. The three thermocouple connections to the pin, Ta, Tb and Tc, in relation to the calorimeter and the pin, are illustrated in figure (4.4). Ta and Tb measure the magnitude of the heat flowing along the pin at the points of their connections; Tc, placed at the pin-end and in contact with the calorimeter casing, measures the ambient temperature of the specimen area, the temperature of the calorimeter and the magnitude of the heat-flow at the pin-end. (43)

A circuit diagram illustrating the external connections of the thermocouples is shown in figure (4.3). The method by which the pin temperature measurements were interpreted to provide data for the Heat Flow Analysis is given in Chapter 5 and ref. (43).

Reliability of the Temperature-Monitoring. To assess the accuracy and the reliability of the chromel-alumel thermocouples, a digital thermometer was used to cross-check the thermocouple readings. Measurements were taken simultaneously at two auto-transformer settings.

Figure (4.7a) illustrates a graphical representation of the readings recorded at the positions Ta and Tb on the pin, with the auto-transformer setting at 80 volts. The faithful monitoring of the temperatures by the pin thermocouples to within $\pm 12^{\circ}c$, at all stages of the heating, is clearly apparent. Figure (4.7b) represents the readings taken at the disc area at a transformer setting of 60 volts. The faithful monitoring of the temperature by the disc thermocouples to $\pm 10^{\circ}c$ is also evident, at all stages of heating.

(iii) Wear Measurement

A continuous measurement of the wear occurring on the pin was achieved by the use of a Linear Voltage Differential Transformer or LVDT. The transducer could detect small changes in the position of the loading shaft and therefore in the change in pin length.

An illustration of the LVDT and its relation to the pin and the loading shaft is shown in figure (4.2) and in schematic form in figure (4.5).

Continuous monitoring of the transducer output was

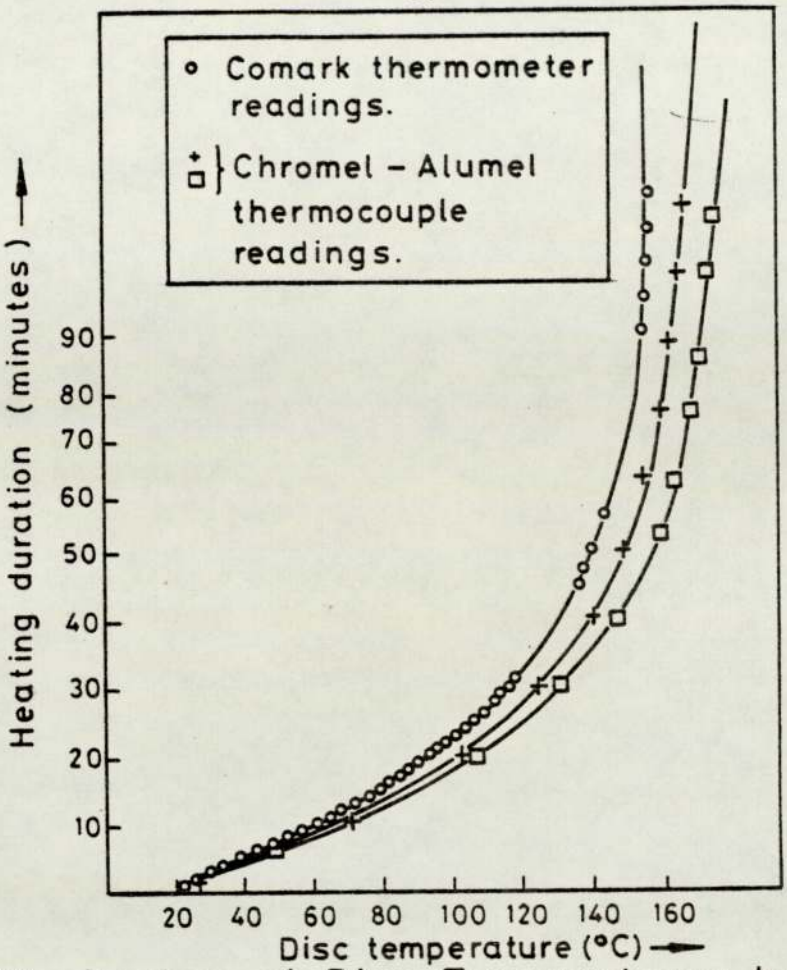

FIG.4.7 (b) Monitoring of Disc Temperatures by Chromel - Alumel Thermocouples.

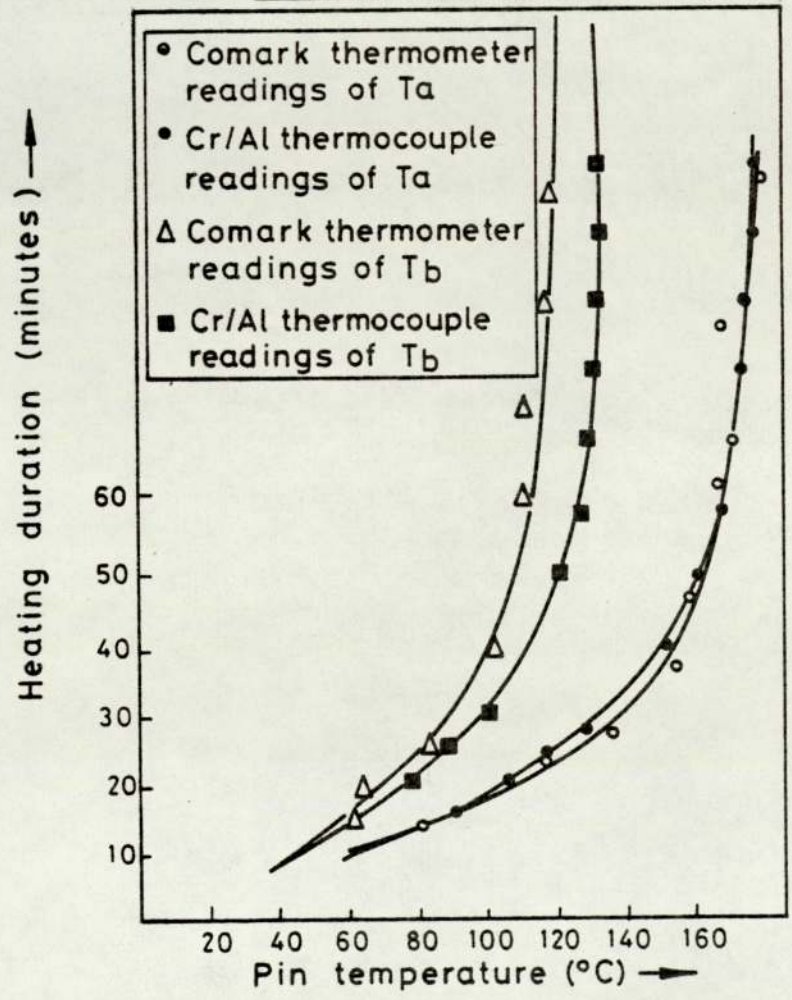

FIG.4.7 (a) Monitoring of Pin Temperatures by Chromel - Alumel Thermocouples.

achieved by amplification and subsequent recording by a x-t recorder. The deflection in the transducer trace, thus produced, with respect to time, indicated directly the rate of wear of the pin.

During experimental runs, equilibrium steady-state conditions were looked for. By examination of the linearity of the LVDT traces such equilibrium wear stages could be identified. The traces could also be used to identify other wear characteristics such as the initial severe wear conditions and major wear transitions.

An alternative method of wear measurement, namely the weight-loss technique, was also used. This technique could be used to deduce pin wear by determining the overall weight loss of the pin. The ratio of the loss in weight of the pin ΔW, expressed with respect to its density, ρ , to the total distance slid, S, by the pin, defined the rate of wear, K , of the pin that is:

$$K = \frac{\Delta W}{\rho}/S \quad cm^3.cm^{-1}$$

Discrepancies. The errors inherent in the LVDT method of measuring wear rates can be due to the results of entrapped wear debris, embedded pin, and electronic and mechanical noise. Firstly, due to the trapped debris between the rubbing surfaces, lower than actual wear rates may be obtained, since the real reduction in pin length cannot be detected. Secondly, the embedding of the pin into the disc wear-track can result in erroneous wear estimates, due to the exaggerated apparent decrease in pin length. Finally, as a result of the electronic noise, generated by the amplifying and recording systems and the low amplitude mechanical vibration at the loading shaft, a wide and spiked wear trace, leading to uncertainties, can be obtained.

By the combined use of the wear data from the LVDT and the weight-loss techniques much improved accuracy is obtained. In the latter method, however, no distinction can be made between the initial running-in wear and the lesser equilibrium wear.

(iv) Friction Measurement.

Continuous monitoring of the friction behaviour was achieved by the use of a strain gauge dynamometer. This could detect the torque exerted on the loading shaft by the frictional force. Figure (4.5) shows the positioning of the dynamometer with respect to the loading shaft and the pin and disc area.

As with wear measurement, the dynamometer output was firstly amplified and subsequently monitored by a x-t recorder.

Due to mechanical vibration and to the repeated bouncing of the friction arm, distortions in the output signal tended to be significantly high. To minimise this, mechanical damping was introduced to restrain the bouncing and to restrain the mechanical vibration.

4.1.3 Specimen Preparation

The stainless steel disc materials were recieved in the softened and descaled states. These were initially plasma cut to approximate size and subsequently accurately machined to exact size. The discs were of dimensions 120mm dia., x 8mm. The pins, also in the softened and descaled state, were machined to dimensions of 0.064mm dia., x 31.8mm.

To achieve representative wear, the surface finishes (an important part of the overall specimen preparation) needed to

match those of the pins at the rubbing faces. Surface finishes, achieved by grinding (for the discs) and machining (for the pins), were maintained at a standard 1 μm CLA level, but found to vary with individual specimens within the range 0.75-2.0 μm CLA.

Prior to testing, thorough degreasing and cleaning of the specimens was essential. A procedure of cleaning in hot water and soap solution and degreasing in petroleum vapour was adopted. To avoid contamination or damage to the rubbing faces of the specimens careful handling when mounting on the wear test machine was required. After testing, immediate weighing of the pins was carried out.

4.1.4 Wear Tests at Room Temperature

(i) In Air:

Loads in the range 3N to 130N and sliding speeds of $0.5ms^{-1}$ and $2.0ms^{-1}$ were used for the tests conducted under air at room temperature. The effect of high temperatures under air was not investigated.

In the setting-up procedure, pin adjustment, to ensure correct alignment against the disc prior to loading, was essential. Sample wear debris, for analyses, was collected during all tests.

(ii) In Co_2

For the Co_2 experiments, similar setting-up procedures and operating conditions were observed. However, in addition, purging of the air from the specimen area to develop the Co_2 environment was necessary. Repeated filling of the environment container with the denser Co_2 gas, to the required pressure, satisfactorily achieved

purging. The subsequent upkeep of this pressure ensured a predominantly Co_2 environment.

4.1.5 Wear Tests at Elevated Temperatures

Loads in the range 3N to 130N, a sliding speed of $0.5ms^{-1}$ and temperatures of 300°c and 500°c were used for the tests conducted under Co_2 at high temperatures.

Due to the cooling effect of the Co_2, the gas environment was firstly developed and the specimens heated subsequently. In heating the specimens, the pin was loaded against the disc and the heating of the latter commenced. In this way, the indirect heating of the pin was achieved without the necessity of a separate pin heater. The temperature of the disc was gradually raised to the required value and allowed to reach steady-state.

4.2 WEAR RESULTS

4.2.1 Wear of the AISI 316 Stainless-Steels (No External Heating)

In general, the wear behaviour of the AISI 316 stainless steels, under the conditions investigated here, is characterised by a transitional two-phase wear pattern. Mild and severe wear phases separated by a transition defines the two-phase wear pattern. Under all conditions, a critical load is found to induce the transition between the two phases. Above the critical load severe wear is encountered whilst mild wear predominates at loads below the critical condition.

Figure (4.8) illustrates the general wear behaviour of the austenitic AISI 316 stainless steels when sliding at speeds of $0.5m.s^{-1}$ and $2.0m.s^{-1}$, under an air and Co_2 environment.

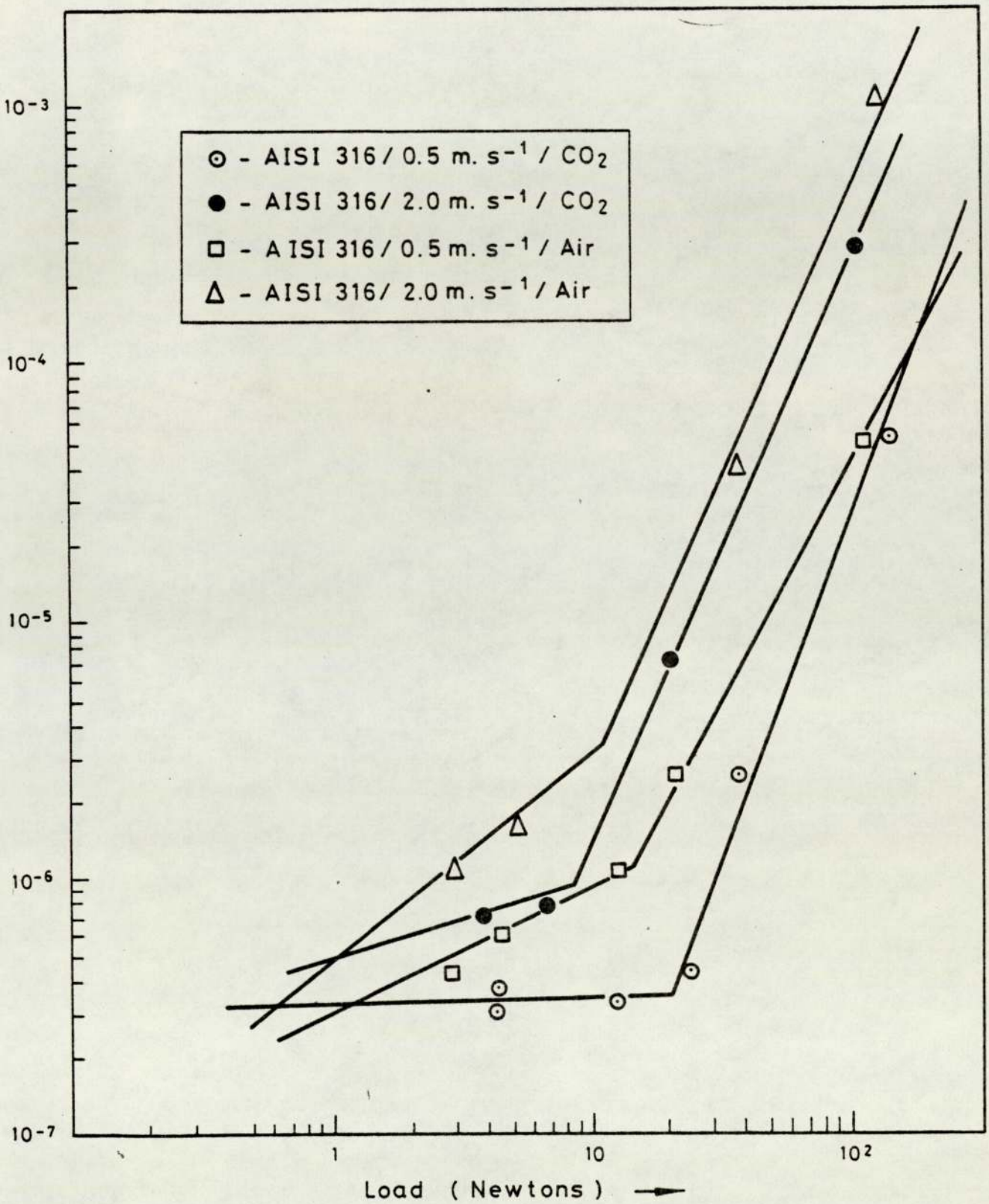

FIG. 4.8 The Wear Behaviour of the AISI 316 Stainless Steels at 0.5 & 2.0 m.s^{-1} in Air and CO_2

(i) Wear Under Air

It is apparent from figure (4.8) that the wear behaviour under an air environment is strongly load dependent, about a critical loading condition. A transition at the critical load produces steeply rising wear rates, indicative of adhesive and galling wear, from a much less energetic and milder wear process.

The effect of sliding velocity upon the wear behaviour is illustrated by figure (4.8). Lowering the sliding speed to 0.5 $m.s^{-1}$ appears to lower the wear rates by one half of an order of magnitude, to a range between 5×10^{-7} $mm^3.mm^{-1}$ to 2×10^{-4} $mm^3.mm^{-1}$ from 1×10^{-6} $mm^3.mm^{-1}$ to 1×10^{-3} $mm^3.mm^{-1}$ at $2.0ms^{-1}$. and at corresponding loads. The critical load, however, is unaffected by a change in sliding speed and is retained constant at the 1.0 - 1.5kgm load.

The effect of environment and sliding velocity upon the wear rate and the load transition is illustrated in tabular form by Tables 4.1a) and b).

(ii) Wear Under Carbon Dioxide.

As shown by figure (4.8), operation within a Co_2 - gas environment has the effect of reducing the overall sliding wear, relative to the wear in air.

Considering the wear patterns produced under the extreme operating conditions, a decrease in the wear rates by one order of magnitude at all loads is typical. Wear rates in the range 3×10^{-7} $mm^3.mm^{-1}$ at 0.4kgm to 5.6×10^{-5} $mm^3.mm^{-1}$ at 15.0kgm for $s = 0.5$ ms^{-1} and 6.5×10^{-7} to 5.0×10^{-4} $mm^3.mm^{-1}$, for corresponding loads, at $s = 2.0$ ms^{-1} are found. (Tables 4.1a) and b).)

As with air, a strongly load dependent wear pattern about a critical loading condition characterises the overall wear behaviour.

(iii) The Effect of Sliding Speed

For all environments, a sliding speed dependent wear behaviour is apparent. The effect of reducing the sliding speed is to significantly lower the wear rates and to displace the critical load.

In the severe wear region, for Co_2 conditions, a reduction of above one order of magnitude in the wear rates is produced, giving values of 4×10^{-7} $mm^3.mm^{-1}$ at 2.0kgm and 5.6×10^{-5} $mm^3.mm^{-1}$ at 15.0kgm, for a speed of 0.5 ms^{-1}, from 7.0×10^{-6} $mm^3.mm^{-1}$ and 5×10^{-4} $mm^3.mm^{-1}$, at the 2.0 ms^{-1} speed, respectively. In the mild wear region, however, a change in the sliding velocity has a very much smaller effect. The large reductions as seen in the severe wear region are not repeated. Decreases of less than one half of an order of magnitude, as a miximum, are found giving typical wear rates in the region of 6.0×10^{-7} $mm^3.mm^{-1}$.

Wear Transition. A sliding speed dependent wear transition is apparent under Co_2 conditions. By reducing the sliding speed the position of the transition is displaced to higher loads and to a new critical loading value. At a speed of 2.0 ms^{-1} the transition is found to occur at 0.9kgm but with a change in sliding speed to 0.5 ms^{-1}, displacement to a higher load of 2.0kgms occurs. (Figure 4.8)

4.2.2 Wear of the AISI 310 Stainless Steels (No External Heating)

In general, the wear behaviour of the austenitic AISI 310 stainless steels is characterised by a distinctly non-transitional and a directly load dependent wear pattern. A single-phase wear mode defines the overall wear pattern and predominates in the wear behaviour under all operating conditions.

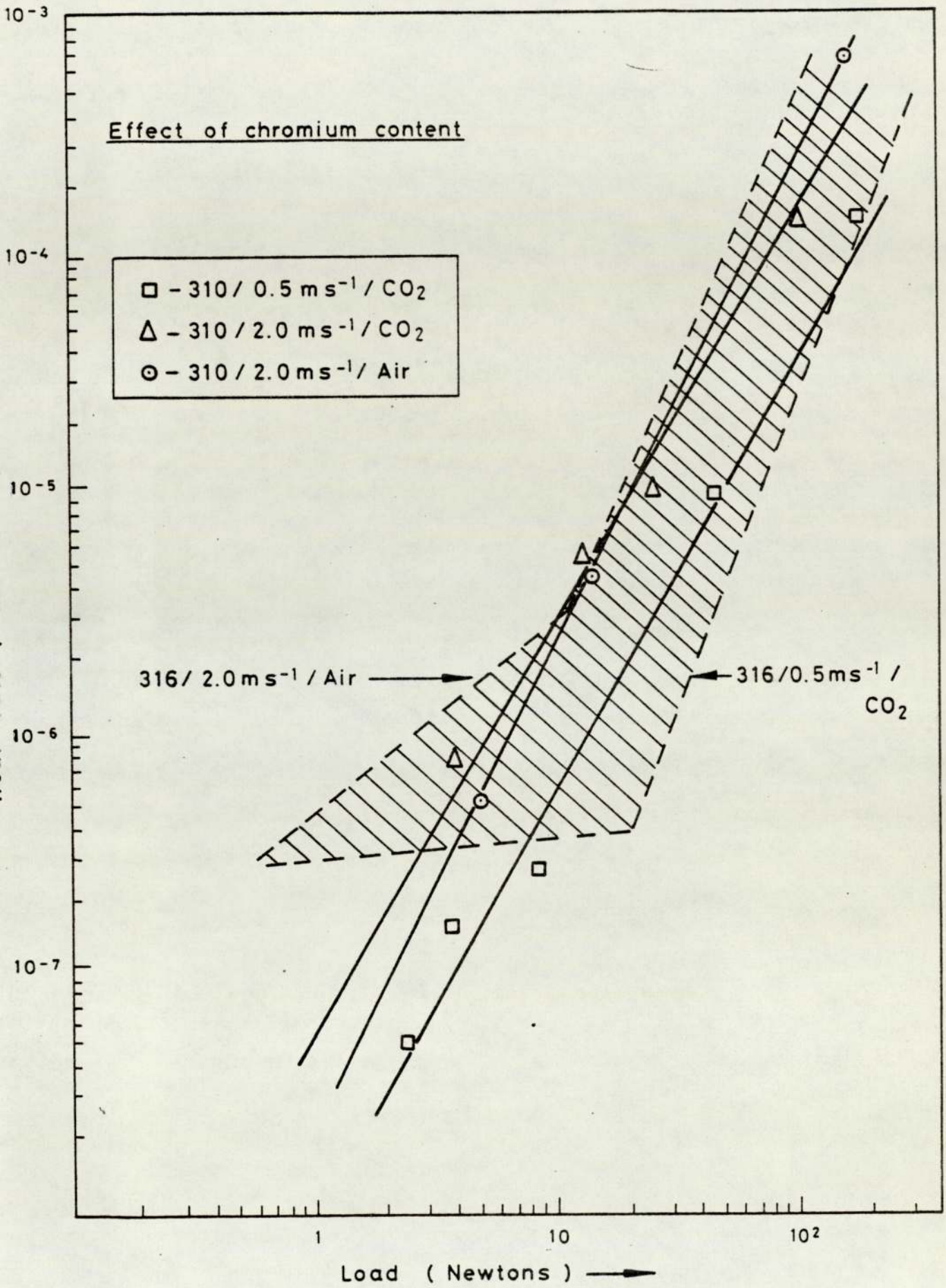

FIG. 4.9 The Wear Behaviour of the AISI 310 Stainless Steels at 0.5 m.s^{-1} & 2.0 m.s^{-1} in Air and CO_2

Figure (4.9) illustrates the general wear behaviour of the AISI 310 steels when operating at speeds of $0.5m.s^{-1}$ and $2.0m.s^{-1}$ under air and Co_2 environments.

(i) Wear Under Carbondioxide

The wear of the AISI 310 steels under a Co_2-gas environment is clearly non-transitional. A strongly load dependent and steeply rising wear pattern, indicative of severe wear, is seen.

By reducing the sliding speed, to $0.5m.s^{-1}$, lower wear rates are obtained, but a change to a transitional wear pattern is not observed. Typical wear rates in the range 6.0×10^{-7} $mm^3.mm^{-1}$ to 4×10^{-4} $mm^3.mm^{-1}$ are found between the loads of 0.4 kgms and 15.0kgms, for $2.0ms^{-1}$, and 1×10^{-7} to 7.5×10^{-5} mm^3mm^{-1} for $0.5ms^{-1}$. (Table 4.2)

By considering the similarities in the slopes of the wear patterns (figure 4.9) it would seem, that for the AISI 310 steels, the wear transition is displaced to much lower loads. In consequence, only the region of wear above the transition load is revealed.

(ii) Wear Under Air

Wear under an air environment at $2.0m.s^{-1}$ shows the expected higher wear rates and the characteristic non-transitional and directly load dependent wear behaviour. (Table 4.2)

4.2.3 Wear at Elevated Temperatures

The wear behaviour of the AISI 316 stainless steels sliding at $0.5m.s^{-1}$ under a Co_2 environment at high temperatures Vi_3, 300°c and 500°c, is illustrated by figure (4.10).

The general wear behaviour is clearly transitional and

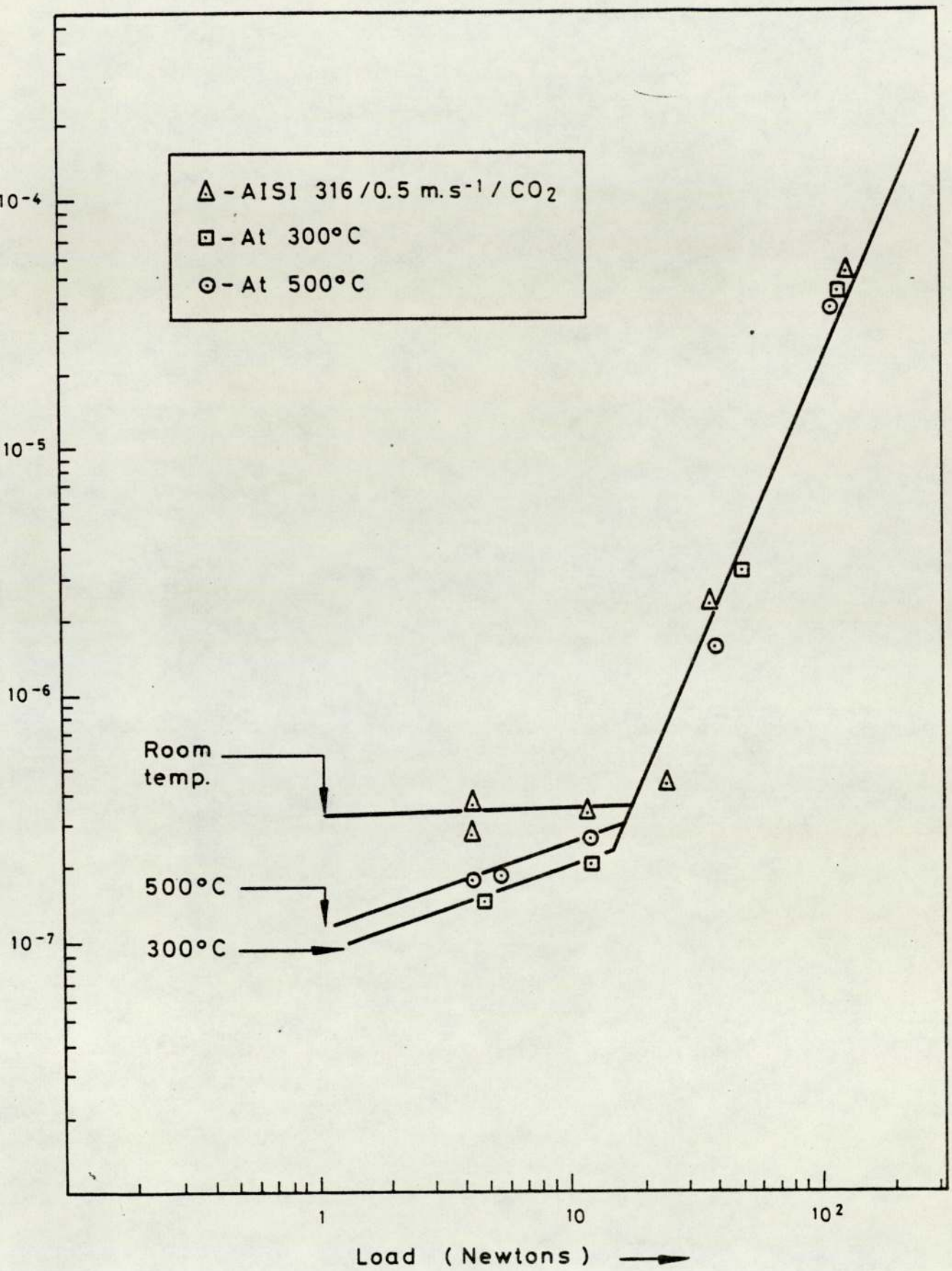

FIG.4.10 Wear Behaviour of the AISI 316 Stainless Steels at Elevated Temperatures (300°C & 500°C)

Load (kgms)	W_{Air} $(mm^3.mm^{-1})$	W_{CO_2} $(mm^3.mm^{-1})$
0.40	5.0×10^{-7}	3.0×10^{-7}
0.90	9.0×10^{-7}	3.1×10^{-7}
1.50	1.3×10^{-6}	3.3×10^{-7}
1.60	1.4×10^{-5}	3.4×10^{-7}
2.00	2.5×10^{-6}	4.4×10^{-7}
8.00	3.5×10^{-5}	1.2×10^{-5}
15.00	2.0×10^{-4}	5.6×10^{-5}

TABLE 4.1a) Room temperature Wear Data for the AISI 316 Steels at $S = 0.5\ m.s^{-1}$.

Load (kgms)	W_{Air} $(mm^3.mm^{-1})$	W_{CO_2} $(mm^3.mm^{-1})$
0.40	1.4×10^{-6}	6.5×10^{-7}
0.90	2.8×10^{-6}	9.0×10^{-7}
1.10	3.2×10^{-6}	1.9×10^{-6}
2.00	1.3×10^{-5}	7.0×10^{-6}
8.00	4.0×10^{-4}	1.2×10^{-4}
15.00	1.3×10^{-3}	5.0×10^{-4}

TABLE 4.1b) Room Temperature Wear Data for the AISI 316 Steels at $S = 2.0\ m.s^{-1}$.

Load (kgms)	W_{CO_2} (300°C) ($mm^3.mm^{-1}$)	W_{CO_2} (500°C) ($mm^3.mm^{-1}$)
0.40	1.8×10^{-7}	1.5×10^{-7}
0.90	2.3×10^{-7}	1.9×10^{-7}
1.50	2.7×10^{-7}	2.2×10^{-7}
1.60	2.8×10^{-7}	2.8×10^{-7}
2.00	4.4×10^{-7}	4.4×10^{-7}
8.00	1.2×10^{-5}	1.2×10^{-7}
15.00	5.6×10^{-5}	5.6×10^{-5}

TABLE 4.3 High Temperature Wear Data for the AISI 316 Steels at S = 0.5 $m.s^{-1}$, 300°C and 500°C.

Load (kgms)	W_{CO_2} ($mm^3.mm^{-1}$)	W_{Air} ($mm^3.mm^{-1}$)	W_{CO_2} ($mm^3.mm^{-1}$)
0.40	1.0×10^{-7}	4.0×10^{-7}	6.0×10^{-7}
0.90	4.4×10^{-7}	2.0×10^{-6}	2.5×10^{-6}
2.00	2.0×10^{-6}	1.0×10^{-5}	1.0×10^{-5}
8.00	2.6×10^{-5}	1.6×10^{-4}	1.5×10^{-4}
15.00	7.5×10^{-5}	5.5×10^{-4}	4.0×10^{-4}

TABLE 4.2 Wear Data for the AISI 310 Steels.

load dependent. A very close resemblance to the wear behaviour of the AISI 316 steels at room temperature is found. Above a transition load of 15.0N an identical wear pattern is followed. In the mild wear region, an increase in ambient temperature appears to lower wear-rates and enhance wear resistance.

At very light loads, namely 300gms and less, increasingly wider differences in wear rates between the room and high temperature values are observed. Whereas the wear rates below the transition load, at room temperature, remain constant with decreasing load, the effect of high temperature is to rapidly reduce the wear rates and as a result inhibit wear. (Table 4.3)

4.3 HEAT-FLOW DATA

Tables 4.4, 4.5 and 4.6 represent the measurements made by thermocouple of the frictionally generated heat flowing along the pin, during sliding. Monitoring of the heat-flow along the pin can be used to provide useful information about the wear process. Detailed descriptions are given in Chapter (5) and in (43)and (44).

Tables 4.4 (a) and (b) represent the thermal data for the sliding wear of the AISI 316 steels at $0.5 m.s^{-1}$ in air and Co_2 environments, respectively. The asterisked tests represent those which exhibited mild wear. It is these that are used in the heat flow analysis.

Tables 4.5 (a) and (b) show the heat data for the wear of the AISI 310 and AISI 316 steels at $2.0 m.s^{-1}$ in Air. Table 4.6 represents the heat-flow data for the tests conducted at high temperatures.

(a)

AISI 316 - 0.5 $m.s^{-1}$ - Air			
Load (Newtons)	TA(^{o}C)	TB(^{o}C)	TC(^{o}C)
107.5	193	97.0	55.0
19.62	53.0	37.0	29.4
12.26	47.0	28.0	25.0
9.81	41.0	30.5	26.0
7.85	36.0	28.2	24.0
5.89	33.0	27.0	24.0
4.41	30.0	26.0	22.5

(b)

AISI 316 - 0.5 $m.s^{-1}$ - CO_2			
Load (Newtons)	TA(^{o}C)	TB(^{o}C)	TC(^{o}C)
127.4	-	-	-
34.30	-	-	-
24.50	67.0	53.0	32.0
15.68	51.0	41.0	28.5
9.80	40.0	33.0	24.0
6.86	35.0	29.0	23.0
3.92	27.0	25.0	22.0

TABLE 4.4 a) Heat flow data for AISI 316 steel at 0.5 $m.s^{-1}$ in Air

b) Heat flow data for AISI 316 steel at 0.5 $m.s^{-1}$ in CO_2.

AISI 316 - 2.0ms^{-1} - Air			
Load (kgms)	T_A(°C)	T_B(°C)	T_C(°C)
11.5	440.0	164.0	32.0
4.0	220.0	84.0	31.0
1.25	63.0	52.0	36.0
0.5	-	-	-
0.3	-	-	-

(a)

AISI 310 - 2.0ms^{-1} - Air			
Load (kgms)	T_A(°C)	T_B(°C)	T_C(°C)
12.5	168.0	58.0	38.0
1.25	82.0	46.0	38.0
8.45	40.0	30.0	29.0

(b)

TABLE 4.5 a) Data for AISI 316 steel at 2.0ms^{-1} in Air

b) Data for AISI 310 steel at 2.0ms^{-1} in Air

AISI 316 - 0.5ms^{-1} - Co_2				
Load (kgms)	TA(^{o}c)	TB(^{o}c)	TC(^{o}c)	Bulk Temp.(^{o}c)
12.50	394.0	368.0	354.0	300
5.00	365.0	358.0	349.0	300
1.25	332.0	328.5	323.5	300
0.45	333.5	328.0	326.0	300
11.50	618.0	582.0	564.0	500
4.00	582.0	-	546.0	500
1.25	49.0	27.0	25.0	500
0.50	-		-	500

Table 4.6 . Heat flow data for AISI 316 steel at 0.5ms^{-1} in Co_2at bulk temperatures of 300^{o}C and 500^{o}C.

4.4 FRICTION RESULTS

In the present section the sliding friction behaviour of the austenitic stainless steels is described. The effects of operating parameters such as those of load, sliding speed and temperature upon the friction are reported. The effect of steel composition i.e. Cr Content, is also reported.

4.4.1 Effect of Load

In general, the variation in the friction coefficient, , with applied load was found to be transitional about a critical narrow range of loads. Three distinct regions of frictional behaviour were identified: (1) A transition region. (2) A load independent region and (3) A load dependent region. Figures (4.11), (4.12), (4.13) and (4.14) illustrate such regimes of frictional behaviour and demonstrate the transitional character of the friction.

(i) Transition Region

Within a narrow range of loads, typically between 2.2 kgm-4.0kgm, a sharp transition in the overall friction pattern was found to occur. As shown by figures (4.11), (4.12), (4.13) and (4.14) the transition produces a marked decrease in the friction coefficient from a range varying between 0.7-1.9, to a steady mean value of 0.6. The former range represents an equilibrium friction stage and the latter indicates a non-changing uniform stage.

(ii) Load Independent Region

The load independent region (W_{IL}) of the friction behaviour as illustrated in figure (4.13) and defined by the load-zone $W_T \leqslant W_{IL} \leqslant 12.0$kgm, where W_T is the transition load region, represents a static and non-changing uniform phase in the friction

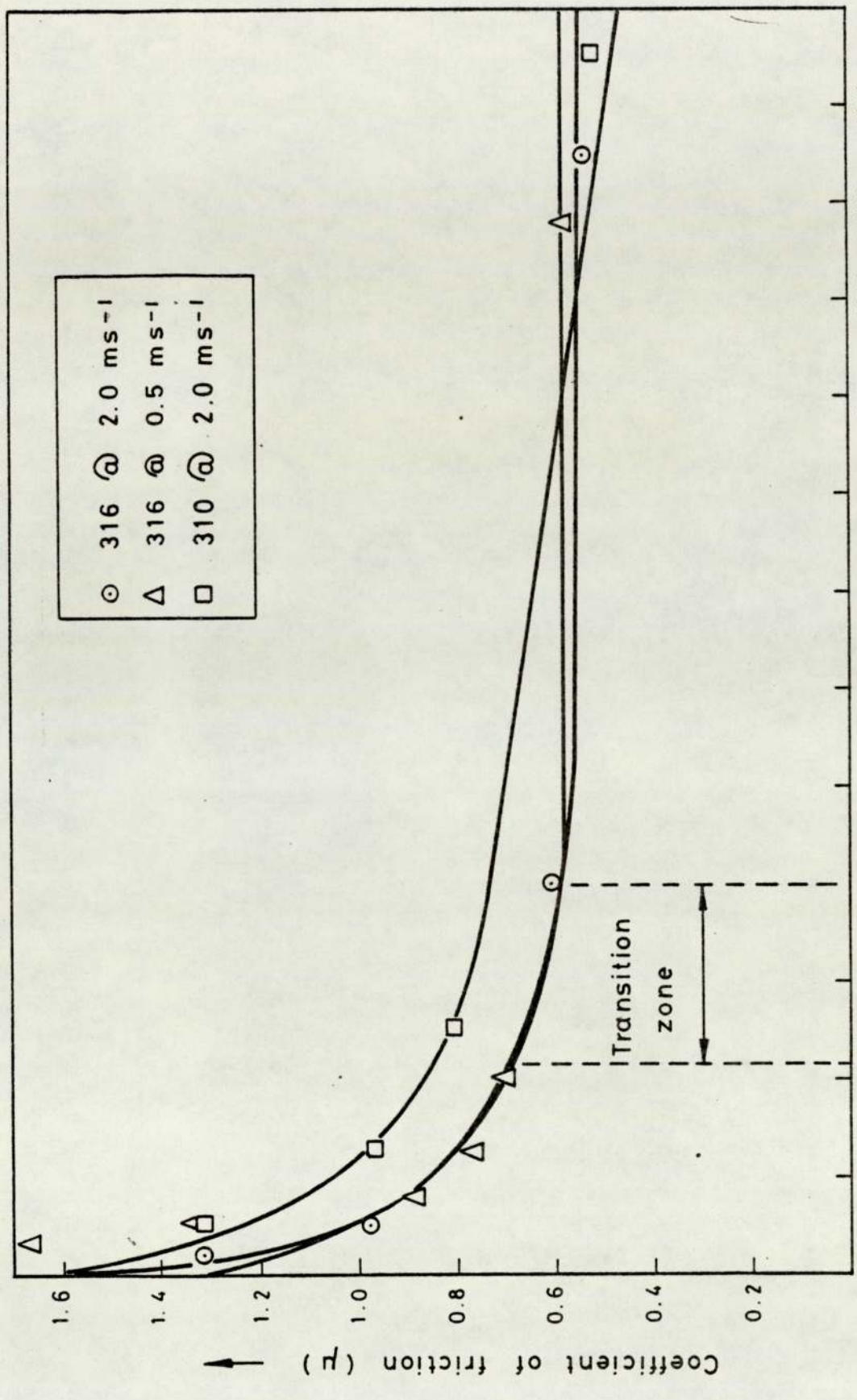

FIG.4.11 Variation of Friction with Load (Under Air)

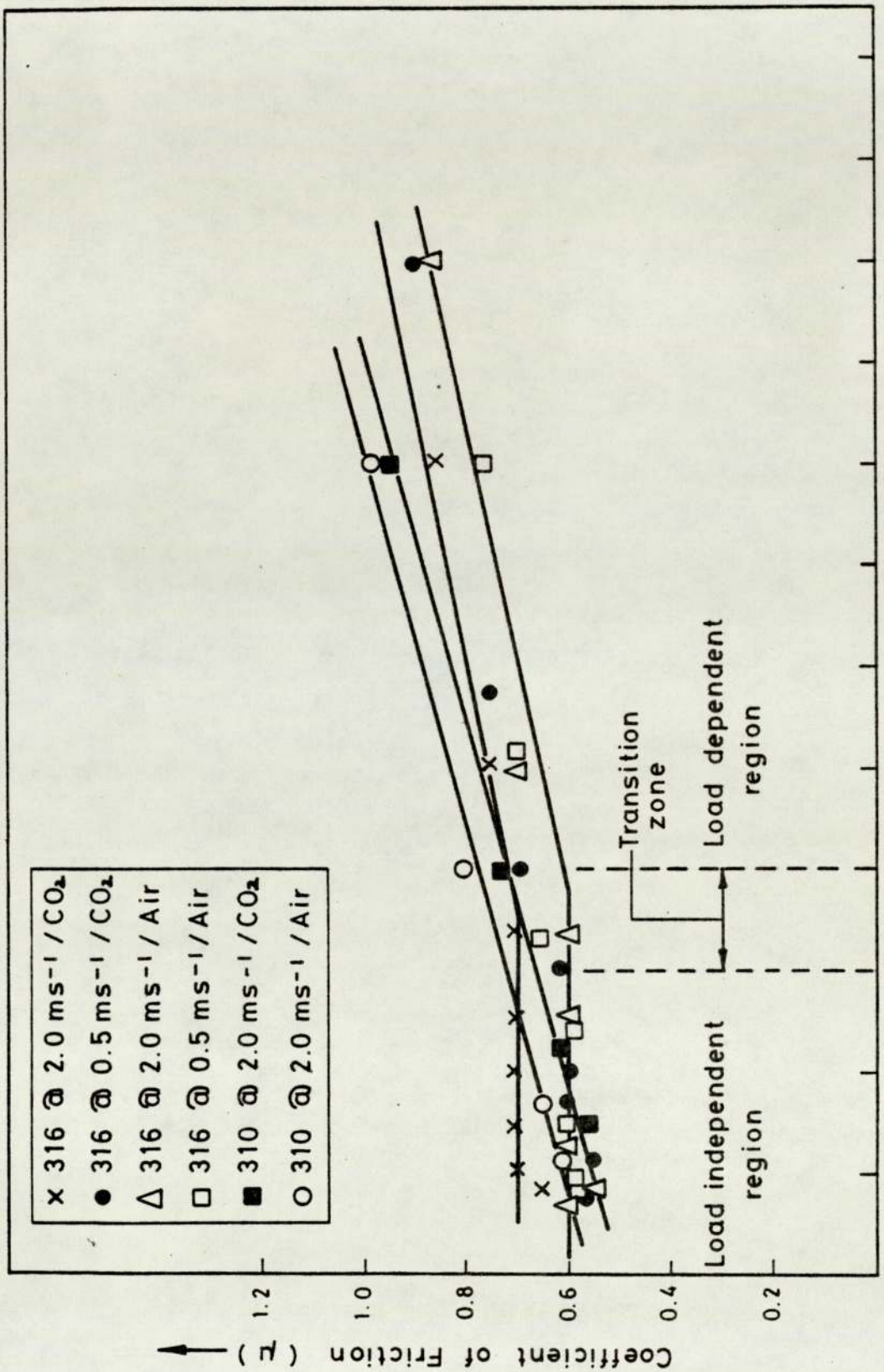

FIG.4.12 Variation of Friction with 1/Load.

behaviour. With increasing load, in this region, the sliding friction was found to be non-dependent upon the applied load and could be defined by μ(for $W_{IL} \geq W_T$) = K(constant). For all sliding conditions, K was found to fall within a narrow range 0.55 to 0.70.

By comparison with the general wear behaviour patterns of figures (4.8) and (4.9), it is evident that the load independent friction region corresponds to the severe wear regime. Whereas large variations in wear rates were found at the severe wear regions, the lack of fluctuation in μ would appear to show the insensitivity of the friction to the wear magnitudes but strongly indicative of the existence of a common regime of wear.

(iii) Load Dependent Region.

The load dependent region (W_{LD}) as defined by the load zone $W_T \geq W_{LD} \geq 0.25$kgm, represents an equilibrium phase in the friction behaviour. With decreasing load, below the transition region, the sliding friction was found to be wholly load-dependent and closely following Amonton's law of friction. An approximation to this law is found to accurately define the friction behaviour in this region, and given by the expression:

$$\mu \text{ (for } W_{LD} \leq W_T) = F/W + C$$

where, F = frictional force; W = applied load; and C = a constant, lying between 0.4 and 0.6 for all sliding conditions. The friction coefficient, F/W + C, in this region, although fluctuating slightly, was found to fall within a range of 0.7(for $W_{LD} = W_T$) to 1.9 (for $W_{LD} < 0.3$kgm).

By comparison with the general wear patterns of figures (4.8) and (4.9), it is evident that the load dependent friction

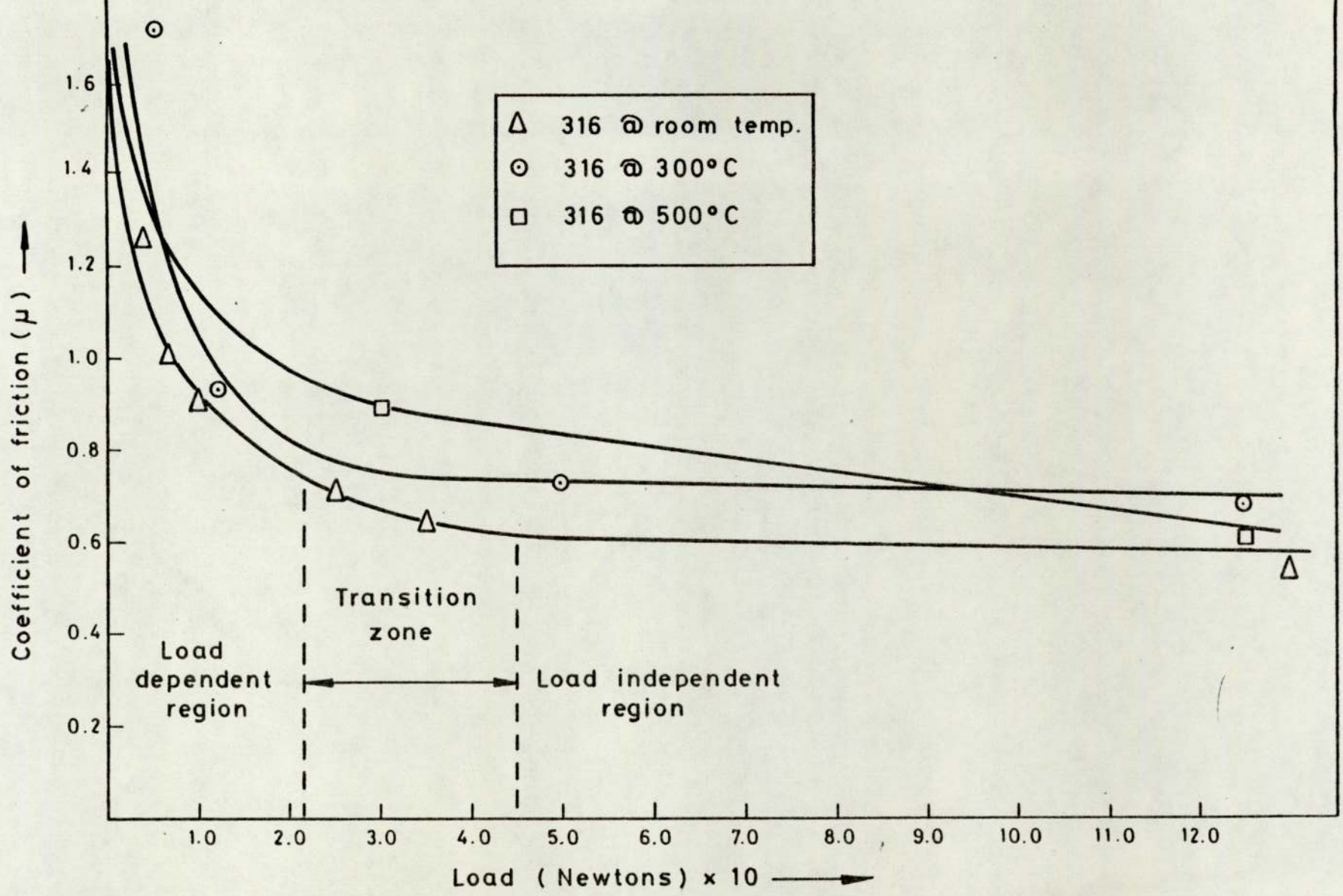

FIG.4.13 Variation of Friction with Temperature and Load (under CO_2)

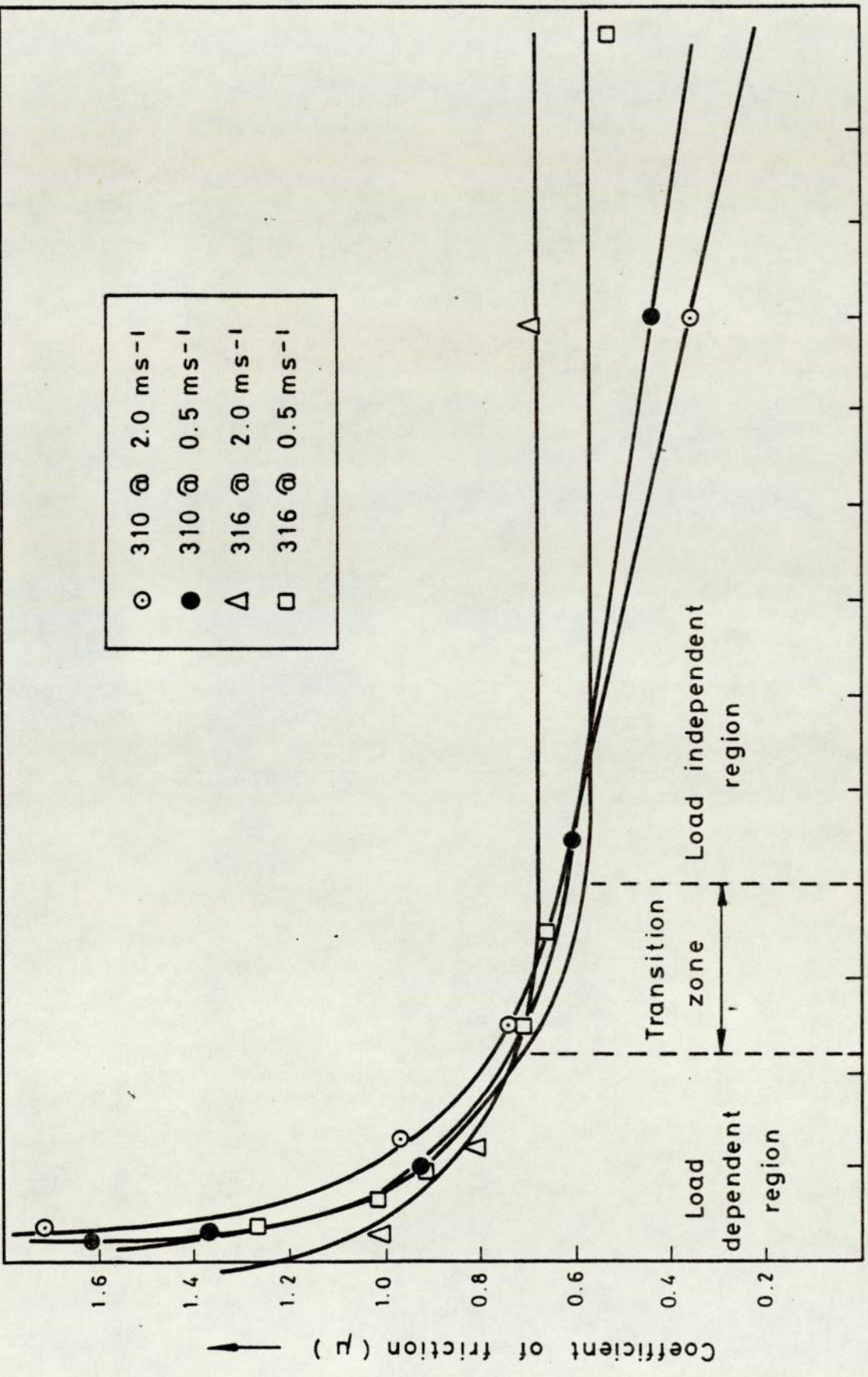

FIG. 4.14 Variation of Friction with Load (under CO_2)

region corresponds directly to the mild wear regime. The accordance of the friction to Amonton's law is clearly representative of a mild and equilibrium wear mode.

4.4.2 Effect of Sliding Speed

In general, a marked effect upon the friction due to changes in the sliding speed was not observed.

At the speeds considered, the friction was found to be wholly independent of the sliding speed at the higher loads i.e. for $W > 2.5$kgms, but relatively dependent at the very light loads. This feature is illustrated in figure (4.15) where at $0.5 m.s^{-1}$ much higher friction coefficients (μ_1) are apparent over the lighter loads or load dependent friction region, in comparison to the values (μ_2) at $2.0 m.s^{-1}$. Typical differences in μ_1 and μ_2 for $W < 0.2$kgm, of between 0.4 and 0.6 are found. μ_3, representing the friction at the load independent friction region is clearly non-varying with changes in the sliding speed. Also illustrated in figure (4.15) is the non-variation of the friction coefficient at the transition zone.

4.4.3 Effect of Chromium Content

Figure (4.14) illustrates the affect of the Chromium content of the steels upon the friction coefficient. In general, a distinctly non-transitional friction pattern was found for the higher chromium AISI 310 steels (24.2% Cr).

As shown by figure (4.14), the three staged frictional behaviour, typical of the lower chromium AISI 316 steels, is not obtained at higher chromium levels. A totally load dependent

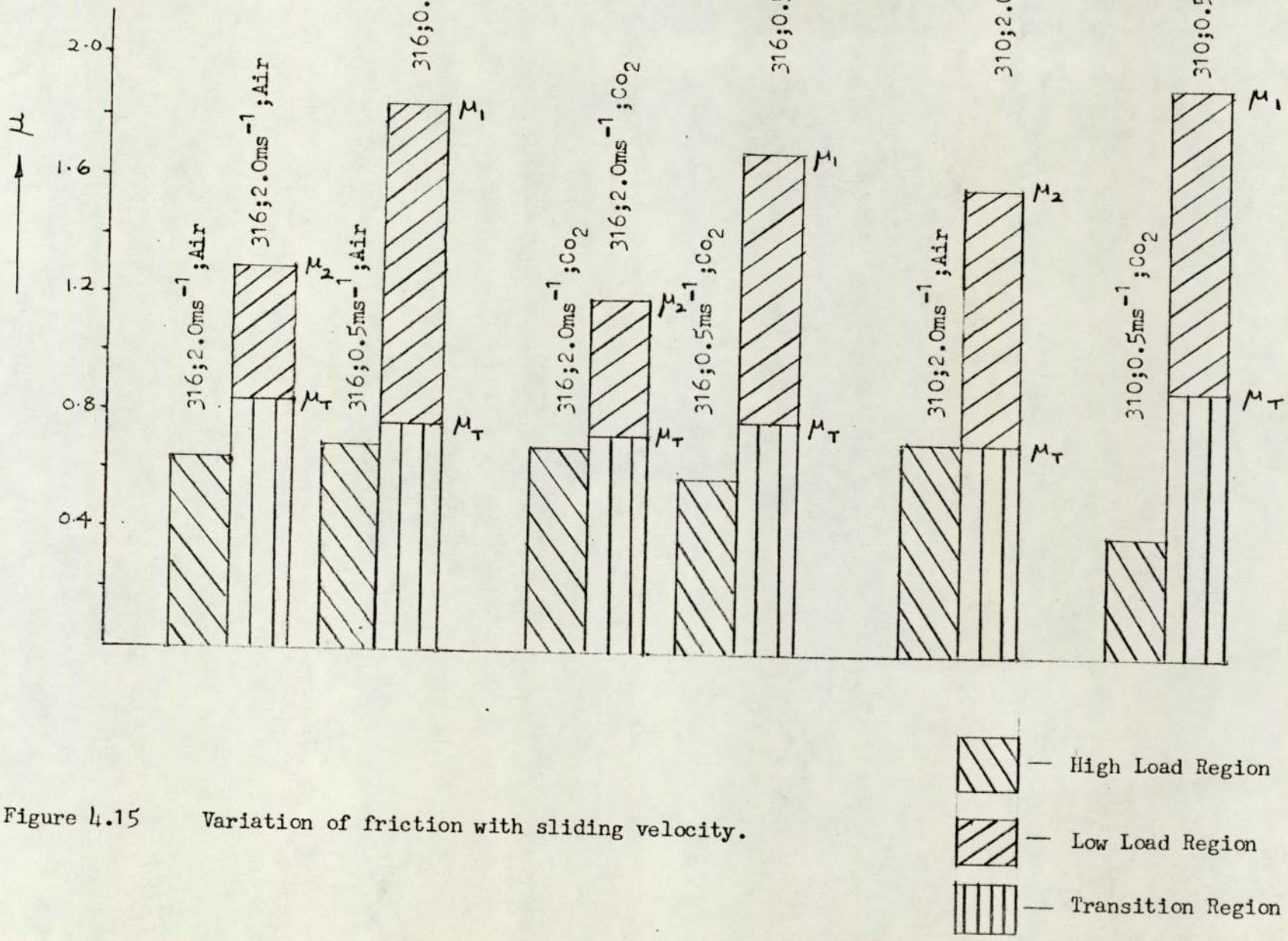

Figure 4.15 Variation of friction with sliding velocity.

behaviour is found to dominate with the apparent absence of the load independent and transition regions. In the region above the load range $0.35 \leqslant 1/W \leqslant 1.0$ the variation in the friction with applied load is found to be similar between the 17% Cr steels and the higher 24.2%,Cr steels, where this is indicated by the similarities in the slopes. In general, for all loads, higher values of the friction coefficient are found with increasing Cr content.

By comparison with the general wear patterns of figures (4.8) and (4.9) it is evident that the non-transitional friction behaviour of the AISI 310 steels is representative of the non-transitional severe wear behaviour of the steels. As such, a single common wear mode would seem to be indicated for the AISI 310 steels over all range of loads.

The range of values for μ_{316} and μ_{310} under air and Co_2 environments are specified in the table below.

For $2.0\,kg \leqslant W \leqslant 12.0\,kg$		For $0.1\,kg \leqslant W \leqslant 1.5\,kg$	
17.0 % Cr	24.3 % Cr	17 % Cr	24.3 % Cr
$0.6 \geqslant \mu_{AIR} \geqslant 0.5$	$0.8 \geqslant \mu_{AIR} \geqslant 0.5$	$1.4 \geqslant \mu_{AIR} \geqslant 0.85$	$1.75 \geqslant \mu_{AIR} \geqslant 0.95$
$0.75 \geqslant \mu_{CO_2} \geqslant 0.7$	$0.7 \geqslant \mu_{CO_2} \geqslant 0.35$	$1.2 \geqslant \mu_{CO_2} \geqslant 0.8$	$1.55 \geqslant \mu_{CO_2} \geqslant 0.95$

It is evident that much larger variations in the friction are found, for corresponding loads, at the higher Cr-content levels than at the 17% Cr level.

4.4.4 Effect of Temperature

Figure (4.16) illustrates the effect of temperature upon the friction coefficient at the load-dependent and load-independent

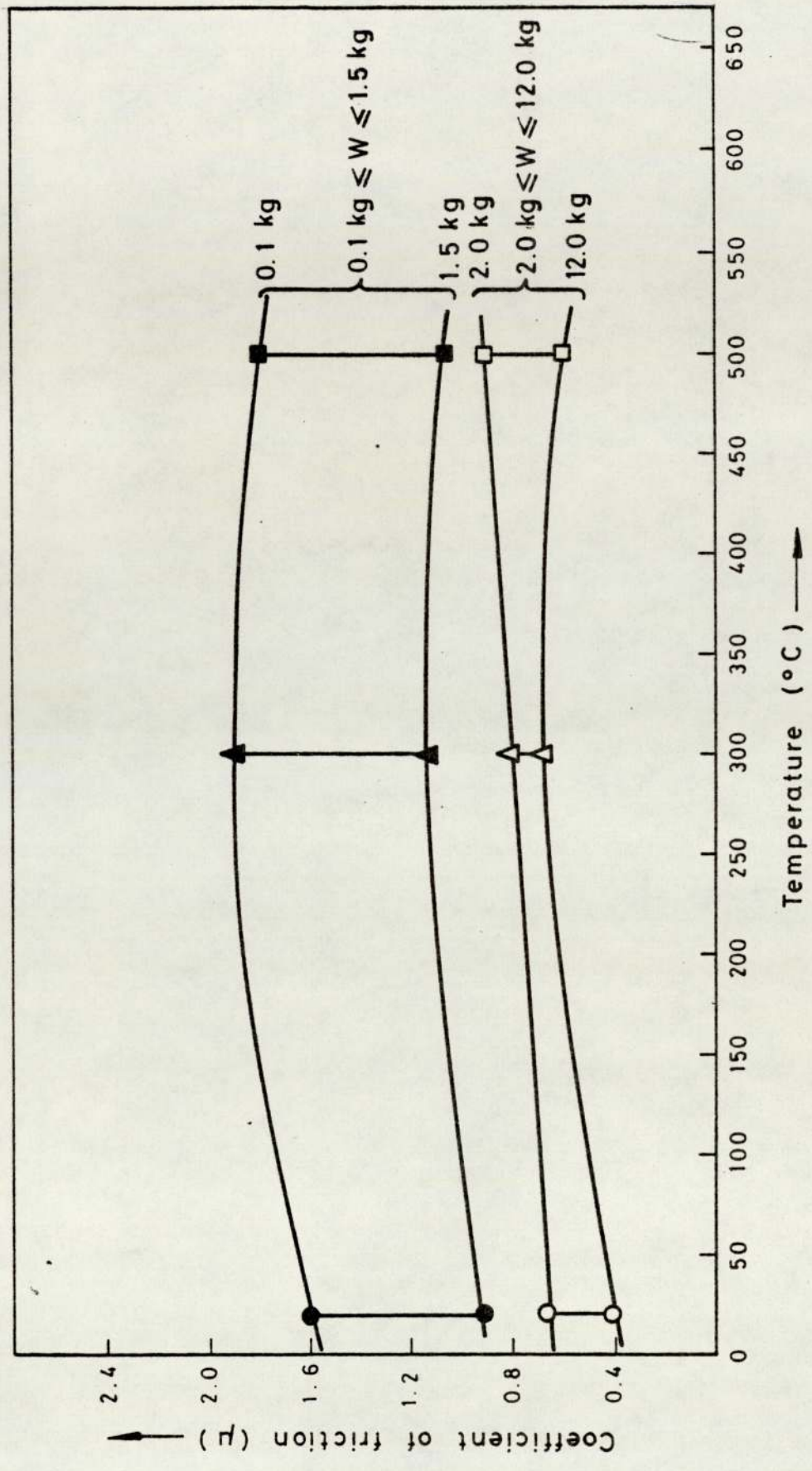

FIG. 4.16 Variation in Friction with Temperature.

regions. In general, a non-dependency of friction upon temperature was found.

Under the conditions considered, the friction at 300°C and 500°C were found to be within the ranges 0.7 - 0.75 (for 2.0kg $\leq$ W $\leq$ 12.0kg) and 1.1 - 1.9 (for 0.1kg $\leq$ W $\leq$ 1.5kg) and 0.8 - 0.85 (for 2.0kg $\leq$ W $\leq$ 12.0kg) and 1.0 - 1.8 (for 0.1kg $\leq$ W $\leq$ 1.5kg), respectively. In comparison with the friction at room temperature under a Co_2 environment (μCo_2), of the values 0.55-0.6 (for 2.0kg $\leq$ W $\leq$ 12.0kg) and 0.9 - 1.6 (for 0.1kg $\leq$ W $\leq$ 1.5kg), it is apparent that a significant difference does not exist, although in general, μCo_2 at 300°C and 500°C are nominally higher.

4.5 ANALYSIS OF THE WEAR DEBRIS AND THE WORN SURFACES

4.5.1 Introduction

In the present section the analysis of the wear debris by X-ray diffraction and the analysis of the wear scars by scanning electron microscopy are described.

For the purposes of identifying the composition and structure of the wear-debris produced during the wearing processes, the Debye-Scherrer X-ray diffraction technique was used.[45]

Debye-Scherrer X-Ray Diffraction

In the Debye-Scherrer technique, incident monochromatic radiation striking a cylindrical polycrystalline specimen is diffracted into two sets of cones: the forward-reflected and the back-reflected diffraction cones. Each cone of rays is diffracted from a particular set of lattice planes. A narrow strip of film is used

to record the diffraction cones. The intersection of the cones with the film forms a diffraction pattern consisting of a series of short lines. The distance of the lines from the incident radiation entrance hole (for the low-angle diffraction lines) or from the exit hole (for the high-angle diffraction lines) can be interpreted in terms of the lattice interplanar spacing parameter, d.

4.5.2 X.Ray Diffraction Analysis of the Wear Debris

The wear debris, in general, can be of three types: (1) Purely metallic in form, (2) purely of oxide form or (3) of a mixed metallic and oxide form.

While the metallic debris is readily identified by X-ray diffraction, the identification of the oxide debris, particularly of Fe - Cr alloys, is much more difficult. Such difficulties are due to the continuous range of solid solutions obtainable between Fe and Cr oxides, within their rhombohedral, spinel and wustite phases.[46]

The rhombohedral oxide phase can exist as a solid solution of Cr_2O_3 and α-Fe_2O_3 with lattice constants varying from $a_0 = 5.43$ (for 100% α-Fe_2O_3) to $A_0 = 5.33$ (for 100% Cr_2O_3). The Wustite phase can be present in two forms, one associated with pure iron oxidation (with $a_0 = 4.31$) and the other associated with chrome-steel oxidation (with $a_0 = 4.29$). The spinel oxide phase, the most difficult of the oxide phases to identify, has a complex structural configuration, of the general form $Fe\ Fe_{(2-x)}\ Cr_x\ O_4$ where $0 \leq x \leq 2$.

The analyses of the wear debris in the present work is described in relation to the severe and the mild regimes of wear.

(i) Wear Debris - Mild Wear Region

Figures (4.17a),(4.17b),(4.17c) and (4.17d) illustrate typical examples of X-ray powder diffraction patterns obtained from the wear debris of the AISI 316, 316 and 310 steels respectively, operating within the mild-wear region. Table 4.7 illustrates the composition of the wear-debris produced and identifies the inter-planar lattice spacings, d, of the debris constituents.

(a) AISI 310 Steel Debris

The nature of the debris produced in the wear of AISI 310 steels, in the region below the transition load, was found to be clearly metallic. This feature is well illustrated in Table 4.7 where only Austenite, and a rhombohedral oxide i.e. Cr_2O_3 are identified. The lack of spinel oxide phases and other oxide phases. representative of mild-wear, is distinctive, and suggests a generally severe mode of wear.

(b) AISI 316 steel Debris (No External Heating)

In the wear of AISI 316 steels, a clearly non-metallic, finely powdered and oxidised character of the wear debris was found. The oxidised nature of the debris is well identified by X-ray diffraction, as is demonstrated by Table 4.7 .

In general, the oxides identified can be classed into four oxide systems: (1) Rhombohedral, (2) Wustite, (3) Cubic and (4) Spinel. In addition to the oxides, austenite was also identified. Rhombohedral Oxides. The rhombohedral oxides found were Cr_2O_3, α-Fe_2O_3 and $(Cr,Fe)_2O_3$. The two former oxide-forms characterise the extremes of the oxide system. The latter represents the continuous range of solid solution oxides obtainable.

4.17a) Debye-Scherrer diffraction pattern of AISI 316 wear debris ($S = 2.0ms^{-1}$; in Air).

4.17b) Debye-Scherrer diffraction pattern of AISI 316 high temperature wear debris ($S = 0.5ms^{-1}$; in Co_2).

4.17c) Debye-Scherrer diffraction pattern of AISI 316 severe-wear debris ($S = 2.0ms^{-1}$; in Air).

4.17d) Debye-Scherrer diffraction pattern of AISI 310 wear debris ($S = 0.5ms^{-1}$; in Co_2).

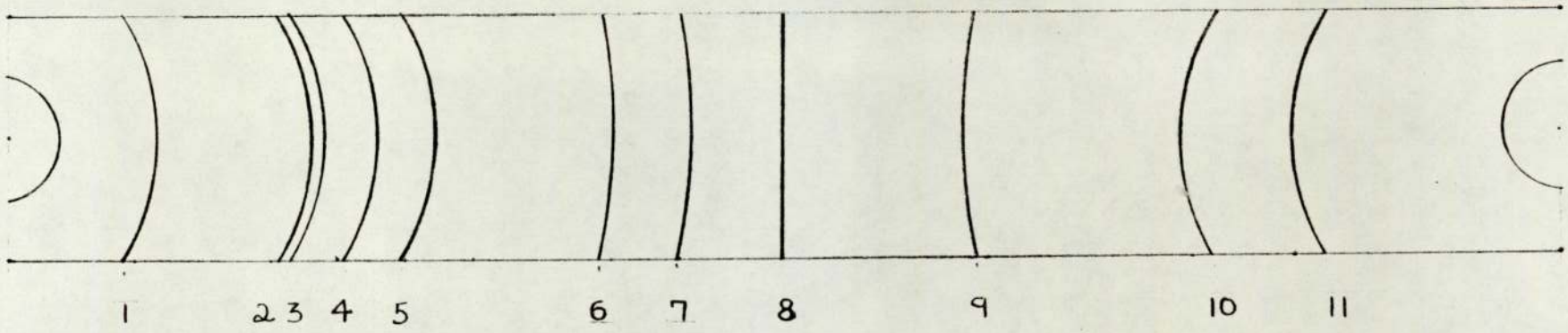

Figure 4.17(a)

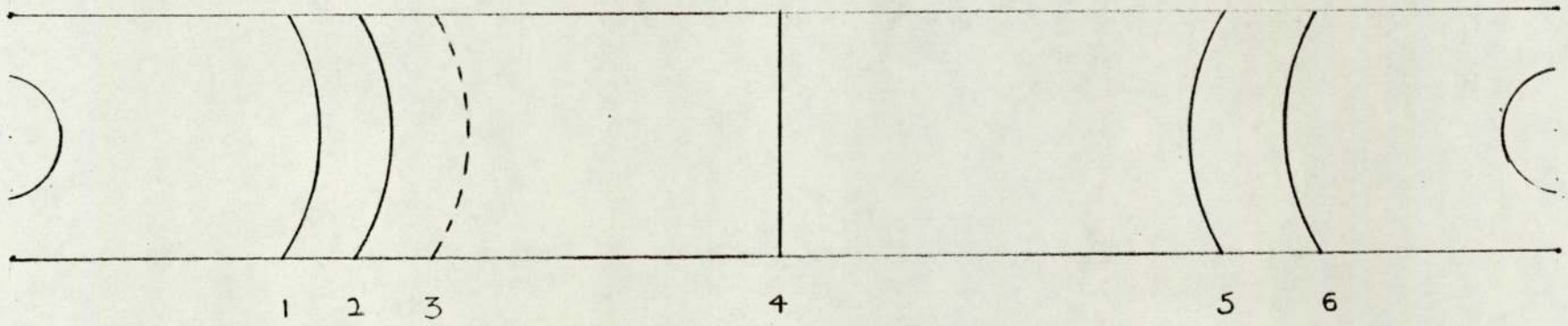

Figure 4.17(c)

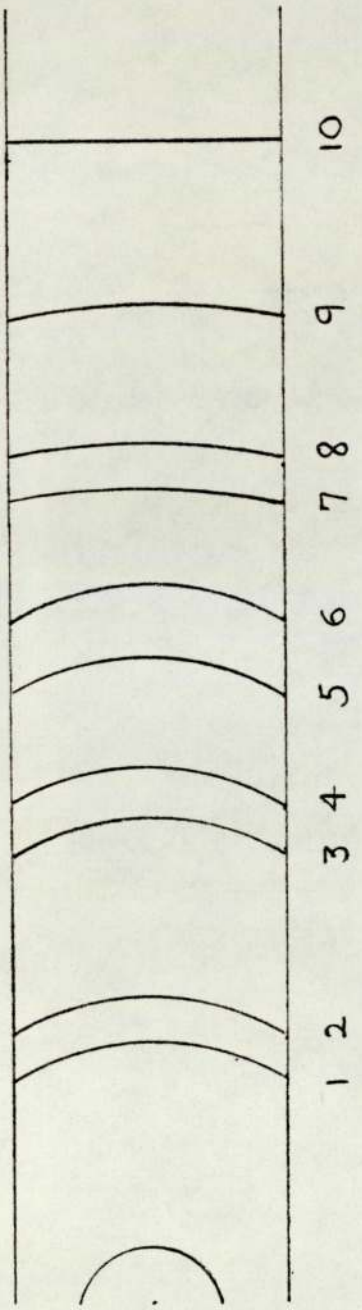

Figure 4.17(b)

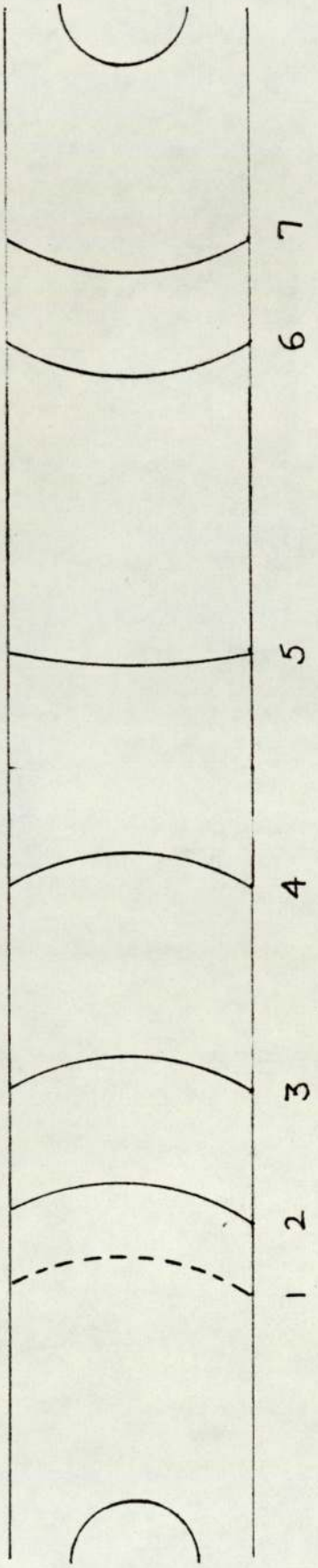

Figure 4.17(d)

Diffraction Line		2θ (Cms)	Identity
	1	39.550	γ -Fe_2O_3;Cr_2O_3
***	2	51.00	Austenite
*	3	52.15	Austenite
**	4	59.55	Austenite
	5	64.80	Cr_3O_4;$(Cr,Fe)_2O_3$ α -Fe_2O_3;Cr_2O_3
	6	77.15	$(Cr,Fe)_2O_3$; γ-Fe_2O_3 Cr_3O_4
	7	81.80	$(Cr,Fe)_2O_3$;α-Fe_2O_3
**	8	89.55	Austenite
	9	100.30	-
	10	112.30	Austenite
	11	120.00	Austenite

Figure:4.17(a) Powder diffraction pattern for AISI 316 wear debris produced under mild wear. (Sliding speed = 2.0ms^{-1}; Environment=Air.)

*** = Very strong intensity line.

** = Strong intensity line.

* = Fairly strong intensity line.

Diffraction Line		2θ (Cms)	Identity
	1	38.90	Cr O
*	2	41.20	Austenite Cr_2O_3;Fe_2O_3
	3	48.80	Cr_2O_3
***	4	50.90	Austenite
	5	56.60	α -Fe_2O_3
***	6	59.50	Austenite
	7	64.70	α -Fe_2O_3
	8	66.90	$(Cr,Fe)_2O_3$ α -Fe_2O_3;Cr_2O_3
	9	73.10	$(Cr,Fe)_2O_3$;Cr_2O_3
*	10	89.30	Austenite

Figure: 4.17(b) Powder diffraction pattern for AISI 316 wear debris produced under mild wear at 500°C. (Sliding speed = 0.5ms^{-1}; Environment = Co_2.)

*** = Very strong intensity line.

* = Fairly strong intensity line.

Diffraction Line		2θ (Cms)	Identity
***	1	51.00	Austenite
**	2	59.50	Austenite
v.f.	3	67.15	Fe_3O_4; γ -Fe_2O_3 α -Fe_2O_3; Cr_3O_4
	4	89.40	Austenite
*	5	101.05	Austenite
*	6	112.95	Austenite

Figure: 4.17(c) Powder diffraction pattern for AISI 316 wear debris produced under severe wear. (Sliding speed = 2.0ms^{-1}; Environment=Air.)

Diffraction Line		2θ (Cms)	Identity
v.f.	1	45.57	-
**	2	52.20	Austenite
**	3	60.60	Austenite
v.f.	4	77.47	Austenite
	5	90.57	Austenite
*	6	100.85	Austenite
*	7	112.45	Austenite

Figure: 4.17(d) Powder diffraction pattern for AISI 310 wear debris produced under severe wear. (Sliding speed = 0.5ms^{-1}; Environment=Co_2.)

*** = Very strong intensity line.

** = Strong intensity line.

* = Fairly strong line.

v.f. = Very faint intensity line.

The rhombohedral oxides are found to exist at all operating sliding speeds, environments and loads.

Cubic Oxides. The cubic oxide identified in the debris was γ - Fe_2O_3. The latter, although synonymous to the Spinels and in particular to magnetite, Fe_3O_4, is indicative of different oxidation properties due to its very common occurence as an oxidation product, but separation between the two oxide phases by X-ray diffraction is difficult.

As with the rhombohedral oxides, γ -Fe_2O_3 was found to be present in the debris at all operating conditions, within the mild wear region.

Spinel Oxides. The Spinel oxide phases identified in the wear debris were Fe_3O_4 (cubic-form) and Cr_3O_4 (tetragonal-form). As seen in Table 4.7, intermediate solid solution phases are not apparent but due to their small propertions and weak intensities are difficult to identify.

While Cr_3O_4 is found to be a common oxidation product in the debris, Fe_3O_4 is found to occur only under an air environment. However, the difficulties in separating γ -Fe_2O_3, which is commonly occurring, from Fe_3O_4 may suggest a wider occurence of the latter.

Wustite Oxides. The FeO constituent of the debris, wherever identified, was found to be of small proportions and not commonly occurring as an oxidation product. From Table 4.7 , FeO is seen to be restricted to occuring at sliding speeds of $0.5 m.s^{-1}$ only with a significant absence at $2.0 m.s^{-1}$.

(c) AISI 316 Steel Debris (at 300° and 500°C Disc Temperature)

At operating temperatures of 300°C and 500°C a markedly oxidised debris character was found. As with the room temperature debris, rhombohedral, spinel and wustite oxide phases were again identified but in much larger proportions, in general (Table4.7).

At 500°C a noticeable absence of metallic material in the debris was apparent. However, the austenite phase was still strongly identified in the diffraction pattern. Even at the higher temperatures, within debris containing much larger proportions of oxide, better resolutions of the solid solution series of oxide-types for the rhombohedral and spinel phases was not obtained.

Temperature Dependency

The common or selective occurences of the various oxide phases at only certain operating conditions can be related to surface temperatures during wear. Investigations by several workers (47,48,36) on the dependency of oxide formation upon temperature have shown the existence of definite temperature transitions in relation to specific oxide phases. That is, for Fe-Cr alloys, at ~270°C rhombohedral phases and γ-Fe_2O_3 are formed; at ~350°C the spinel phases begin to appear and finally at >500°C the wustite phases occur.

A direct comparison can be made with the present results. The uncommon occurence of wustite, would suggest that few sliding wear conditions generate surface temperatures greatly in excess of 500°C - 600°C, but that temperatures upto this range are produced. Hence the common appearance of spinel oxides, (stable at temperatures >350°C), in the debris.

Exptl. d-value	Exptl. I/I1	Identity	Index d-value	Experimental conditions
3.03		Cr_3O_4	3.05	4, 9
2.64	20	γ -Fe_2O_3	2.64	9
		Cr_2O_3	2.66	
2.686		$(Cr,Fe)_2O_3$	2.69	14
		α -Fe_2O_3	2.69	
		Cr_2O_3	2.66	
2.54		Fe_3O_4		14
		γ - Fe_2O_3		
		Cr_3O_4		
2.37	20	Cr_3O_4	2.39	11, 13
2.08	100	Austenite	2.08	1,2,3,4,5,6,7,8, 9,10,11,12,14,
1.08	80	Austenite	1.8	1,2,3,4,5,6,7,8, 9,10,11,12,14,
1.67	40	Cr_2O_3	1.672	9, 14
		Cr_3O_4	1.655	
		α -Fe_2O_3	1.69	
		$(Cr,Fe)_2O_3$	1.68	
		Austenite		

TABLE 4.7(a) Wear-debris Identification.

TABLE 4.7(b) Wear-debris Identification.

Exptl. d-value	Exptl. I/I1	Identity	Index d-value	Experimental conditions
1.61	10	Cr_3O_4	1.59	10
		$(Cr,Fe)_2O_3$	1.59	
		Fe_3O_4	1.616	
		γ -Fe_2O_3	1.61	
		α -Fe_2O_3	1.596	
1.43	30	Cr_2O_3	1.43	1,2,4,5,9,11
		Cr_3O_4	1.432	
		$(Cr,Fe)_2O_3$	1.44	
		γ -Fe_2O_3	1.43	
1.366	5	$(Cr,Fe)_2O_3$	1.34	9
		α -Fe_2O_3	1.349	
		Cr_3O_4	1.348	
		Fe_3O_4		
1.27	70	Austenite	1.27	1,2,3,4,5,6,7,8, 9,10,11,12,14
1.16	30	$(Cr,Fe)_2O_3$	1.18	1,2,4,5,6,7,9
		α -Fe_2O_3	1.162	
1.08	60	Austenite FeO	1.083	1,2,3,4,5,6,7,8, 9,10,11,12,14,
1.03	40	Austenite	1.037	1,2,3,4,5,6,7,8, 9,10,11,12,14
1.01	10	α -Fe_2O_3	0.989	2, 5
		γ -Fe_2O_3	1.03	
		FeO	0.998	

Experimental Conditions

Numbers	Steel (AISI)	Sliding Speed ($m.s^{-1}$)	Temperature ^{o}C	Transition	Environment
2	316	0.5	R.T.	T1	Co_2
3	316	0.5	R.T.	T2	Co_2
4	316	0.5	R.T.	T1	Air
5	316	0.5	R.T.	T1	Air
6	316	0.5	R.T.	T2	Air
7	316	2.0	R.T.	T1	Co_2
8	316	2.0	R.T.	T2	Co_2
9	316	2.0	R.T.	T1	Air
10	316	2.0	R.T.	T2	Air
11	310	0.5	R.T.	T1	Co_2
12	310	0.5	R.T.	T1	Co_2
13	310	0.5	R.T.	T2	Co_2
14	316	0.5	500°C	T1	Co_2

1 Standard Austenite Sample.

R.T. = Room Temperature.

T1 = Mild Wear Region below transition.

T2 = Severe Wear Region above transition.

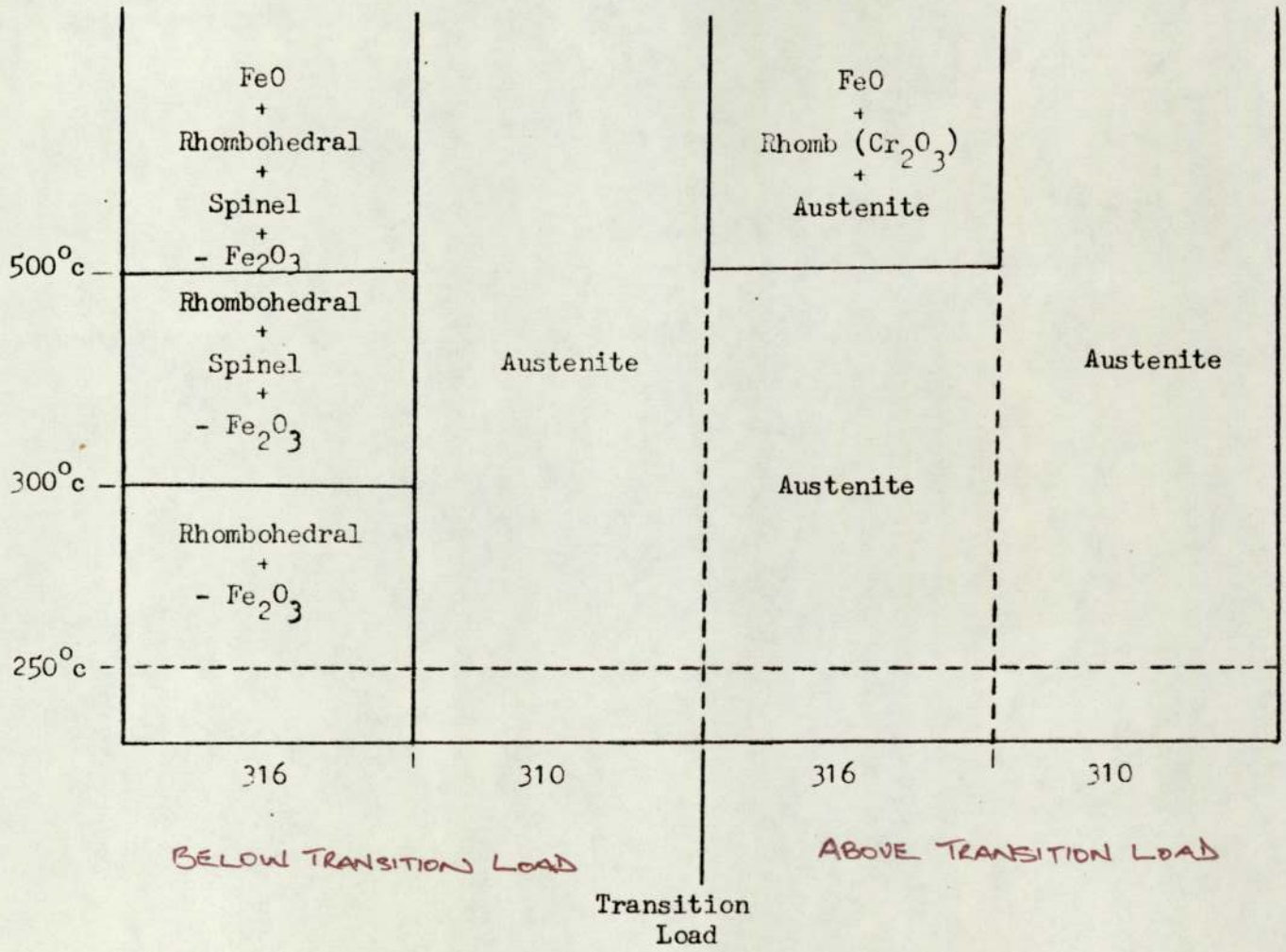

Figure 4.18 Schematic diagram of the variation in wear debris composition with operating conditions.

(ii) Wear Debris - Severe Wear Region

In all cases, the wear debris of the region above the transition loads was found to constitute chiefly of Austenite. While small proportions of rhombohedral Cr_2O_3 oxide and wustite were found in the debris, particularly at high temperatures, no oxide phase of significant proportions were identified. (Table 4.7)

In general, the variation in composition of the wear-debris with operating conditions can be summarised schematically by the diagram shown in figure (4.18).

4.5.3 Wear Surface Topographies

By means of the Scanning electron microscope, the surface topography of the wear areas of representative pin and disc specimens were analysed. Specimens indicative of the severe and mild wear regimes were examined.

(i) Wear Topography - Mild Wear Region

Figures (4.19), (a), (b), (c), and (d) illustrate the general nature of the wear scars of the steels worn under mild-wear conditions. Typically, the wear topography of the steels are characterised by a smooth and even surface appearance. The absence of gross surface deformation is clearly evident. Also evident are the well defined pattern of wear grooves, demonstrating clearly the direction of sliding.

The illustrations demonstrate the chief modes of material removal occuring during mild-wear. Mainly, removal by shearing, by parallel-plate dislocation, by hollowing and by oxide-formation.

Hollowing. As shown in figure (4.19)(a), hollowing results in

the removal of material in large lumps leaving a greatly disturbed wear surface in the form of a cavity. This form of removal is localised and discrete.

Shearing. The transverse shearing of the surface, in a direction perpendicular to the direction of sliding, leads ultimately to the dislocation of material (figure (4.19),(b)). This is achieved by the gradual weakening of the surface layers.

Plate Dislocation. In contrast to hollowing, by and large, material removal is obtained by the uniform dislocation of material along the wear grooves, in the form of well defined miniscule plate-like debris. By its nature, the plate-like debris removal leads gradually to the parallel dislocation of material over the total wear surface. Figure (4.19),(c) illustrates such a process.

Oxide-Formation

Figure (4.19,(d) illustrates the wear surface created by continuous sliding at 500°C. The oxide layer, formed during the wearing process, is clearly in evidence. The oxide once formed in this way, subsequently fractures at a critical thickness to produce a wear particle. As a result, gradual removal of material is achieved. The high magnification (x1.5k) micrograph of figure (4.19), (d) demonstrates clearly the fracturing of the oxide into a small wear fragment. The well compacted oxide layer, as described here is evidenced by numerous workers, mainly Stott et al (49,50) where greatly compacted oxide, forming glazed layers, are noticed.

(ii) Wear Topography - Transition Region

Figure 20(a) illustrates the wear surface formed in the transition region between the load range $2.2kg \leq W \leq 4.0kg$. The

smooth and even surface character evident in the mild wear region is clearly absent. A much greatly deformed surface is seen where material removal is achieved generally by tearing, plucking and ploughing. Removal by parallel plate dislocation, however, is still in evidence. The well defined wear grooves, characteristic of mild-wear, are feintly apparent but largely obscured by surface deformation.

(iii) Wear Topography - Severe Wear Region

Figure (4.20),(c,d) illustrates the wear surface formed in the severe wear region. The very grately deformed surface character is markedly evident. The total lack of delineation by wear grooves and sliding direction is indicative of a severe adhesive mode of wear. The gross smearing of surface material by plastic de-formation, causing as a result, a widely undulating surface topography, is much in evidence.

It is apparent that the mechanisms of material removal, such as those of plate dislocation and oxide formation are not appliable to the severe wear process. In general the main mechanism is that of adhesion between the sliding surface layers followed by the shearing, tearing and rupturing of the adhesion junctions to form course and angular debris. In additon, the transfer of material to opposite surfaces by the adhesion mechanism is also achieved.

a.

b.

Figure 4.19 Typical mild wear topographies showing a) hollowing (x 200) and b) shearing (x 1500).

c)

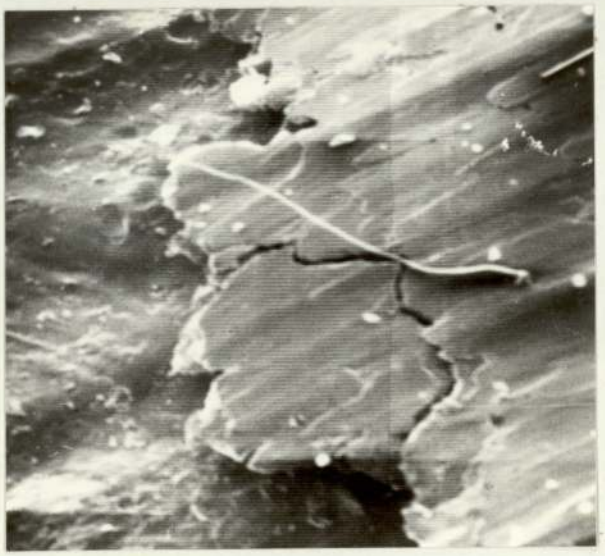

d)

Figure 4.19 Typical mild wear topographies showing
c) parallel plate dislocation (x 1k) and
d) oxide layer fracturing (x 1.5k).

Figure 4.20 a) Wear topography at the Transition Region showing increased surface deformation (Magnification x 1K)

Figure 4.20 b) and c) Wear topography at the Severe Wear Region showing extensive surface deformation and surface flow. (Magnification x 200.)

Figure
4.20(a)

Figure
4.20 (b)

Figure
4.20 (c)

CHAPTER FIVE

DISCUSSION

5.1 DISCUSSION OF STATIC OXIDATIONAL BEHAVIOUR

5.1.1 Introduction

The good corrosion resistance qualities of stainless steels are well known and it is for this reason that they are widely used in many oxidising and corrosive environments. However, under conditions where such qualities are found to break down, the subsequent inferior nature of the steels is less well-known or understood.

The importance of understanding the nature of the steels after the breakdown of the initial oxidation resisting properties, in terms of their subsequent oxidational behaviour, is self evident. Such an understanding becomes particularly important in the situation where the stainless steel components exhibit such a breakdown early in their operating lives. Moreover, equally important is the understanding of the nature of the breakdown process itself and of the factors and mechanisms involved.

In the present section the static oxidational behaviour of the AISI 316, 310 and 321 stainless steels is discussed. This is described with respect to the nature of the breakdown process and the subsequent oxidational behaviour of the steels in terms of their oxidation kinetics, subsurface elemental constitution and diffusion mechanics.

5.1.2 General Oxidation Characteristics

Evidence provided by oxidation kinetic determinations and by the physical analysis of the overall oxidation process suggests that significant differences exist between the oxidational behaviour of the three steels. Figure (2.10) clearly summarises

these differences. However, at later stages of oxidation the behaviour of the three steels are in close resemblance. Essentially, whereas the AISI 310 and AISI 316 steels exhibit a gradual and normal Wagnerian-type oxidation pattern, the AISI 321 steels follow a very much more abnormal logarithmic pattern of oxide growth.

The consistent nature of such oxidational behaviour within the austenitic stainless steels, under AGR-type environments, is clearly apparent if a direct comparison is made with the oxidational work of Rowlands, Whitlow and Wootton[51]. This work carried out on the oxidational properties of the AISI 321 and AISI 316 steels under simulated AGR conditions, shows very close resemblance to the oxidation patterns observed in the present work, That is, as indicated by the weight gain-time curves of figure (2.10) two forms of behaviour are apparent: (i) the sudden transitional abnormal behaviour of the AISI 321 steels and (ii) the normal parabolic behaviour of the AISI 316 and AISI 310 steels.

(i) Protective Oxidation

With reference to figure (2.10), initially the behaviour of all the steels is similar showing typical parabolic oxidation.

This initial oxidation, as identified in a previous section, can be attributed to the gradual formation of a thin protective layer of an essentially chromium III oxide. It is such an oxide layer that gives stainless steels good resistance against oxidising environments since the protective oxide layer precludes the possibility of any further oxidation, and as such is the normally required behaviour[52,53].

Following the first temperature-cycle, protective oxidation is still found to dominate the behaviour of the AISI 316 and AISI 310 steels. However, such normal oxidation which for most austenitic stainless steels remains intact for long periods, is found to eventually fail during the later stages of oxidation.

Examination of the oxidation kinetics of the early oxidation process indicate that the protective oxidation of this nature can be described by a typically parabolic relation of the form:

$$(\Delta W/A)^2 = k_p t + C$$

where ΔW = the gain in weight; k_p = parabolic reaction rate constant. That is, the oxidation rate continuously decreases with increasing time of exposure.

It is identified in a previous section, that although protective oxidation clearly follows Wagnerian oxidation kinetics it cannot, however, be described by a single parabolic rate. An apparently two stage parabolic mechanism is found to occur, namely, an initial high oxidation rate described by kp_1 and a final lower oxidation rate described by kp_2.

Similar kinetics have also been observed by Hill and Hales, Boggs et al and Hussey and Cohen. In general, the initial 'fast' oxidation rate is commonly superceded by an oxidation rate that is an order of magnitude slower. (54,55,56)

(ii) Anomalous Oxidation

The anomalous non-parabolic oxidational behaviour indicated in figure (2.10) is found to occur in all of the three austenitic steels. However, such oxidation is particularly prominent in the

AISI 321 steels. Associated with such behaviour is the nucleation and subsequent growth of mixed oxides in the form of duplex scales. As identified in Section 3.6, the scales consist of an upper Fe_3O_4 layer and a lower, commonly below surface, mixed spinel oxide layer.

The very different nature of duplex oxidation in comparison to protective oxidation is clearly apparent in terms of their respective oxidation kinetics. There is no simple rate law that can be used to define anomalous oxidation but the irregular nature of the oxide growth can be best approximated by a logarithmic rate-law of the form: (as illustrated by figure (2.12))

$$\text{Log } (\Delta W/AC) = a\,t$$

where ΔW is the gain in weight and 'a' is the logarithmic reaction-rate constant.

5.1.3 Mechanisms Causing Anomalous Oxidation

In general, anomalous oxidational behaviour can be identified by the occurance of the initial failure of the protective Chromium III oxide and the subsequent nucleation and growth of duplex spinel oxides.

The physical mechanisms supporting and encouraging such behaviour can be attributed to a combination of effects arising as a result of (a) the treatment received by the steels during manufacture, (b) the treatment received during specimen preparation and (c) the treatment received under test.

It is thought that any one or all of such treatments could eventually lead to a profound alteration in the metallurgy or elemental constitution of the steels.

(i) Austenite Phase Transformation

In comparing the oxidational behaviours of ferritic steels and ferritic stainless steels, which have high contents of ferrite and martensite, with austenitic stainless steels, the ferritic steels are well known to be greatly inferior in oxidation resistance. Many such steels containing 9%, 12% or 17% Cr and 2%Ni when exposed to AGR conditions have been observed to also behave anomalously showing the classic symptoms of protective oxide failure and subsequent incidence of spinel growth (Rose 1973 (57)).

Synonomous behaviour of this nature of the ferritic steels would tend to suggest that the ferrite content within the structure of the austenitic steels may contribute significantly to their oxidational behaviour.

Assuming that it is the ferritic content of the austenitic steels that supports anomalous oxidation and causes the failure of the protective oxide scale, it remains to deduce the manner by which the ferrite is generated. The occurrence of this could be due to the accumulation of retained ferrite during manufacture or the generation during specimen preparation or generation as a result of temperature cycling.

The fast quenching treatment normally used in the manufacture of austenitic steels in order to soften and normalise the grain structure tends to promote the retention of ferritic material. However, this is not generally significantly large. (58,59)

(a) Cold Working

The application of cold work to steel surfaces in the form of surface polishing and machining, during preparation, can

commonly lead to the generation of ferrite in austenitic steels. The magnetic properties of steels having received a high degree of surface polishing are invariably found to be much strenghtened as a result of the extensive cold working.

As is suggested by several investigators (Angel 1954 (60), Yamaguchi 1956 (61), Fisher et al 1973 (62)), the ferrite generated in this way, by cold working, can be attributed entirely to the partial transformation of austenite.It is thought that the stresses introduced into the surface structure provides sufficient energy for the phase transformation to occur.

However, X-ray diffractometry traces of austenitic steels not exhibiting anomalous oxidation, namely the AISI 316 steels, indicate that the generation of ferrite by cold working is not always successful. Such a trace is illustrated in figure (5.1a) where the ferrite b.c.c. phase peak is clearly absent in contrast to figure (5.1b), which illustrates a trace from an AISI 321 steel exhibiting anomalous oxidation. This evidence would tend to suggest that only those steels where an unstable composition exists, that is the existence of unstable or metastable austenite, is the influence of cold working sufficient to induce the phase transformation.

(b) Temperature Cycling and Differential Contraction

By reference to figure (2.10) it is apparent that the onset of anomalous oxidational behaviour is initiated at the first stage of temperature cycling. From this it would be logical to conclude that, as with cold working, the treatment of temperature cycling encourages the formation of ferrite from metastable austenite. It is thought that the slow cooling process, rather than the heating,

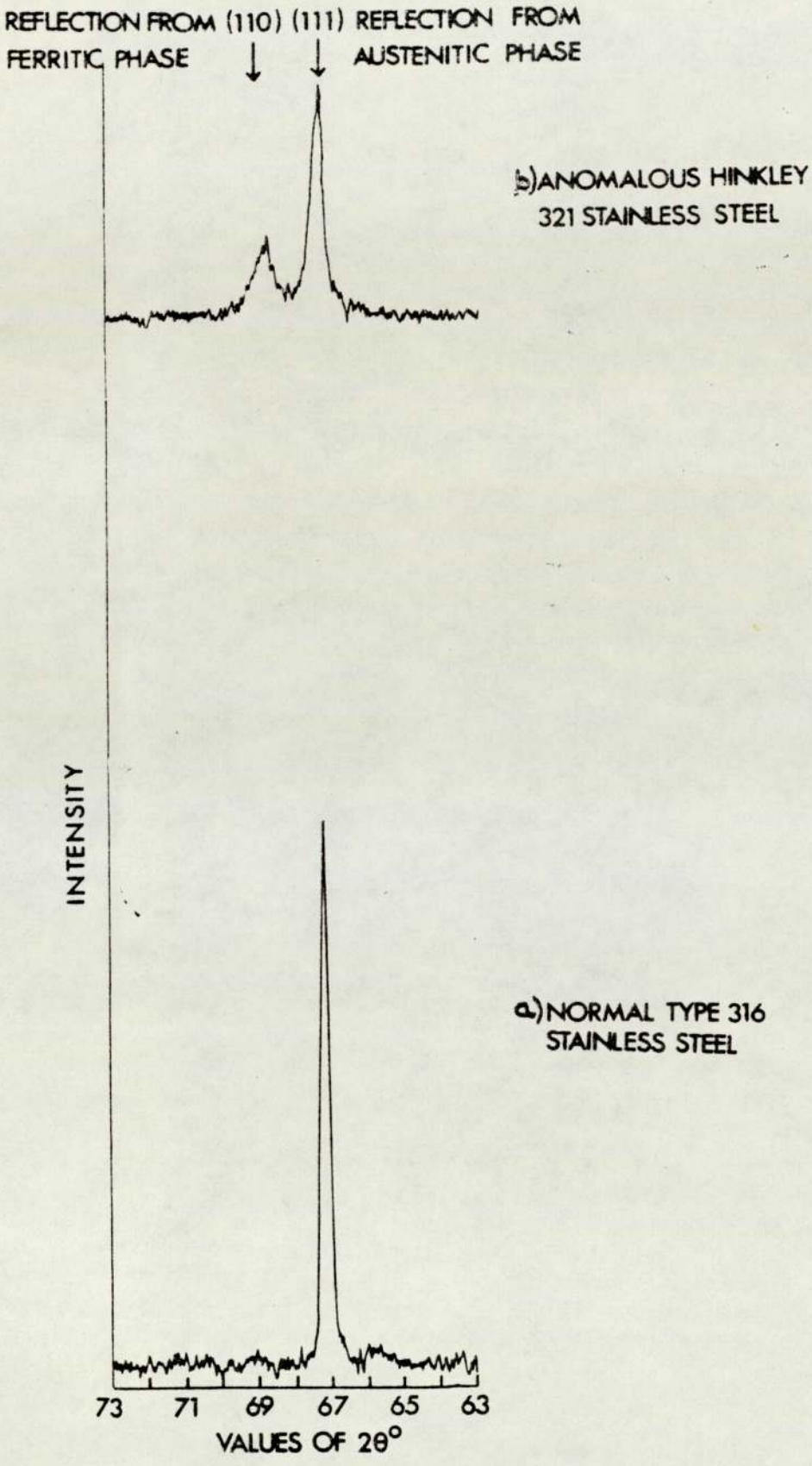

X-RAY DIFFRACTOMETER TRACES OBTAINED WITH
FILTERED Cr RADIATION

FIGURE 5.1 a) and b)

leads to phase transformation and therefore subsequent anomalous oxidational behaviour.

Due to the slow cooling and re-heating processess associated with temperature cycling, a further possible mechanism encouraging anomalous oxidational behaviour can be that due to differential thermal contraction. This, a physical rather than a metallographic effect, could lead to the cracking and spalling of the oxide scale through the differences in the rates of cooling and thermal contraction between the alloy substrate and the oxide scale.

Non-Temperature Cyclic Oxidation

Very close resemblances in oxidational behaviour between the continuously oxidised steels, that is the non-temperature cycled steels, and the temperature-cycled steels is apparent from the experimental results. However, in the case of the non-cycled AISI 321 steels, although anonmalous behaviour is found to re-occur, the onset of such behaviour is significantly delayed.

Differences in behaviour of this nature would seem to suggest that although temperature-cycling considerably hastens the onset of anomalous oxidation by encouraging phase transformation, it is not however vital in the producing of anomalous behaviour. Moreover, without the initial cold working procedure, a process which would appear to cause a substantial amount of phase transformation, the occurence of anomalous behaviour would be much delayed and diminished.

(ii) Normal Oxidation and Nickel Content

There is evidence to believe that austenite instability

and therefore the promotion of anomalous oxidation may also be directly related to nickel content.

It is suggested by Cina, 1954, (63) that in those austenitic steels where the nickel contents lie within the lower limits of a 7-20wt% range, the stability of the f.c.c. austenite phase is very often found to be of a metastable character. It would seem that to generate a truly stable austenitic structure a high nickel content is particularly beneficial. Furthermore, austenitic steels consisting of high nickel contents would be expected to show stable austenitic structures and a great deal of resistance to phase transformation. Since the formation of ferrite by phase transformation is directly related to anomalous oxidational activity, a strong resistance to such formation would therefore also offer a strong resistance to anomalous oxidation.

In accordance with the above, the high levels of nickel content in the AISI 316 and AISI 310 austenitic steels, namely, 12.4 % and 19.95% respectively, would suggest that a strongly stable nature of the austenite would prohibit the generation of ferrite and therefore, in turn, the occurrence of anomalous oxidation. Moreover, in such stable austenitic steels the phase transforming mechanisms such as cold working and temperature cycling would be expected to have little effect. Conversely, however, with the AISI 321 steels of low nickel content, namely 9.1 %, a metastable austenitic structure would be expected to be very vulnerable to anomalous oxidation and to the phase transforming mechanisms.

In comparing the above predictions with the experimental evidence, a very close correlation is clearly evident. Firstly,

as predicted, the influences of cold working and temperature cycling, that is the phase transforming mechanisms, have no direct effect upon the behaviour of the AISI 316 and AISI 310 steels. Secondly, a consequently normal oxidation pattern is followed, with a greatly reduced vulnerability to anomalous oxidation. Finally, the AISI 321 steels are profoundly affected by the phase transforming mechanisms and consequently exhibit severe anomalous oxidation.

(iii) Spinel Nucleation and Chromium Depletion.

The selective removal of chromium from a narrow zone just below the surface during oxidation is seen to be a characteristic feature of the overall oxidation process. The consequence of such behaviour is the creation of a very shallow zone that is deficient in chromium. It is thought that such a zone provides a further important mechanism for the eventual nucleation and growth of spinel oxidation.

Normally, in stainless steels, the high content of chromium combines readily with the oxidising environment to form a thermodynamically favoured chromium III oxide phase. Selective oxidation of this nature precludes the formation, under steady state conditions, of any other species of oxide. The depletion of chromium from the bulk alloy at the surface regions, however, disturbs the steady state conditions and reduces the thermodynamic favourability of the chromium to oxidise. In consequence, the most stable oxide phase to nucleate is no longer the chromium III oxide but that of the mixed spinel oxides, that is the mixed solid solution oxides of iron and chromium.

However, evidence from the results suggests that even at the most advanced stages of chromium depletion, the immediate nucleation of spinel is not observed. Such behaviour is only observed subsequent to the complete failure of the protective oxide. Hence, it would seem that although chromium depletion is an important mechanism in the initiation of anomalous oxidation it does not become effective until a depleted alloy surface is exposed. Moreover, depletion of this nature does not immediately affect the stability of the protective oxide, once this has nucleated, since the continued growth of this oxide is sustained even through the severe states of chromium depletion.

5.1.4 Diffusion Mechanisms

The physical and chemical characteristics of anomalous oxidation may be further understood by considering the general electronic diffusion patterns occurring during oxidation. Consideration of the cationic, anionic and electron diffusion behaviour, within the solvent metal and oxide can be used to explain the oxidational developments giving rise, eventually, to anomalous behaviour.

In the present discussion, two tentative diffusion models are suggested to help in the understanding of anomalous oxidation.

(i) Multiple Stage Oxidation; Duplex-Oxide Formation

The important oxidational phases leading eventually to anomalous behaviour may be defined by five distinct stages:

Stage 1. In the first stage the oxidation of the iron and chromium is found to occur, which eventually results in the formation of Wustite and Chromium III oxide. The former initially occurs as a very thin-layer oxide, replaced in parts by isolated scales of the latter, nucleating as a subscale (figure (5.2)).

With further oxidation a thickening and the eventual coalescence of the chromium III subscale is produced. In this way a compact protective chromium III oxide layer is formed, precluding the further formation of Wustite.

Stage 2. In the second stage, cracking and exfoliation of the protective oxide, following thermal cycling treatments, is produced, leading to the formation of mixed spinal oxides. Spinel oxide nucleation is seen to occur in isolated areas where cracking has exposed fresh metal surfaces (figure (5.2)).

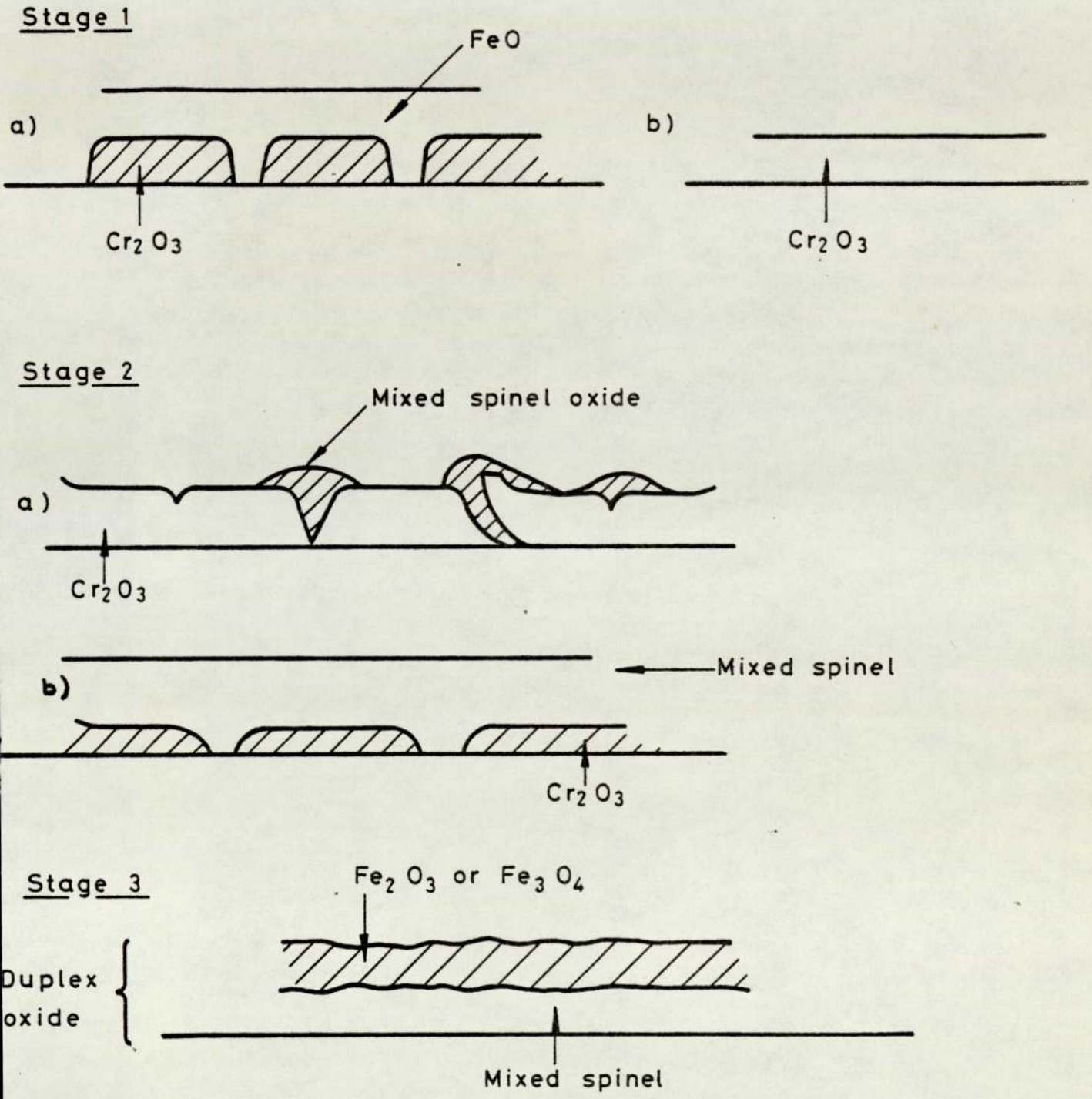
Stage 1
FeO
a)
b)
Cr_2O_3
Cr_2O_3
Stage 2
Mixed spinel oxide
a)
Cr_2O_3
Mixed spinel
b)
Cr_2O_3
Stage 3
Fe_2O_3 or Fe_3O_4
Duplex oxide
Mixed spinel

FIG 5.2

Subsequent oxidation and additional cracking produces lateral extension and eventual coalescence of the spinel oxide. In this way the protective chromium III oxide is eventually replaced (figure (5.2)).

Stage 3. In the third and final oxidation stage where anomalous behaviour eventually arises, a double layered oxide consisting of mixed spinel (lower layer) and Fe_2O_3/Fe_3O_4 (upper layer) forms of oxides, is ultimately formed.

Electrochemical-Cell Model.

The mechanisms producing the various stages of oxidation can be resolved if viewed from the point of view of ionic and electronic transport within the lattices of the oxide layers. Moreover, using the idea of Hoar and Price (64) and Jost (65), we can consider the oxidation process as occuring within an electrochemical cell. An illustration of such an electrochemical cell is indicated in figure (5.3) where this is used to describe the oxidation of a metal Me, by a gas X_2.

Under these terms, the transport of ions and electrons through an oxide layer can be visualised as being a flow of current

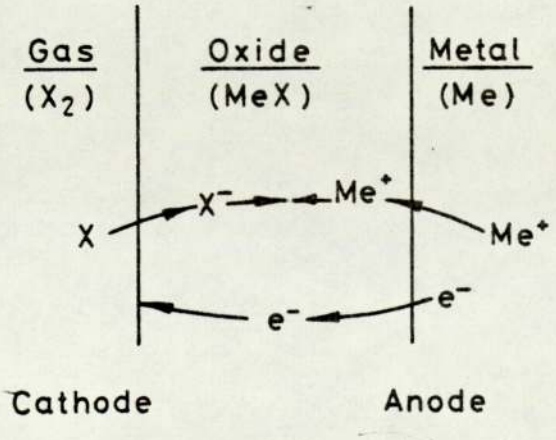

FIG. 5.3

through a cell, in which the oxidation film provides both the electrolyte for the cell, by virtue of ionic transport, and the external circuit, because of electronic conduction. The e.m.f. of the cell is provided by the decrease in free-energy of the electrochemical reactions.

(ii) Electronic Mechanisms of Oxidation

Using an electrochemical model of this kind, the electronic diffusion patterns within the various stages of the oxidation process, in terms of ionic and electron transport mechanisms, can be determined.

In general, the oxidation process consists of two phases: (1) The simultaneous passage of the solvent and solute metals, ie. iron and chromium respectively, into the oxidic state where conversion into the most favoured oxides is achieved and (2) The subsequent transport of solvent and solute cations and oxygen anions, inwards or outwards, within the oxide lattices.

(a) Stage 1.

In stage 1, the transport of solvent and solute metals into the oxidic state results in the formation of Wustite and Chromium III oxides. An illustration of the electronic diffusion mechanisms taking place within this stage is given in figure (54).

Since Wustite and Chromium III oxide are both p-type conductors the main oxidation controlling transport mechanism is predominantly cationic diffusion outwards via vacant cation sites rather than anionic diffusion inwards. That is, oxide growth is not due to the diffusion of oxygen ions from the surface to the metal-oxide interface but to the transport of chromium and iron ions outwards towards the oxide-gas surface. However, due to the unusually

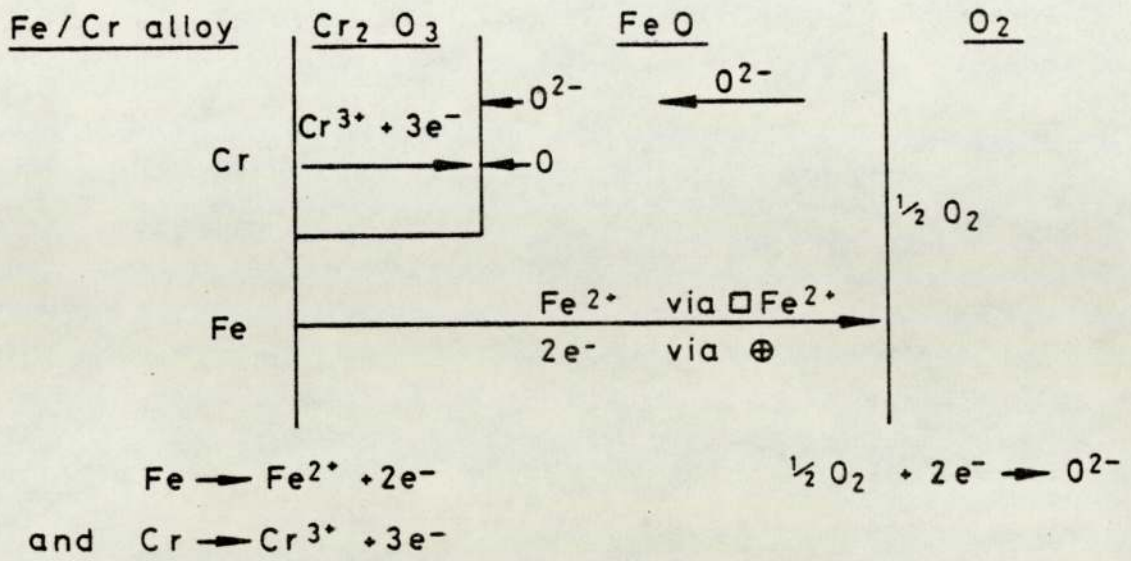

FIG. 5.4

high concentration of lattice defects in Wustite, the diffusion of oxygen anions to the metal-oxide interface is still achieved but to a limited extent. In this way, further oxidation of chromium is achieved.

Chromium Oxidation

At this stage the preferential oxidation of chromium is absent since initially the diffusion of chromium to the alloy-oxide interface is slow. Consequently, the iron oxidises in preferance, although not exclusively, to form a fully covering thin film of wustite.

However, as more chromium diffuses to the alloy-oxide interface, with increasing time of oxidation, a much increased rate of growth of Chromium III oxide is achieved, via the interaction with an increasing concentration of inwardly diffusing oxygen anions. In this way, a thin but compact subscale of Chromium III oxide is formed. However, due to the inaccessability of oxygen anions to the alloy-

oxide interface and to the low concentration of chromium cations reaching the oxide-gas interface, the chromium is still not preferentially oxidised.

As more of the chromium at the alloy surface is oxidised a very shallow chromium depleted zone is created. Such depletion subsequently leads to the development of a concentration gradient immediately below the alloy surface. In this way a driving force is provided for the diffusing chromium which leads to the increase in diffusivity of the latter. In consequence, an abundant supply of chromium at the surface results which eventually leads to a much increased rate of growth of chromium III oxide. Such oxide expansion ultimately produces a fully covering compact scale of Cr_2O_3 which precludes any further formation of Wustite and hence behaves protectively. In conclusion, the preferential oxidation of the chromium at this stage eventually leads to the replacement of the wustite by a protective chromium III oxide.

Carbon Dioxide Decomposition.

Since the oxidising environment is predominantly carbon dioxide, the direct combination of cations with diffusing oxygen anions is not possible but is eventually achieved by a three stage process. Firstly, the decomposition of the Co_2 at the high temperatures leads to the formation of free oxygen.

$$CO_2 = \frac{1}{2}O_2^- + CO$$

Secondly, the free oxygen produced in this way, is gradually chemisorbed into the oxide-gas surface. Finally, the ionisation of the chemisorbed oxygen provides a source of diffusing oxygen anions for direct combination with outwardly diffusing cations. Ionisation of this kind is achieved by virtue of the cathodic reaction:

$$\tfrac{1}{2}O_2 \text{ chemisorb} + 2e^- = O^{2-}$$

(b) Stage 2

The diffusion pattern which controls the oxidation process at stage 2 is illustrated by figure (5.5). Since there exists a strong chromium depletion profile under the protective chromium III oxide, the subsequent oxidation at the ruptured Cr_2O_3 areas proceeds predominantly by the oxidation of the iron in preferance to the chromium. However, the oxide thus created is of a mixed spinel structure.

In general, it can be seen that two main oxidation controlling mechanisms co-exist at this stage. Firstly, the passage of Cr^{3+} cations whithin the chromium III oxide, to establish the continued growth of the oxide, and secondly the predominantly outward diffusion of bivalent Fe^{2+} and trivalent Fe^{3+} ions, via tetrahedral and octahedral cation sites, at the ruptured Cr_2O_3 regions.

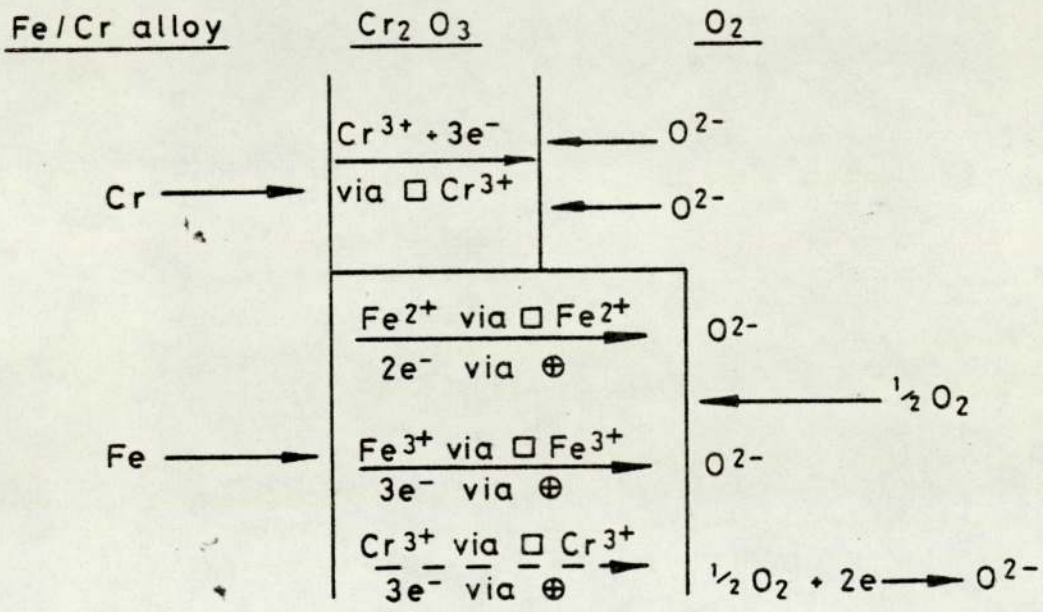

FIG. 5.5

Since the mixed spinel and Cr_2O_3 structures are not as defective as the wustite lattice structure, the process of new oxide formation is by combination with chemisorbed oxygen anions at the oxide-gas surface, rather then by the combination with inwardly diffused oxygen at the alloy-oxide interface.

The most probable composition of the spinel oxide created at this stage must be a combination of the sort:

$$Fe^{2+}\ Cr_2^{3+}\ O_4^{2-} + Fe_x^{3+}$$

and of the form $(Fe, Cr)O_4$. Such an oxide would have a general structure of the form:

$$(Fe_{2-x}^{3+}\ Cr_x^{3+}\ Fe^{2+})\ O_4^{2-}$$

Owing to the high volume ratio of the spinel oxide,[66] subsequent oxidation causes further rupturing of the Cr_2O_3 by expansion of the spinel against the resistance of the existing protective oxide. In this way, larger areas of unprotected alloy surface are exposed resulting in the further nucleation of the mixed spinel oxide. Eventually, the continuation of such an oxidation process leads to the replacement of the chromium III oxide by the spinel $(Fe\ Cr)O_4$.

(c) Stage 3

At the final stage, the upper parts of the mixed spinel oxide is gradually replaced by the nucleation of an Fe_2O_3-type oxide. The growth of such an oxide is initiated by the decrease in concentration of iron ions at the mixed spinel oxide-gas surface. A decrease in concentration, in this way, leads eventually to an insufficient supply of Fe^{2+} and Fe^{3+} ions to the oxide-gas surface and in consequence to the failure to maintain the growth of the

spinel oxide. Moreover, the rate of growth of the Fe_2O_3-type oxide is enhanced by the greater mobility of the cations in diffusing through the oxide.

Since the newly formed Fe_2O_3 oxide is chiefly a p-type conductor and the spinel oxide an n-type conductor, the formation of oxide can be expected to take place mainly at the spinel oxide - Fe_2O_3 oxide interface and very little at the oxide-gas surface. That is, cations diffusing through the inner oxide combine with inwardly diffusing oxygen anions at the spinel-Fe_2O_3 oxide interface.

Phase-Boundary Reactions

Consideration of the phase boundary reactions at the junctions between the various oxide layers (figure (5.6)) would seem to indicate that rather than a double layered oxide being formed a multi-layered oxide is produced. That is, oxide phases ranging in composition from $(Fe^{3+}_{2-x}\ Cr^{3+}_{x}\ Fe^{2+})O^{2-}_{4}$, $(Fe^{3+}_{1-x}\ Cr^{3+}_{x})_2O^{2-}_{3}$ + Fe_2O_3 to α-Fe_2O_3 are formed. However, due to the inter-solution between some oxides a double layered structure is apparent.

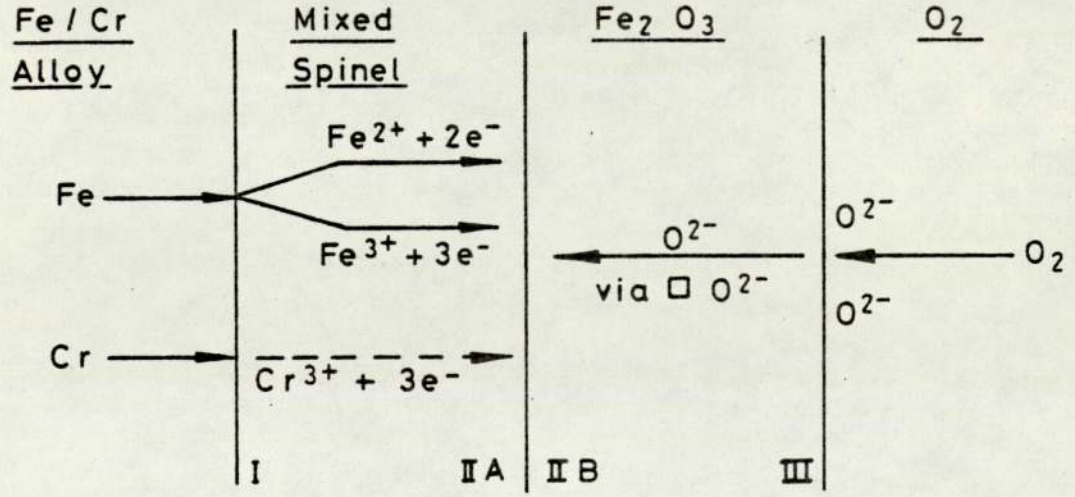

FIG. 5.6

The phase boundary reactions, I, IIA, IIB and III at the oxide junctions can be expressed by the equations:

I. $2Fe + Cr + [\square Fe^{2+} + \square Fe^{3+} + \square Cr^{3+} + 8\oplus] = \text{zero}$

or $2Fe + [\square Fe^{2+} + \square Fe^{3+} + 5\oplus] + Cr + [\square Cr^{3+} + 3\oplus] = \text{zero}$

IIA. $(Fe_2O_3)Cr_x = 2[Fe^{3+}\ Cr^{3+}\ Fe^{2+}]O_4^{2-} + [\square Fe^{3+} + \square Fe^{2+} + \square Cr^{3+} + 8\oplus] + [\square O^{2-} + 2\ominus]$

IIB. $2[Fe^{3+}_{2-x}\ Cr^{3+}_x\ Fe^{2+}]O_4^{2-} = 2Fe_2O_3.Cr_x + [2\square O^{2-} + 4\ominus]$ for all x

III. $\frac{1}{2}O_2 + [\square O^{2-} + 2\ominus]_{Fe_2O_3} = \text{zero}$

5.1.5 Diffusion Controlled Oxidation

It is apparent from the discussion that the development of a concentration gradient at the viscinity of the alloy-oxide interface has a strong affect upon the subsequent oxidational behaviour.

However, it is suggested by a diffusion model that whereas such gradients affect the type of oxide to be nucleated (by limiting the rate at which the oxidising elements reach the interface) they do not control the rate of growth of an oxide. That is, if $M_t < [C_S]$, where M_t is the amount of oxidising element diffusing at any instant from the alloy-oxide interface and C_S the concentration at the interface, then the oxidation growth-rate is not controlled by the diffusion of the oxidising element within the alloy but by the diffusion of the latter within the oxide.

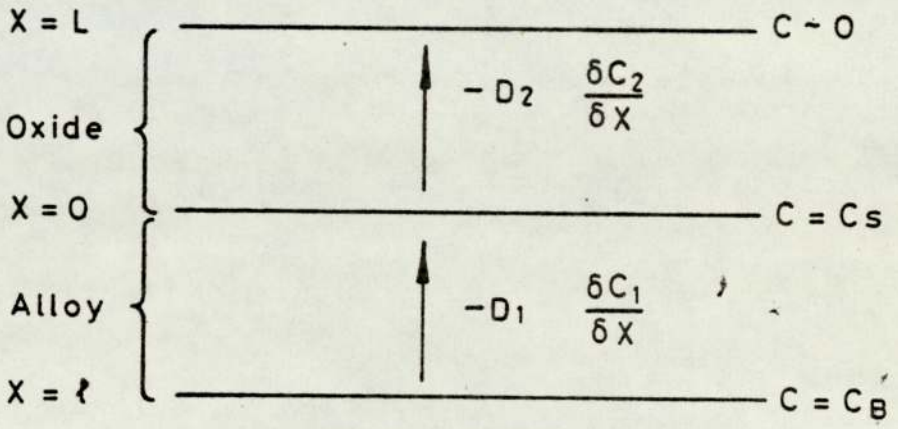

Consider the diagram shown above which represents the diffusion through an oxidised iron alloy of high chromium content, where under steady state conditions the oxidising element concentrations at the alloy-oxide interface and at a depth, l, within the alloy are maintained at C_S and C_B respectively. The diffusion process is represented by the diffusion coefficients D_2 and D_1 and the concentration gradients $(\delta C_2/\delta_x)$ and $(\delta C_1/\delta_x)$.

Assumptions implicit in the model are that the oxide is single layered, the overall oxidation is parabolic and the rate of transfer of diffusing substances is proportional to the parabolic oxidation reaction-rate.

Using Fick's laws of diffusion (Ref. 36,65) to define the rate of transfer of diffusing cations through the alloy and oxide layers, i.e., $-D_1 (\delta C_1/\delta_x)$ and $-D_2 (\delta C_2/\delta_x)$ respectively, we can see that if:

$$-D_1 (\delta C_1/\delta_x) = -\gamma D_2 (\delta C_2/\delta_x) \qquad [5.1]$$

where γ is a constant of proportionality and

$$-D_1 (\delta C_1/\delta_x) = D_{1/1} (C_S - C_B)$$

then substituting into [5.1]

$$\frac{D_1}{1} (C_S - C_B) = -\gamma D_2 (\delta C_2/\delta_x)$$

It can be shown that $-D_2 (\delta C_2/\delta_x) = kpt/2B$ where $1/B$ is a constant of dimensions $g.cm^{-2}$.

$$\therefore \quad \frac{D_1}{1} (C_S - C_B) = -\gamma kpt/2B$$

$$C_S - C_B = -\gamma kpt.1/D_1 2B$$

Hence $$C_S = -\frac{\gamma kpt.1}{D_1 2B} + C_B$$

Since $m^2 = kpt$ (defining parabolic oxidation)

$$C_S = -\frac{\gamma m^2.1}{D_1 2B} + C_B \qquad [5.2]$$

Assuming that M_t is equal to the rate of transfer of diffusing material to the oxide-gas surface, $-D_2 (\delta C_2/\delta_x)$ then:

$$M_t = \frac{1}{2B} m^2 \qquad [5.3]$$

Substituting [5.3] into [5.2] we see that:

$$C_S = -\frac{\gamma_1}{D_1}.M_t + C_B$$

Hence $M_t < C_S$.

5.2

5.2.1 Analysis of the Wear Behaviour

The results reported in the present work show that under conditions of low-speed unlubricated continuous sliding the wear behaviour of the AISI 316 and AISI 310 steels is described by two clearly defined modes of wear; namely, mild equilibrium wear and severe metallic wear. For the AISI 316 steels a well defined transitional behaviour between the two wear modes is exhibited, with the dominant prevalance of one or other of the wear modes either side of the transition. The linear representation of the change in volumetric wear rate with applied load vividly illustrates such transitional behaviour as shown by figures (5.7) and (5.8). For the AISI 310 steels, it is the predominantly severe wear mode which is observed.

With respect to the frictional behaviour, a three staged friction pattern is observed in general. A load dependent friction region, a transition region and a load independent friction region characterise the overall friction behaviour. In the case of the AISI 310 stainless steels, an essentially single staged friction pattern, as defined by a load dependent behaviour, is observed to dominate the friction behaviour.

(i) Adhesive Wear

By consideration of figure (5.8) it can be seen that above the transition load the wear-rate gradients, dw/dW are closely similar in magnitude whereas, however, below the transition the gradients vary widely. It is thought that such similarity in dw/dW

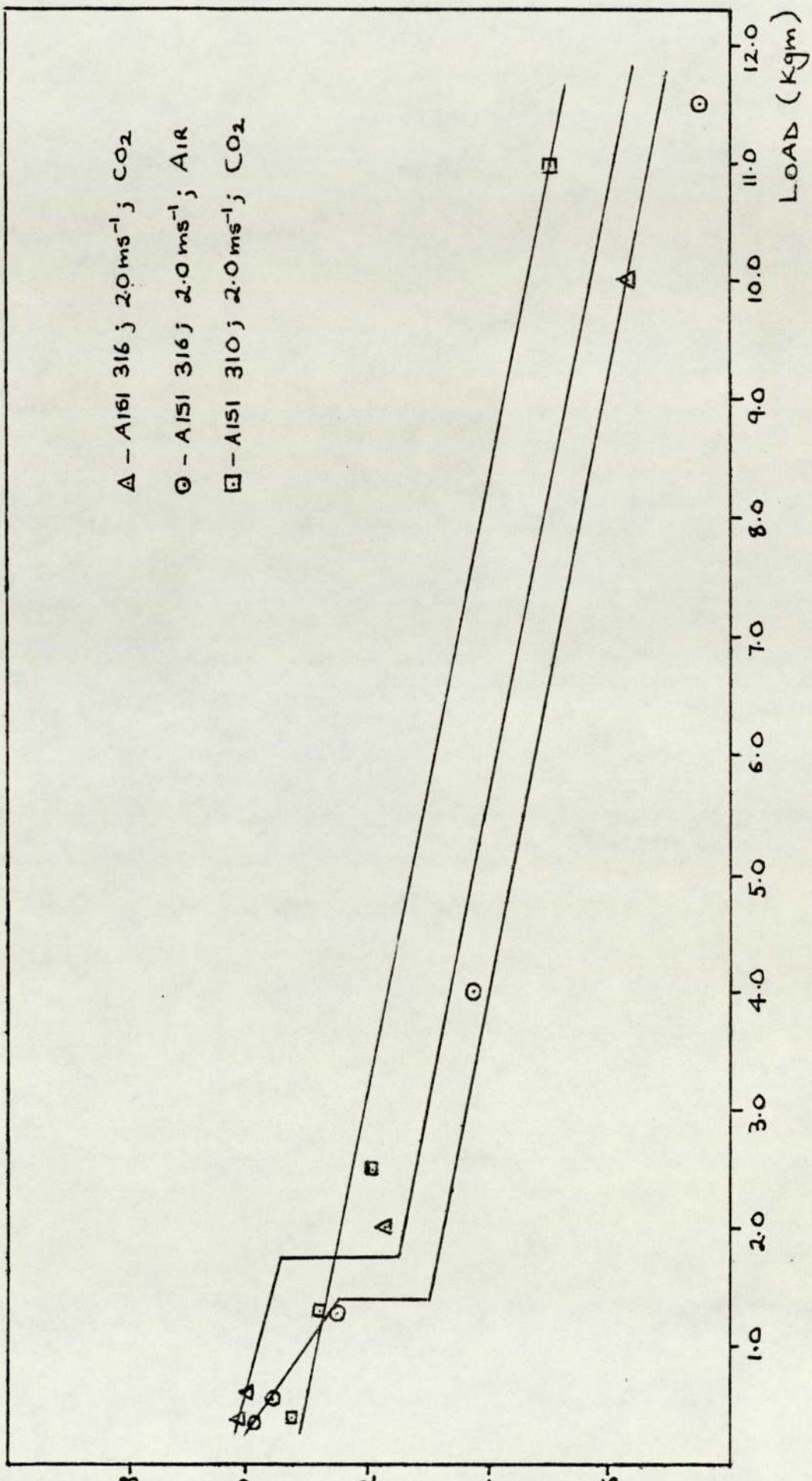

FIG. 5.7 LINEAR REPRESENTATION OF 316/310 WEAR BEHAVIOUR.

above the transition zone is indicative of a common wear mode. Assuming this, it can be inferred that the wear mode characterising the wear of the AISI 310 steels, for all loads, is similar in nature to the wear process occuring above the transition in the wear of the AISI 316 steels. Examination by Scanning electron microscopy of representative AISI 316 and AISI 310 steel specimens from the corresponding high wear regions, as illustrated by the micrographs of figures 4.20, show many similarities inwear scar topographies, thus again suggesting the occurrence of a synonymous wear process in each case.

For all wear surfaces in the high wear regions, a greatly deformed wear substrate is observed with much evidence of gross smearing of surface material by plastic deformation. In addition, the presence of a widely undulating surface profile suggests the occurrence of substantial material transfer during sliding. Since adhesive wear, as classified by Burwell and Strang, is often recognised by the presence of gross plastic deformation, rough undulating wear scars, metallic debris and metal transfer, it can be concluded that the dominant wear process occurring at the high wear regions above the transition zone is chiefly adhesive.

The atomic model for adhesive wear, as derived by Holm,[67] forms the basis of Archards wear law. In Holm's adhesive wear model is postulated the idea of the removal of groups of atoms from the substrate by virtue of their adhesive junction strength becoming greater than the cohesive strength of the material. This postulation is used as the basis to derive the volume of wear (w) for a slider undergoing adhesive wear, as given by:

$$w = \frac{ZPS}{Pm}$$

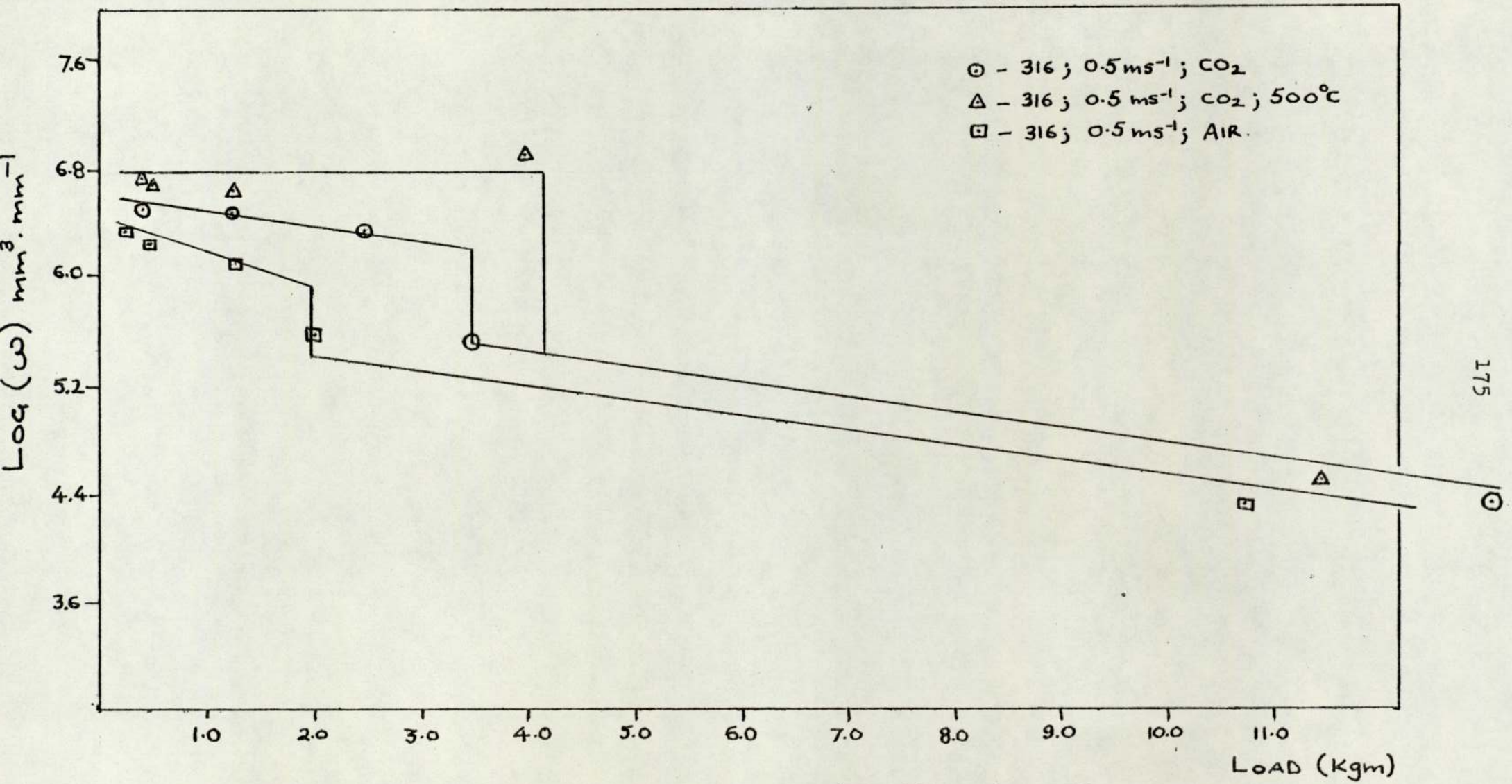

FIG. 5.8 LINEAR REPRESENTATION OF AISI 316 WEAR BEHAVIOUR.

where Z = number of atomic layers removed; S = sliding distance; P = applied load and Pm = flow pressure. Archard [68], using Holm's atomic model, defines the adhesive wear process by considering plastic deformation of the asperity junctures, assuming that a hemispherical particle results from the sliding, and postulating that the adhesion along the base is stronger than the sum of the cohesive shear forces along the hemispherical surface of the potential fragment. Denoting by K the probability of a juncture yielding a fragment, Archards adhesive wear law is given by:

$$w = KPS/3Pm$$

The value of K is a non-dimensional constant for a given pair of surfaces and known as the adhesive wear co-efficient.

It follows from this equation that for adhesive wear mechanisms the wear coefficient K is a constant and that abrupt changes are found only for (1) contact pressures exceeding the yield strength of the material and (2) for non-adhesive wear mechanisms. As such, the variation of K during wear can be used as an indicator of adhesive wear. Table 5.1 shows the variation of K with applied load for the high wear-rate regions above the transition zone. A clearly constant relation for K is evident and supports the view of the occurence of adhesive wear.

(ii) Oxidational Wear

Table 5.1 illustrates the variation of K at the region below the transition zone for the AISI 316 steels. The non-constancy of K suggests the occurence of a predominantly non-adhesive wear mechanism.

Operating Parameters	Wear Condition	
	Mild Wear ($w \leqslant Wc$)	Severe Wear ($w \geqslant Wc$)
316 . 2.0ms^{-1}.Co_2	0.166	0.182
316 . 2.0ms^{-1}.Air	0.571	0.160
316 . 0.5ms^{-1}.Air	0.266	0.133
316 . 0.5ms^{-1}.Co_2	0.086	0.110
316 . 0.5ms^{-1}.Co_2 (500°C)	0.00	0.110
310 . 2.0ms^{-1}.Co_2	-	0.150

Figure 5.1 Variation of K with wear.

Additional evidence in support of this view is provided by the analysis of representative wear scars and wear debris. The analysis of the debris produced from the region below the transition shows the debris to consist largely of oxide in the form of very fine granular material with small quantities of coarser metallic fragments. The oxides, in general, are shown to belong to four oxide systems: (1) Rhombohedral, (2) Wustite, (3) Cubic and (4) Spinel. The most commonest of the oxides, namely, Cr_2O_3, α-Fe_2O_3 and $(Cr, Fe)_2O_3$, belonging to the rhombohedral system, represent the continuous series of solid solution oxides obtainable between Fe and Cr. Other less common oxides present in the debris, namely, γ-Fe_2O_3, Spinels (Fe_3O_4 and Cr_3O_4) and Wustite (FeO) indicate the sliding surface conditions during wear, e.g. surface temperatures. Since a purely adhesive wear mechanism generate predominantly coarse metallic wear debris, with virtually no oxide, it can be concluded that the oxide debris generated in the region below the transition is due to a milder and essentially non-adhesive wear mode.

The topography of the wear scars are characterised by a smooth and even surface appearance with the total absence of gross surface deformation, as illustrated by the micrographs of figure (4.19). Delineation by well defined wear grooves clearly demonstrate the direction of sliding. The absence of such wear topography in the wear scars from the corresponding adhesive wear regions is in addition to the view that two fundamentally different wear mechanisms are in existence.

In conclusion, it is considered that (1) above the transition zone, in the case of the AISI 316 steels, and for all

regions, in the case of the AISI 310 steels, a predominantly adhesive wear mechanism prevails, producing as a result a highly energetic severe mode of wear; and (2) below the transition zone, predominantly oxidative and delamination wear mechanisms prevail, producing as a result mild wear.

(iii) Delamination Wear

A closer examination of the wear scars produced under mild wear conditions shows that where surface covering by compacted oxide is not in evidence a distinctive smooth laminated wear surface consisting of thin horizontal wear sheets parallel to the surface is observed. It is shown by Suh [69] that materials demonstrating such surface character have undergone delamination wear. Scanning electron micrographs illustrating typical forms of delamination wear are shown by figures (4.19b) and (4.19c). As initially propounded by Suh, delamination wear is considered to be due to the nucleation of subsurface cracks and the subsequent growth, coalescence and propagation of the cracks to the surface to form sheet-like wear particles. The magnitude of the wear, w/s, by such a process is given by:

$$\frac{w}{s} = \left(\frac{B_1{}^1h_1}{dc_1} + \frac{B_2{}^1h_2}{dc_2}\right) \frac{P}{Pm}$$

where dc and h denote the critical plastic dis-placement and surface layer thickness respectively and B denotes a complex parameter dependent upon surface topography.

(iv) Contact Mechanisms

The basic mechanism by which delamination wear arises, namely that of crack propagation to the surface, is evidenced in the

present work by figure (4.19) which illustrates a scanning electron micrograph of a delamination crack delineating the wear surface. By sectioning wear-scars exhibiting delamination wear Suh showed that such delamination cracks were initially observed to begin in the subsurface layers parallel to the surface, nucleating along lattice dislocations and vacancies.

It is suggested in the present discussion that such delamination cracks are caused by stress inducing cyclic contact loads.

Consider the case of a stationary flat-faced cylindrical pin loaded against a stationary flat surface of a disc. Under such conditions a uniformly distributed load is applied over the area of a circle of radius, a, where 2a is the diameter of the pin. The consequent distribution of pressure over the contact surface can be represented by the ordinates of a hemisphere of radius, a, constructed on the surface of contact, as illustrated in figure (5.9).

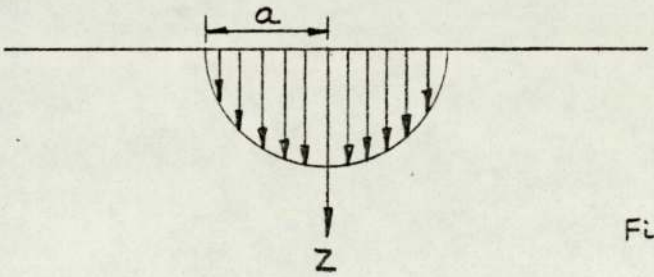

Figure 5.9

As a result of the contact pressures, stresses are produced within the contact area. The distribution of such stresses are distributed beyond the contact surface, unlike the distribution of the pressure which is confined within the contact surface.

The magnitude of the stresses induced in this way can be determined by resolving the principal stress components, σ_z, σ_r and σ_θ. It is shown by Timoshenko [70] that the stress component

σ_Z due to a normal force P acting on the plane boundary of a semi-infinite solid is given by :

$$\sigma_Z = - \frac{3P}{2\pi} Z^3 (r^2 + Z^2)^{\frac{-5}{2}} \qquad [5.4]$$

where Z = distance along the Z-axis of the contact and r = radius of the contact surface. The pressure, q, acting on a ring-area of radius r and width dr (figure (5.10)), due to a load distributed over a circular surface of contact of radius, a, is $P/2\pi$ rdr. Therefore, the load P in terms of the pressure, q, is $2\pi r.\ dr\ q$. Substi-

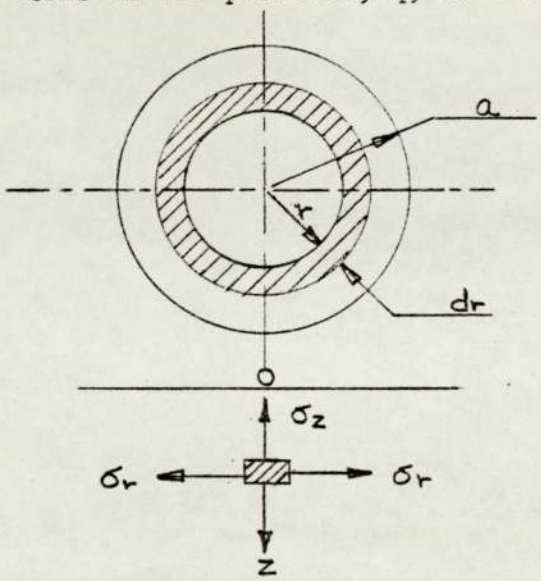

Figure 5.10

tuting for P in equation [5.4] gives the stress $d\sigma_Z$ produced at a point on the Z-axis (figure (5.10)) by a load distributed over a ring-area of radius, r, and width dr:

$$d\sigma_Z = -3\ q\ r\ d\ r\ Z^3 (r^2 + Z^2)^{\frac{-5}{2}}$$

The stress σ_Z produced by the load uniformly distributed over the entire circular area of radius, a, is therefore:

$$\sigma_Z = -\int_o^a 3\ q\ r\ d\ r\ Z^3 (r^2 + Z^2)^{\frac{-5}{2}}$$

$$= q\ Z^3 \left[(r^2 + Z^2)^{\frac{-3}{2}}\right]_o^a$$

$$\therefore \sigma_z = q\left[-1 + \frac{z^3}{(a^2 + z^2)^{\frac{3}{2}}}\right] \qquad [5.5]$$

for $Z = 0$ $\quad \sigma_z = -q$

Hence, at the surface the stress is equal to q and gradually decreases with increasing Z.

Timoshenko and Goodier [70] show that the stress components σr and σ_θ due to a normal P acting on a plane boundary of a semi- infinite solid are given by:

$$\sigma_r = \frac{P}{2\pi}\left\{(1 - 2\nu)\left[\frac{1}{r^2} - \frac{z}{r^2}(r^2 + z^2)^{-\frac{1}{2}}\right] - 3r_z^2 (r^2 + z^2)^{-\frac{3}{2}}\right\} \qquad [5.6]$$

and $$\sigma_\theta = \frac{P}{2\pi}(1 - 2\nu)\left\{-\frac{1}{r^2} + \frac{z}{r^2}(r^2 + z^2)^{-\frac{1}{2}} + z(r^2 + z^2)^{-\frac{3}{2}}\right\} \qquad [5.7]$$

where ν = Poisson's Ratio.

Considering four elements of the loaded area (figure (5.10)) each of which carries a load $qr.\,d\phi.\,dr$, and using equations [5.6] and [5.7] the stresses produced by their respective loads can be determined. These are shown by Timoshenko to be of the form:

$$d\sigma r = d\sigma_\theta = \frac{qr.d\phi.dr}{\pi}\left[-2(1 + \nu)\, z\,(r^2 + z^2)^{-\frac{3}{2}} + 3z^2(r^2 + z^2)^{-\frac{5}{2}}\right]$$

Integrating with respect to $\phi(0 \longrightarrow \pi/2)$ and with respect to r, from o to a, determines σr and σ_θ produced by the entire loaded area:

$$\sigma r = \sigma_\theta = \frac{q}{2}\left[-(1 + 2\nu) + \frac{2(1+\nu)z}{\sqrt{a^2 + z^2}} - \left(\frac{z}{a^2 + z^2}\right)^3\right] \qquad [5.8]$$

At the centre of the circular loaded area, for the point 0, where $Z = 0$

$$\sigma r = \sigma_\theta = \frac{-q(1 + 2\nu)}{2}$$

The maximum shearing stress τmax at any point on the Z-axis is given by $1/2(\sigma_\theta - \sigma_z)$. Hence using equations [5.5] and [5.8]

$$\tau max = \frac{q}{2}\left[\frac{1-2\nu}{2} + \frac{2}{q}(1 + \nu)\sqrt{2(1 + \nu)}\right] \qquad [5.9]$$

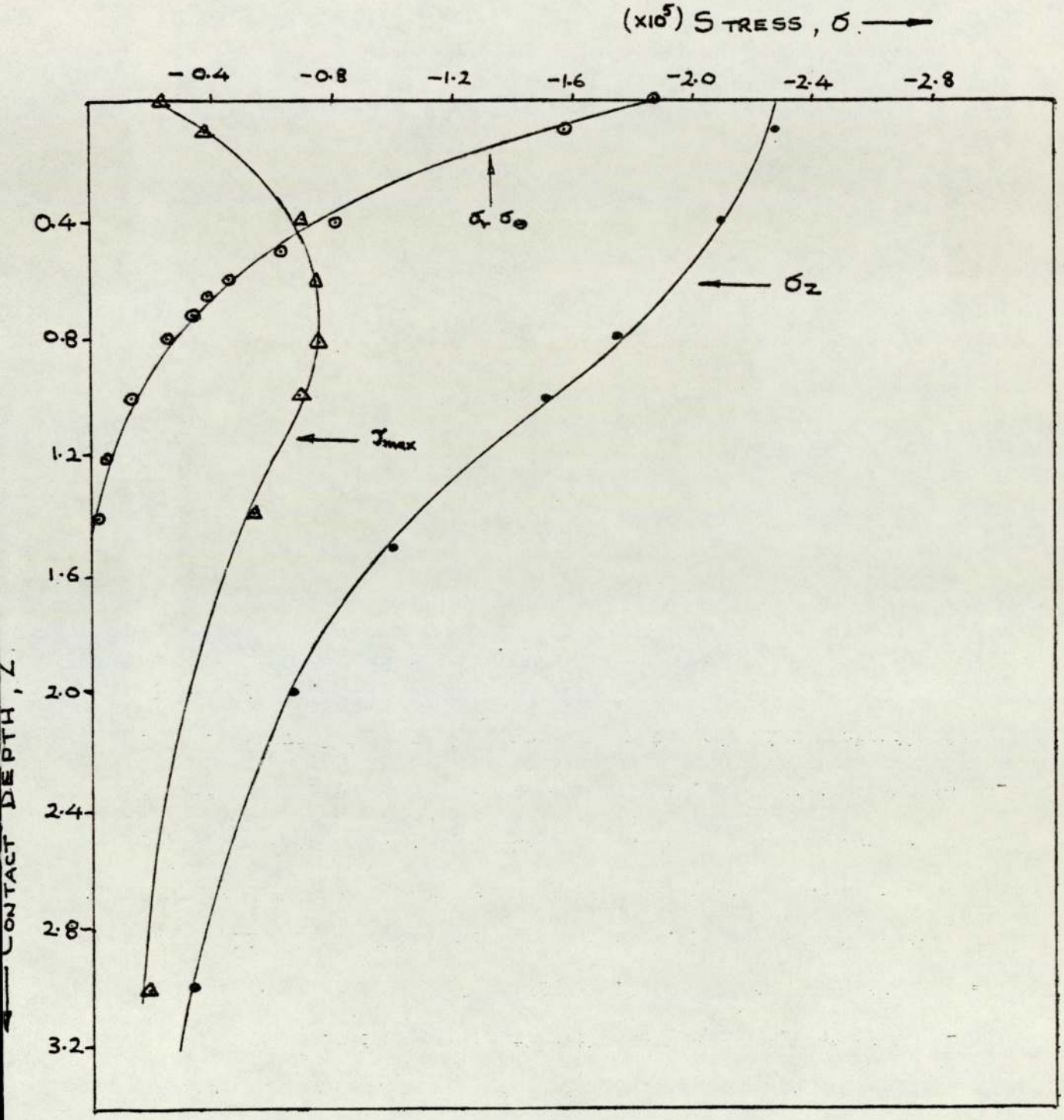

FIG. 11 a). VARIATION OF PRINCIPAL STRESS COMPONENTS. FOR 0.75 Kgm LOAD.

Under conditions of continuous sliding the stresses, σ_z, σ_r, and τ_{max} are applied and unlike the stationary case are instantaneously relieved. This occurs at all points of contact between the pin and disc once per revolution. For large sliding distances, however, where many hundreds of sliding revolutions are necessary, the stresses are applied and relieved repeatedly. In this way, all points of contact at the surface and corresponding regions below surface, bounded by the volume of a hemisphere, undergo cyclic stresses. The volume of material below surface which is immediately affected by the contact loading for the present case is given by the volume of a hemisphere of radius equal to the radius of the pin.[71][72]

Using equations [5.5], [5.8] and [5.9] the principal stress components σ_z, σ_r and σ_θ and τ_{max} and their variation with depth have been calculated for the continuous sliding condition at loads of 0.75 kgms, 10 kgms and 15 kgms. Figure (5.11), (a), (b) and (c) illustrate graphically the calculated magnitude of the stresses and their variation with increasing depth beyond the contact surface.

For all loads it is evident that very high stresses exist and that for the normal and radial compressive stresses σ_z, σ_r and σ_θ the maximum magnitudes are found at the surface, at Z = 0, e.g., σ_r and σ_θ = and σ_z = at 15 kgms load. The stresses gradually decline with increasing depth. The shearing stress, τ, however, upon which the yielding of such material as steel depends is comparatively small at the surface. With increasing depth a maximum is reached in the shear stress at a depth of 0.7a, with a subsequent decline with further increase in depth. As such, the view that delamination wear is initiated below surface is well supported by the stress determinations made here.

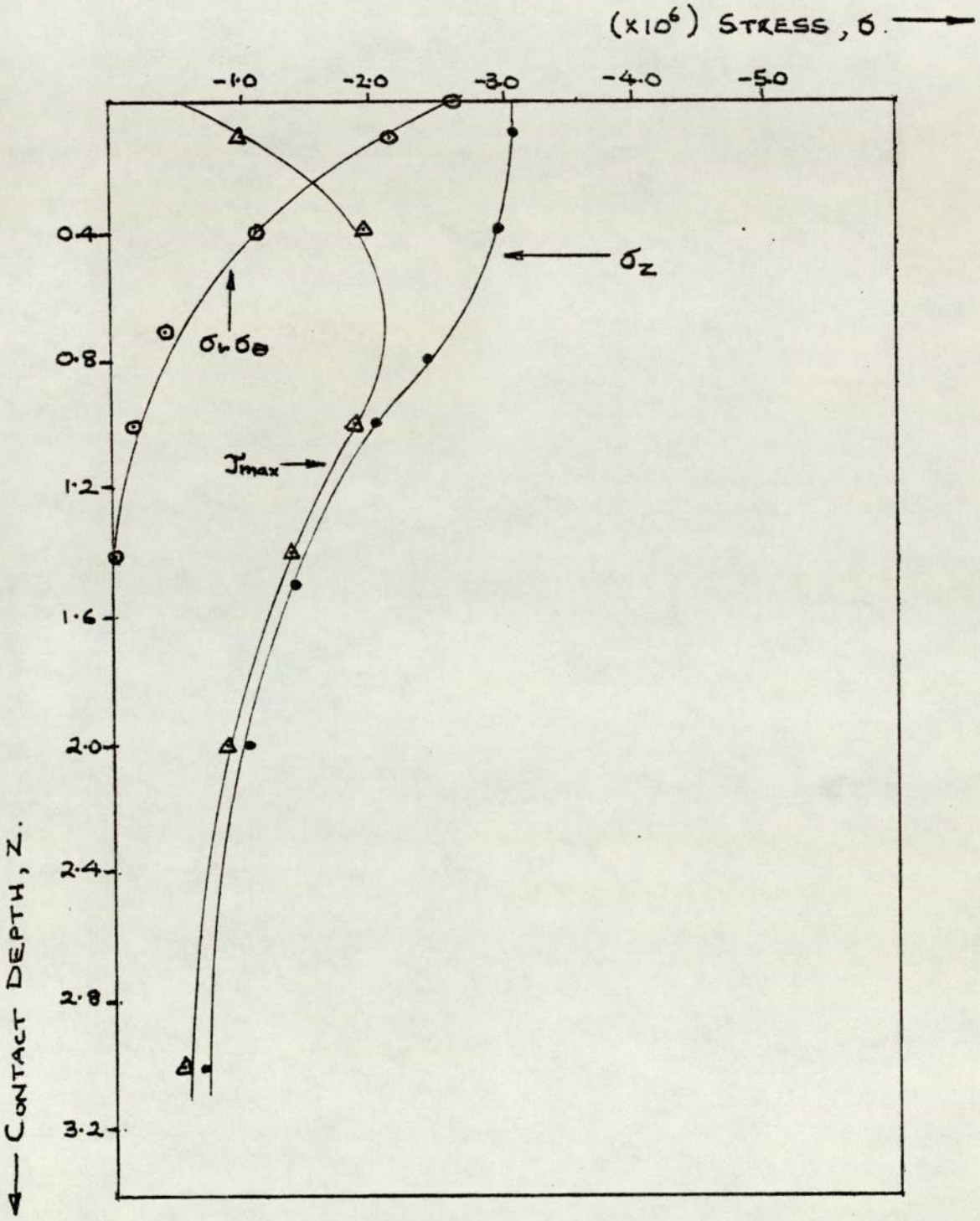

FIG. 11 b) VARIATION OF THE STRESS COMPONENTS FOR 10.0 Kgm LOAD

Since, amongst other factors, it is the magnitude of the shearing stress that decides upon the likelihood of material failure, it is noteworthy that a maximum in the shearing stress occurs at a region below the surface. Hence, it is at a depth corresponding to τ max within the contact surface at which material failure, by way of crack nucleation, is most likely to occur. Since delamination wear is initiated by sub-surface material failure and subsequent crack propogation, the stress determinations made in the present work would clearly seem to be in accordance with the mechanisms describing delamination wear.

Thermal Stress

In order that material failure can occur it has been shown by many workers that the relation $\tau_{max} \geqslant$ F.S must be satisfied, where F.S. = fatigue strength of the material in shear. That is, the maximum shear stress induced by surface loads must be sufficiently large to exceed the fatigue strength. However, it is apparent for the present case, figure (5.11), that although the maximum shearing stress is large at the loaded contacts, it is, however, not sufficiently large to satisfy this shear stress to fatigue strength relation. In consequence, it can be concluded that in order for material failure of the kind evidenced to occur there must be additional stress inducing processes acting to sufficiently increase τ max.

The additional stress inducing processes it is suggested may be due essentially to the thermal stresses produced by frictional heating and to a lesser extent by processes such as the frictional force. It has been shown by several workers that due to

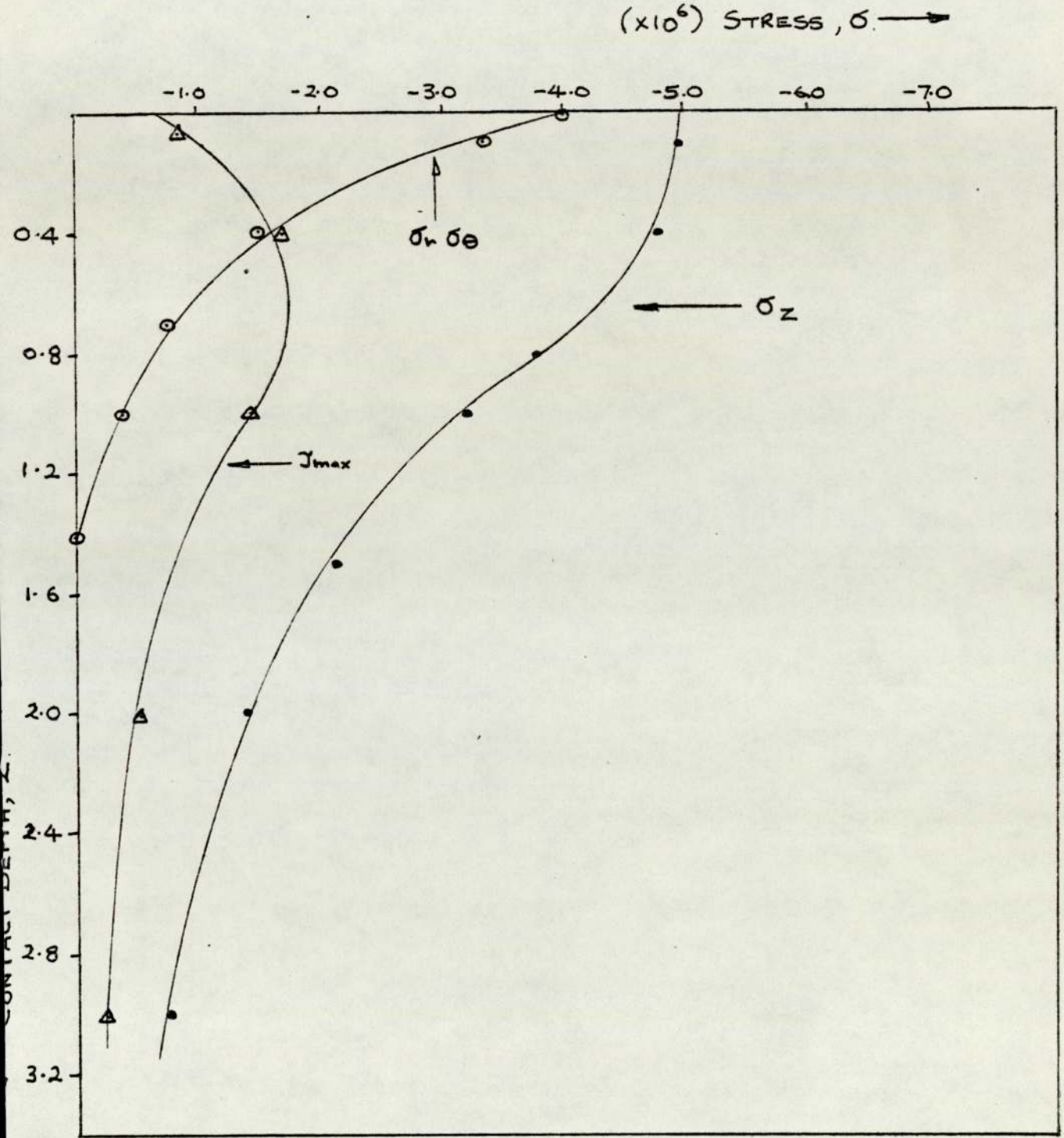

FIG. 5.11c) VARIATION OF PRINCIPAL STRESS COMPONENTS. FOR 15 Kgm LOAD

the frictional heating at the surface steep thermal gradients are produced between the surface and sub-surface layers, as a result of large differentials in their maximum temperatures. Kelly [73] demonstrates this clearly by his temperature calculations for the case of steel on steel contact for a relative sliding volocity of 1.25 $m.s^{-1}$ and a load contact per unit length of $kgm.m^{-1}$.(74)(75)

If the surface material is at a higher temperature than the sub-surface material then the expansion of the surface against the restraining sub-surface must produce surface compressive stresses, σ_T. Such stresses, known as thermal stresses, as a result add to the overall stress produced at the contact surface. Stresses produced in this way can be considerably large and in consequence cause the yield strength to be exceeded and material failure to occur. In addition, material failure is most likely to occur at regions of lattice dislocations, stacking faults and lattice voids where in general the yield strength would be much reduced below the overall bulk value. Consequently, the additional stresses produced by thermal and frictional processes would exceed the local, if not the bulk, yield strength. Under conditions of continuous sliding, the repeated application of the generated stresses to the failed regions would therfore gradually increase the material damage and ultimately cause the failure to propagate to other regions within the contact surface.

5.2.2 Heat Flow Analysis

In the preceding section, the delamination wear theory has been used in helping to define the wear mechanisms giving rise to the mild wear in the region below the transition. In the following

section the oxidational wear theory is investigated for the purpose of helping to further elucidate the wear behaviour.

It is evident, by examination of the wear debris and the wear scars, that much oxidation of the wear surface is produced during the mild wear stage. A large proportion of the wear debris is found to consist of oxides of iron and chromium and that the wear scars show the formation of compacted oxide over-lying the substrate, as illustrated by figure (4.19d). Clearly, it must be the gradual failure of such an over-lying oxide by a micro-fatigue process and the subsequent shearing into minute fragments which must produce the oxidised wear debris.

A wear process exhibiting such wear behaviour exemplifies, as defined by Quinn [76], typical oxidational wear. As such, it is thought that Quinn's oxidational wear theory is readily applicable in an attempt to further define the mild wear behaviour.

(i) <u>A Brief Description of Quinn's Oxidation Theory of Mild Wear</u>

Essentially, the oxidation theory of mild wear states that under conditions of oxidational wear, the wear rate, w, of one of the members of a sliding pair of steels may be given by:

$$w = \frac{W.d.Ap.\exp(-Qp/RT)}{U.Pm.f^2.\rho_o^2.\varepsilon_c^2} \qquad [5.10]$$

where W is the applied load, U is the sliding velocity, Pm is the substrate flow pressure, f is the fraction of oxide which is oxygen, ρ_o is the oxide density and ε_c is the critical thickness at which the oxide becomes unstable; d is the distance between wearing asperity contacts and given by $d = \sqrt{W/\pi}.N.Pm$ where N is the number of areas of contact sharing the load.[77]

Quinn [77] uses the oxidational wear equation to describe the wear process in terms of the critical oxide film thickness (εc), the temperature of oxidation at the interface (To) and the number of contacting asperities (N). This is achieved by substituting the appropriate oxidation constants, Ap and Qp, consistent with the oxidation debris type, and the experimentally derived wear rate into the wear expression (equation [5.10]).

The exact method used by Quinn et al is comprehensively described elsewhere. In short, however, the salient features are discussed in the following:

By use of the temperature measurements made of the heat flow along the pin, the division of heat at the interface δexpt. can be determinded, as given by:

$$\delta_{expt.} = \frac{H1}{HTotal}$$

where H_1 = Heat flow at the interface; H_{total} = total heat flow. In addition a theoretically derived expression for the division of heat at the interface, δtheory, in terms of a surface model consisting of N asperities of approximately the same area of contact upon which an oxide film of thickness, ε, is situated, is also determined and given by:

$$\delta_{theor} = Td/(Tp + Td) \qquad [5.11]$$

where Tp and Td are temperature excesses at the interface assuming all heat flows into the pin and the disc respectively.

By its definition, δtheor is N and S dependent since

$$Td = \frac{\gamma H_{Total}}{4 a k_S} \cdot \frac{1}{N}$$

and $$Tp = \frac{H_{Total}}{4\,a\,k_S} \cdot \frac{1}{N} + \frac{H_{Total}}{\pi a^2 k_O} \cdot \frac{1}{N} \cdot \varepsilon$$

where a = the radius of the real area of contact; k_S and k_O = thermal conductivities of the steel and oxide respectively.

Letting $\beta = H_{Total}/4\,a\,k_S$

Equation [5.11] can be expressed as:

$$\delta theor = \frac{1}{N} \cdot \gamma\beta \,/\, \gamma\beta + \frac{H_{Total}\,\varepsilon}{\pi a^2 k_O N} + \frac{\beta}{N} \qquad [5.12]$$

By inserting appropriate values of N into equation [5.12], for a range of values of ε, a set of values of N can be found which satisfy the relation:

$$\delta theor = \delta expt.$$

By substituting values of N and into equation [5.13]

$$To = (\delta theor \,.\, Tp) + Ts \qquad [5.13]$$

corresponding values of To, temperature at the area of contact, can be determined which are consistent with δ theor and δ expt.

Using the values of To the corresponding values of N, and assuming that

$$W theor = W expt.$$

Qp can be determined by substitution into equation [5.10], for a range of values of ε.

Finally, only those combinations of N, ε and To which give the correct Qp are selected. A computer is used to search for the appropriate combinations of N, ε and To, consistent with the wear theory.

5.2.3 The Application of the Oxidation Theory of Mild Wear to the Present Work

In applying the oxidational wear theory to the present work, several assumptions have been made. Firstly, it has been assumed that the relevant Ap factor is that which defines the static

oxidation of austenitic stainless steels, namely, 1×10^{-7} $kg^2 . m^{-4} s^{-1}$. Secondly, the dominant constituent of the surface oxides at the sliding interface is Cr_2O_3 and thirdly, that the correct Activation Energy Qp is that found by experiment in the present work for the parabolic oxidation of austenitic stainless steels,

Using the theory as previously described, in accordance with the assumptions, the heat-flow measurement for loads below the transition are analysed. Tables 5.2 and 5.3 illustrate the analysis results for air and CO_2 environments, respectively, for oxide thicknesses of 1 μm and 5 μm.

It must be pointed out that in order to satisfy the initial assumptions the parameters Qp, k_0, f and ρo which are used in the analysis are those relating to chromium (III) oxide and not to Iron oxides or any intermediate forms of combined iron and chromium oxides.

(i) Low Qp

Examination of Tables 5.2 and 5.3 show that in general, for all test loads and environments, very low Qp values are found compared to the experimentally derived values of Qp = 90 kJ as found by static oxidation experiments. It is evident that assuming thicker oxide formation viz., ε = 5 μm higher Qp values are found, but are still inconsistent with the experimental values. However, it is encouraging that in general the values of all Qp's are very similar, not widely varying, and remain reasonably constant for all loads and environments.

Load (Newtons)	ε = 1 μm			ε = 5 μm		
	N	To(^{o}C)	Qp(KJ.mole^{-1})	N	To(^{o}C)	Qp(KJ.mole^{-1})
19.62	390	106.2	15.94	7	289.1	29.48
9.81	123	104.8	15.17	-	-	-
7.85	173	90.5	16.03	3	342 3	31.8
5.87	196	83.6	16.06	5	278.8	31.34
4.41	407	72.8	17.03	13	235.1	31.46

TABLE 5.2 Heat Flow Data Analysis (In Air) for Ap = 1.0×10^{-7}.

Load (Newtons)	ε= 1 μm			ε = 5 μm		
	N	To(^{o}C)	Qp(KJ.mole^{-1})	N	To(^{o}C)	Qp(KJ.mole^{-1})
15.70	500	101.7	13.53	16	260.2	24.19
9.81	421	83.9	12.85	12	238.8	24.62
6.86	262	83.1	14.22	7	265.6	27.96
3.9	430	63.2	15.13	11	218.8	28.80

TABLE 5.3 Heat Flow Data Analysis (In Co_2) for Ap = 1.0×10^{-7}.

(ii) N, To and ξ

The values of N appear to be consistent with the oxidational wear theory in that in general relatively few asperities are in contact between the sliding surfaces at any one time. It is noticeable that with an increase in oxide thickness there is a large decrease in N. Clearly, this would seem to suggest that the dimensions of asperity heights are of the order of microns and hence readily buried by a few microns increase in oxide thickness and thereby exposing fewer asperities.

The values of To appear to be low, for oxide thicknesses of 1 μm but markedly higher for $\xi = 5$ μm. The variation of To with load is evidently consistent since for all experiments, in general, a decrease in To is found with decreasing applied load. However, there appears to be no direct linear relationship between To and N. The variation of N with decreasing load and To show no direct trend. If To were wholly dependent upon the number of contacting asperitites a corresponding decrease would be found in the values of N with decreasing To. However, To must to some extent be dependent upon N since it is to a large extent the extent of intermetallic contact and asperity-asperity interaction that determines the heat generated at real areas of contact.

The thickness of the oxide at the interface, it would seem, is an important factor in the overall oxidation process. Additionally, since any change in ξ results in substantial changes in N and To it is also suggested that the oxide thickness significantly influences the micro-mechanical and micro-thermal processes at the interface.

(iii) Alternative Ap

It has been shown that the value of the activation energy, Qp, can be considerably changed by changing the value of ξ. However, to be realistic the value of ξ cannot be made larger than a few microns. Consequently, to find agreement with the experimentally derived Qp, an alternative parameter must be considered. The alternative parameter considered is Ap, the Arrhenius reaction-rate constant. It has been shown by numerous workers (primarily Quinn, Sullivan et al) that Ap is a greatly varying parameter and strongly dependent upon experimental conditions.

Table 5.4 illustrates the affect of using an alternative Ap. The data relates to the wear of the AISI 316 steels under conditions of 0.5 $m.s^{-1}$ sliding speed and an air environment.

It is evident from the table 5.4 that changing Ap also substantially changes Qp. By changing Ap to a value of 2.0×10^{-12} $kg^2.m^{-4}.s^{-1}$ from the original 1×10^{-7} $kg^2.m^{-4}.s^{-1}$ a large increase in Qp is found. It is interesting that using the alternative value for Ap significant changes in N and To are not found but remain consistent with the corresponding values for the original Ap.

(iv) In Conclusion

It appears to the author that while there are certain inconsistencies between predictions of the oxidational wear theory and the experimental results these are mainly due to the use of inappropriate oxidation constants. Firstly, it would appear that the Ap derived by Gulbransen and Andrew [38], from static oxidation experiments, is not directly applicable to the wear theory.

ε = 2.5 μm			
Load (Newtons)	N	To(^{o}C)	QP $(KJ.mole)^{-1}$
19.62	58	163.2	60.8
7.85	23	164.8	61.7
5.87	27	153.9	60.6
4.41	41	153.2	60.6

TABLE 5.4 Heat Flow Data Analysis (In Air) for Ap = 2.0×10^{-12}.

It is suggested that under 'dynamic' oxidation conditions, such as are produced during continuous-sliding oxidational wear, an Ap greatly different to the static-oxidation Ap describes the parabolic oxidation occurring at the interface.

Secondly, it is evidenced by X-ray diffraction that the surface oxide formed during sliding is not purely Cr_2O_3 but consists of numerous other phases of oxide e.g. Wustite and Spinels. Hence, to be strictly representative, oxidation parameters ko, f and ϱ_o must reflect in their values the contribution of these oxides to the oxide film. In the present work, of course, the values for pure Cr_2O_3 only have been used.

Finally, it is seen by examination of the wear topography and the wear debris that the mild wear process being discussed here is not purely oxidational but also consisting of delamination-wear mechanisms. Consequently, since the oxidational wear theory has been derived for strictly oxidational wear there must certainly be discrepancies due to the inhomogeneity of the wear process.

5.2.4 Application of the Oxidation Theory of Mild Wear to Wear at High Temperatures

It is difficult to foresee the effects of high ambient bulk temperatures upon the true theoretical division of heat, δ theor, the temperature at the real areas of contact and more importantly the heat flow parameters. Such uncertainties must of course arise as a result of the fact that the oxidation theory of mild wear is proposed in essence for conditions of wear occurring at ambient room temperature.

The careful examination of the heat flow theory ([43]) shows that certain assumptions implicit in the derivation of the theory may not be directly applicable to the wearing situation at high temperatures. It is assumed in the theory that the surface temperature, at the apparent area of contact, of the pin and disc is uniform and that, in addition, there is no temperature gradient across the pin. However, since the temperature of the environment around the pin and the disc cannot be considered to be comparable to the bulk temperature of the sliding members, a thermal gradient must exist and that also temperature uniformity cannot be fully achieved.

In addition, the cooling effect of the gas environment upon the sliding members in terms of heat loss per unit area at high temperatures must enevitably be much greater compared to the cooling effects at room temperatures. Consequently, the heat transfer coefficient (h) normally used in the heat flow calculations may therefore be inapplicable to the high temperature case. In general, it is considered, that heat flow parameters such as H, H_2, H_3, h, Q_a and Q_i may well be inaccurate in describing the heat flow conditions at high bulk temperatures.

In determining the theoretical division of heat at the interface at high bulk temperatures Tp and Td must become even greater abstract quantities since it is clear that at bulk temperatures of 500°C the ability of the pin and the disc to act as heat sinks for excess temperatures must be considerably reduced. In consequence, to achieve equality between the experimental division of heat δexpt. and δtheor unrealistic solutions in terms of

N, the number of contacting asperities, To, the temperature at the asperity contacts and ε_c, the critical oxide film thickness, may be obtained.

The effect of the high bulk temperatures upon mechanical phenomena such as the load bearing capacity at high temperatures, the ability of asperity-asperity adhesion, thermal conductivity and the flow pressures of the steels cannot be deduced straight forwardly by experiment and must therefore remain, to certain extents, as uncertain parameters. As a result, such uncertainties must inevitably introduce additional in-accuracies into the heat flow derivations.

In conclusion, it would seem that in order to be able to apply the oxidational theory of mild wear to a wearing situation, at high ambient temperatures, modifications may need to be made firstly, to the heat flow theory, in order to faithfully process the heat flow data, and secondly, as a result, to the oxidational theory. At a future date, it is thought, that with suitable modifications to the heat flow and oxidational wear theories, the heat flow data described in Chapter 4 will prove useful in describing more realistically the wear occurring at high ambient temperatures.

CHAPTER SIX

CONCLUSION

6. CONCLUSION

The experiments carried out in the present work investigate the oxidational and tribological behaviour of austenitic stainless steels under conditions of high temperatures and CO_2 - based environments.

Since the austenitic stainless steels are widely used by the CEGB as the major structural material for the fabrication of many mechanical components for use in the Advanced Gas cooled reactors, the importance of understanding the behaviour of such steels under AGR-type conditions is self evident. In respect to this, the present studies show that:

Oxidational Behaviour

1. An oxidation apparatus to simulate AGR environments (i.e. AGR temperatures and coolant-gas) is developed. The apparatus is subsequently used to oxidise austenitic stainless steel specimens. An accurate mixture of a CO_2-based AGR-type coolant gas is used. Flow-control is achieved by means of mass-flow controllers and flow rotameters. A very low flow-rate is used. The high temperatures are produced by baffle furnaces and temperature-monitoring and control is achieved by means of temperature regulators.

2. Characteristic differences between the general oxidational behaviour of the AISI 316 and AISI 310 steels and the AISI 321 steels are observed. While the former exhibit protective oxidation the latter steels are found to rapidly lose the protective oxide and subsequently develop a coarse and nodular replacement oxide. The occurrence of such behaviour is identified to be evoked by thermal cycling. However, after prolonged periods of oxidation the AISI 316 and AISI 310 steels are also observed to nucleate nodular oxide.

3. Oxidation kinetic determinations show the protective oxidation exhibited by the AISI 316 and AISI 310 steels to be in accordance with typical Wagnerian parabolic oxidation, while the oxidation of the AISI 321 steels is shown to be distinctly abnormal in nature, non-parabolic and in accordance with logarithmic oxidation kinetics. Determination of parabolic kinetics for the AISI 316 and 310 steels show the existence of a two staged parabolic oxidation process characterised by k_{p1} and k_{p2}, the respective Arrhenius reaction-rate constants. Corresponding reaction-rate activation energies, Q_{p1} and Q_{p2} are calculated and found to lie in the range -74.5 to 100.96 $KJ.Mole^{-1}$.

In general the parabolic laws:

$$(\frac{\Delta W}{A})^2 = k_{p1}.t \quad \text{and} \quad (\frac{\Delta W}{A})^2 = k_{p2}.t + c$$

define the AISI 316 and AISI 310 steel behaviour. The logarithmic law:

$$\log (\frac{\Delta W}{AC}) = a.t$$

defines the behaviour of the AISI 321 steels.

4. A very distinctive double layered character of the nodular oxide nucleating on AISI 321 steels is observed by metallographic examination. The outer layer is shown to be above surface, nodular and porous in morphology, while the inner layer is found to be totally below surface and deeply penetrating the subsurface alloy via the grain boundaries.

5. Elemental analysis of the protective oxide and the nodular double-layered oxide (duplex oxide) are shown to be chromium and iron rich respectively. While the protective oxide is found to be predominantly of the structural form, Cr_2O_3, the nodular duplex oxides are shown to be much more complicated in composition, consisting of a Fe_2O_3 - type upper layer and a complex spinel-oxide lower layer. Electron-robe micro analysis of typical cross sections of duplex oxide

nodules are shown to exbibit a characteristic Fe-rich upper layer and a prominently Cr-rich lower layer.

6. Variation in the elemental composition of the inner and outer layers of the duplex oxides with increasing oxidation is observed. It is shown that the outer layer is Fe and Mn abundant and Cr and Ni deficient ($< 2\%$) but with increasing time of oxidation becomes progressively diluted in Fe. The inner oxide is shown to be Cr and Ni abundant with a fairly high content of Fe ($\sim 20\%$) but that the latter rapidly diminishes to $< 2\%$ with increasing oxidation.

7. Elemental concentration profiles taken with the Electron Probe micro-analyser show the development of Cr depletion zones immediately below the alloy-oxide interface. Such depletion zones are not so distinctly observed for any other major oxidising element. The depletion zone is shown to increase in depth with increasing time of oxidation upto 23 μm after 3500 Hrs. Cr depletion levels to 5% within the depleted zone are observed as a consequence of such behaviour.

8. Two oxidation models are developed to further understand the oxidational behaviour. The first, an electronic model, is developed on the basis of electronic, cationic and anionic transport mechanisms. It is shown by such a model that the chemical structure of the Cr-rich inner spinel-oxide layer is of the form:

$$(Fe^{3+}_{2-x}\ Cr^{3+}_{x}\ Fe^{2+})\ O^{2-}_{4}$$

but that due to inter-solution of oxides, the structure is more likely to be a mixture of the oxide phases

$$(Fe^{3+}_{2-x}\ Cr^{3+}_{x}\ Fe^{2+})\ O^{2-}_{4} \quad \text{and} \quad (Fe^{3+}_{1-x}\ Cr^{3+}_{x})_2 O^{2-}_{3}$$

The outer oxide is predicted to be of a P-type Fe_2O_3 oxide.

The second model, developed on the basis of Fick's laws of diffusion, shows that the concentrations C_s and C_B (at the interface and within the bulk alloy respectively) are given by the relation:

$$C_S = \frac{-\gamma 1 Mt}{D_1} + C_B$$

From this, Mt, the amount of oxidising element diffusing at any instant from the alloy-oxide interface, is shown to be less than C_S, i.e.

$$Mt < C_S$$

Tribological Behaviour

1. Differences in the sliding wear behaviour of the AISI 316 steels and the AISI 310 steels are shown. The AISI 316 steels are shown to exhibit transitional load-dependent wear behaviour, where above a critical load severe wear is found to predominate and mild wear for loads below the critical load. The AISI 310 steels are observed to exhibit non-transitional load-dependent wear, for all conditions, where only the severe wear mode is encountered.

2. In general, the mild wear rates of the AISI 316 steels are found to lie within the narrow range $3.5 \times 10^{-7} mm^3.mm^{-1}$ to $4.0 \times 10^{-6} mm^3.mm^{-1}$, whereas, however, the severe wear rates, for all steels, are observed to occur over a very much wider range covering five orders of magnitude i.e. 5×10^{-7} to $1 \times 10^{-3} mm^3.mm^{-1}$ for the AISI 310 steels and 3.5×10^{-7} to $1 \times 10^{-3} mm^3.mm^{-1}$ for the AISI 316 steels. In all cases, for the severe wear regions, sharply rising wear patterns are observed.

3. Under Co_2 environments lower wear rates are observed for all steels, in comparison to the relatively higher wear rates found under air environments. The effect of environment is found to produce changes in wear rates of approximately 1/2 an order of magnitude. Changes in the overall transitional wear pattern of the AISI 316 steels is, however,

not observed. Similarly, a transitional wear behaviour for the AISI 310 steels is not obtained.

4. The effect of a change in sliding speed is observed to be ineffective in changing the overall general wear pattern of the steels. However, by reducing the sliding speed it is shown that lower wear rates, in general, are found and that the critical load is displaced to higher loads, i.e. from 0.9 kgm at 2.0 ms^{-1} to 2.0kgm at 0.5ms^{-1}, under Co_2. Under air, however, the position of the critical load is unchanged. A reduction of over one order of magnitude in wear rates is observed for severe wear as a consequence of reducing the sliding velocity.

5. The wear behaviour of the AISI 316 steels at high ambient temperatures i.e. 300°c and 500°c is observed to exhibit the typical transitional and load-dependent wear pattern. Mild wear and severe wear modes are again observed. The wear rates encountered are found to be similar in magnitude to those observed at room temperature, i.e. $\sim 1 \times 10^{-7}$ to $3.5 \times 10^{-7} mm^3.mm^{-1}$ for mild wear and $\sim 3.5 \times 10^{-7}$ to $3 \times 10^{-4} mm^3.mm^{-1}$ for severe wear.

6. The friction behaviour for the AISI 316 steels is shown to be transitional in character about a critical load. For loads above the critical load, $W_{IL} \geqslant W_T$, a load independent friction region is observed, and for loads below the crtical load, $W_{LD} \leqslant W_T$, a wholly load dependent region is encountered. The critical load region, i.e. $W_{LD} \geqslant W_r \leqslant W_{IL}$, is observed to form a third friction region i.e. the transition region. The critical load is shown to vary within the range 2.2 kgm to 4.0kgm.

7. In general, the friction behaviour at the load independent region is observed to be independent of sliding speed. For light loads in the load dependent region, however, a reduction in sliding speed is shown to produce higher friction coefficients.

8. For the region, $W_{II} \geqslant W_T$, typical friction coefficients in the range 0.55 to 0.70 are found. For the region, $W_{LD} \leqslant W_T$, however, a wide range of friction coefficients are observed between the values 0.7 (for $W_{LD} = W_T$) to 1.9 (for $W_{LD} < 0.3$kgm).

9. In the region above the critical load, i.e. the load independent region, it is observed that Amonton's law is not obeyed; the behaviour in this region is described by the relation:

$$\mu \text{ (for } W_{II} \geqslant W_T) = k(\text{const})$$

Within the load dependent region, however, it is shown that the friction behaviour is well defined by Amonton's law i.e.:

$$\mu \text{ (for } W_{LD} \leqslant W_T) = F/W + C$$

10. Two forms of wear debris are identified: (1) Oxidised wear debris and (2) Unoxidised metallic debris. The former type is observed to be associated exclusively with mild wear and in consequence is found only for the wear of the AISI 316 steels. The latter type is associated with severe wear although it is also found within mild wear debris.

11. By X-ray diffraction analysis of the wear debris the major constituent of the metallic debris is found to be austenite. Mild wear debris, however, is found to consist of a mixture of 4 major oxide groups: (1) Rhombohedral (2) Cubic (3) Spinel and (4) Wustite. The specific oxide species found are Cr_2O_3, α-Fe_2O_3, and $(Cr,Fe)_2O_3$ [Rhombohedral], γ-Fe_2O_3 [Cubic], Fe_3O_4 and Cr_3O_4 [Spinel] and FeO [Wustite].

12. Examination of wear-surface topographies from the mild wear region, by Scanning electron microscopy, show the prevalance of four major wear mechanisms: (1) Hollowing (2) Shearing (3) Parallel-plate dislocation and (4) Oxide formation.

Topographies formed under severe wear conditions, however, show exclusively the occurrence of gross plastic flow, plastic deform-

ation and severe adhesive wear.

13. It is shown by comparison of Archard's k-factors, that the wear occurring above the wear transition load is similar in nature to that occurring under all conditions for the AISI 310 steels. Similarly, by determination of the k-factor it is shown that the wear occurring under mild wear conditions is not typical adhesive wear. The k-factor values for wear above the transition load are shown to lie within the range 0.0110 to 0.182, while for wear under mild wear conditions a greatly diverse range of values are found, i.e. 0.001 to 0.571.

14. A contact mechanical model is proposed, developed on the basis of Contact Mechanics, to understand the observed shearing and plate-dislocation wear mechanisms, by virtue of sub-surface crack propagation. The contact load stress components σ_z, σ_r, σ_θ and τ_{max} are determined for loads of 0.75kgm, 10.0kgm, and 15.0kgm.

$$\sigma_z = q\left[-1 + \frac{z^3}{(a^2+z^2)^{\frac{3}{2}}}\right]$$

$$\sigma_r = \frac{P}{2\pi}\left\{(1-2\nu)\left[\frac{1}{r^2} - \frac{z}{r^2}(r^2+z^2)^{\frac{-1}{2}}\right] - 3r_z^2\,(r^2+z^2)^{\frac{-3}{2}}\right\}$$

$$\sigma_\theta = \frac{P}{2\pi}(1-2\nu)\left\{\frac{1}{r^2} + \frac{z}{r^2}(r^2+z^2)^{\frac{-1}{2}} + z(r^2+z^2)^{\frac{-3}{2}}\right\}$$

and $$\tau_{max} = \frac{q}{2}\left[\frac{1-2\nu}{2} + \frac{2}{q}(1+\nu)\sqrt{2(1+\nu)}\right]$$

The stresses, in general, within the range 10^5 - 10^6, for the loads considered, are found.

15. The oxidational theory of mild wear is used to predict surface contact parameters, Vi3, N, the number of contacting asparities, E, thickness of surface oxides and To, the temperature at the real areas of contact.

For E = 1 μm and 5 μm, values of N in the order of 200 - 500 are found and surface temperatures, To, in the range 60°C - 100°C.

However, the theory is found to predict much lower values for Qp, i.e. $Qp = 30KJ.mole^{-1}$, than is observed by experiments. By the use of an alternative value for Ap, the Arrhenius reaction rate constant, i.e. $Ap = 2.0 \times 10^{-12}\ kg^{2}.m^{-4}.s^{-1}$, much higher values of Qp are predicted.

BIBLIOGRAPHY

BIBLIOGRAPHY

(1) Burwell,J.T., 1957, Wear, Vol., 1.

(2) Wright, K. H. R., 1969, Wear, Vol., 3.

(3) Archard,J.F., 1953, J.Appl.Phys, 24.

(4) Bowden,F.P., Tabor,D., 1950, Friction and Lubrication of Solids, Oxford Univ.Press.

(5) Burwell,J.T., Strang,C.D., 1952, Proc.Roy.Sco., 212.

(6) Archard,J.F., Hirst,W., 1956, Proc.Roy.Soc., Vol.236, 397.

(7) Quinn,T.F.J., 1978, Proc.Int.Conf. on Fundamentals of Trib., Massachusetts.

(8) Quinn,T.F.J., Sullivan,J.L., Rowson,D.M., 1979, Personel Communication.

(9) Gordelier,S.C., Skinner,J., 1975, CEGB Report.

(10) Greenwood,J.A., 1967, J.Lubr.Technol., 9.

(11) Hertz,H., 1882, Jl.fuer Mathematik Von Crelle, 92, 156-171.

(12) Courtney-Pratt,J.S., Eisner,E., 1957, Proc.Roy.Soc., A238,529.

(13) Rabinowicz,E., 1965, Friction and Wear of Materials, Wiley, New York.

(14) Dokos,S.J., 1946, J.Appl.Mechanics, 13A, 148.

(15) Archard.J.F., 1961, J.Appl.Phys., Vol.12, 1420.

(16) Quinn,T.F.J., 1971, Wear, 18, 413.

(17) Suh,N.P., Jahanmir,S., Abrahamson,E.P., Turner,A.P.L., 1974, J.Lubr.Techn., 96.

(18) Engel,P.A., 1978, Impact Wear of Materials, New York.

(19) Chivers,T.C., Gordelier,S.C., Roy,J.,Wharton,M.

(20) Levy,G., 1979," Patterns of Tribology ", 4th. Int. Trib. Conf.

(21) Best,J.V., Wickham,A.J., Wood,C.J., 1974, Proc, Fourth London Int. Carbon and Graphite Conf.

(22) Wood,C.J., 1976, CEGB Research.

(23) Cocks,A.T., Mathews,J.F., Surman,P.L., 1977, Proc. Sixth European Corrosion Congress; Soc. Chemical Industry, 113.

(24) Cocks,A.T., Surman,P.L., 1978, CEGB Research, 6.

(25) Goodison,D., Norton,J.F., Wall,P.M., 1972, BNDC Interim Report, BNDC/R.511, RDC/CM/P(72)51.

(26) Rowlands,P.C., Whitlow,W.H., Wootton,M.R., 1972, RD/B/R2445, RPC/CM/P(72)83.

(27) Norton,J.F., Wall,P.M., Williams,W.M., 1973, BNDC Report, BNDC/R.569, RPC/CM/P(73)61.

(28) Norton,J.F., 1976, NPC Report, NPC/R.69(Nuclear Power Company).

(29) Allan,S.J., 1975, BNDC Report, BNDC/R.709, RPC/CM/P(75)19.

(30) Stevens,P.A., 1974, BNDC Report, TN/605.

(31) Smith,G.H.S., April 1974, BNDC Internal Memo to J.D.Cooksey.

(32) Smith,G.H.S., May 1974, BNDC Internal Memo.

(33) GEC/REL. Report No. REL/R(72)91, "Hartlepool Hot Box Re-entrant Gas Seal Tests".

(34) Wild Barfield, 1970, Technical Information Sheet for Tubular Furnaces and Temperature Monitoring Equipment.

(35) Wagner,C., 1951, Seminar on Atom Movements, Amer.Soc. of Metals, Cleveland.

(36) Kubaschewski,O., Hopkins,B.E., 1962, "Oxidation of Metals and Alloys", Butterworths.

(37) Dunn,J.S., 1926, Proc.Roy.Soc., 111, 203.

(38) Gulbransen,E.A., Andrews,K.F., 1962, J.Elect.Chem.Soc., 104, 334.

(39) Goodison,D., Norton,J.F., Wall, P.M., 1972, BNDC/R.511 (BNDC Report).

(40) Fujii,C., Meussner,R.,1963, J. Electrochem. Soc., 110.

(41) Greaves,R.H., Wrighton,H., 1950, Practical Microscopical Metallography, Chapman and Hall, London.

(42) Dunckley,P.M., Quinn,T.F.J., 1978, Proc.Inst.Mech.Engs.

(43) Coy,R.C., 1971, MSc Thesis, University of Aston in Birmingham.

(44) Dunckley,P.M., 1977, PhD Thesis, University of Aston in Birmingham.

(45) Culliby,B.D., 1956, Elements of X-Ray Diffraction, University of Notre Dame.

(46) Isherwood,B., Quinn,T.F.J., 1967, Brit. J. Appl. Phys.

(47) Quinn,T.F.J., 1968, Proc.Inst. Mech. Egnrs., 182, 3N.,201.

(48) Caplan,D., Cohen,M., 1966, Corr. Sci., Vol.6, 321.

(49) Stott,F.H., Lin,D.S., Wood,G.C., 1973, Corr. Sci., Vol.13,449.

(50) Buckley,D.H., Johnson,R.L., 1960, ASLE. Trans., 3,93.

(51) Rowlands,P.C., Whitlow,W.H., Wootton,M.R., 1972 CEGB Report, RPC/CM/P(72)83.

(52) Vernon,W.H.J., Wormwell,F., Nurse,T.J., 1944, J. of Iron. Steel. Inst., 150.

(53) Evans,U.R., 1961, The Corrosion and Oxidation of Metals, Edward Arnold, London.

(54) Hill,A.C., Hales,R., 1974, CEGB Report.

(55) Boggs,W.E., Kachik,R.H., Pellissier,G.E., 1965, J.Electrochem Soc., 112, 539.

(56) Hussey,R.J., Cohen,M., 1971, Corr. Sci., 11, 699.

(57) Rose,D., 1973, Unpublished CEGB Work.

(58) Bodsworth,C.,"Phys.Chem.of Iron & Steel Manufact", Longmans.

(59) Lake,E., 1948," Comp & Ht Treat of Steels", McGraw Hill.

(60) Angel,T., 1954, J.Iron and Steel Inst., 177, 165.

(61) Yamaguchi,S., 1956, Z.Metallunde, 47, 95.

(62) Fisher,S.B., Swallow,G.A., Hooper,A.J., 1973, Unpublished work.

(63) Cine,B., 1954, J.Iron and Steel Inst., 177, 406.

(64) Hoar,T.P., Price,L.E., 1938, Trans.Faraday Soc, 34, 867.

(65) Jost,W., 1952, Diffusion in Solids, Liquids and Gases, New York.

(66) Wyckoff,R.W.G., 1951, Crystal Structures, Interscience, New York.

(67) Holm,R., 1967, Electrical Contacts, New York.

(68) Archard,J.F., 1959, New Scientist, 5, 1299.

(69) Suh,N.P., 1973, Wear 25, 111-124.

(70) Timoshenko,S., Goodier,J.N., 1969, Theory of Elasticity, McGraw Hill, New York.

(71) Seely,F.B., Smith,J.O., 1952, Advanced Mechanics of Materials, Wiley, New York.

(72) Hamilton,G. M., Goodman,L.E., 1966, J.Appl. Mech, 33.

(73) Lipson,C., Colwell,L.V., Handbook of Mechanical Wear, Ann A bor, Univ. Michigan Press.

(74) Blok,H., 1955, Appl. Scientific Research, Sect.A, 5.

(75) Smith and Lin, 1952, A.S.M.E. Paper No.52-A-13.

(76) Quinn,T.F.J., Sullivan,J.L., 1977, Proc.ASME Conf. on Wear of Materials, 110.

(77) Quinn,T.F.J., Sullivan,J.L., Rowson,D.M., 1979.

APPENDIX REFERENCES

(1) Heath,H.H., Philips,K.F., 1962, Proc. Inst. Mech. Engrs. Meeting on Non-Conventional Lubricants.

(2) Houghton,J.E., Mitchell,L.A., 1968, Inst. Mech. Engrs. Proc., 183, Dart 31.

(3) Savage,R.H., 1948, J.Appl. Phys, 19.

(4) Deacon,R.F., Goodman,H.F., 1964, Proc. Roy. Soc., 243.

(5) Lancaster,J.K., 1963, Lubrication and Wear Conv., Proc. Inst. Mech. Engrs.

(6) Levy,G., 1979, Patterns of Tribology, 4th. Inst. Tribology Conf. Paisley.

(7) Midgley,J.W., Tear,D G., 1963, Trans.ASME.J.Baric Engg., 85, 488.

(8) Allan,S.J., Norton,J.F., Popple,L.A., 1974, Proc.Int.Conf. on Corr. of Steels in Co_2, British Nuclear Energy Soc.

(9) Garrett,J.C.P., Lister,S.K., Nolan,P.J., Crook,J.T., 1974, Proc.Int,Conf. On Corr. of Steels in Co_2, B.Nuc.Energy Soc.

(10) Gordelier,S.C., Skinner,J., 1979, Int.Conf. on Wear of Materials, ASME.

APPENDIX

1. INTRODUCTION

Most of the components of the AGR internals are fabricated from austenitic stainless steel, employed because of its high temperature strength, oxidation resistance and relatively low cost. A large number of these components are subject to functional, thermal or vibratory movement, and unfortunately the tribology of austenitic stainless steel is not always satisfactory in the carbon-dioxide based environment of an AGR coolant. Much attention has therefore been given to finding suitable bearing materials to employ at moving interfaces (e.g. [1] and [2]). In these bearing materials studies, graphite was consistently found to be tribologically benevolent, and as such it has been widely employed as a bearing partner for stainless steel.

The behaviour of graphite was not unexpected, the tribology of graphite having been the subject of much work (e.g. [3], [4], [5] and [6]). However, full scale tests of components and oxidation studies of stainless steels showed that a problem could arise that resulted in high graphite wear. Some austenitic materials were found to grow a different oxide from that conventionally expected ([7], [8] and [9(10)]) and this could appear in a variety of morphologies, some of which were extremely nodular on a microscopic scale, as shown in the scanning electron micrographs of figure (A1). Oxides of this nodular form were found to wear graphite mating surfaces abrasively, with resultant wear rates orders of magnitude larger than expected in normal sliding wear. A series of studies on the abrasive wear of graphite was therefore initiated.

2. BACKGROUND

2.1 The Effect of Gas Flow on Debris Clearance

A series of experiments carried out by Gordelier and Skinner on the abrasive wear of graphite showed the excessively high wear of graphite obtainable by rough counterbearing surfaces. The following describes in brief some of their experiments and results.

The production of oxidised stainless steel specimens with the correct nodular morphology was difficult and time consuming, because neither the nature nor morphology of the resultant oxide could be guaranteed in advance. Much of the work on abrasive wear was therefore conducted with the 'artificial' abrasive surfaces of aluminium oxide paper (Al_2O_3), silicon carbide paper (SiC) and grit and bead blasted stainless steels.

In the initial experiments flat ended graphite pins of 10mm diameter were repeatedly traversed with a stroke length of 270mm across an aluminium oxide abrasive paper. It was found that the initial wear rate was high ($10^{-4}mm^3/Nmm$) but rapidly reduced with the number of traversals as graphite debris clogged the abrasive surface. Figure (A2) shows some of these results, which have been discussed more fully elsewhere by Gordelier and Skinner [9].

In the component tests the wear rate did not appear to decrease in this fashion, remaining at around $10^{-4}mm^3/Nmm$, and neither was there any evidence of graphite transfer and abrasive surface clogging. The components examined in these prototype tests were mainly seals across which there was a pressure difference of $240kN/m^2$ and it was postulated that an interface gas flow driven by this pressure difference could prevent saturation of the abra-

sive; subsequent experiments confirmed this postulate. In these experiments a flow of gas, either nitrogen or carbon-dioxide, was introduced down a central hole in a graphite pin of 12mm diameter. The flat end of this pin was reciprocated with a stroke length of 10mm against a variety of abrasive surfaces, and the results of these experiments are shown in figure (A3). It can be seen that a relatively small pressure difference across the wearing interface was sufficient to prevent graphite transfer and maintain the wear rate at the high levels associated with 'fresh' abrasive. Again these results have been discussed more fully elsewhere [9].

2.2 Large Amplitude Abrasive Wear

Within the reactor system a number of components either function as seals with a deliberately imposed pressure difference across them, or operate in regions of high dynamic head where a pressure difference could result from the gas flow in which they are immersed. The effect of a gas flow, as illustrated in figure (A3), was therefore of real practical significance as it could result in maintaining a fully abrasive wear regime. The rate of material removal resulting from continued abrasive wear was obviously of practical concern, and a theoretical analysis was developed for the large amplitude wear. This was based an on idealised abrasive surface of uniformly sized hemispherical oxide nodules, randomly dispersed on a surface with an initially Gaussian height distribution. The details of this analysis are available in earlier published work [10] and the results for a typical practical situation are shown in figure (A4). Here the logarithm of the specific wear rate is plotted against the radius of the growing

oxide nodules for a range of contact and surface feature parameters; 'n' is the number density of the nodules, σ the standard deviation of the initial surface roughness, P/H the ratio of the interface pressure to the hardness of graphite, and ψ a factor representing the ratio of the volume of material completely removed by an abrading nodule to the total volume of material displaced by the nodule. From the results in figure (A4) it can be seen that the wear climbs very rapidly and typically has already risen by three orders of magnitude from the normally expected level of around $10^{-8} mm^3/Nmm$ when the excrescences have grown to a size of only a few microns. The peak abrasive wear rate is some five orders of magnitude larger than this value.

3. WEAR AT LOW SLIP AMPLITUDES

3.1 General

The analysis discussed above was adequate to deal with the large amplitude movements seen by components as part of their design function or due to large thermal displacements induced by reactor start up and shut down. However, the coolant flow rates in gas cooled reactors are necessarily very large, a typical value for a full core flow being 3,700 kg/s. In the reactor, flows of this magnitude can induce vibrations of the components either directly from flow excitation, or from the transmitted noise generated by the large gas circulators. A number of components were therefore likely to be subjected to a continuous small amplitude movement from vibration in addition to the occasional large amplitude movements. While the amplitude of such movements is small their frequencey of occurence is high, typically some tens of Hertz. The integrated

sliding distance can therefore be very large and can be considerably in excess of that expected from the total large amplitude sliding.

Many components could tolerate wear rates as large as those shown in figure (A4) for the occasional large amplitude movement, but their lives would be exceedingly short if the high wear rates persisted during the small amplitude vibratory movement. This could happen when an interface gas flow was effective in removing the debris during the wear process. If a simplified model such as shown in figure (A5) is considered, then it seems possible that this need not be the case as the wear may be a strong function of amplitude. When the amplitude of movement is less than the typical inter-nodule linear spacing, the wear groove from each nodule will not interact with that of its neighbour. After a very brief initial period of high wear, the nodules cut themselves cavities and the load is taken by the surrounding flatter surface areas. If the remaining area of surface abraded is sufficient to support the load then the wear process should rapidly change from abrasive wear on the nodules to a much slower adhesive wear on the base surface between the nodules. However, if the amplitude of movement is increased the cavities produced by the nodules will begin to interact and the wear process should revert to the higher abrasive mode.

3.2 Experiment

A series of experiments were begun to check this hypothesis that the wear at low slip would be strongly amplitude-dependent. Due to the length of time and difficulty involved in their production, there was a shortage of specimens showing the nodular oxide. The first experiments were therefore conducted using plasma sprayed corumdum (Al_2O_3) as the abrasive surface.

In these experiments flat ended graphite pins of 5.8mm diameter were reciprocated at small amplitudes, and at 50 Hz against flat ended plasma sprayed pins of 7.6mm diameter, with central holes of 1mm diameter. The flat faces were dead weight loaded together by a lever arm and the drive was provided by a large vibrator. Specimen were run two pairs at a time to balance the loading on the vibrator, as shown in the schematic diagram of figure (A6), giving two data points for each experiment. Within the limits of the drive the amplitude was infinitely variable and was measured with a capacitive transducer mounted very close to the specimen position, to minimise possible errors from lost movement in the apparatus.

In a second series of experiments the same apparatus was used with the smaller specimens being pre-oxidised AISI 321 stainless steel showing nodular oxide morphology, and the larger specimens being graphite again with a central hole. In both series the graphite used was a nuclear grade, Gilsocarbon moderator B, manufactured by Morganite Ltd. As in the previous experiments [9,10] with larger amplitude sliding a gas flow was injected down the central hole of one of the specimens in each matching pair to provide an interface gas flow and scour the debris from the wear process. The gases employed were again nitrogen and carbon dioxide.

The results of the first series of experiments, using plasma sprayed corundum as the abrasive surface, are shown in figure (A7). The load employed for all specimens was 2 kg, giving an interface pressure of 0.75 N/mm^2, and the total sliding distance varied from 25m to 686m, as shown on the figure. The interface gas flow was maintained at all times to ensure that the abrasive surface would not become clogged with debris which would reduce its abrasiveness.

From the results shown in figure (A7) it is apparent that a fairly sharp transition of some two orders of magnitude in specific wear rate occurs at an amplitude (half peak to peak displacement) of some 500 μm. While the specimens in the high and low wear groups had experienced widely different total sliding distances, both groups contained long and short endurance data points. The transition was not therefore associated with a 'running in' phenomena, the specific wear rate being approximately independent of total sliding distance within either group.

The graphite surfaces were examined after the experiments and they showed a very grooved appearance in the direction of motion, as would be expected from wear against a rough surface. Typical examples from a large and a small amplitude experiment are shown in figure (A8). It is interesting that the grooves for the larger amplitude specimen appear to be continuous over considerable distances in the photograph, the ridge features look sharp and the larger graphite porosity can be clearly seen as dark patches. In contrast a distinct length of groove feature can be identified in the specimen for the smaller amplitude experiment, and this corresponds to the 300 μm peak to peak slip distance. The surface is also generally more 'smudged' in appearance and evidence of any porosity present has been obliterated, indicating a wear process which is much less abrasive.

In this first series of experiments therefore, the features of the worn graphite surface and the results for wear rate as a function of displacement both confirm that in the present of a gas flow an amplitude effect does exist in abrasive wear at low slide magnitudes.

In the second group of experiments, using preoxidised stainless steel against graphite, the specimens were loaded with 2kg or 5kg, giving interface pressures of 0.75N/mm^2 and 1.89N/mm^2 respectively, and the total sliding distance varied between 795m and 10,000m. The results are shown in figure (A9) and extend up to amplitudes approaching 1000μm. The results strongly suggest that a transition is occuring at about this amplitude, but the experimental facility was not capable of producing larger amplitudes and the trend could not be followed further. Both series of experiments therefore indicate that an effect of amplitude on wear is occuring.

3.3 Theory

The experimental evidence shows that gas flow can lead to high graphite wear rates, but that below a critical amplitude more conventional material removal rates are observed. The transition is dependent on morphology, which is very variable, and hence to assess the implications and the boundaries of the wear regimes in service a theoretical model is necessary.

To develop this model, consider the schematic diagram in figure (A10), which shows an array of uniformly sized hemispherical nodules randomly dispersed on a flat surface. Depending on the amplitude of the movement the wear track from nodule 1 will interact with those from nodule 2, 3, etc. It can be seen that if the removed surface area, which is associated directly with a given nodule, can be found, then the load bearing capacity of the remaining surface can be evaluated. If this bearing capacity is sufficient to support the imposed load the nodules will merely cut themselves grooves until they no longer abrade the graphite surface. The wear rate will then revert to a much lower rate of removal as

the graphite slides against the smooth hinterlands. When the hinterlands can no longer support the load they will collapse and wear will proceed abrasively. In figure (A10) the area removed associated directly with nodule 1 is shown shaded. If the average of all such areas has a value A, then the amount removed per unit area is nA, where n is the number of excrescences per unit area. The area left to support the load is then (1-nA) per unit area.

The philosophy of this calculation is simple, but in practice the exercise becomes rapidly complicated unless further simplifying assumptions are introduced. The approximation whereby all excrescences whose centres fall within $\pm$ R of the locus of the centre of the nodule of interest (bb for nodule 1 in fig.(A10)) are considered to have centres <u>on</u> the line, and all excrescences whose centres fall within $12RI \geqslant ly \geqslant IRI$ are ignored enables the calculation to proceed relatively simply. This assumption means that, of the population of nearest neighbours, the half that have the most influence are given an artificially increased status and the half that have the least influence are completely ignored. By this device the problem becomes much more tractable, and a quantitative feel for the amplitude below which severe abrasive wear occurs can still be obtained.

(i) <u>Surface Area Removed Per Nodule</u>

Consider now the rows of in line hemispherical nodules shown in figure (A11). In figure (A11a), a single excrescence forms a wear groove in the opposing surface which is being slid through a peak to peak distance of 'a'. The area removed from the abraded surface is obviously $2Ra + \pi R^2$. In b) of this figure, two neighbouring nodules are shown separated by d_1, where d_1 is less

than 'a'. The surface area removed is $2R(a + d_1) + \pi R^2$ in this case. Similarly in c) of the diagram a row of nodules is shown and it can be seen that in general, for a number of excrescences in a row, the surface area removed is given by:

$$\text{total area removed} = 2R(a + d_1 + d_2 + d_3 + \ldots + d_t) + \pi R^2$$

for t excrescences in a row with $d < a$.

The area removed by each excrescence is thus:

$$\text{Individual area removed} = 2Rd \text{ when } d < a$$
$$\text{Individual area removed} = 2Ra + \pi R^2 \text{ when } d > a \qquad [1]$$

With this result it is possible to calculate the average area, A removed per nodule, if the distribution of nearest neighbour distances can be found.

(ii) Nearest Neighbour Distance Probability Density Function

If we consider the position of nodules to be defined by their centres, and these centres are randomly distributed over a surface, then it is reasonable to assume that the numbers of centres that occur per unit area are distributed with a probability defined by the Poisson distribution. That is, the terms of the series

$$e^{-n}\left(1 + n + \frac{n^2}{2!} + \frac{n^3}{3!} + \frac{n^4}{4!} + \frac{n^5}{5!} + \ldots.\right) \qquad [2]$$

represent in turn p(0), p(1), p(2), p(3), etc., where p.(0), p(1) etc., are the probability of no nodules in a unit area, one nodule in a unit area, and so on, and n is the average number per unit area. The result still holds as n increases provided we allow nodules to overlap. If we now consider a specific nodule, as in figure (A12), then if p(0) is the probability of no nodules occurring in unit area, the probability of no nodules occuring up to the point x in a band

of width 2R, is given by:

$$P_x(0) = (p(0))^{2Rx}$$

In the next element of length δx the average number that would be expected to occur is $2Rn\ \delta x$. Thus the average number of first neighbours that would be expected at a distance between x and $x + \delta x$ is given by the product of these two terms, namely,

$$\delta N(x, x + \delta x) = (p(0))^{2Rx}\ 2Rn\ \delta x$$

Hence, the probability density function for the distance to the nearest neighbour in this bandwidth of 2R is given by:

$$\frac{dN(x, x + \delta x)}{dx} = 2Rn\ (p(0))^{2Rx} = s(x)$$

where s (x) is defined as this probability density function. The value of p(0) is given by the first term of the series defining the Poisson distribution, equation [2], and hence:

$$p(0) = e^{-n}$$

Thus

$$s(x) = 2Rne^{-2Rnx} \qquad [3]$$

The probability density function for the nearest neighbour distance in a band of width 2R thus decays away exponentially.

Note that $\int_0^\infty s(x)dx = \int_0^\infty 2Rne^{-2Rnx}\ dx = 1$

as would be expected; i.e. the probability of a nearest neighbour lying at a distance between zero and infinity is 1.

(iii) Load Bearing Area Removed.

Given the probability density function, equation [3], derived in the previous section, it is then possible to calculate the total surface area removed per unit area, when the peak to peak amplitude of reciprocation is 'a'. Recalling the result for the area

removed by an individual nodule, given at [1], then the total area removed per unit area is given by:

$$nA = 4R^2n^2 \left\{ \int_0^a xe^{-2Rnx}\,dx + a\int_a^\infty e^{-2Rnx}\,dx \right\} + n\pi R^2 \int_a^\infty 2Rne^{-2Rnx}dx$$

The last term accounts for the area which is removed by the bases of nodules where $d > a$. It is only when 'a' is finite that this term should be included, because when 'a' is zero the graphite surface is in intimate contact with the hemispherical surfaces of the nodules, and the projected area of this contact (i.e. their base areas) is obviously available to support load.

Hence, by integrating the above equation:

$$nA = 1 - e^{-2Rna}(1 - \pi R^2 n), \quad (a > 0)$$

Now nA is the fractional area removed, and thus that fractional area remaining to support load is given by:

$$(1 - nA) = e^{-2Rna}(1 - \pi R^2 n), \quad (a > 0) \qquad [4]$$

When 'a' = 0 the term in $\pi R^2 n$ does not appear, for the reasons discussed above. Hence, the function shown in equation [4] behaves as expected, being unity at an 'a' value of zero, and decaying to zero as 'a' approaches infinity.

(iv) Amplitude Criterion for Low Wear

The result at [4] above defines that area that is left to support the load, and it remains to be decided how much load this area can support. The regions that remain unabraded have a geometry such that some constraint on their deformation is provided by the increasing area of material beneath them, much as in the case for normal surface asperities under compression. However, to employ the hardness of the material as a measure of its strength seems unduly optimistic in this case, because the geometry is not as favourable as that of surface asperities. In practice the strength of the

material remaining should be closer to its compressive yield strength, although this should be a lower bound. The compressive yield strength is therefore used to derive the condition that the area remaining cannot support the load, and this should thus provide a slight underestimate of the amplitude at which this condition occurs. Hence, from the result at [4]:

$$\text{Load supporting capacity/unit area} = Y_c e^{-2Rna}(1 - \pi R^2 n) \qquad [5]$$

where Y_c is the compressive yield strength.

The surface will be capable of supporting the load provided that the averaged interface pressure, P, is not greater than this load supporting capacity, i.e.

$$Y_c e^{-2Rna} (1 - \pi R^2 n) \geqslant P \qquad [6]$$

When this inequality does not hold the 'support' area left begins to collapse and the abrasive wear regime begins to remove material at a much higher rate. Hence, by taking logarithms of [6], the condition that the wear remains low is given by:

$$\ln(1 - f) - \ln \frac{P}{Y_c} \geqslant 2Rna \qquad [7]$$

where f is the value of $n \pi R^2$; when the number of excrescences is small (i.e. there are few overlaps) f is approximately the fraction of the surface covered with oxide.

Hence:
$$\frac{a}{R} \leqslant \frac{\pi}{2f} \left(\ln(1 - f) - \ln \frac{P}{Y_c}\right) \qquad [8]$$

The results of this analysis are shown in figures (A13) and (A14) and are discussed in the following section.

4. DISCUSSION

From earlier work [9, 10] it was apparent that the abrasive wear of graphitic material could continue at a high level if an interface gas flow across the wearing specimens was effective in

removing the wear debris. The mechanism by which this flow was effective was to prevent the physical burying of the abrasive features of the opposing surface by a transferred layer of graphite. This previous work had been conducted at moderately large sliding amplitudes (10mm); the present work shows that the effect of gas flow still continues at much smaller amplitudes. The results show that the effect was clearly present at amplitudes of only a few hundred microns, because the higher wear rates, reaching approximately $10^{-4}mm^3/Nmm$, were far in excess of the levels that would be expected for graphite wearing in a non-abrasive regime, with typical wear values of $10^{-8}mm^3/Nmm$. Also, in these high wear experiments, clouds of black graphite debris were blown from the interface, the wear rate was sensibly constant with sliding distance, and the worn graphite surfaces showed clean, sharp grooving, all indicative of continuing abrasive wear.

From the technological view point it was important to establish if the high wear rates that had been previously reported at the large sliding amplitudes would also occur when the amplitude of sliding was very much smaller, at the levels that could occur from component vibration. As the gas flow effect was still present at these small amplitudes it was a possibility that the wear at small slips could be high, leading to the phenomena of 'abrasive fretting'. Normally of course, without the complication of the debris scouring effect of interface flow, such a wear process would not be possible because the majority of the debris would be retained between the mating surfaces, rapidly reducing the degree of abrasion that could occur. As discussed in the earlier sections, it was postulated that wear in the presence of gas flow would be amplitude dependent, because if the magnitude of slip were small enough the wear grooves

from the abrasive features of the surface would not interact, and the bearing load would quickly be borne by their non-abrasive hinterlands. Below a certain amplitude therefore, the wear could be expected to be much reduced. The results of the present work support this postulate for both the plasma sprayed rough surface and the technologically more important nodular oxide surface. In both cases a threshold amplitude is found above which the wear increases rapidly.

A theoretical model for this amplitude effect has also been developed for an idealised surface morphology and the results from this model are shown in figures (A13) and (A14). Figure (A13) shows the variation of the ratio of the theoretical amplitude threshold limit for low wear, non-dimensionalised by the nodule radius, as a function of nodule radius. These results are for one specific loading condition ($P/Y_c = 10^{-2}$) and a family of curves is shown for a range of numerical nodular surface densities. An individual curve therefore represents the reduction of threshold amplitude as the oxide grows, provided that the number of nucleation sites for nodular growth remains constant. Figure (A14) is a carpet plot of the full theoretical solution for a wide range of the non-dimensional variables of loading condition and nodular oxide surface coverage.

For the experiments against nodular oxide it should be possible to relate the threshold amplitude at which wear begins to increase, to the theoretical prediction for that surface. The specimens employed showed considerable nodular growth, but also showed a number of areas which had nucleated raised plateaus of oxide, and a variation in the extent of oxidation, both across an individual specimen and from specimen to specimen. In addition the specimens had a surface ground finish, and the oxide nodules tended

to nucleate preferentially in the direction of the grinding marks. The theoretical assumptions of randomly dispersed and uniformly sized hemispheres were therefore a little strained for these conditions.

However, an attempt was made to ascribe a typical numerical surface density and radius of nodule to the surface employed and these were found to be roughly 13 nodules per mm^2 with a radius of approximately 60μm. Adopting these values the fractional surface coverage of nodules was 0.15. The compressive yield strength for graphite is of the order of $50N/mm^2$ and the value of P/Y_c at 5kg load was calculated to be 0.04. Interpolating on the carpet plot of figure (A14) it can be seen that the ratio of a/R for these parameters would be predicted to be 28. In practice the amplitude threshold was found to be about 900μm, giving an a/R of 15 for 60μm radius nodules. The theoretical prediction and the expermimental value are therefore in agreement to within a facor of 2, which was considered to be tolerably good, allowing for the necessity for numerous assumptions and the large possible range of the variables employed.

The significance of this work for the practical problems that initiated these studies is considerable, because for most situations the predicted threshold amplitude for higher wear rates is large compared to the likely amplitudes of adventitious vibration movement. In the experiments presented here the threshold amplitude of 900μm is large in comparison with typical structural response movement levels of less than 100μm. Also, considering the carpet plot of figure (A15), typical practical applications would generally have theoretical a/R values of some 30 to 100. For nodules

of up to 100μm radius tolerable amplitudes of the order of millimetres are predicted, well in excess of the normal levels of vibration encountered. Generally, therefore, the large sliding distances accumulated by small amplitude high frequency movement will only cause material removal at a low rate, while the larger but much less frequent movements anticipated for components will have a much higher rate of wear predicted by the earlier studies [10].

5. CONCLUSIONS

It has previously been shown that an interface gas flow can maintain materials such as graphite in a high abrasive wear regime in large amplitude (10mm) reciprocating sliding, by continuously removing the debris of the wear process from the interface. It was therefore possible that high wear rates could be encountered when such materials were worn against rough surfaces in a small amplitude oscillatory motion. This possibility was of practical significance to the life estimates for graphite bearings in some components of gas cooled nuclear reactors. The present studies have shown that:

1. The effect of gas flow is maintained at much smaller amplitudes.
2. A threshold amplitude occurs under such conditions, below which the wear is not of an abrasive nature and is much slower.
3. This threshold amplitude is related to the way in which wear grooves from neighbouring abrasive surface features interact.

A theoretical model for the wear of graphite against an idealised rough surface has been developed to examine the practical case of the reactor graphite bearings wearing against a rough nodular oxide. From the results of this analysis it can be concluded that:

4. When the nodular morphology of the oxide is known a theoretical prediction of the threshold amplitude can be made.
5. The theoretical predictions are in tolerable agreement with the limited experimental evidence available to date.
6. For a wide range of practical situations the threshold amplitude for abrasive wear is sufficiently large that typical vibratory movements will not produce a high abrasive wear rate.

The experiments and results described in the present section have been published as an external paper and were presented at the 4th. International Tribology Conference. The paper was written in co-authorship with Mr.S.C.Gordelier of the C.E.G.B. South Western Scientific Services Department.

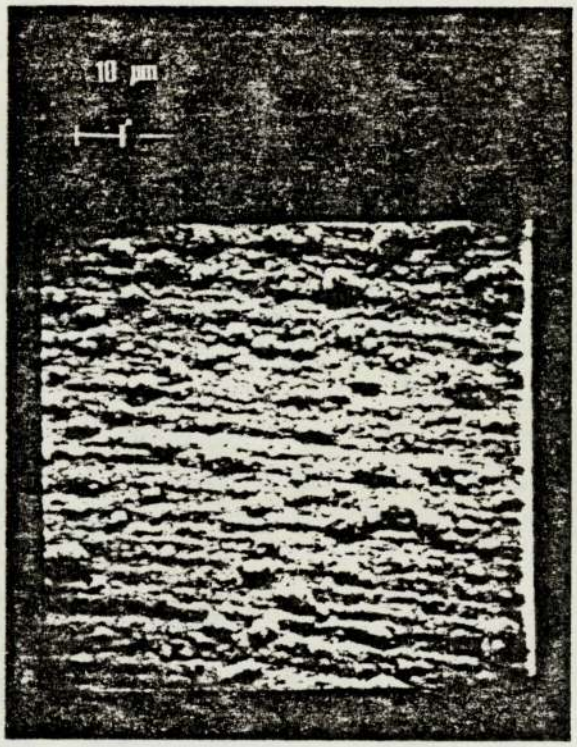

a)

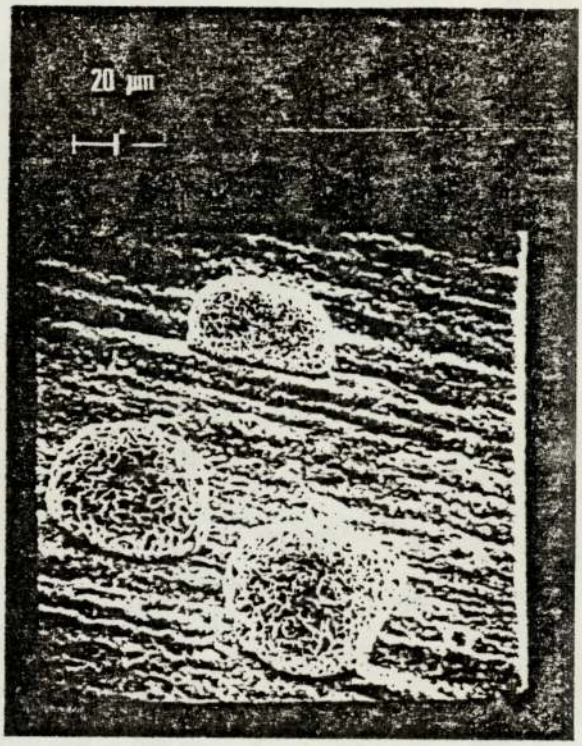

b)

FIG. A1

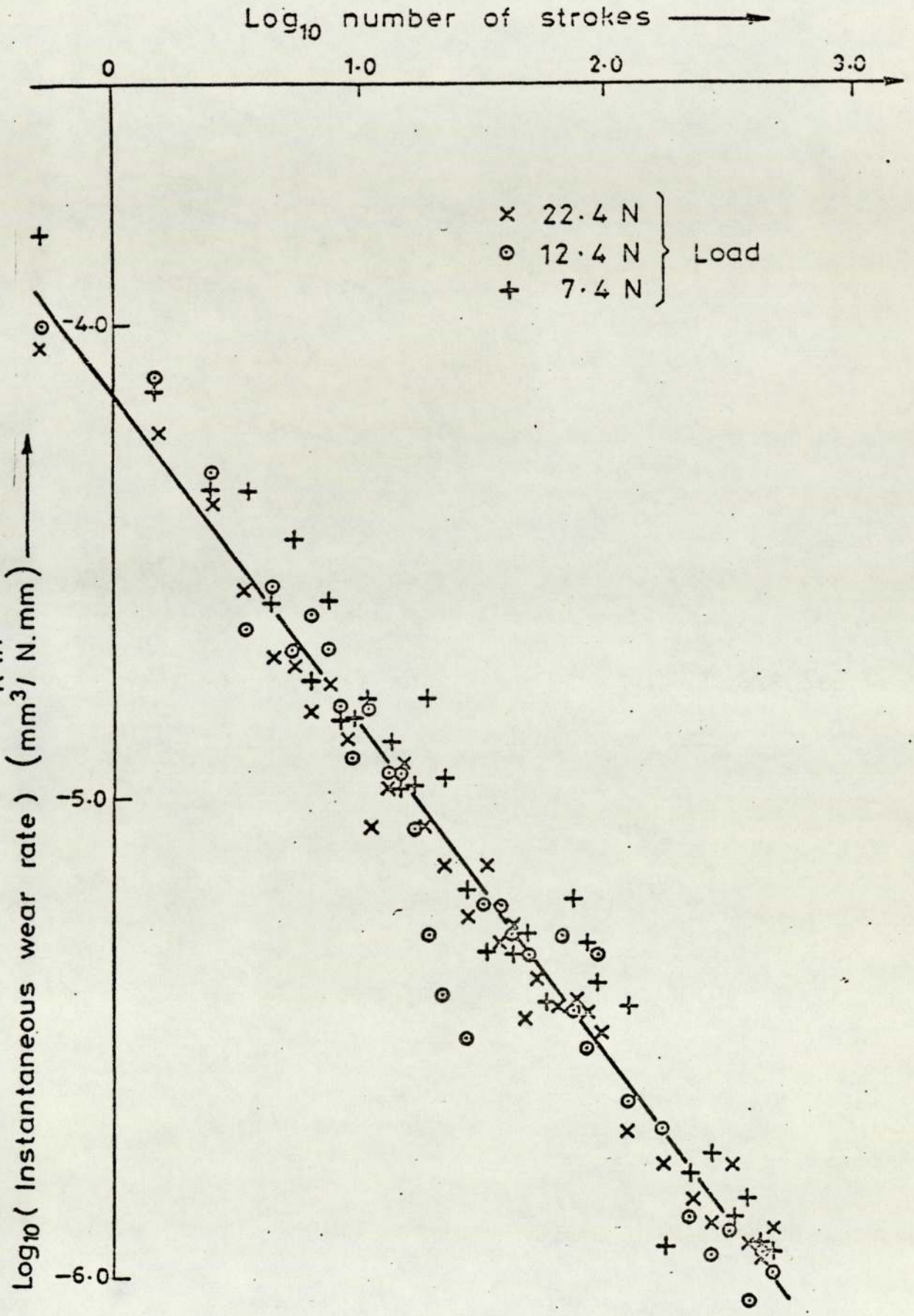
Log10 number of strokes
0
1·0
2·0
3·0
× 22·4 N
⊙ 12·4 N
+ 7·4 N
Load
-4·0
-5·0
-6·0
Log10 (Instantaneous wear rate) K in (mm3/ N.mm)

Fig. A2

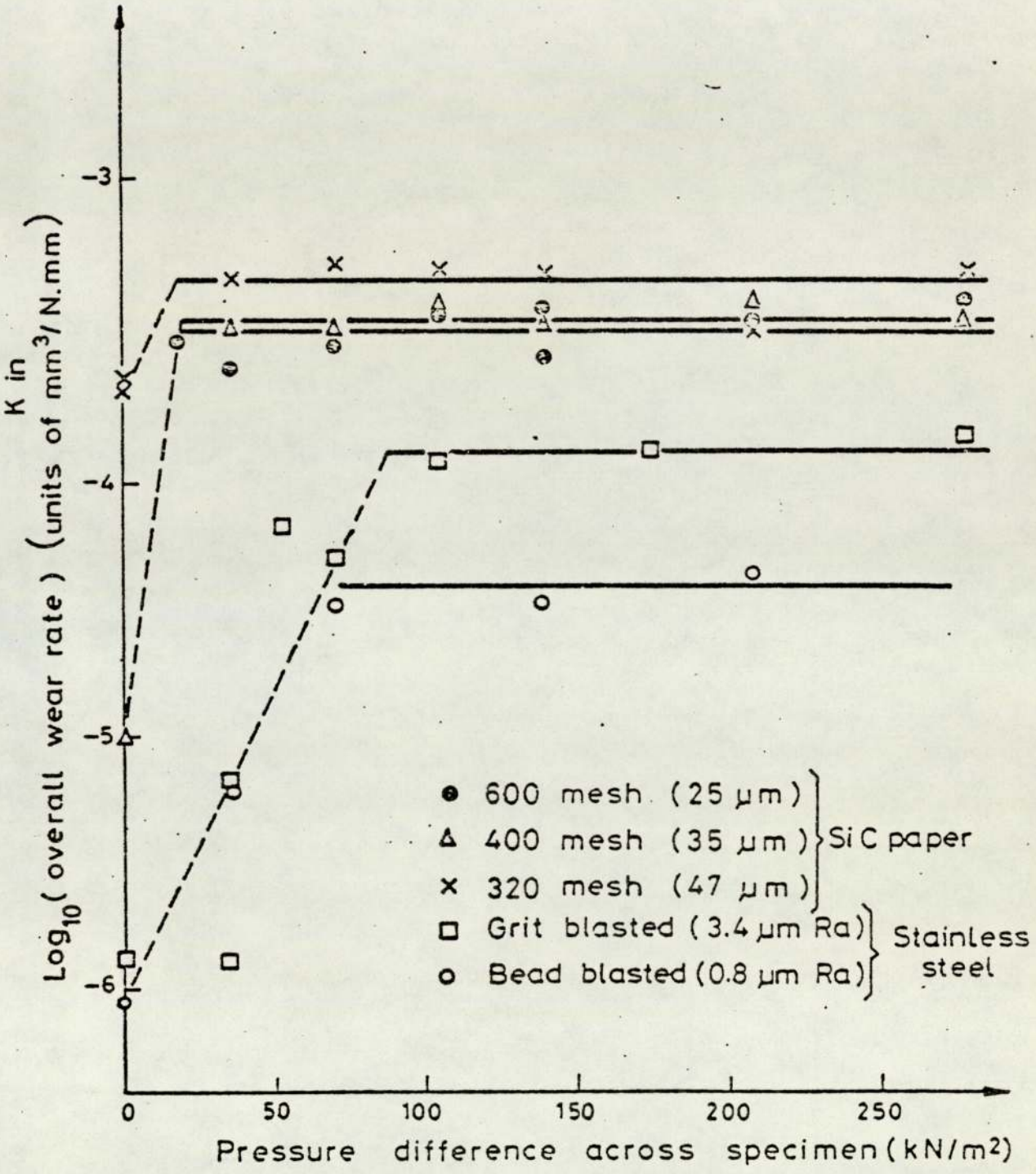
K in
Log_{10} (overall wear rate) (units of mm^3/ N.mm)
-3
-4
-5
-6
0
50
100
150
200
250
Pressure difference across specimen (kN/m^2)
600 mesh (25 μm)
400 mesh (35 μm)
320 mesh (47 μm)
SiC paper
Grit blasted (3.4 μm Ra)
Bead blasted (0.8 μm Ra)
Stainless steel

Fig. A3

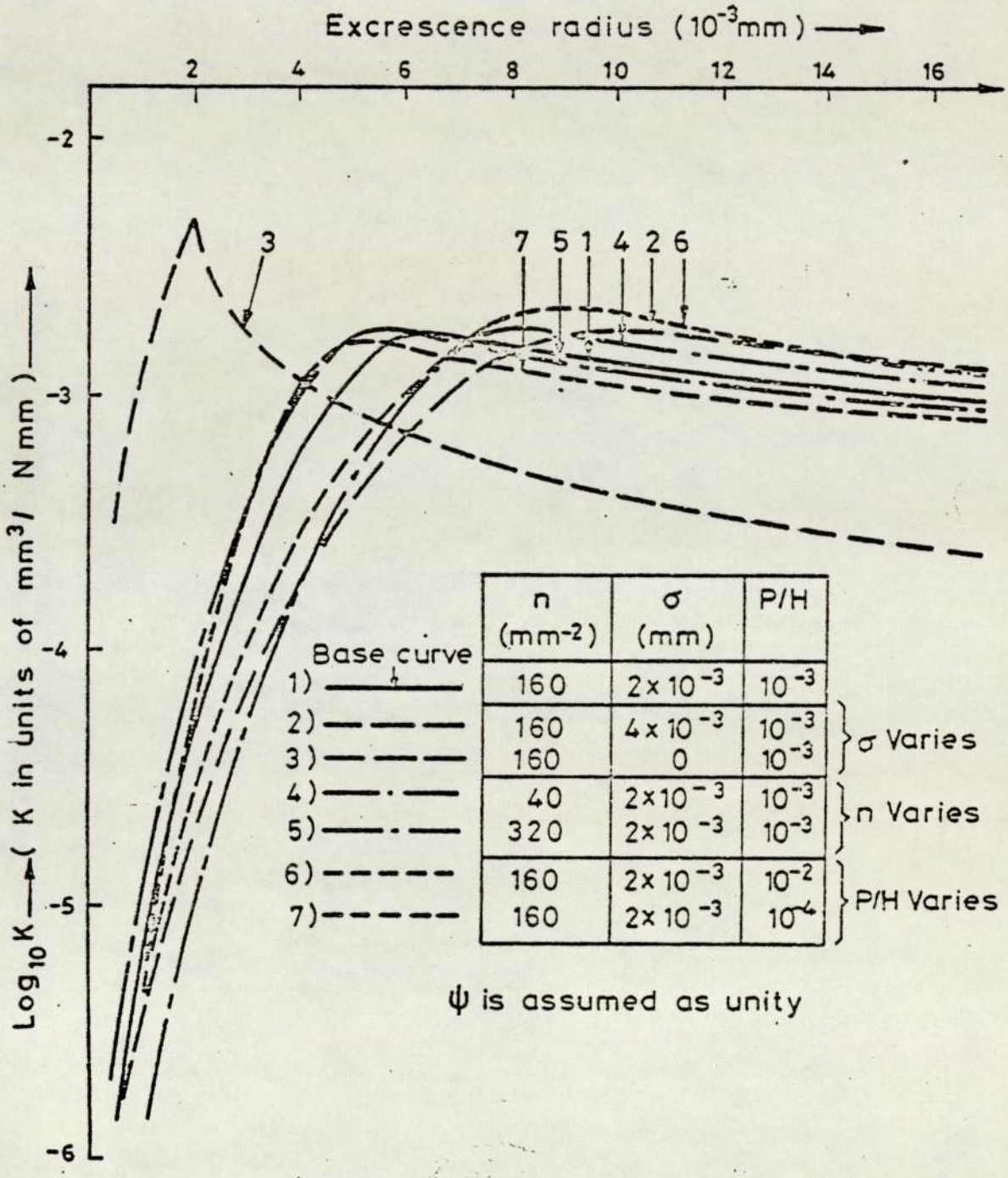

	n (mm^{-2})	σ (mm)	P/H	
1) Base curve	160	2×10^{-3}	10^{-3}	
2)	160	4×10^{-3}	10^{-3}	σ Varies
3)	160	0	10^{-3}	σ Varies
4)	40	2×10^{-3}	10^{-3}	n Varies
5)	320	2×10^{-3}	10^{-3}	n Varies
6)	160	2×10^{-3}	10^{-2}	P/H Varies
7)	160	2×10^{-3}	10^{-4}	P/H Varies

Fig. A4

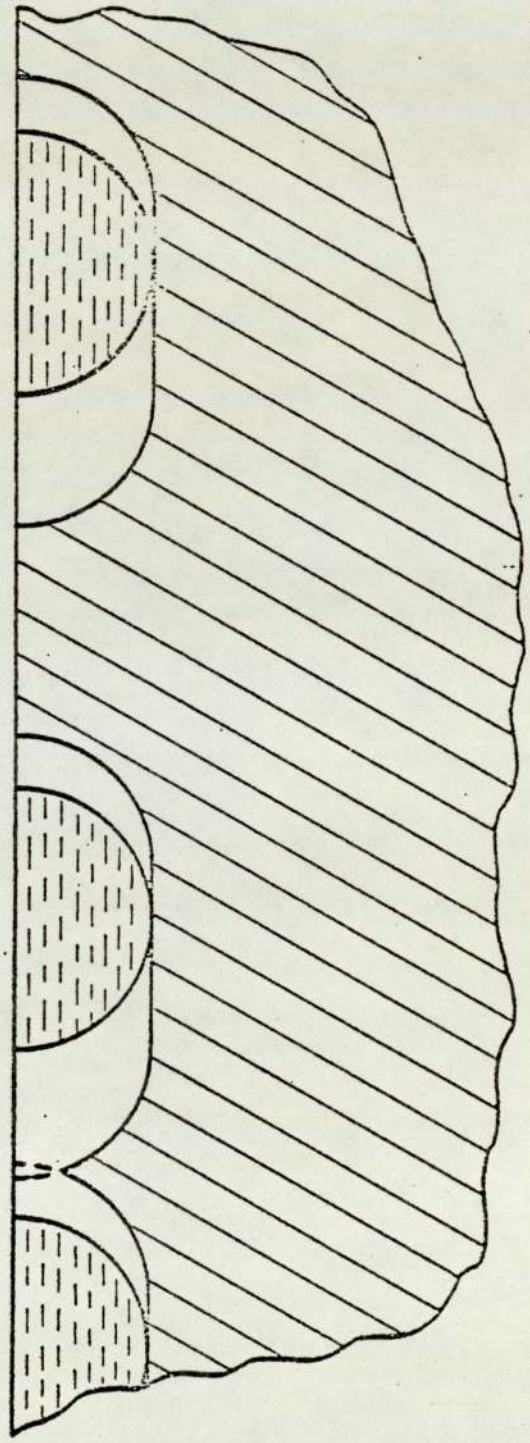

FIG. A5

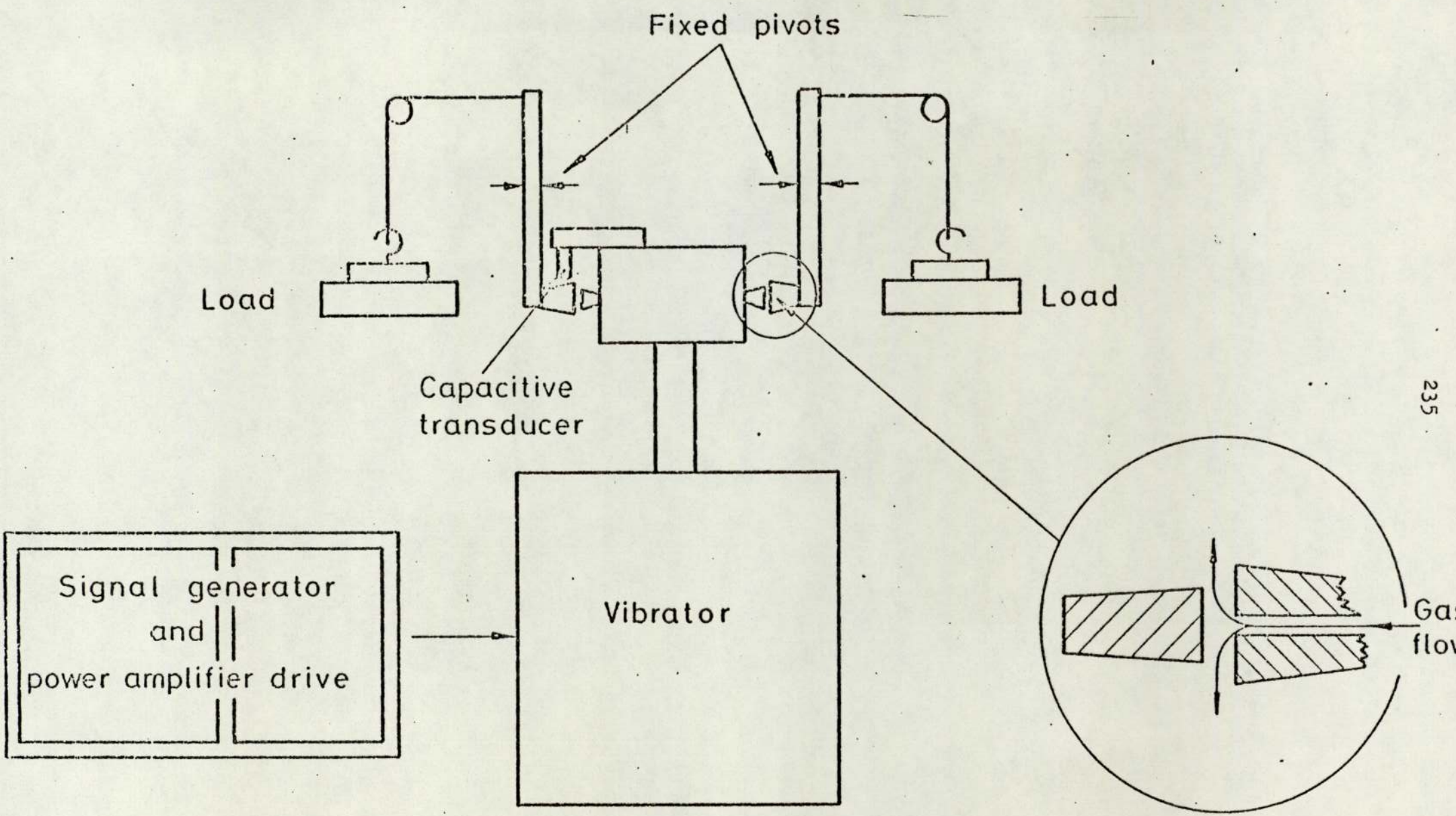
Fixed pivots
Load
Load
Capacitive transducer
Signal generator and power amplifier drive
Vibrator
Gas flow

FIG. A6

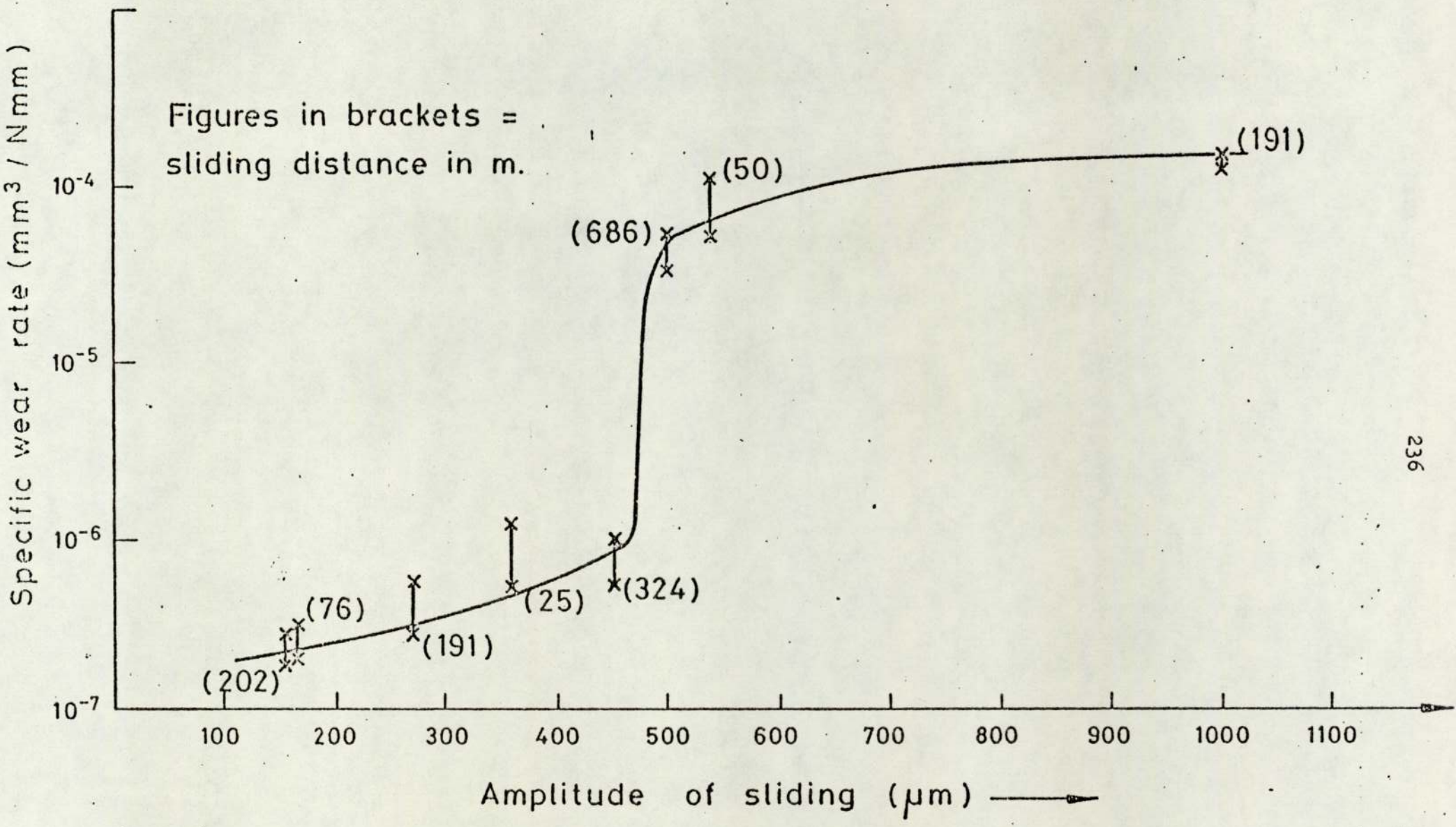
Figures in brackets =
sliding distance in m.
Specific wear rate (mm³ / Nmm)
10⁻⁴
10⁻⁵
10⁻⁶
10⁻⁷
(202)
(76)
(191)
(25)
(324)
(686)
(50)
(191)
100
200
300
400
500
600
700
800
900
1000
1100
Amplitude of sliding (μm)

Fig. A7

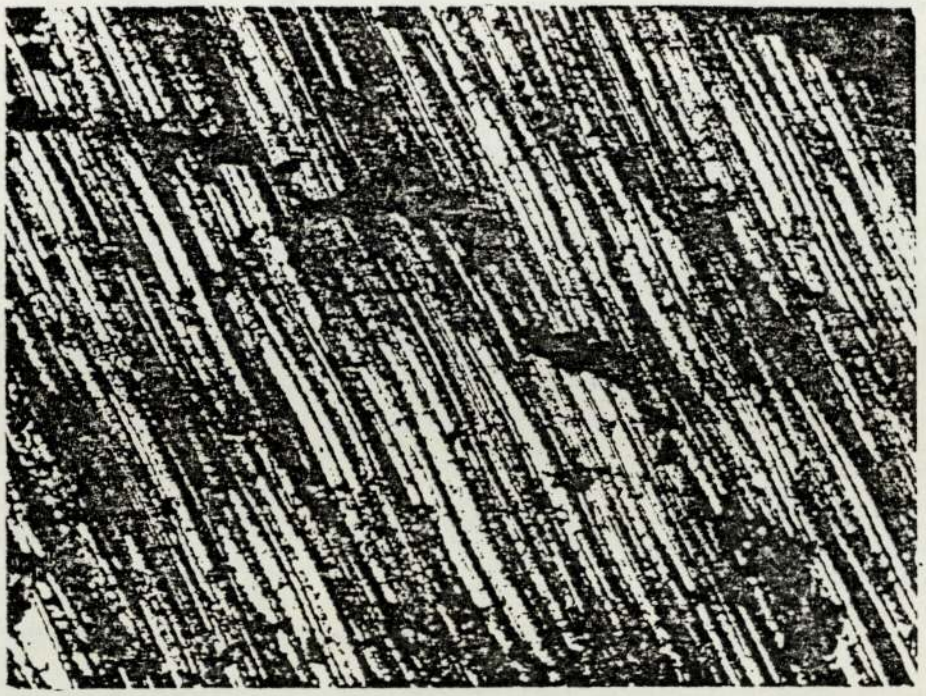

125 µm

a)

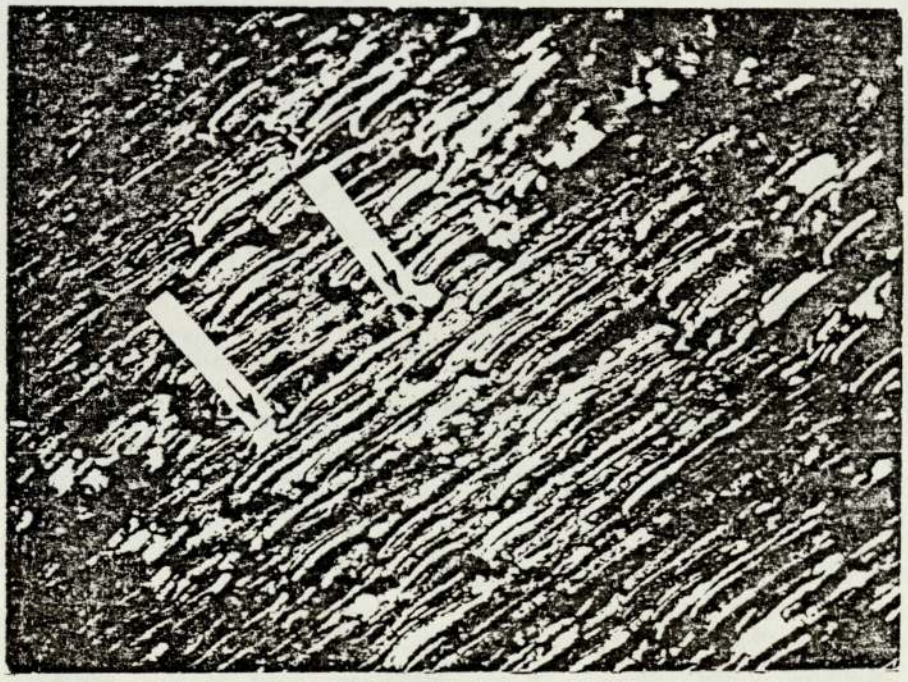

143 µm

b)

FIG. A8

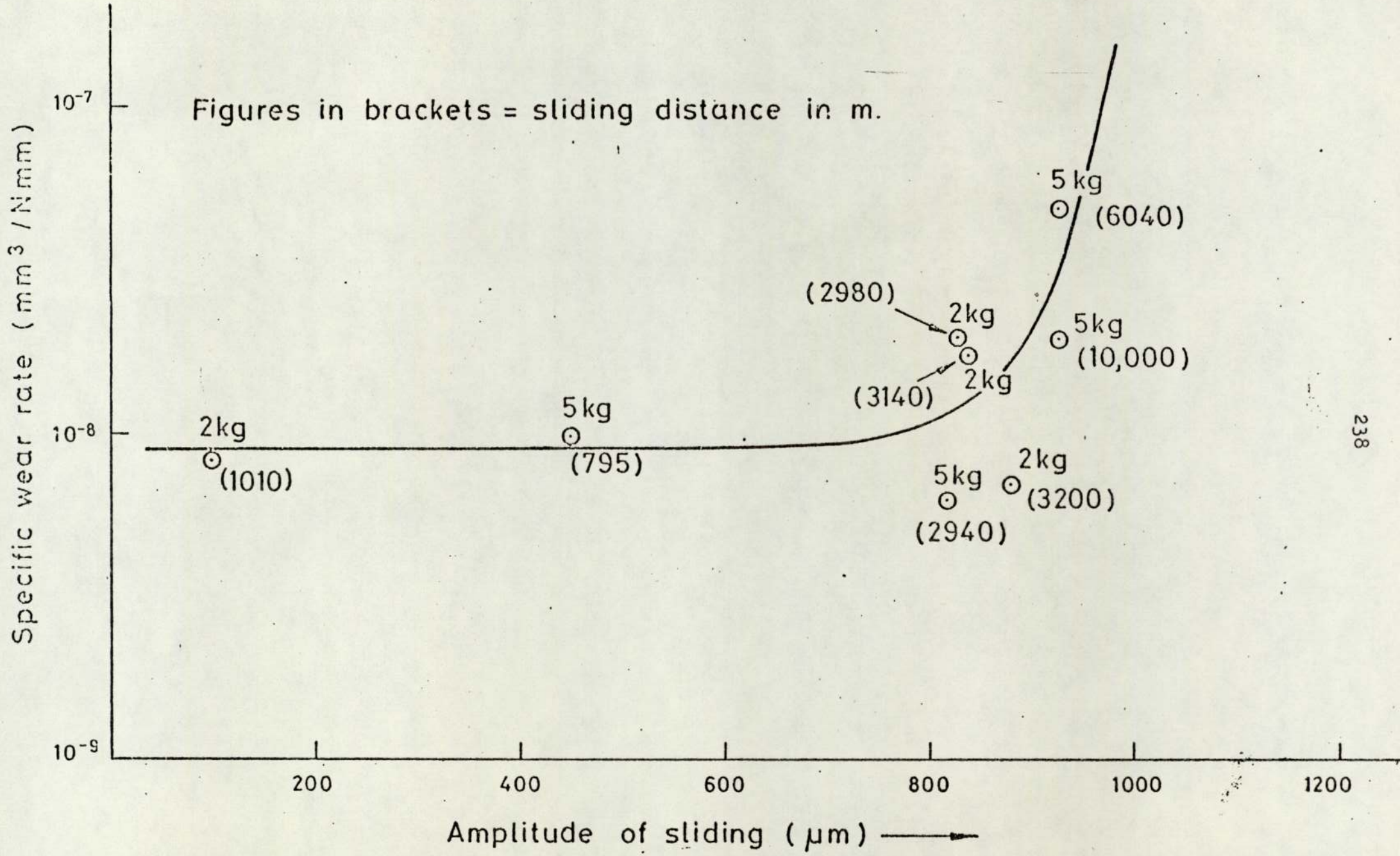
Figures in brackets = sliding distance in m.
Specific wear rate (mm³/Nmm)
10⁻⁷
10⁻⁸
10⁻⁹
2kg
(1010)
5kg
(795)
(2980)
2kg
(3140)
2kg
5kg
(6040)
5kg
(10,000)
5kg
(2940)
2kg
(3200)
200
400
600
800
1000
1200
Amplitude of sliding (μm)

Fig. A9

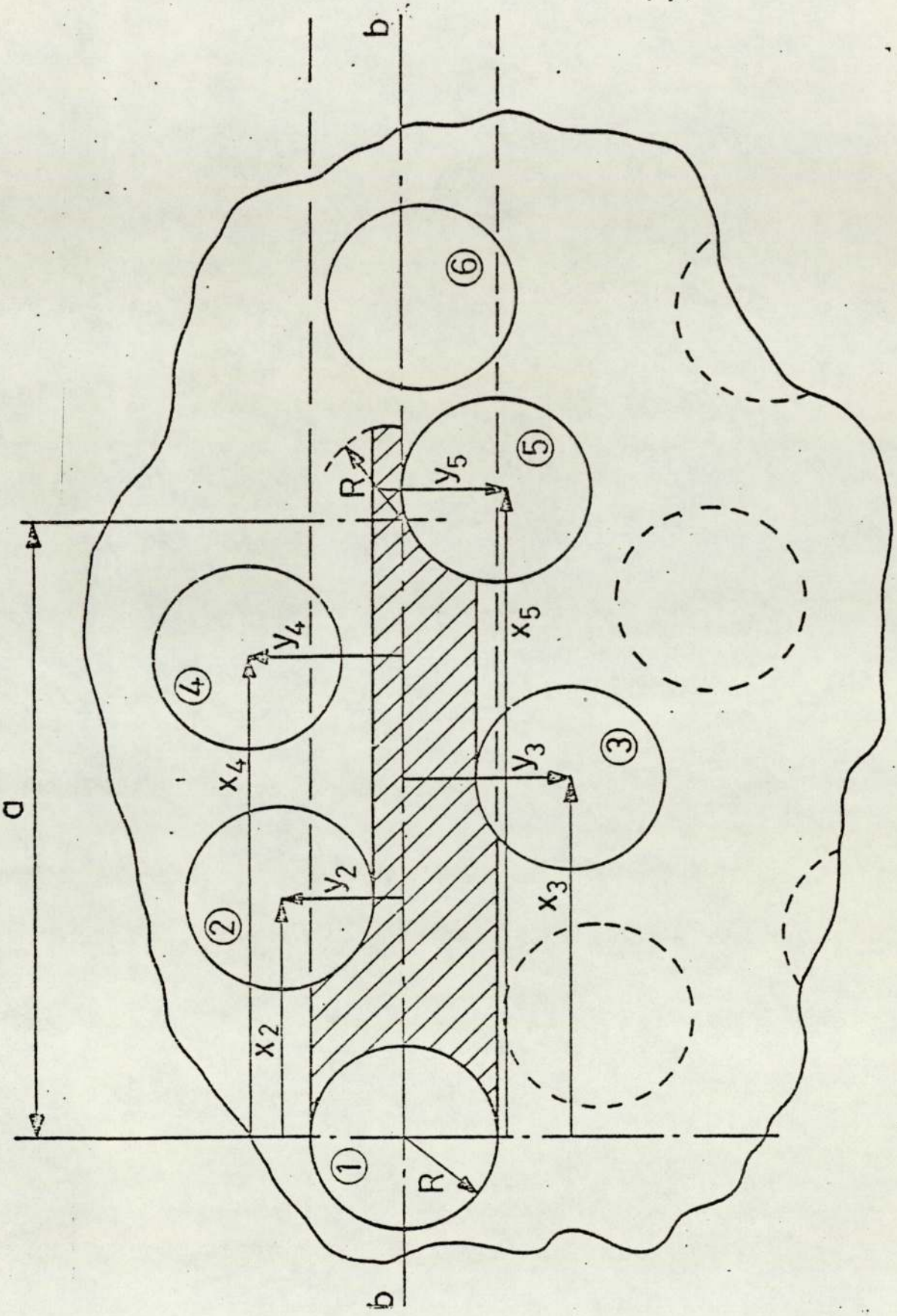

FIG. A10

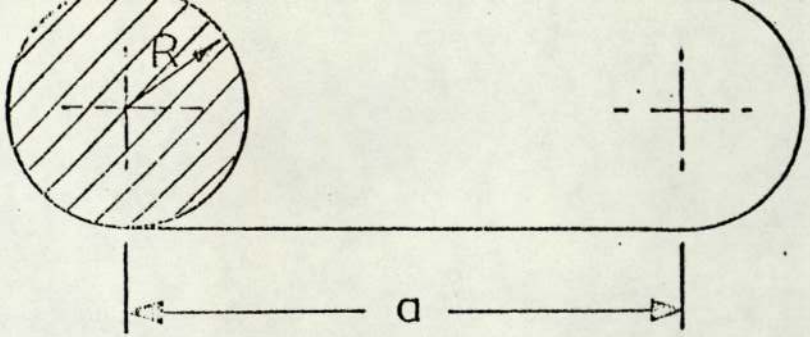

a)

Groove Area $= 2Ra + \pi R^2$

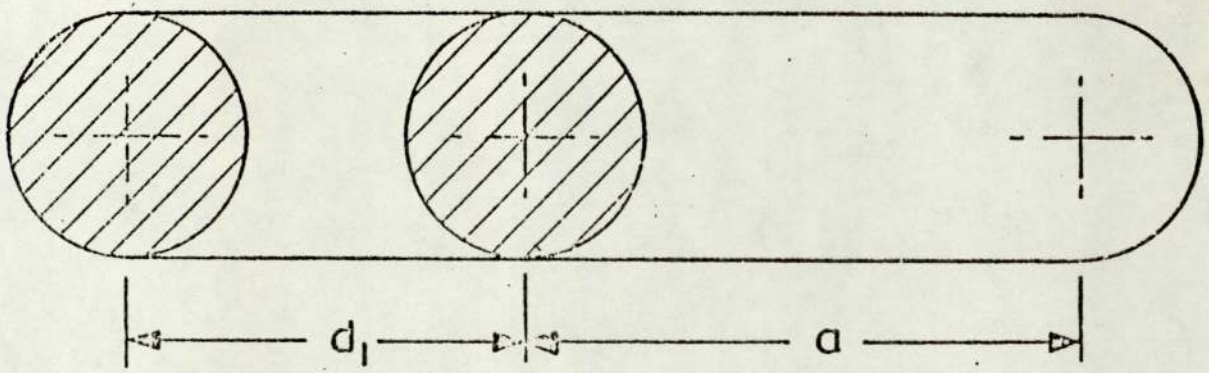

b)

Groove Area $= 2R(a + d_1) + \pi R^2$

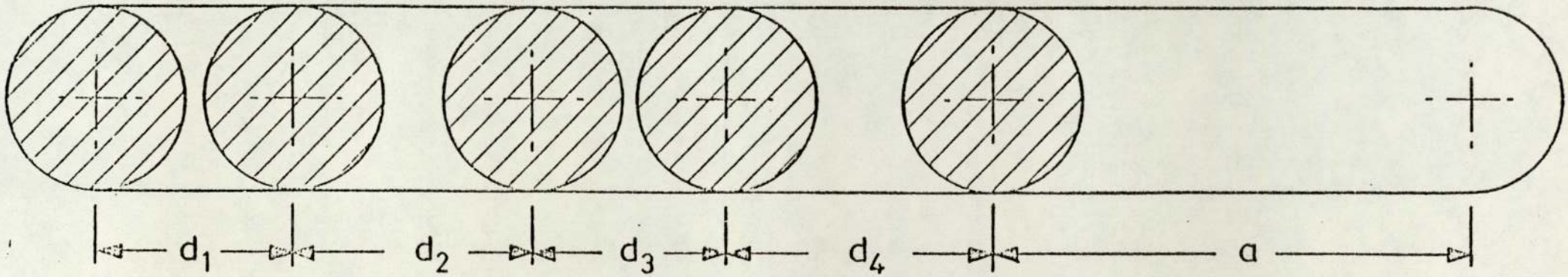

c)

FIG. A11

Groove Area $= 2R(a + d_1 + d_2 + d_3 + d_4) + \pi R^2$

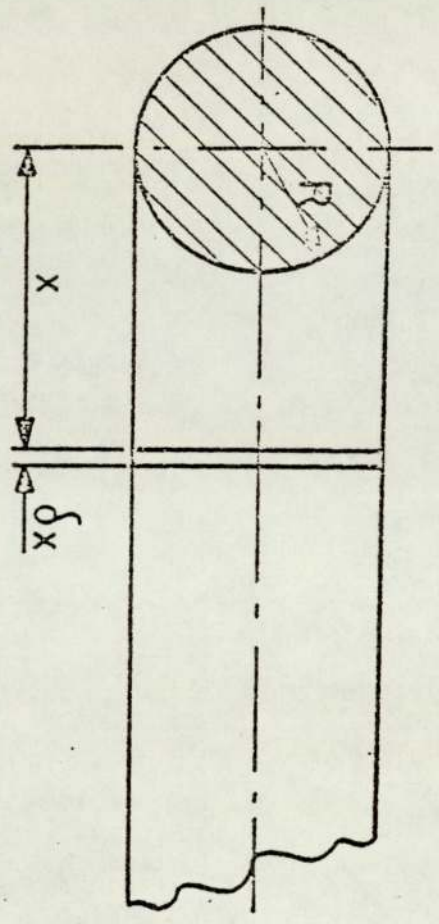

FIG. A12

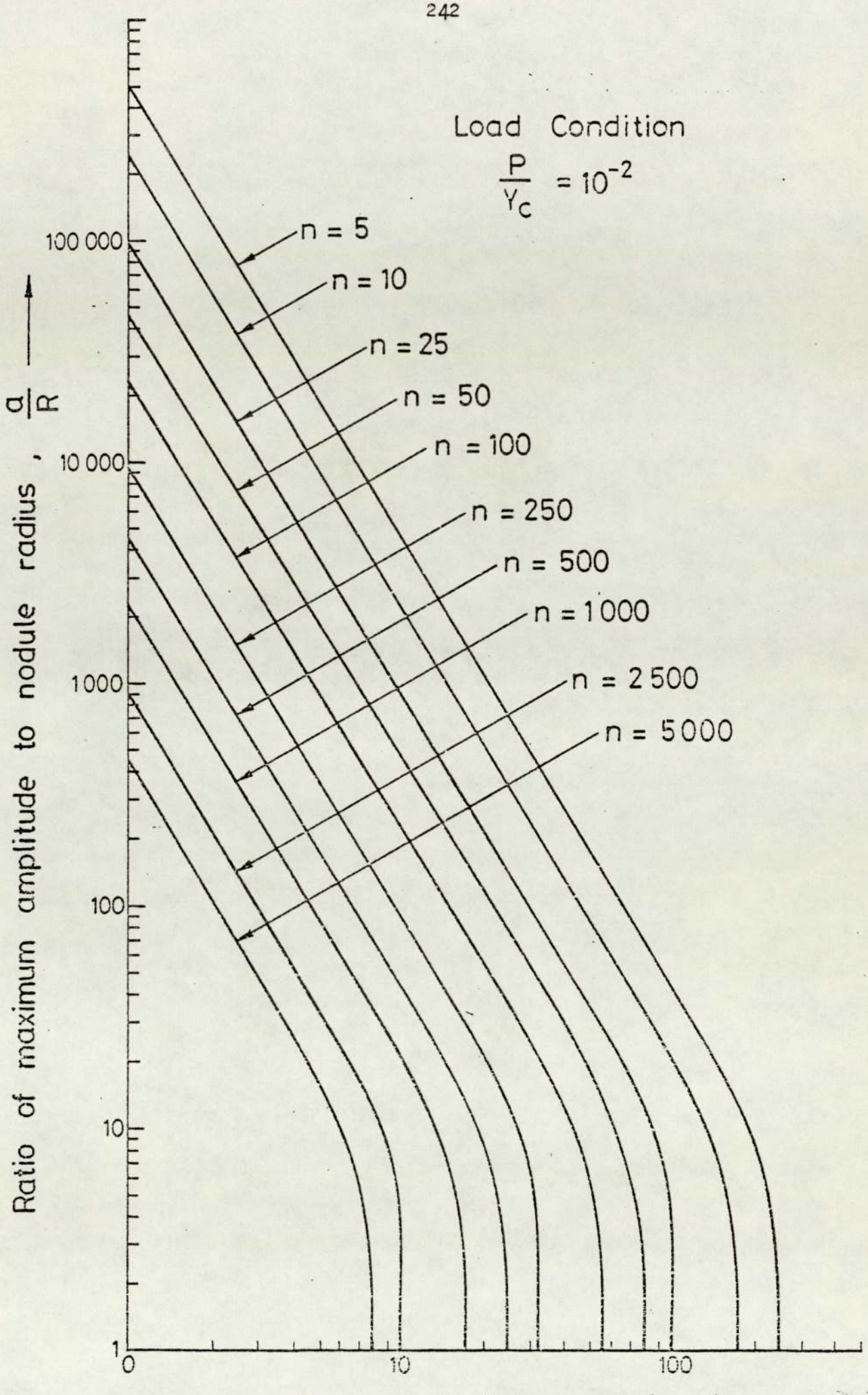
Load Condition
P/Yc = 10^-2
n = 5
n = 10
n = 25
n = 50
n = 100
n = 250
n = 500
n = 1000
n = 2500
n = 5000
Ratio of maximum amplitude to nodule radius, a/R
100 000
10 000
1000
100
10
1
0
10
100
Radius of Nodules R (μm)

Fig A.13

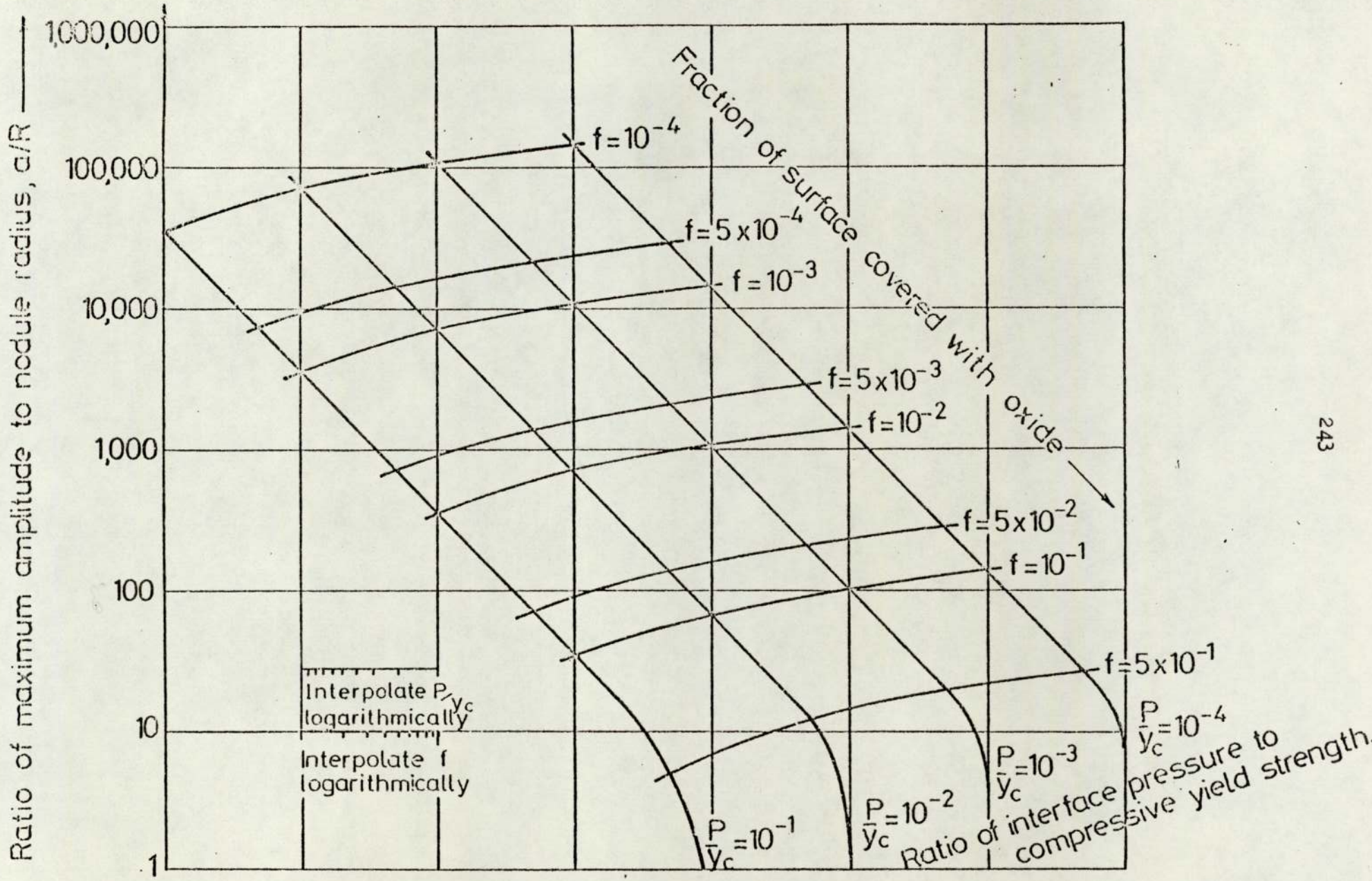
Ratio of maximum amplitude to nodule radius, a/R
1,000,000
100,000
10,000
1,000
100
10
1
Fraction of surface covered with oxide
f = 10⁻⁴
f = 5 x 10⁻⁴
f = 10⁻³
f = 5 x 10⁻³
f = 10⁻²
f = 5 x 10⁻²
f = 10⁻¹
f = 5 x 10⁻¹
Interpolate P/yc logarithmically
Interpolate f logarithmically
P/yc = 10⁻⁴
P/yc = 10⁻³
P/yc = 10⁻²
P/yc = 10⁻¹
Ratio of interface pressure to compressive yield strength.

Fig A14.